

Insights into Perovskite Solar Cells: Performance Enhancement and Degradation Mechanisms

Kun Sun

Vollständiger Abdruck der von der TUM School of Natural Sciences der Technischen Universität München zur Erlangung eines

Doktors der Naturwissenschaften (Dr. rer. nat.)

genehmigten Dissertation.

Vorsitz: Prof. Dr. David Egger

Prüfende der Dissertation:

1. Prof. Dr. Peter Müller-Buschbaum
2. Prof. Dr. Johanna Eichhorn

Die Dissertation wurde am 31.10.2024 bei der Technischen Universität München eingereicht und durch die TUM School of Natural Sciences am 12.12.2024 angenommen.

For my parents Juan Li
and Yuancheng Sun.

*Family support is the wind beneath my wings, empowering me
to soar*

.

Abstract

The thesis is focused on the fabrication of highly efficient perovskite solar cells (PSCs), upscaling the PSCs, and investigating their operational stability under external stressors, particularly with advanced X-ray scattering methods. The thesis is divided into three projects: The first project focuses on modifying the buried interface of the perovskite/electron blocking layer (EBL) to facilitate hole transport and, consequently, achieve a higher power conversion efficiency (PCE). The second project investigates the operational stability of PSCs under AM 1.5G illumination and $75 \pm 5\%$ relative humidity. The third project studies the reduced-dimensional perovskites (RDPs) to gain a better understanding of their phase purity, orientation, charge carrier dynamics, and photostability.

Diese Arbeit fokussiert auf der Herstellung hocheffizienter Perowskit-Solarzellen (PSCs), der Skalierung der PSCs und der Untersuchung ihrer Betriebsstabilität unter externen Stressfaktoren, insbesondere mit fortschrittlichen Röntgenstreuungsmethoden. Die Arbeit ist in drei Projekte unterteilt: Das erste Projekt konzentriert sich auf die Modifikation der inneren Grenzfläche der Perowskit/-Elektronenblockierschicht (EBL), um den Lochtransport zu erleichtern und dadurch eine höhere Energieumwandlungseffizienz (PCE) zu erzielen. Im zweiten Projekt wird die Betriebsstabilität von PSCs unter AM 1.5G-Beleuchtung und $75 \pm 5\%$ relativer Luftfeuchtigkeit untersucht. Das dritte Projekt befasst sich mit reduzierten dimensionalen Perowskiten (RDPs), um ein besseres Verständnis ihrer Phasenreinheit, Orientierung, Ladungsträgerdynamik und Photostabilität zu gewinnen.

Contents

Abstract	i
List of Abbreviations	vii
1 Introduction	1
2 Theoretical Background	5
2.1 Perovskites	5
2.1.1 3D Perovskites	5
2.1.2 Reduced-Dimensional Perovskites	7
2.2 Perovskite Crystal Growth and Thin Film Crystallization	11
2.2.1 Nucleation and Growth	12
2.2.2 Formation Energy	15
2.3 Perovskite Solar Cells	15
2.3.1 Solar Spectrum	15
2.3.2 Working Principles of Perovskite Solar Cells	17
2.3.3 Power Conversion Efficiency of Solar Cells	19
2.4 Operation Stability of Perovskite Solar Cells	20
2.4.1 Moisture-Induced Degradation	22
2.4.2 Heat-Induced Degradation	23
2.5 X-ray Scattering Techniques	25
2.5.1 X-ray Diffraction	27
2.5.2 Grazing-Incidence Small-Angle X-ray Scattering	28
2.5.3 Grazing-Incidence Wide-Angle X-ray Scattering	30
3 Sample Preparation	35
3.1 Substrates	35
3.2 Materials	36

3.3	Electron Blocking Layer	36
3.4	Hole Blocking Layer	36
3.5	Perovskite Layer	38
3.5.1	Perovskite Layer Used in Chapter 5	38
3.5.2	Perovskite Layer Used in Chapter 6	38
3.5.3	Perovskite Layer Used in Chapter 7	38
3.6	Metal Electrodes	39
3.7	Devices	39
4	Sample Characterization	41
4.1	Scanning Electron Microscopy	41
4.2	Atomic Force Microscopy	42
4.3	Optoelectronic Characterization	43
4.3.1	Photoluminescence Spectroscopy	43
4.3.2	Confocal Photoluminescence Mapping	45
4.3.3	UV-Vis Spectroscopy	45
4.3.4	Transient Absorption Spectroscopy	47
4.4	Solar Cell Characterization	48
4.4.1	Current density-Voltage measurement	48
4.4.2	External Quantum Efficiency	49
4.5	Experimental Setups for X-ray Scattering	49
5	Unraveling the Modification Effect at NiO_x/Perovskite Interfaces	53
5.1	Preface	54
5.2	Solar Cell Performance and Morphology	55
5.2.1	Crystallinity and Orientation	59
5.3	Optoelectronic Properties and Chemical Reaction	61
5.4	Impact of Iodine Locations on the Optoelectronic Properties.	65
5.5	Long-term Stability	70
5.6	Conclusion	73
6	Degradation of Perovskite Solar Cells under Light and Humidity	75
6.1	Preface	76
6.2	Solar Cell Evolution under Light and Humidity	77
6.3	Structural Evolution during Device Operation	82
6.4	Crystallinity Evolution	87
6.5	Conclusion	91

7	Structure and Charge Carrier Behavior in Reduced-Dimensional Perovskites	93
7.1	Preface	94
7.2	Phase Purity and Spatially Vertical Homogeneity	95
7.3	Growth Mechanisms of RDPS	101
7.4	Charge Carrier Behavior	104
7.5	Solar Cell Performance and Stability	112
7.6	Discussion	118
8	Summary and Outlook	119
	List of Publications	147
	Acknowledgements	153

List of Abbreviations

<i>FF</i>	fill factor
<i>J_{SC}</i>	short-circuit current
<i>PCE</i>	power conversion efficiency
<i>V_{OC}</i>	open-circuit voltage
AFM	atomic force microscope
AM	air mass
BCP	Bathocuproine
CB	chlorobenzene
CsI	Cesium iodide
DI water	deionized water
DMF	N,N-Dimethylformamide
DMSO	Dimethyl sulfoxide
DWBA	distorted wave Born approximation
EBL	electron blocking layer
FAI	Formamidinium iodide
FWHM	full width at half maximum
GISAXS	grazing-incidence small-angle X-ray scattering
GIWAXS	grazing-incidence wide-angle X-ray scattering

HBL	hole blocking layer
ITO	indium doped tin oxide
LITFSI	Bis(trifluoromethane)sulfonimide lithium salt
LMA	local monodisperse approximation
MAI	Methylammonium iodide
PbI ₂	lead iodide
PCBM	[6,6]-Phenyl C61 butyric acid methyl ester
PDMA	1,4-phenylenedimethan ammonium
PEAI	Phenethylammonium iodide
PEDOT:PSS	(Poly(3,4-ethylenedioxythiophene) Polystyrene Sulfonate)
PL	photoluminescence
PSCs	perovskite solar cells
RDPs	reduced-dimensional perovskites
SDD	sample-to-detector distance
SEM	scanning electron microscopy
SLD	scattering length density
SnO ₂	tin(IV) oxide
spiro-OMeTAD	titanium(IV) bis(ammonium lactate) dihydroxide
TA	transient absorption spectroscopy
tBP	4-tertbutylpyridine
UV	ultra-violet
XRD	X-ray diffraction

Introduction

Organic–inorganic hybrid metal halide perovskites have become a groundbreaking class of light-harvesting materials in solar cell applications. With less than two decades of research, the power conversion efficiency (PCE) of perovskite solar cells (PSCs) has experienced explosive growth, recently reaching a remarkable value of 26.1% for single junction PSCs and 33.9% for perovskite-Si tandem PSCs [1].

Depending on the sequence of device layers deposited on the substrate, PSCs can be divided into two types of architectures, namely regular architecture (negative-intrinsic-positive, n-i-p) and inverted architecture (positive-intrinsic-negative, p-i-n). Ever since the utilization of tin oxide (SnO_2), the PCEs of n-i-p type of PSCs have skyrocketed. Nevertheless, in the aforementioned highly efficient PSCs, stability issues persist, mainly due to their commonly used charge transport layers (Spiro-OMeTAD), which require additional doping and are prone to oxidation. Typically, a good dopant with high conductivity is hydrophilic and prone to ion migration, which enhances device instability [2]. Inverted PSCs require no additional doping or oxidation, making their charge transport layers more stable compared to those in PSCs with a regular structure. In the perovskite field, the use of self-assembled monolayers (SAMs) has enabled inverted PSCs to gradually catch up with and even surpass the PCEs of PSCs with a regular structure [3], despite some wettability issues remained. In addition to SAMs, inorganic materials, particularly oxides such as NiO_x and CuO_x , can also be used as electron-blocking layers (also called as hole transport layers, HTLs) in inverted PSCs. However, some challenges, such as surface defects and relatively low mobility, hinder their application in this field [4]. Hence, the first project (Chapter 5) aims to resolve this issue.

In addition to improving the PCE of PSCs, operational stability is another obstacle hindering their real-world applications. For example, compared to the average lifetime of silicon-based PV panels (25 to 30 years), PSCs currently only maintain their original PCE for a maximum of a few thousand hours [5]. The stability of PSCs depends on many

factors (aging conditions, perovskite composition, charge transport layers, electrode, passivation, encapsulation, and so on) and is not an easy-to-solve issue. In terms of aging conditions, in 2020, a consensus statement of stability assessment was released, and the researchers are encouraged to utilize the International Summit on Organic Photovoltaic Stability testing protocols (ISOS protocols) to achieve comparable results [6]. Despite significant enhancements in the stability of PSCs over the past few years, their stability, particularly under external stressors (humidity, light, heat, bias), still falls short of industry standards, and their degradation mechanisms remain poorly understood. Hence, in the second project (Chapter 6), I aim to understand the light and humidity-induced degradation of PSCs with the help of the X-ray scattering method.

To further use perovskite solar cells on a large scale and integrate them into industrial fabrication production lines, high throughput coating, for example, slot-die coating, roll-to-roll coating, and inject printing, is required. Slot-die coating stands out from other scalable methods mainly because of its variable coating speed and the ability to coat over rigid and flexible substrates [7]. In addition, reduced-dimensional perovskites have demonstrated superior environmental stability compared to their 3D counterparts, although their PCE still lags behind. Despite their widespread use as passivation layers in 3D PSCs and active layers in quasi-2D PSCs, there is still a lack of comprehensive understanding of their utilization in PSCs. Therefore, the third project (Chapter 7) aims to systematically explore reduced-dimensional perovskites with varied dimensionalities using a scalable slot-die method.

In this thesis, I first introduce the reader to the theoretical background in Chapter 2. This covers the fundamental knowledge of perovskites, including 3D and reduced-dimensional perovskites and their optoelectric properties, and the formation and crystallization process. Hereafter, I move on to the fundamentals of perovskite solar cells, from their basic working principle to the basic physic model. Afterward, I discuss the operational stability issue of perovskite solar cells and their degradation mechanism under light, humidity, and heat conditions. Furthermore, the principles of X-ray scattering are detailed since this is the main technique utilized in this thesis. After that, I continue with experimental details on the sample fabrication and the materials used in this thesis in Chapter 3. This covers the substrates used for film deposition and device fabrication, including the fabrication details about the hole and electron blocking layer, perovskite layer, e.g., 3D and reduced-dimensional perovskites, as well as electrode deposition. Chapter 4 outlines the characterization methods used in this thesis, including techniques that probe their optoelectronic properties, surface morphology, structure and crystallinity, and device performance, together with the experimental setups and sample environments at the synchrotron facilities.

The first project (Chapter 5) particularly addressed the intrinsic defects (Ni vacancies) in NiO_x film and I vacancies at the buried interface of the perovskite layer in inverted perovskite solar cells by using iodine-substituted phenyl acids (Figure 1.1, top left panel). This modification demonstrates that the acid functional groups strongly coordinate with the Ni vacancies, leading to high conductivity and improved hole transport capacity. As a result, the power conversion efficiency and long-term stability of inverted PSCs are enhanced.

After achieving a decent power conversion efficiency of perovskite solar cells, I shift to study their operation stability and degradation mechanism. Chapter 6 presents results and discussion on the degradation mechanism of PSCs under AM 1.5G illumination and $75 \pm 5\%$ humidity (Figure 1.1, bottom left panel). In addition, different types of PSCs are used in this study to further investigate the effects of buried interface engineering on the stability of PSCs.

Chapter 7 discusses the structural and photophysical properties of reduced-dimensional perovskites with different dimensionalities (Figure 1.1, right panel).

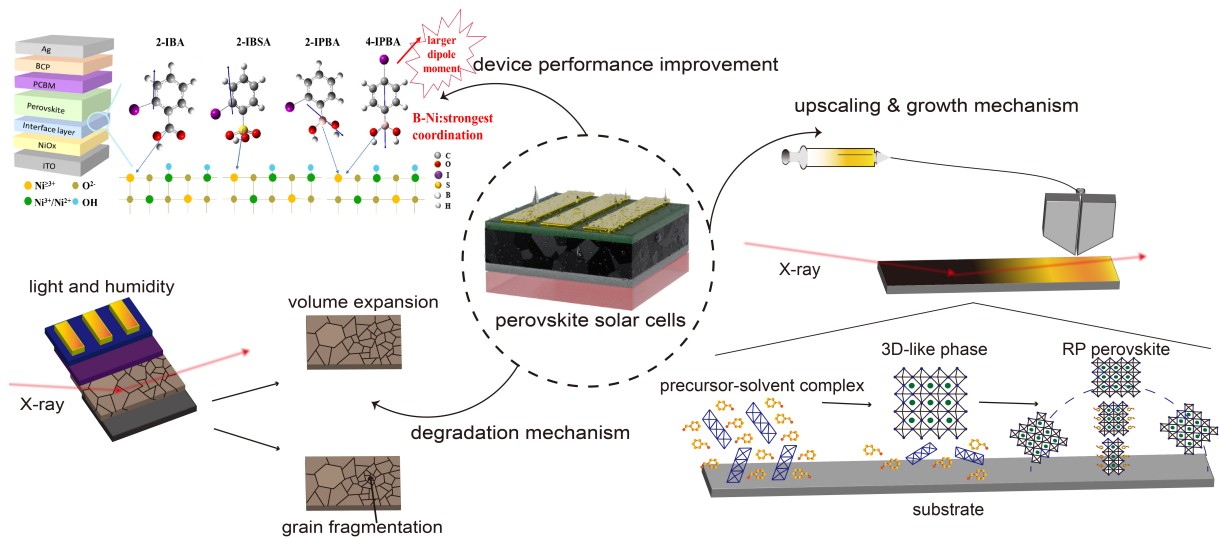


Figure 1.1: Overview of the projects covered in this PhD thesis. Top left panel: Schematic illustration of utilizing phenyl acids to reduce Ni vacancies in inverted perovskite solar cells; Bottom left panel: Illustration of the degradation mechanism of perovskite solar cells under light and humidity; Right panel: Diagram of the growth mechanism of the slot-die coated reduced-dimensional perovskite.

This chapter underlines the utilization of Ruddlesden-Popper (RP) RDPs with lower dimensionality ($n=2$) as passivation layers and the utilization of Dion-Jacobson (DJ) with higher dimensionality ($n=4$) RDPs as the active layer in quasi-2D PSCs. In addition, I further emphasize the growth mechanism of reduced-dimensional perovskites and their

photostability.

I summarize the thesis in Chapter 8, followed by the references listed in the Bibliography. Then, the first and coauthor publications, as well as scientific contributions, including contributed talks and posters, are listed.

Theoretical Background

This chapter gives an introduction of the theoretical background of this thesis, in Section 2.1, 3D perovskites and reduced-dimensional perovskites, their structural and optoelectronic properties are elucidated. Section 2.2 describes the nucleation and crystallization process of perovskites in detail. Section 2.3 and Section 2.4 further elaborate on the working principles of perovskite solar cells (PSCs) and their operational stability under external stressors. In addition, the fundamental knowledge of the X-ray scattering technique is elaborated in Section 2.5.

2.1 Perovskites

2.1.1 3D Perovskites

Structural Properties

The 3D perovskite structure is typically defined as ABX_3 with a corner-sharing BX_6 octahedra surrounding a larger A-site cation, where cations A, B, and anion X refer to methylammonium (MA) or formamidinium (FA), lead or tin, and halogen, respectively. A tolerance factor t (also called as Goldschmidt factor) is commonly used to validate the structural stability of perovskites according to the chemical formula and the ionic radii of respective ion:

$$t = \frac{r_A + r_X}{\sqrt{2}(r_B + r_X)} \quad (2.1)$$

In general, perovskites with a tolerance factor in the range of 0.9–1.0 have a cubic structure, where a tolerance factor of 0.7–0.9 leads to a distorted perovskite structure with tilted octahedra. In particular, when $t < 0.8$, perovskites tend to form an orthorhombic structure (Figure 2.1), while a hexagonal structure forms when $t > 1.0$ [8].

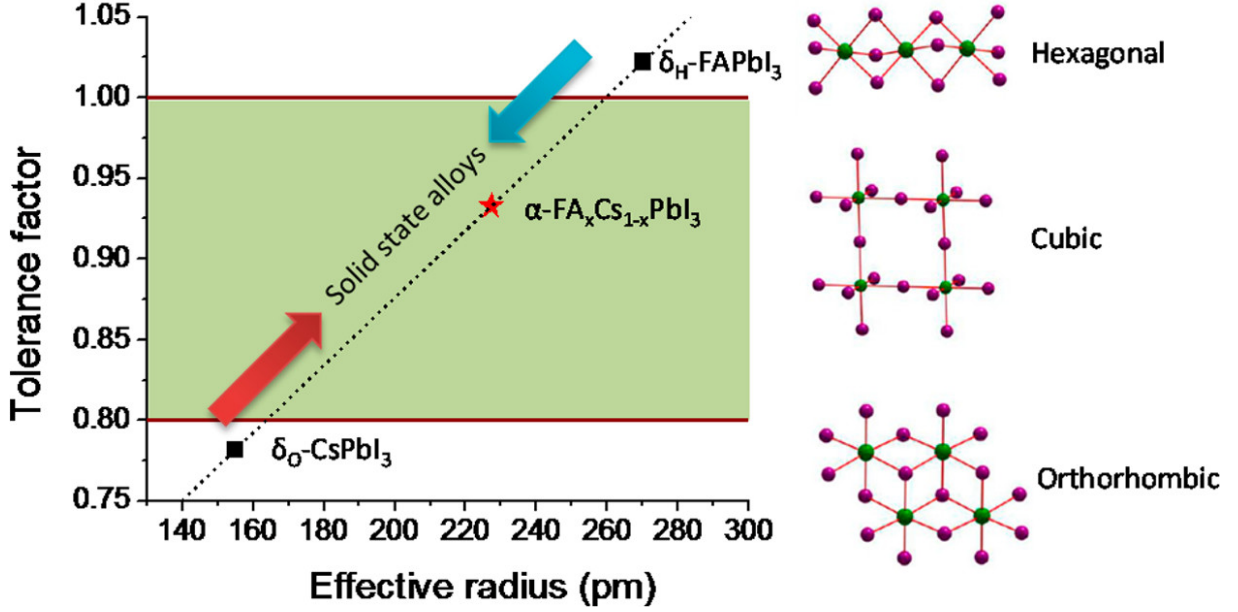


Figure 2.1: Relations between tolerance factor and crystal structure of perovskites. Reproduced from Ref. [8] with permission. Copyright 2016, American Chemical Society.

Optoelectronic Properties

The charge carrier dynamics is characterized by the diffusion coefficient ($D_{n,p}$) and charge carrier mobility ($\mu_{n,p}$), which can be expressed by the Einstein equation:

$$\mu_{n,p} = \frac{eD_{n,p}}{k_B T} \quad (2.2)$$

where e , k_B , and T are electronic charges, Boltzmann constant, and temperature, respectively. The diffusion length (L_D) is highly related to the diffusion coefficient and the photoluminescence lifetime (τ). In other words, high mobility and long charge carrier lifetime contribute to a long diffusion length.

$$L_D = \sqrt{\frac{k_B T \mu_{n,p} \tau}{e}} = \sqrt{D_{n,p} \tau} \quad (2.3)$$

Charge recombination dynamics in perovskite solar cells can be expressed by:

$$\frac{dn}{dt} = k_1 n + k_2 n^2 + k_3 n^3 \quad (2.4)$$

where k_1 , k_2 , k_3 , n represent the monomolecular recombination constant, bimolecular recombination constant, Auger recombination constant, and the total charge carrier concentration, respectively (Figure 2.2). Monomolecular recombination is governed by the trap-mediated process, which typically dominates under low excitation densities and high

2.1. Perovskites

trap densities ($< 10^{15} \text{cm}^{-3}$). On the other hand, bimolecular recombination is a non-geminate recombination of charge carriers. In contrast, Auger recombination involves an energy transfer from an electron or hole to a third charge carrier [9].

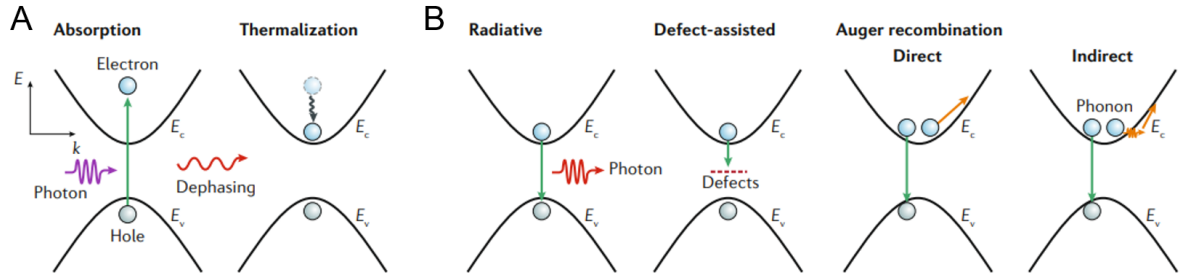


Figure 2.2: Charge carrier recombination kinetics. (A) Photoexcitation process in perovskite, where E_C and E_V correspond to the conduction band minimum and valence band maximum, respectively. (B) Recombination dynamics of the photo-excited charge carriers, showing the radiative, defect-assisted, direct, and indirect Auger recombination processes. Reproduced from Ref. [10] with permission. Copyright 2020, Springer Nature Limited.

2.1.2 Reduced-Dimensional Perovskites

Structural Properties

Reduced-dimensional perovskites (RDPs) consist of single or multiple inorganic layers separated by long ligands (Figure 2.3).

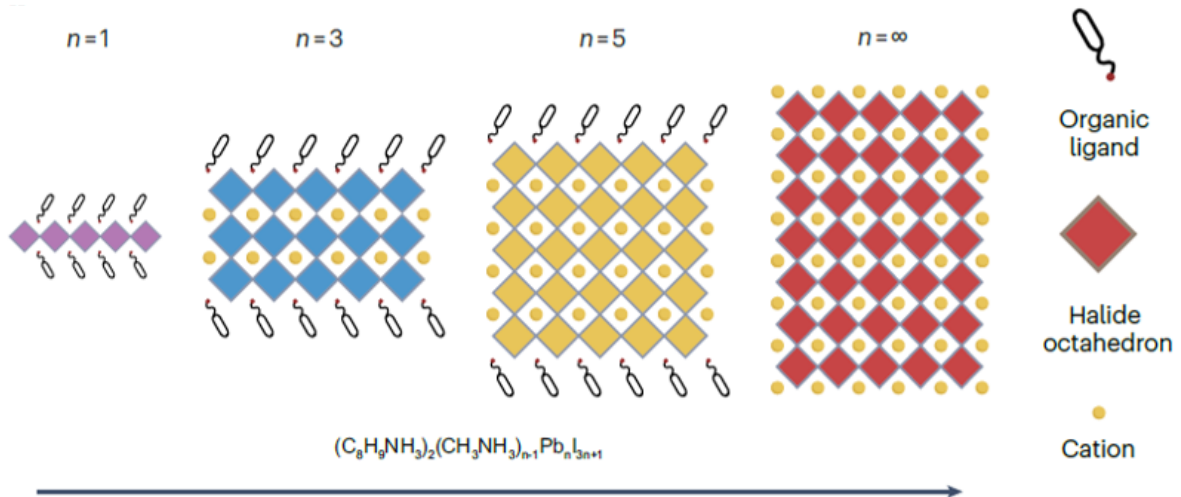


Figure 2.3: The crystal structure of RDPs with different n -values, showing the dimensionality evolution from 2D to quasi-2D and 3D. Reproduced with permission from Ref. [11]. Copyright 2023, Springer Nature Limited.

2D perovskites have a general formula $RA_{n-1}B_nX_{3n+1}$, where R and A refer to additional bulky organic cations and organic cations, respectively. B denotes tin or lead, X is a halide, and n represents the thickness of the inorganic layers. In contrast to 3D perovskite structure, the layered structure alleviates the constraints on cation dimensions imposed by the Goldschmidt tolerance factor, thus facilitating the accommodation of cation R in between the inorganic layers [12].

Typically, these 2D perovskites can be categorized as Ruddlesden–Popper (RP) phases, Dion-Jacobson (DJ) phases, and the alternating cation (ACI) phases. In terms of the RP phase, there is a relatively weak van der Waals gap between two adjacent inorganic layers. The general formula of RP can be written as $A'_2A_{n-1}B_nX_{3n+1}$, where the representative A' cations are aryl ammonium or alky cation, e.g., phenylethylammonium (PEA^+) and butylammonium (BA^+). The octahedra layers in RP are typically offset by an octahedra unit, resulting in an in-plane displacement (Figure 2.4A). In contrast to the RP structure, the adjacent inorganic sheets of DJ are directly connected by diamine compounds, which form hydrogen bonds on both ends such that the structure of DJ is more rigid [13]. Moreover, the inorganic sheets in DJ phases are well-aligned without offsets (Figure 2.4B). Notably, for ACI-perovskite, the small A cation (Figure 2.4C) resides in both the inorganic layers and the interlayers with additional bulky organic cations, whereas guanidinium (Gua^+) is the only cation reported so far that can form the ACI structure [14].

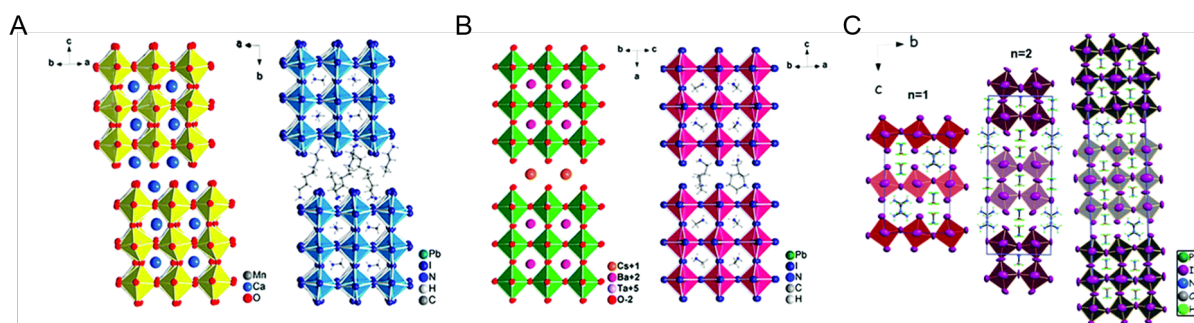


Figure 2.4: Examples of (A) RP-, (B) DJ-, and (C) ACI-phase perovskite structure, where the atoms are indicated in the figures. Reproduced with permission from Ref. [14]. Copyright 2020, Royal Society of Chemistry.

Optoelectronic Properties

2D perovskite and RDPs exhibit strikingly different optoelectronic properties. Overall, RDPs have larger bandgaps compared with their 3D counterparts, giving rise to a narrower absorption window, which varies with the thickness of inorganic layers [15]. Contrary to 3D counterparts, the large exciton binding energies up to hundreds of meV at room

2.1. Perovskites

temperature make the electron-hole pairs difficult to dissociate [15, 16]. The large exciton binding energy (E_b) results from the contrasts of dielectric constants of high organic and inorganic layers [17], where the quantum well (QW) structure of RDPs is shown in Figure 2.5A. The exciton binding energy reduces with the increasing thickness of the inorganic layers, that is, from 2D to 3D structures. This flexibility of bandgap and composition tuning makes RDPs suitable for various applications, e.g., light-emitting applications and solar cells. When $n \leq 2$, perovskites display strong exciton behavior due to the quantum confinement effect, which leads to a high photoluminescence yield and, therefore, makes them good candidates for LED application. Nevertheless, the large E_b in turn causes a considerable loss for electron-hole pairs dissociation, which is not ideal for photovoltaic applications. The quantum confinement effect largely affect the bandgap of RDPs, that is, the bandgap reduces with the increasing thickness of the inorganic sheets (Figure 2.5B). For example, the bandgap of BA-based RP perovskites decreases from 2.24 eV to 1.52 eV with the increasing inorganic layer thickness (from $n=1$ to ∞) [15]. In addition, the bandgap of RDPs is determined by the component of a 3D-like phase and extra quantization energies of electrons and holes [18].

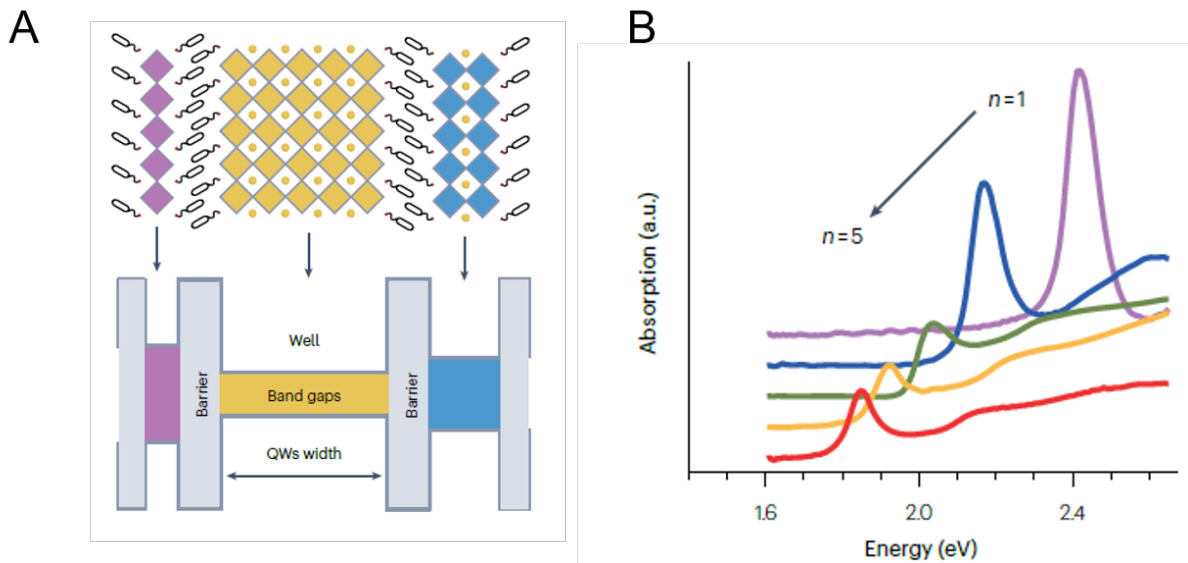


Figure 2.5: (A) Schematic illustration of RDPs structure with organic and inorganic layers as well as their energy alignment, showing the QW feature. (B) Absorption spectra of RDPs with varying inorganic thickness. Panel (A) reproduced from Ref. [11]. Copyright 2023, Springer Nature Limited. Panel (B) reproduced with permission from Ref. [19]. Copyright 2017, American Association for the Advancement of Science.

The quantum confinement nature of RDPs also leads to an anisotropic conductivity and

sult from the reorientation of the organic molecules in the lattice on a time scale of 1 to 10 ps [27]. In particular, the self-trapping of exciton is caused by the lattice distortion [28]. Moreover, the dominant process in the exciton and charge carrier dynamics is charge or energy transfer, which typically takes place on a time scale ranging from 1 to 100 ps. In RDPs ($n > 1$), excitons can diffuse over 100 ps to crystal surfaces or interfaces where they might dissociate partially to electron-hole pairs and have a longer radiative recombination lifetime (1–10 ns). There is still debate in the radiative recombination lifetime where a previous study reported a lifetime of about 1 ns [29], whereas a recent work discloses a lifetime of free exciton states up to 80 ns [30]. This discrepancy in the lifetime originates from the quality of RDPs crystal or thin films and uncertainty of the origin of the optical transition.

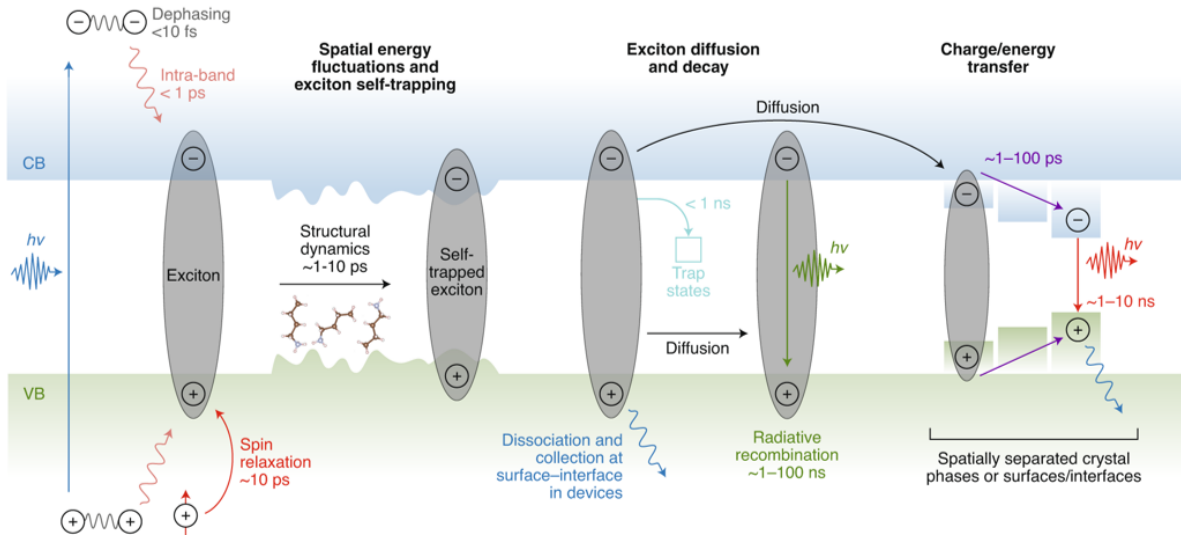


Figure 2.7: Schematic illustration of the charge carrier dynamics in RDPs after photoexcitation, showing the exciton dynamics and charge transport behavior. Reproduced from Ref. [31] with permission. Copyright 2020, Springer Nature Limited.

2.2 Perovskite Crystal Growth and Thin Film Crystallization

Understanding the perovskite crystallization process is the prerequisite to fabricating a highly efficient solar cell. In particular, to achieve a phase-pure or monodisperse quasi-2D perovskite thin films with the desired orientation, a comprehensive understanding of the crystallization and growth process is essential. Therefore, in this section, I introduce the classical nucleation and growth model and summarize the state-of-the-art growth mechanism of perovskite. Furthermore, I discuss the growth process with a special focus on the

thermodynamic perspective and the fabrication methods that have a direct influence on the crystallization process.

2.2.1 Nucleation and Growth

Nucleation can be divided into homogeneous nucleation and heterogeneous nucleation, where heterogeneous nucleation is initiated at preferential sites, e.g., phase boundaries, surfaces, and impurities [32]. In contrast, homogeneous nucleation typically takes place when the nucleation starts in the parent phase and forms a stable second phase. In addition, nucleation is promoted by the supersaturation state, where the formed nuclei-clusters favor the crystal growth. The nucleation is determined by the Gibbs free energy (ΔG), which is a function of the critical nucleus size. There are two factors that determine the Gibbs free energy, namely the bulk free energy (ΔG_V) and surface energy (γ), where the bulk free energy is related to the difference between the solid and liquid phases and the surface energy is correlated with the formation of a solid-liquid boundary. The Gibbs free energy is given by:

$$\Delta G = \frac{4}{3}\pi r^3 \Delta G_V + 4\pi r^2 \gamma \quad (2.5)$$

Accordingly, ΔG of homogeneous nucleation as a function of radius is depicted in Figure 2.8A. When the radius is below r_c , the growth of embryos leads to an increase in the free energy, whereas in the case of radius above r_c , the free energy of the embryonic system decreases such that the embryos transit to stable nuclei. The number of crystal nuclei formed per unit volume of liquid per unit time (i.e., nucleation rate) is determined by the nucleation work factor and the probability factor of atomic diffusion, which is given by:

$$I = K \exp\left(\frac{-\Delta G^*}{kT}\right) \times \exp\left(\frac{-Q}{kT}\right) \quad (2.6)$$

where K , ΔG^* , Q , T refer to the proportional constant, the required Gibbs energy to form a critical nucleus, the diffusion activation energy, and the absolute temperature, respectively. Heterogeneous nucleation is easier to form compared to homogeneous nucleation, because of low surface energy and energy barrier.

The overall nucleation and growth processes are detailed in the Lamer graph (Figure 2.8B), including three stages. First, the monomers are accumulating in the perovskite solution. With solvent removal and temperature increase, a supersaturation point is reached where nucleation initiates. In the third stage, the crystal subsequently grows with concomitantly further nucleation. In addition, nucleation is terminated when the concentration is below the supersaturation point. Finally, the crystal growth ends when the concentration of monomers is lower than the solubility value ($[M]_{sol}$).

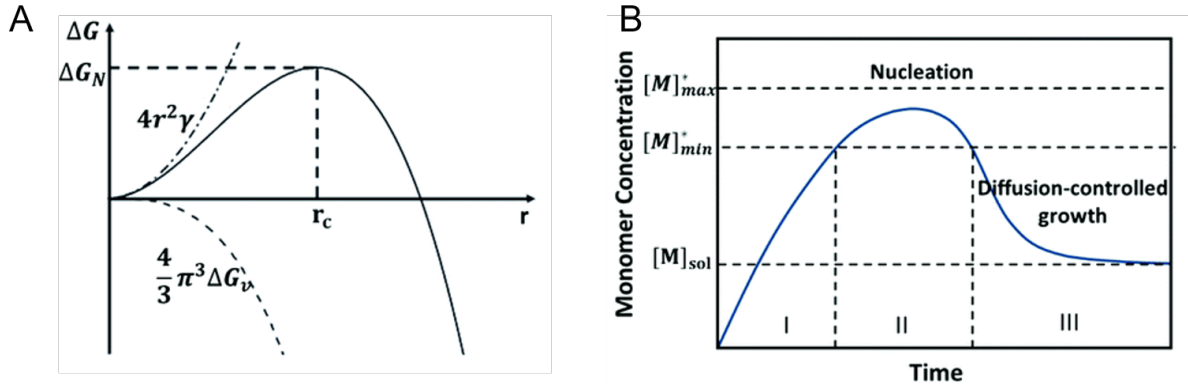


Figure 2.8: (A) Diagram of classical homogeneous nucleation, where r_c is the critical radius, (B) Lamer diagram, showing the nucleation and growth process, where the critical values are indicated in the figure. Reproduced from Ref. [33] with permission. Copyright 2020, Royal Society of Chemistry.

Stable nuclei start to grow in order to reduce the overall free energy and reach the energy equilibrium when the solute concentration is above the solubility limit. For films, there are typically three main growth mechanisms, namely island growth, layered growth, and layer-island growth [34]. In terms of island growth, the nuclei grow both along the vertical and lateral direction via monomers attachment, as shown in Figure 2.9, where the bonding between the monomers and the growth phase is stronger than that between monomers and substrate surface. Eventually, the island coalescence and forms a dense perovskite thin film. On the other hand, layer growth occurs in an epitaxial system, where the bonding between monomers and substrate is much stronger. Analogous to layer growth, island-layer growth also occurs in an epitaxial system. However, the bonding between monomers and the substrate surface is not strong. In reality, island growth is the most likely dominant mechanism in perovskite thin film growth. The overall nucleation and growth kinetics regarding the transformed fraction of material can be modeled by the Johnson-Mehl-Avrami-Kolmogorov (JMAK) equation:

$$y = 1 - \exp \left[\frac{\pi}{3} I \left(\frac{dr}{dt} \right)^3 t^4 \right] \quad (2.7)$$

where the expression for I is given by Equation 2.6 and the JMAK equation can be expressed as:

$$y = 1 - \exp(-K_3 t^n) \quad (2.8)$$

where K_3 is a temperature-dependent nucleation or growth rate, and n is the exponent, respectively. In reality, typically, K and n can be extracted by fitting the I - t curve.

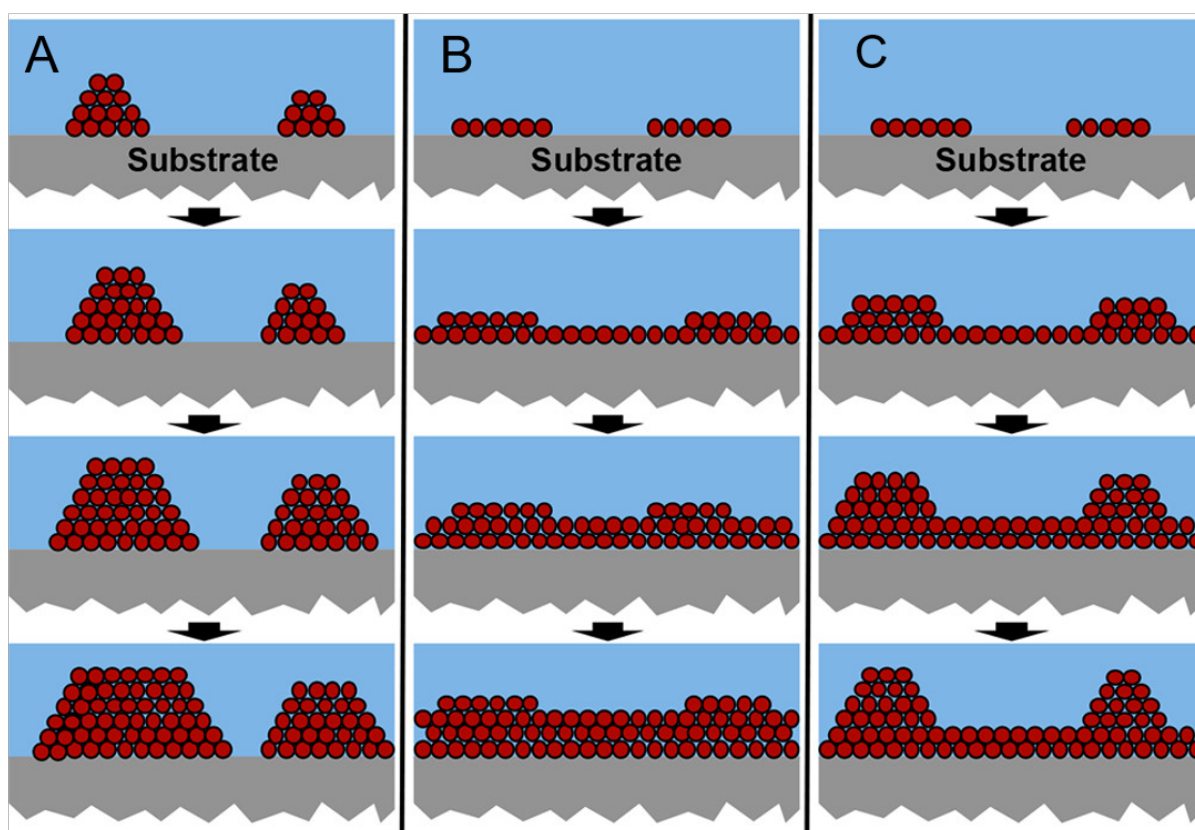


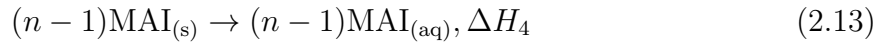
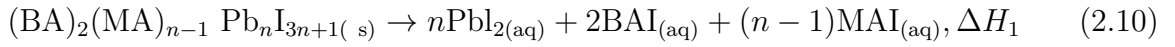
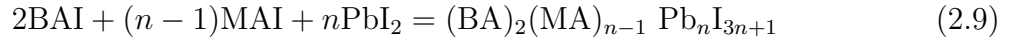
Figure 2.9: Schematic illustration of growth mechanism. (A) island growth, (B) layer growth, and (C) layer-island growth. Reproduced from Ref. [34] with permission. Copyright 2018, American Chemical Society.

It should be noted that the transformed fraction is difficult to measure directly; therefore, other easily accessible proxies are used, e.g., peak intensity in X-ray diffraction, scattering data [35], and absorption features [36].

Ostwald ripening is a subset of general coarsening and particularly refers to coarsening in the presence of a second phase, typically a liquid [34]. The perovskite film growth may also involve Ostwald ripening, where smaller crystals can dissolve back in the perovskite solution by tuning their small radius of curvature, resulting in partial saturation. At the same time, the monomers from this saturated solution will deposit on large crystals, making them grow by merging smaller crystals. The continuous growth of large crystals consumes the nearby crystals, and the isolated crystals are eventually connected as the growth of large crystals progresses.

2.2.2 Formation Energy

In this subsection, I discuss the formation enthalpy with a BA-based RP phase as a reference. To obtain phase-pure RDPs, a favorable formation energy for a controllable crystallization is required, which can be achieved by tuning the composition of the perovskite precursor and casting temperature. This is due to the formation energy of different n -value phases in RDPs, particularly perovskite with large- n values. As an example, the formation reaction of BA-based RP phase is given by:



$$\Delta H_f = -\Delta H_1 + \Delta H_2 + \Delta H_3 + \Delta H_4 \quad (2.15)$$

where s and aq refer to the solid state of the substance and the aqueous solution, respectively, and ΔH_f is the formation enthalpy of the RDPs. In general, the ΔH values are negative for RDPs with lower dimensionality (typically $n \leq 5$) but positive for RDPs with higher dimensionality. In addition, empirically the $-T\Delta S$ is positive, therefore, a negative ΔH is needed for favorable formations, in other words, a negative Gibbs free energy (ΔG) [11]. The ΔG is negative for RDPs ($n \leq 5$), showcasing that these phases are thermodynamically stable and the natural formation of these phases from stoichiometry components. Notably, as n increases, ΔG destabilizes sharply, indicating the reduced possibility of the formation of large- n phases. This analysis illustrates that obtaining pure phase in RDPs with higher dimensionality is difficult.

2.3 Perovskite Solar Cells

2.3.1 Solar Spectrum

The spectral radiation is described by Planck's law:

$$B(\lambda) = \frac{2hc^2}{\lambda^5 \left[\exp\left(\frac{hc}{k_B\lambda T}\right) - 1 \right]} \quad (2.16)$$

where c , h , k_B are the speed of light ($2.998 \times 10^8 \text{ ms}^{-1}$), Planck constant ($6.626 \times 10^{-34} \text{ J/s}$), Boltzmann constant ($1.38 \times 10^{-23} \text{ J/K}$), respectively. The sun has a surface temperature of 5762 K and its radiation spectrum can be approximated by a black-body radiator at that temperature. However, the long distance from Earth to the sun indicates that only radiation emitted directly in the direction of Earth contribute to the solar spectrum. Moreover, not all solar light of the extraterrestrial solar spectrum reaches Earth's surface due to scattering and absorption by the Earth's atmosphere. The radiation intensity above the Earth's atmosphere is 1366 W/m^2 , and the spectral distribution is called air mass zero radiation spectrum (AM0), where air mass (AM) refers to the spectral content and intensity of the solar radiation reaching Earth's surface affected by the absorption in the atmosphere. The air mass can be calculated by latitude angle (ϕ):

$$AM = \frac{1}{\cos\phi} \quad (2.17)$$

Hence, AM1 refers to perpendicular sunlight, whereas AM1.5 refers to a latitude of around 47° . The solar spectra are depicted in Figure 2.10, where the sunlight receiving surface of AM1.5 is defined as an inclined plane at 37° tilt toward the equator.

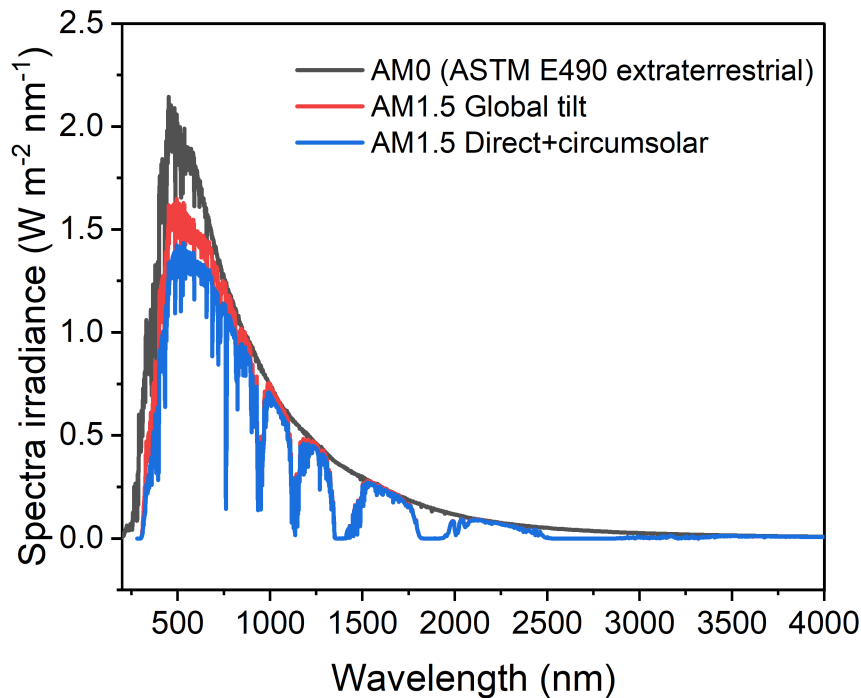


Figure 2.10: Solar irradiance spectra of AM1.0, AM1.5, and AM1.5 Direct+circumsolar after ASTM G173-03 (ISO9845-1) standard, where the raw data was retrieved from <https://www.pveducation.org/pvcdrom/appendices/standard-solar-spectra>.

The integrated power of AM0 (that is, standard spectrum for space application) is 1366

W/m², whereas the integrated power of AM1.5 is 1000 W/m². The AM1.5 Direct+circumsolar with an integrated power density of 900 W/m² is defined for solar concentrator work, which encompasses both the direct beam from the sun and the circumsolar component within a 2.5-degree disk around the sun. It should be pointed out that the light and other measurement conditions, e.g., temperature and atmosphere, should be disclosed to ensure data reproduction when measuring solar cell efficiency and stability [6].

2.3.2 Working Principles of Perovskite Solar Cells

When light is shed on solar cells, the incident photons ($h\nu > E_g$) are absorbed by the active layer, where then the electrons are excited from the valence band (VB) to the conductive band (CB). The bounded electron-hole pairs are separated by the built-in electric field. Followed by charge diffusion, transport, and extraction, the electrons and holes are collected at the respective electrodes (Figure 2.11A). The sketch of a solar cell is depicted in Figure 2.11B, where HBL, EBL, and TCO represent hole blocking layer, electron blocking, and transparent conductive oxide, respectively. Nevertheless, the above process happens in an ideal case, whereas in reality, the charge undergoes non-radiative recombination, including the Auger recombination, the Shockley-Read-Hall (SRH) recombination, and the interfacial recombination, which originates from defects, as explained before in Section 2.1.1. The current-voltage characteristics of an ideal p-n junction without illumination follow the Shockley equation, which is given by:

$$I = I_0[\exp(\frac{eV}{k_B T}) - 1] \quad (2.18)$$

where I_0 , e , k_B , and T refer to the dark current or leakage current of the diode (i.e., non-radiative recombination in the device), the electron charge, the Boltzmann constant, and the temperature, respectively. When a solar cell is illuminated, the IV curve shifts due to additional current (I_{ph}), originating from the photo-generated current, which can be expressed by:

$$I = I_{ph} - I_0[\exp(\frac{eV}{k_B T}) - 1] \quad (2.19)$$

However, in reality, there are some losses during charge transport, e.g., interfaces between the hole blocking layer or electron blocking layer and the interface between the blocking layer (depending on the cell configuration), which can be modeled by adding a series resistance (R_S) in the equivalent electric circuit. Therefore, Equation 2.19 will change to:

$$I = I_{ph} - I_0[\exp(\frac{e(V + IR_S)}{k_B T}) - 1] \quad (2.20)$$

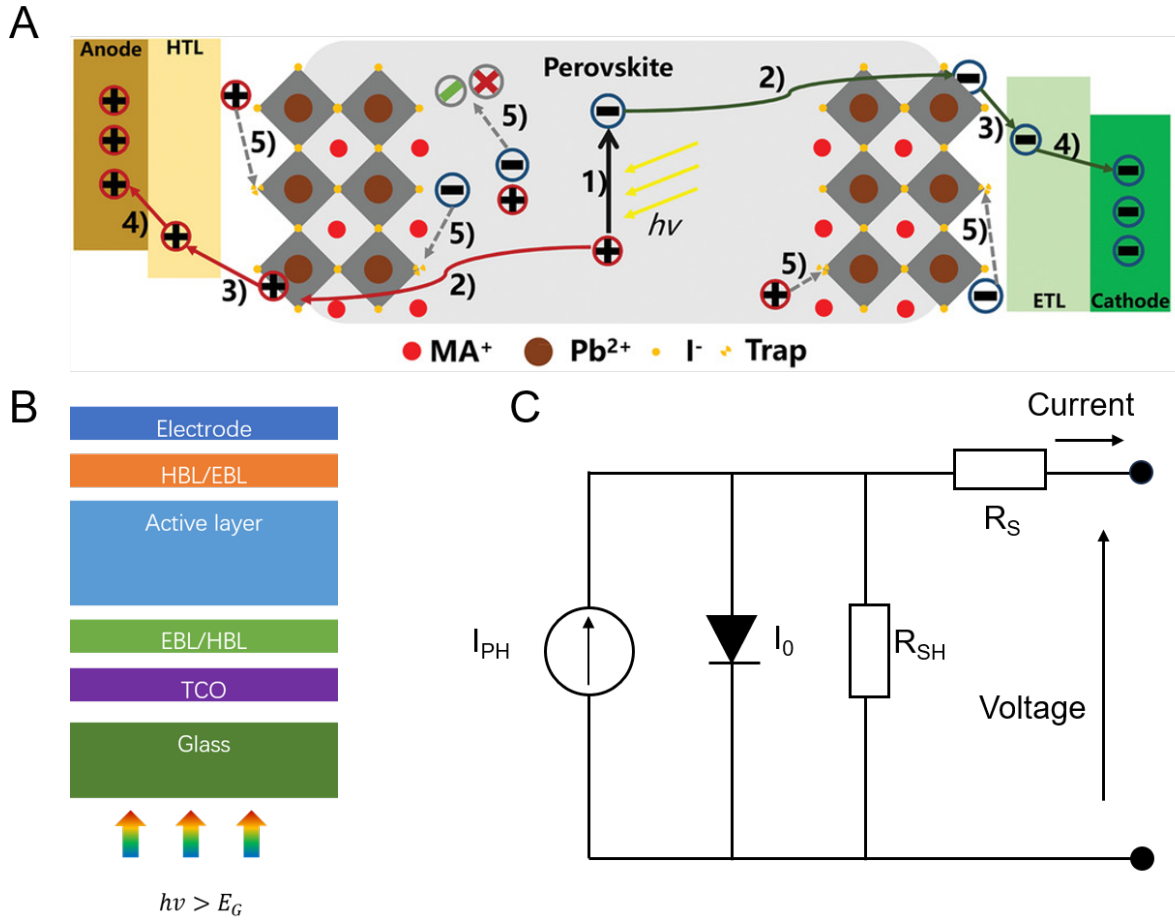


Figure 2.11: (A) Working principle of perovskite solar cells, where processes 1-5 correspond to charge dissociation, charge diffusion, transport, charge extraction, and charge recombination, respectively. Reproduced from Ref. [37] with permission. Copyright 2019, Wiley-VCH. (B) Device configuration of perovskite solar cells. (C) Equivalent circuit model of a solar cell, including the shunting and series resistance.

The presence of a shunting resistance (R_{SH}) also leads to a significant loss of solar cell performance. This originates from the morphological defects, e.g., grain boundaries and pinholes. Then, Equation 2.19 will change to:

$$I = I_{ph} - I_0 \left[\exp\left(\frac{eV}{k_B T} - 1\right) \right] - \frac{V}{R_{SH}} \quad (2.21)$$

In the presence of both R_S and R_{SH} , the IV curve of the solar cell can be described by Equation 2.22, and the equivalent circuit model is shown in Figure 2.11c:

$$I = I_{ph} - I_0 \left[\exp\left(\frac{e(V - IR_S)}{nk_B T} - 1\right) \right] - \frac{V + IR_S}{R_{SH}} \quad (2.22)$$

Thus, these parasitic resistances of IV characteristics largely affect the solar cell performance and can be described by:

$$R_S = \left(\frac{dI}{dV}\right)_{V=V_{OC}}^{-1} \quad (2.23)$$

$$R_{SH} = \left(\frac{dI}{dV}\right)_{V=0}^{-1} - R_S \quad (2.24)$$

2.3.3 Power Conversion Efficiency of Solar Cells

In general, the power conversion efficiency (PCE) η of solar cells refers to the ratio of the maximum power P_{max} per cell area with respect to the incoming power flux (E_{in}), which is given by:

$$\eta = \frac{P_{max}}{E_{in}A} = \frac{V_{MPP}I_{MPP}}{E_{in}} \quad (2.25)$$

To correlate this equation with solar cell parameters, the fill factor (FF) is defined as the ratio of P_{max} with respect to the open-circuit voltage (V_{OC}) and the short-circuit current (J_{SC}):

$$FF = \frac{P_{max}}{P_{ideal}} = \frac{V_{MPP}I_{MPP}}{V_{OC}I_{OC}} \quad (2.26)$$

The theoretical maximum FF is around 89%, whereas the maximum PCE of a solar cell with a bandgap of 1.34 eV is 32.9% (Figure 2.12) according to the Shockley-Queisser (SQ) limit calculation with the following assumptions [38]:

- Photon absorptivity equals 1 at E_g and one absorbed photon gives rise to exactly one electron-hole pair.
- The charge carrier temperature equals the cell and ambient temperature.
- Electron-hole recombination is radiative and there is no ohmic loss between the contacts.

However, there are some certain losses in the energy conversion process, where the efficiency η is given accordingly:

- Spectral losses: no photons absorption below the bandgap of materials.

$$\eta_{abs} = \frac{-J_{SC}}{e} \frac{E_{ph}^{>E_g}}{E_{ph}} \quad (2.27)$$

- Thermalization: intraband relaxation of charge carriers to the band edges, reaching thermal equilibrium with crystal lattice, where an additional reduction of $\approx 3k_B T$, that is, related to the position of quasi-Fermi level is included.

$$\eta_{thermalization} = \frac{E_g + 3k_B T}{E_{ph}} \quad (2.28)$$

2.4. Operation Stability of Perovskite Solar Cells

perovskite solar cells under external stimuli.

It is noteworthy that the stability of PSCs depends on many factors, e.g., aging condition, perovskite composition, configuration, measurement approach, and encapsulation; therefore, it is difficult to resolve stability issues. To unify the measurement condition, a consensus statement of stability was established based on the International Summit on Organic Photovoltaic Stability (ISOS) protocols [6], where D1 and D2 refer to measurement conditions of dark storage at room temperature and dark storage at high temperature, respectively. In addition, D2I, L1I and L2I correspond to tests carried out in an inert atmosphere (intrinsic stability testing), while D3 corresponds to measurement condition under dark storage at high temperature and high humidity. Moreover, L2 refers to the test condition under maximum power point (MPP) tracked under illumination at high temperatures. Figure 2.13 showcases the timeline of world-record certificated efficiency evolution of PSCs with both n-i-p and p-i-n configurations together with their long-term stability. The stability of PSCs has largely enhanced, with the stability of p-i-n devices reaching $T_{80} > 1000$ h under the protocol of ISOS-L2/3 [40].

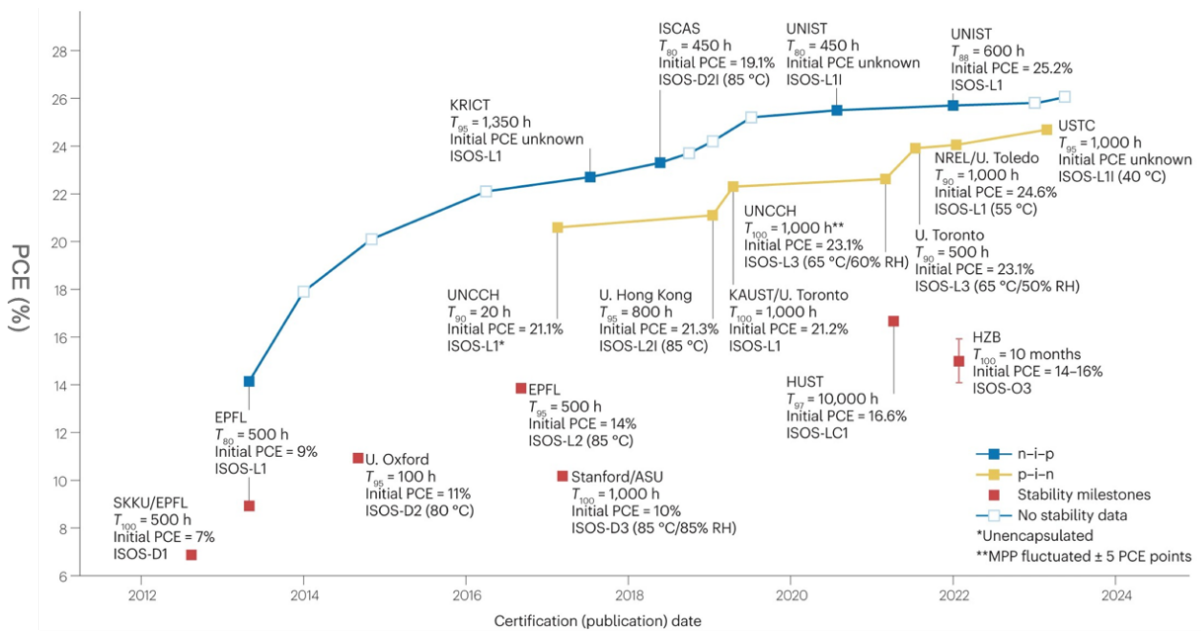


Figure 2.13: PSCs with record certificated efficiency and their stability with time evolution. The blue and yellow lines refer to the record certificated PCE in PSCs with normal and inverted configurations, respectively. The red squares represent the certain stability milestone, where D1, D2, and D3 denote dark storage at room temperature, high temperature, and high temperature and high humidity, respectively; D2, L1I, and L2I, corresponding measurements in an inert atmosphere; L2, maximum power point tracked under light illumination and high temperature; LC1, light-cycled at room temperature. Reproduced from Ref. [40] with permission. Copyright 2023, Springer Nature Limited.

Perovskite solar cells degrade under different stressors, i.e., bias, heat, oxygen, and humidity. Here, only the degradation mechanisms of PSCs under light, heat, and humidity are discussed, where detailed discussion of the degradation mechanism I refer readers to literature [41, 40, 42].

2.4.1 Moisture-Induced Degradation

Moisture is a double-edged sword that can, on the one hand, influence the perovskite crystallization, growth, orientation, and structure integrity, e.g., perovskite precursor, spin-coating process, and annealing steps [41, 43, 44]. On the other hand, it can induce the degradation of perovskite solar cells. Moisture was found to initiate perovskite degradation at the atmospheric interface and move to the grain boundary, in which the grain boundary contains an amorphous region allowing fast moisture penetration into the perovskite [45]. With the further uptake of moisture, the degradation expands towards the grain interiors along the in-plane direction [46], accompanied by the slight expansion of the grains [47, 48]. Previous work showed that the formation of the hydrate phase is not the most important device degradation pathway for methylammonium lead iodide-based PSCs; instead, moisture accelerates the iodine ion migration, leading to the corrosion of the metallic electrode [49]. In addition, Schelhas et al. [50] observed that a binary $\text{FA}_{0.85}\text{Cs}_{0.15}\text{PbI}_3$ perovskite undergoes spatial de-mixing and phase segregation into more pure constituent phases during device operation Figure 2.14.

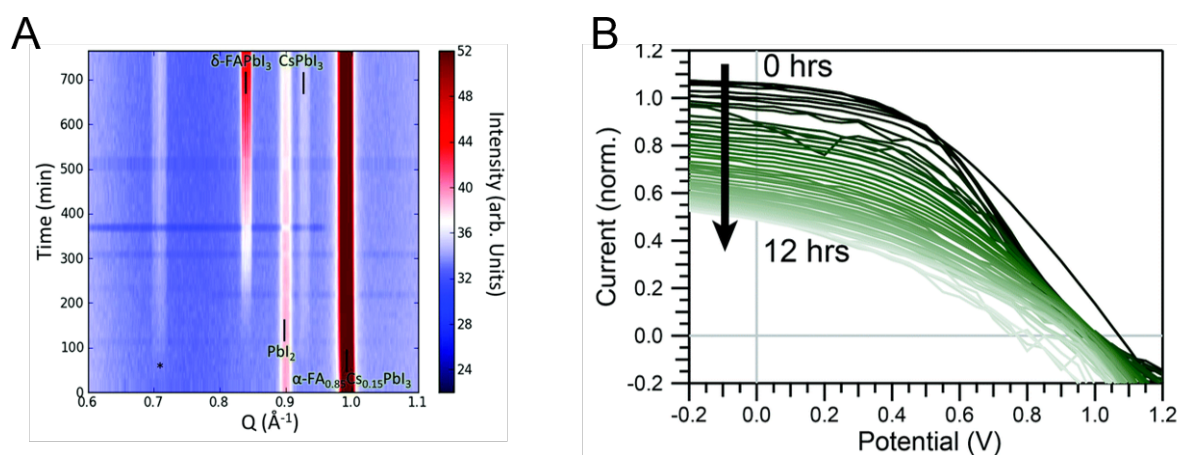


Figure 2.14: (A) *in-situ* X-ray diffraction of $\text{FA}_{0.85}\text{Cs}_{0.15}\text{PbI}_3$ -based PSCs under $\sim 50\%$ RH and room temperature, where the hydrate phases are marked in the figure. The X-ray wavelength is 0.99 \AA . (B) Solar cell performance as a function of time, where the solar cell parameters were measured by the reverse scan with an initial PCE of 18%. The degradation of PSCs performance indicates that the loss mainly originates from the photocurrent decay. Reproduced from Ref. [50] with permission. Copyright 2019, Royal Society of Chemistry.

Perovskites undergo hydration or even decomposition when exposed to humidity for extended periods. For example, our previous work demonstrates that (Figure 2.15), despite the presence of a hydrophobic bulky cation, rapid disproportionation of the initial 2D phase in 2D/3D perovskite into lower- n phases occurs under humidity [51]. For a detailed overview of moisture-induced degradation of perovskites, I refer readers to our review work, *Shedding Light on the Moisture Stability of Halide Perovskite Thin Films* (K. Sun, P. Müller-Buschbaum, *Energy Technology*, **11**, 2201475 (2023)) [41].

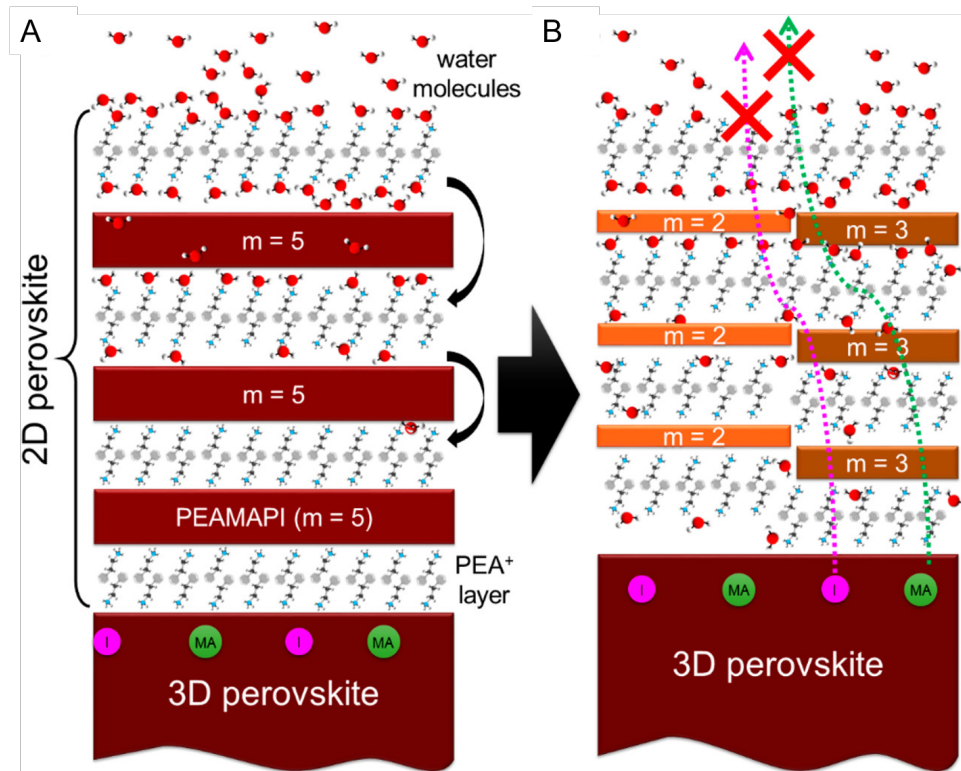


Figure 2.15: Sketch of the proposed moisture-induced degradation in a 2D/3D heterojunction. (A) 2D/3D heterojunction. (B) Disproportionation of high-dimensional 2D perovskite into lower-dimensional phase, where m refers to the thickness of inorganic layers. Reproduced from Ref. [51] with permission. Copyright 2019, American Chemistry Society.

2.4.2 Heat-Induced Degradation

In reality, the solar cells need to be operated under sunlight, where the operating cell temperature can easily reach ~ 70 °C. Depending on the environmental conditions where the solar cells or panels are installed, the cell temperature can experience temperature extreme ranging from -40 °C to 85 °C [52]. In this regard, PSCs need to pass the thermal stability test, e.g., thermal cycling test and dam heat test specified by the International

Summit on Organic Photovoltaic Stability (ISOS) [6].

Early work showed that MAPbI₃ perovskite film undergoes a structural change along with phase transition, leading to a decomposition of MAPbI₃ to CH₃I, NH₃, and PbI₂ after exposure to heating at 100 °C [53]. In addition, depth-dependent GIWAXS measurement (that is, varying the incident angle) disclosed that the decomposition of perovskite initiates at the surface and progresses toward the bulk [52]. In addition, Kim *et al.* monitored the thermal decomposition of MAPbI₃ perovskite with in-situ transmission electron microscopy (TEM) [54]. They found that a broad ring pattern appears in the Fourier transform image corresponding to an amorphous region as the temperature reaches 120 °C. Subsequent heating to 130 °C results in the formation of tetragonal PbI₂. In addition to decomposition, heat can also induce ion migration, leading to perovskite solar cell degradation. For example, Li *et al.* found a significant performance drop of solar cells with the configuration of FTO/NiO_x/MAPbI₃/PC₆₁BM/Ag (Figure 2.16) [55].

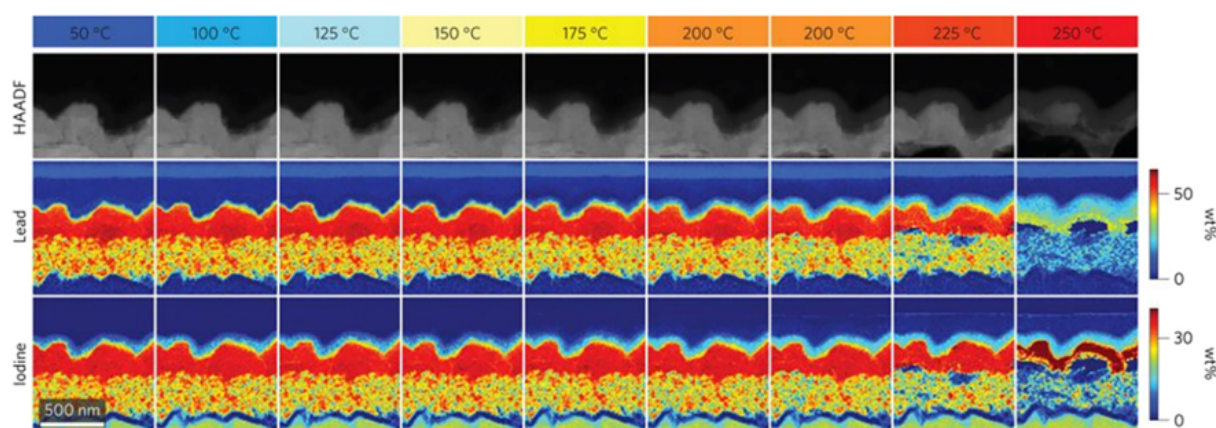


Figure 2.16: High-angle annular dark-field TEM images and energy-dispersive X-ray element maps for iodine and lead of sample after heating at different temperatures, where the heating were performed for 30 min up to 175 °C, and at 200 °C for 15 min. The scale bar is indicated in the figure and applied to all panels. Iodide diffusion into HTL is visible at lower temperatures, whereas lead migration is found at 175 °C or above. Reproduced from Ref. [56] with permission. Copyright 2016, Spring Nature Limited.

This is due to the accumulation of I⁻, I₂⁻, and CN⁻ ions driven by ion migration at the PC₆₁BM/Ag interface, leading to the corrosion of the Ag electrode. In terms of PSCs with normal configuration under heat, a previous study showed that severe iodine ion migration takes place when the temperature is above 175 °C [56]. At even higher temperatures, more pronounced iodide diffusion and morphological change can be observed in the perovskite layer (Figure 2.16).

In addition, temperature variations (or thermal cycling) also challenge PSCs's stability by inducing phase transitions and lattice strain. For example, Li *et al.* found that severe

2.5. X-ray Scattering Techniques

morphological change, e.g., enlarged grain boundaries and voids, emerge during thermal cycling (-60 °C to 80 °C) [57]. By GIWAXS, they also demonstrated that additional peaks at ~ 8.2 and 8.6 nm^{-1} form during the third thermal cycling, corresponding to the hexagonal photoinactive polytypes 4H and 6H from perovskite (Figure 2.17).

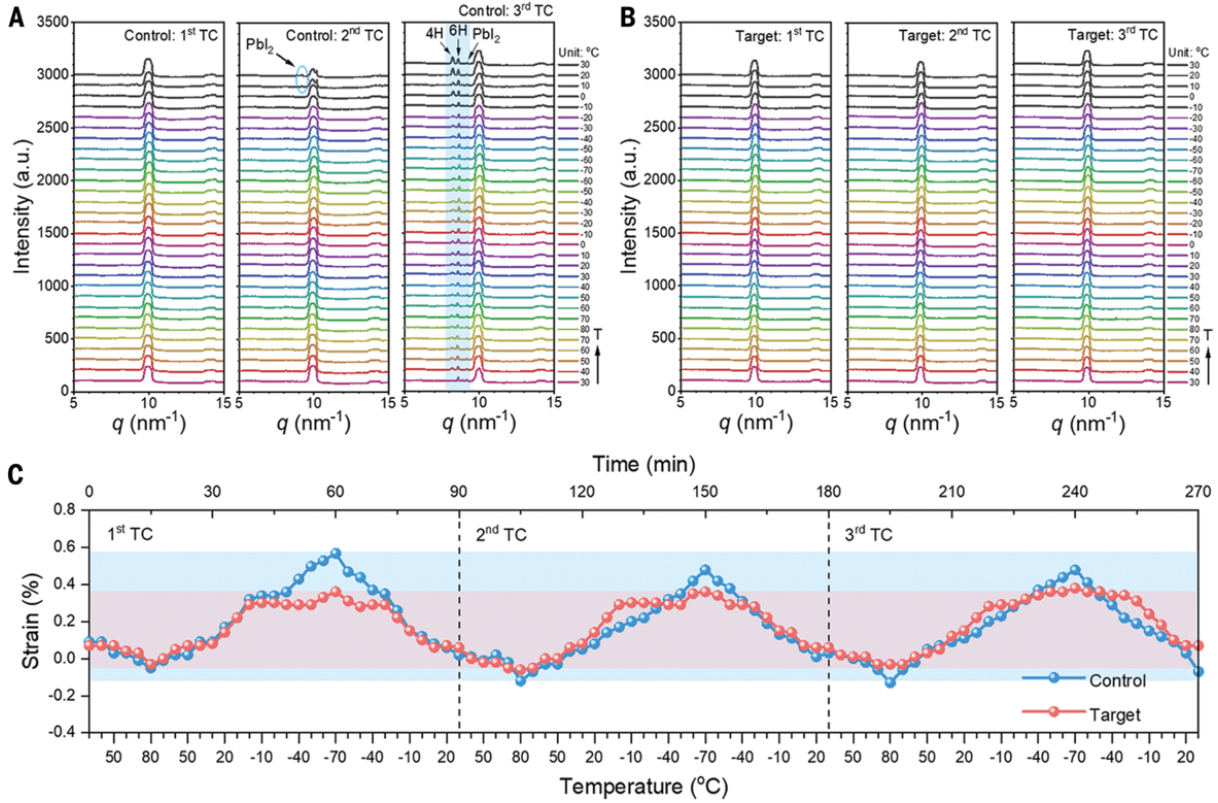


Figure 2.17: The temperature-resolved GIWAXS profiles for (A) control and (B) target perovskites. (C) The lattice strain during thermal cycling for control and target perovskites. (The temperature starts from room temperature, heating to +80 °C and then cooling to -60 °C, where one complete cycle takes 90 minutes.). Reproduced from Ref. [57] with permission. Copyright 2023, The authors.

Moreover, they observed additional peaks of tetragonal phases (β phase), which are retained only in the cold region. This indicates that irreversible PbI_2 , 4H, and 6H, and reversible tetragonal phase transition jointly result in the degradation of device performance.

2.5 X-ray Scattering Techniques

In light of the indispensable usage of the X-ray scattering technique in this thesis, in this section, the basic knowledge of X-ray scattering, including XRD, GIWAXS, and GISAXS

is introduced. In particular, with the high brilliance and time-resolution of synchrotron source, advanced scattering experiments, i.e., in-situ and operando experiments of perovskite film formation and PSCs degradation, can be performed.

X-ray scattering is based on the concept of electromagnetic waves with its electric field vector ($\vec{E}(\vec{r})$), which can be described by the Helmholtz Equation as follows [58]:

$$\nabla^2 \vec{E}(\vec{r}) + k^2 n^2(\vec{r}) \vec{E}(\vec{r}) = 0 \quad (2.31)$$

where \vec{E} is the wave function, k the wave number, and $n(\vec{r})$ the refractive index, respectively. The refractive index centers the light-matter interactions, which can be described as:

$$n(\vec{r}, \lambda) = 1 - \delta(\vec{r}, \lambda) + i\beta(\vec{r}, \lambda) \quad (2.32)$$

Hence, the refractive index is highly dependent on the dispersion coefficient (δ) and absorption coefficient (β). The dispersion (δ) is a function of the specific electron density $\rho_r(\vec{r})$, the classical electron radius $r_e = \frac{e^2}{4\pi\epsilon_0\mu_0c^2}$, and the atomic form factor $f_j(\lambda) = f_j^0 + f_j'(\lambda) + if_j''(\lambda)$, which can be described by:

$$\delta(\vec{r}, \lambda) = \frac{\lambda^2}{2\pi} \rho_e(\vec{r}) r_e \frac{\sum_j c_j (f_j^0 + f_j'(\lambda))}{\sum_j Z_j} = \frac{\lambda^2}{2\pi} Re(SLD) \approx \frac{\lambda^2}{2\pi} \rho_e(\vec{r}) r_e \quad (2.33)$$

Notably, SLD refers to the scattering length density, reflecting the scattering power of a material, which can be calculated by:

$$SLD = \frac{\sum_{i=1}^N b_i}{V_m}, V_m = \frac{M}{\rho N_a} \quad (2.34)$$

where b_i denotes the scattering length contribution, V_M the volume, M the molecular weight, and ρ the bulk density of the material. In terms of the absorption $\beta(\vec{r}, \lambda)$, it can be defined as:

$$\beta(\vec{r}, \lambda) = \frac{\lambda^2}{2\pi} \rho_e(\vec{r}) r_e \frac{\sum_j c_j f_j''(\lambda)}{\sum_j Z_j} = \frac{\lambda^2}{2\pi} Im(SLD) \approx \frac{\lambda}{4\pi} \mu(\vec{r}) \quad (2.35)$$

In general, dispersion coefficient (δ) and absorption coefficient (β) are in the range of 10^{-6} and 10^{-7} , respectively, while β is normally smaller than δ . In this regard, the refractive index is below 1, which is in contrast to visible light. To probe interfaces with a scattering technique, the incoming X-ray needs to experience a change in refractive index, that is, two domains with distinct SLD . High scattering contrast can be realized when there is a huge electron densities mismatch of the materials and it can be defined as:

$$|\Delta|^2 = (\delta_1 - \delta_2)^2 + (\beta_1 - \beta_2)^2 \quad (2.36)$$

2.5.1 X-ray Diffraction

X-ray diffraction technique is normally used to investigate the crystal structure of a material. When the X-ray beam is scattered from two neighboring lattice planes of a crystal, interference will show up, giving rise to peaks in the intensities (Figure 2.18).

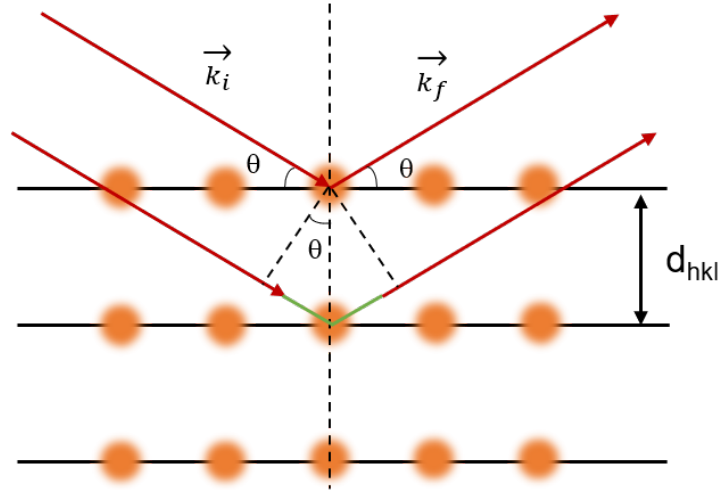


Figure 2.18: Schematic illustration of a diffraction event on a crystal with the lattice spacing being labeled. The difference in path length is demonstrated with green color.

If the Bragg equation (Equation 2.37) is fulfilled [59], constructive interference will occur, resulting in the maximum intensity:

$$2d_{hkl}\sin(\theta) = n\lambda \quad (2.37)$$

where d_{hkl} is the lattice space of the crystal and n the order of reflection. Diffraction angle (2θ) can be calculated for any given set of planes (hkl) by using the plane-spacing equations. For example, for a given cubic crystal with the lattice parameter a , the lattice spacing can be then computed by:

$$\frac{1}{d_{hkl}^2} = \frac{h^2 + k^2 + l^2}{a^2} \quad (2.38)$$

When combined with Equation 2.37, Equation 2.38 can be simplified under the condition of $n=1$ to:

$$\sin^2 \theta = \frac{\lambda(h^2 + k^2 + l^2)}{4a^2} \quad (2.39)$$

This demonstrates that the angles of the diffraction pattern are correlated with the atoms in the unit cell. In addition to the lattice parameter, crystal sizes (D) can be estimated by the Scherrer equation [60]:

$$\Delta \cos \theta = \frac{k\lambda}{D} + 4\epsilon \sin \theta \quad (2.40)$$

$$D = \frac{k\lambda}{\Delta \cos \theta - 4\varepsilon \sin \theta} = \frac{k\lambda}{y - \varepsilon x} \quad (2.41)$$

$$\varepsilon = \frac{\Delta \cos \theta}{4 \sin \theta} = \frac{y}{x} \quad (2.42)$$

where Δ denotes the full width at half maximum (FWHM), K the crystallite shape factor. When $K = 0.9$, it indicates that the crystal has a spherical shape; however, one should keep in mind that K varies with crystallite shape. In addition, when considering the microstrain, plotting $\Delta \cos \theta$ as a function of $4 \sin \theta$ gives rise to D and ε (Equations 2.41, 2.42), a method commonly known as Williamson-Hall method [61].

2.5.2 Grazing-Incidence Small-Angle X-ray Scattering

Grazing-incidence small-angle X-ray scattering (GISAXS) is a powerful technique to probe the surface morphology and buried structure in a relatively large length scale from nanometers to several hundred nanometers. The typical geometry of GISAXS is depicted in Figure 2.19, where the X-ray beam impinges on the sample surface with a very shallow incident angle α_i (typically below 1°), and the scattered intensity is captured with a small exit angle α_f and out-of-plane angle ψ . The very small incident angle leads to a large footprint on the thin film due to the grazing geometry. The projected footprint dimension can be calculated according to:

$$H_{\text{footprint}} = \frac{h_{\text{beam}}}{\tan \alpha_i} \quad (2.43)$$

where h_{beam} denotes the beam height.

The characteristic region of GISAXS can be defined as: the specular beam position at $\alpha_i = \alpha_f$, diffuse scattering if $\alpha_i \neq \alpha_f$, and out-of-plane diffuse scattering when $\Psi \neq 0$. Considering an incoming monochromatic beam with a wave number $k_i = \frac{2\pi}{\lambda} = \text{const.}$, where λ denotes the wavelength, the moment transfer \vec{q} is given by:

$$\vec{q} = \begin{pmatrix} q_x \\ q_y \\ q_z \end{pmatrix} = \vec{k}_f - \vec{k}_i = \frac{2\pi}{\lambda} \begin{pmatrix} \cos \alpha_f \cos \Psi - \cos \alpha_i \\ \cos \alpha_f \sin \Psi \\ \sin \alpha_f + \sin \alpha_i \end{pmatrix} \quad (2.44)$$

With the condition for elastic scattering:

$$|\vec{k}_i| = |\vec{k}_f| = \frac{2\pi}{\lambda} \quad (2.45)$$

The critical angle α_c is highly dependent on materials and is defined by:

$$\alpha_c \approx \sqrt{2\delta} = \lambda \sqrt{\frac{\text{Re}(SLD)}{\pi}} \quad (2.46)$$

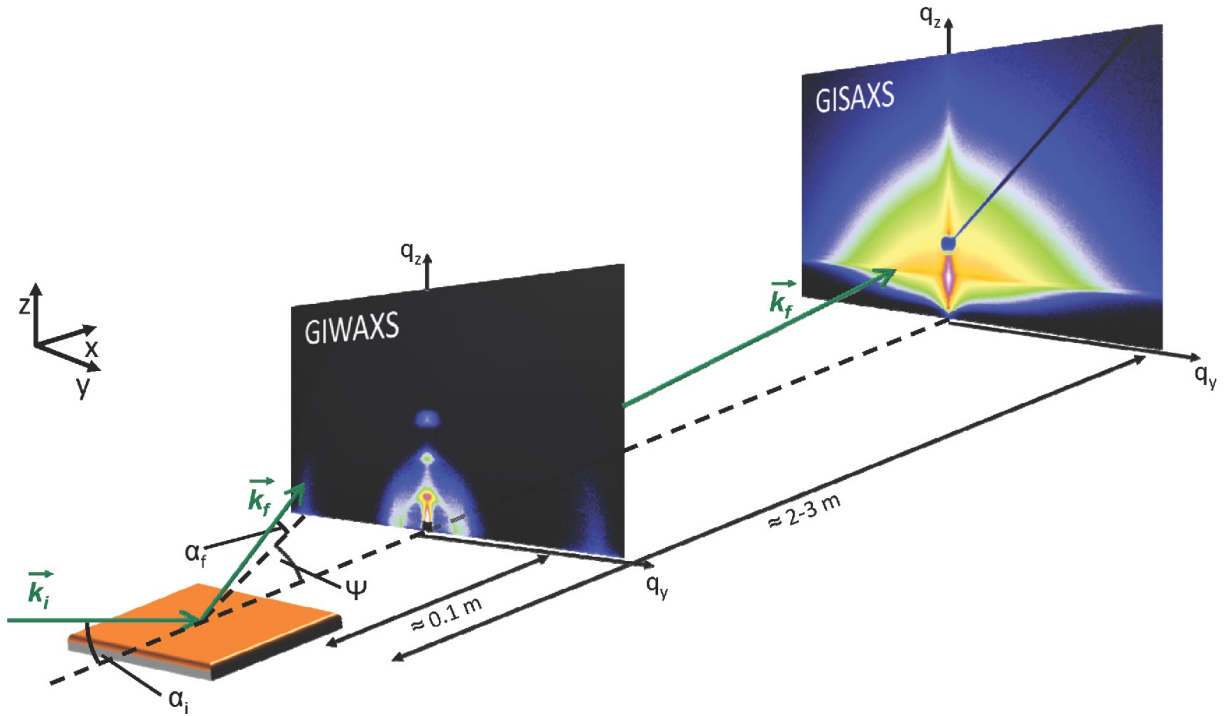


Figure 2.19: Schematic illustration of the typical experimental setup of GISAXS and GIWAXS, where the typical sample-to-detector distance, detector images, incident angle α_i , excit angle α_f , the out-of-plane angle Ψ , and the coordinate-system are given. Reproduced from Ref. [62] with permission. Copyright 2014, Wiley-VCH

For $\alpha_i < \alpha_c$, the X-ray beam can only probe surface information and the penetration depth is limited to several nanometers. For $\alpha_i > \alpha_f$, the X-ray beam can penetrate through the film and average the structure across its entire depth, depending on the absorption and film thickness. In reality, by varying incident angle α_i and critical angle α_c , we can balance obtaining desired information and maximizing the intensity.

- evanescence regime: $\alpha_i < \alpha_c(\text{activelayer})$, probing surface information
- dynamic regime: $\alpha_c(\text{activelayer}) < \alpha_i < \alpha_c(\text{substrate})$, probing bulk information
- kinematic regime: $\alpha_c(\text{substrate}) < \alpha_i$, probing comprehensive information on both the active layer and substrate

For grazing-incidence, reflection and refraction take place at the sample interface and substrate interface. Therefore, the so-called distorted wave Born approximation (DWBA) is applied when taking reflection and refraction into consideration. To further simplify the analysis of horizontal line cuts (with respect to the sample surface), the so-called effective interface approximation (EIA) is applied, meaning that the data is only analyzed against q_y , and therefore, the lateral structure information is retrieved. For $\alpha_i \gg \alpha_c$ and a

constant q_z , the diffuse intensity in the DWBA simplifies for an EIA, and the differential cross ($\frac{d\sigma}{d\Omega}$) section is described by:

$$\left. \frac{d\sigma}{d\Omega} \right|_{df} = \frac{C\pi^2}{\lambda^4} (1 - n^2)^2 |T_i|^2 |T_f|^2 F(\vec{q}) \propto F(\vec{q}) \quad (2.47)$$

where C refers to the illuminated surface area, λ the wavelength, n the refractive index, $T_{i,f}$ the Fresnel transmission functions, and $F(\vec{q})$ the diffuse scattering factor. With the incident angle α_i being equal to the exit angle α_f , the Fresnel transmission functions reach a maximum, contributing to a pronounced scattering density, which is also known as Yoneda peak [63]. The diffuse scattering factor $F(\vec{q})$ can be simplified by using a form factor $P(\vec{q})$ of the individual scattering domains as well as a structure factor $S(\vec{q})$ of the domain:

$$F(\vec{q}) \propto N \langle P(\vec{q}) \rangle S(\vec{q}) \quad (2.48)$$

where N refers to the scattering domains.

In practice, normally, the complete flight path is evacuated to suppress air or window scattering. The sample-to-detector distance (SDD) is set according to the desired q range, where the signal is captured by a 2D area detector. Moreover, the direct beam and specular beam are typically blocked by beam stops. When $\alpha_i = \alpha_c$, the specular and the Yoneda peak overlap, rendering it difficult to resolve large structures. Nevertheless, this configuration is still applied in GISAXS measurements because the strong intensity allows for the detection of weak signals. In terms of $\alpha_i > \alpha_c$, the specular and the Yoneda peak are well separated along the z direction. Nevertheless, the signal decreases rapidly with increasing the incident angle α_i . To ensure sufficient statistics, one needs to consider the sufficient sample exposure time while avoiding radiation damage. For GISAXS data analysis, we start with data reduction, where the 2D GISAXS data is reduced to 1D intensity profiles by the vertical line cut along q_z direction and horizontal line cut at the Yoneda peak (α_c) along q_y . Then the horizontal line cut is modeled in the framework of DWBA (Figure 2.20). It is also stressed that, for data modeling in perovskite samples, the structure factor is typically neglected because perovskite crystals are positioned with uncorrelated distances. Detailed analysis of GISAXS data, including data extraction and modeling, can be found in Section 6.3.

2.5.3 Grazing-Incidence Wide-Angle X-ray Scattering

Grazing-incidence wide-angle X-ray scattering (GIWAXS) is a powerful technique to probe the crystalline structure and molecular orientation and is typically performed using the same scattering geometry as in GISAXS (Figure 2.19) but with a reduced SDD (several hundreds of millimeters).

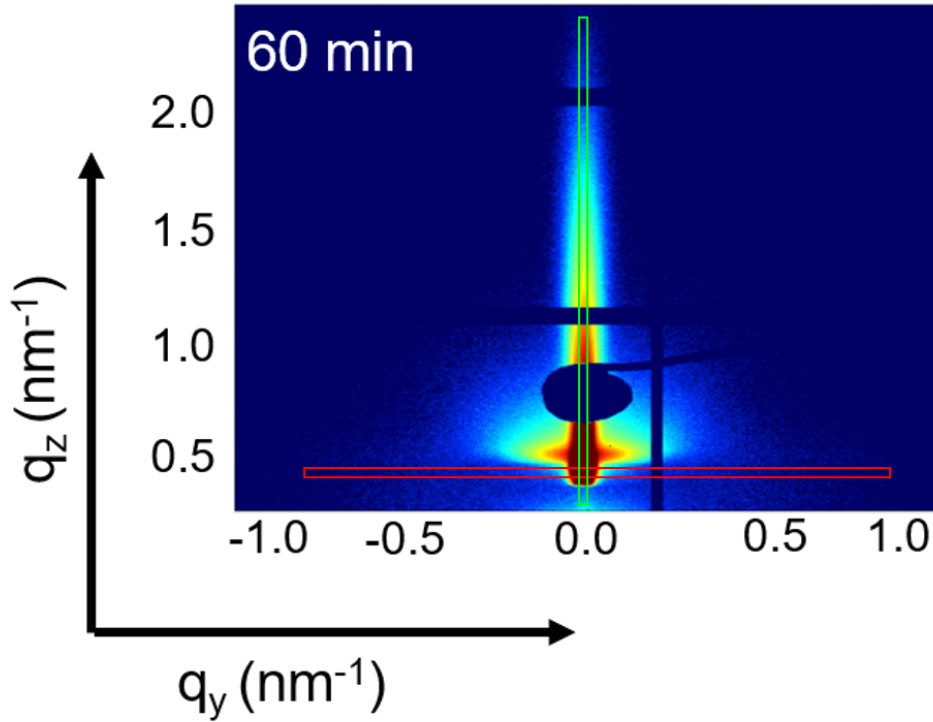


Figure 2.20: Example of a 2D GISAXS detector image with a horizontal line cut (indicated by the red rectangle) and a vertical line cut (indicated by the green rectangle).

Larger q ranges can be realized with this configuration, and therefore, atomic and molecular structures are accessible. Analogous to GISAXS, the incident angle α_i can also be varied in order to probe information at different scattering lengths.

- $\alpha_i < \alpha_c(\text{activelayer})$: probes information about the crystalline structures in the surface region
- $\alpha_c(\text{activelayer}) < \alpha_i < \alpha_c(\text{substrate})$: probes information about crystalline structures in the active layer
- $\alpha_c(\text{substrate}) < \alpha_i$: probes crystalline structure information of both the active layer and the substrate

The penetration depth Λ can be calculated by:

$$\Lambda = \frac{\lambda}{4\pi} \sqrt{\frac{2}{\sqrt{(\alpha_i^2 - \alpha_c^2)^2 + 4\beta^2} - (\alpha_i^2 - \alpha_c^2)}} \quad (2.49)$$

The penetration depth of an X-ray depends on the beam energy and the optical properties of the materials; especially, a lower penetration depth is achieved when the X-ray beam penetrates higher-energy materials. Moreover, in the case of the X-ray beam penetrating into the substrate, the penetration depth is not equal to the scattering depth because the detection of X-ray requires photons to traverse and exit back to the film surface. In

this regard, the attenuation of the diffracted beam, which depends on the incident angle α_i and exit angle α_f , must be considered. Consequently, the scattering depth Λ^* can be calculated by:

$$\Lambda^* = \frac{\sin(\alpha_f)}{\sin(\alpha_i) + \sin(\alpha_f)} \Lambda \quad (2.50)$$

As described by Laue condition, the reciprocal lattice of crystals is probed through constructive interference of X-rays passing a set of lattice planes with the Miller indices $\{hkl\}$, with the momentum transfer \vec{q} being equal to the reciprocal lattice vector \vec{G} :

$$\vec{q} = ha^* + kb^* + lc^* = \vec{G} \quad (2.51)$$

In terms of elastic scattering, the scattering vector \vec{k}_f points onto the surface of the Ewald sphere with radius k . The intersections of the Ewald sphere with the reciprocal lattice points are measured as reflexes on the 2D detector. The Laue condition in reciprocal space is equivalent to the Bragg condition in real space when the path length differences are multiples of the wavelength λ at a certain angle θ (Equation 2.37).

Typically, processing 2D GIWAXS raw images into reshaped 2D GIWAXS images requires transforming pixel space into q space, where in the reshaped 2D GIWAXS image, the scattering intensity is plotted against (q_r, q_z) with $q_r = \sqrt{q_x^2 + q_y^2}$ (Figure 2.21). This transformation results in a reshaped GIWAXS image with a missing wedge, which results from the mathematical correction of projecting a 3D surface on a 2D plane.

To further reduce 2D GIWAXS data into 1D profiles, azimuthal cake cuts–slices over a narrow angular range–can be performed, giving rise to 1D diffraction profiles (also known as pseudo-XRD). In particular of 2D perovskite film, sector integrals, e.g., radial/cake cuts along specific directions (vertical or horizontal) can be also performed to understand the heterogeneity along different directions (in-plane and out-of-plane).

In addition, one can also perform azimuthal tube cuts along the q position of a specific plane to analyze the orientation distribution. Figure 2.22 maps out the typical GIWAXS patterns of different perovskite dimensionality and preferential orientations. A mixture of different phases is easily formed during the fabrication process of perovskite thin films, e.g., 2D/3D heterostructures and quasi-2D perovskites, which gives rise to different scattering patterns. In general, Low-dimensional perovskite can facilitate the formation of highly-ordered structures along either in-or out-of-plane direction. Depending on the degree of crystal orientation within the perovskite thin film, incomplete or complete Debye-Scherrer rings might be observed. In the case of highly oriented thin films, sharp Bragg points can be detected, resulting from the reciprocal lattice of a fixed orientation [64].

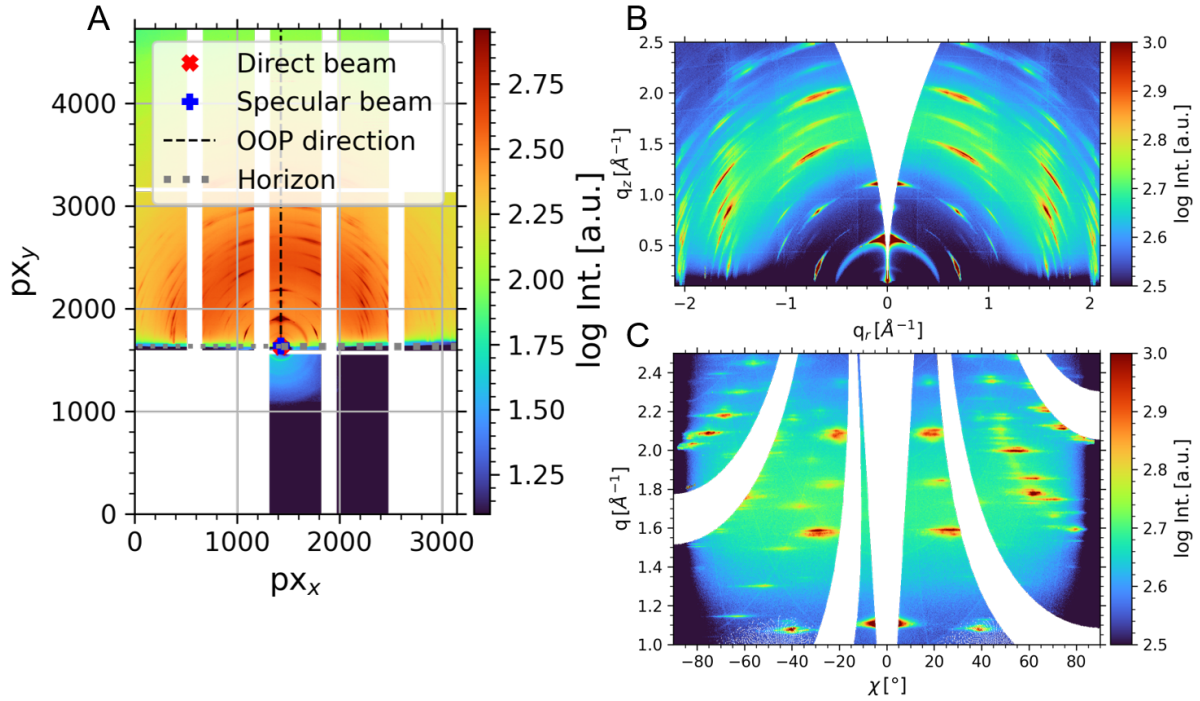


Figure 2.21: Typical GIWAXS image processing. (A) 2D GIWAXS raw image with pixel space, (B) reshaped 2D GIWAXS image with q space, and (C) data plotted as a function of q , χ

Figure 2.23 shows examples of azimuthal cake cuts and pole figures. One should keep in mind that the signal intensity distribution along the azimuthal angles should be the same as the distribution of the actual material quantity. For processing with material quantity MQ , the signal intensity of the azimuthal cake cuts must be Lorentz-corrected, that is, corrected by a factor of $\sin \chi$, which gives rise to the pole figures [65]. In addition, thanks to Manuel, Lennart, and other colleagues who developed the Python-based software (INSIGHT) for reducing and processing 2D X-ray scattering data, enabling fast data analysis for large time-resolved synchrotron datasets [66].

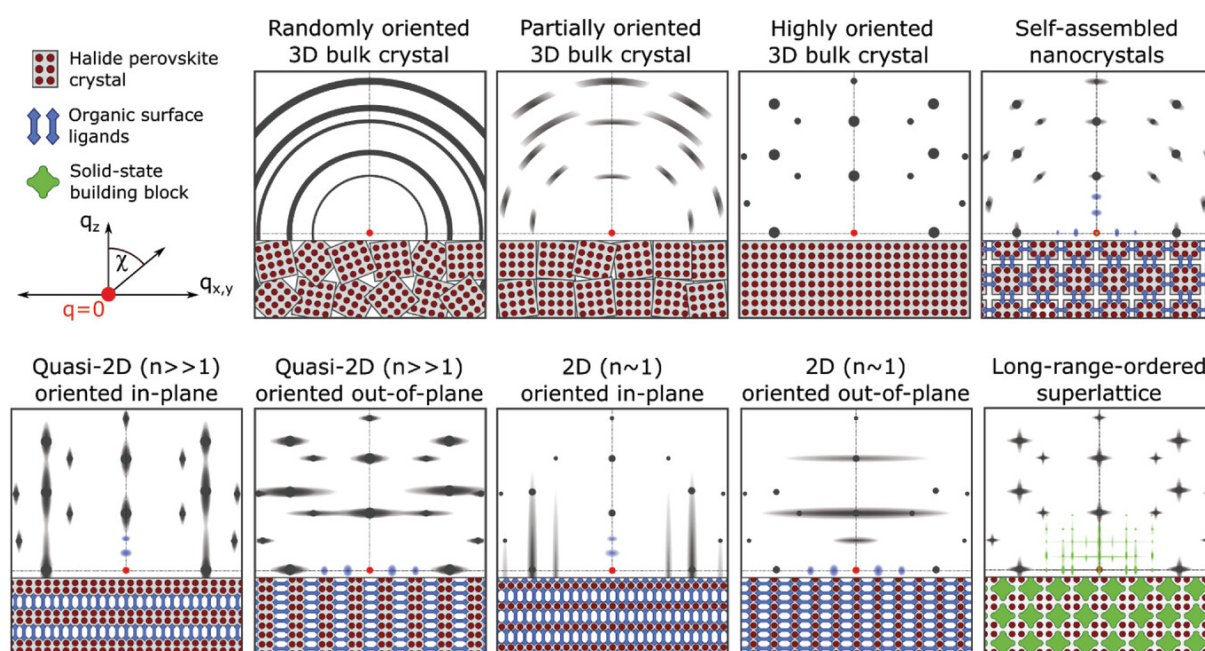


Figure 2.22: Overview of typical GIWAXS patterns for different oriented structures and degrees of order in perovskite thin films. Reproduced from Ref. [64] with permission. Copyright 2023, Wiley-VCH.

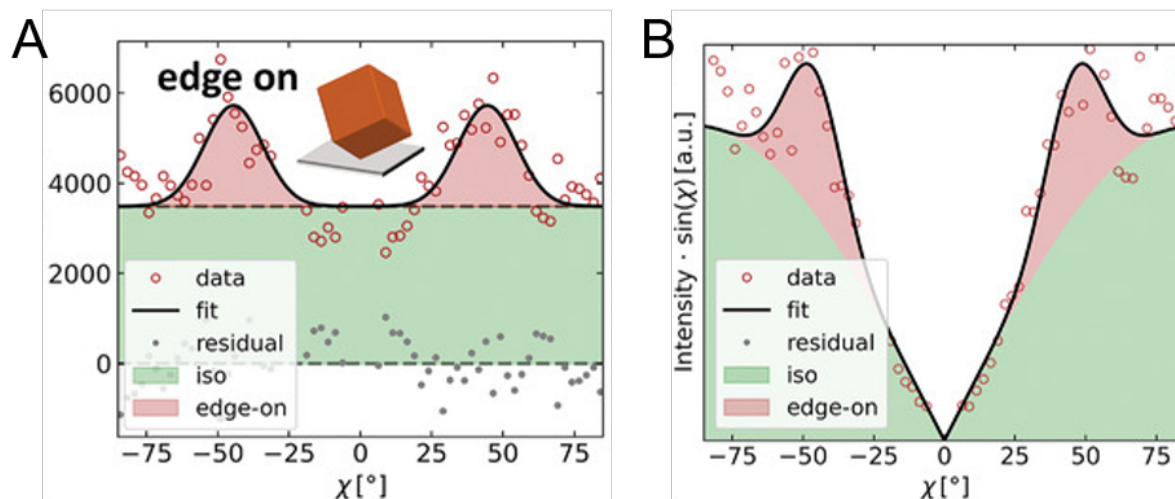


Figure 2.23: (A) Example of azimuthal tube cuts (points) with fits (lines). (B) Example of a pole figure with red and green shaded area corresponding to the edge-on and isotropic material quantity MQ , respectively. Reproduced from Ref[65] with permission. Copyright 2022, Wiley-VCH.

Sample Preparation

This chapter is based on the publications *Morphological Insights into the Degradation of Perovskite Solar Cells under Light and Humidity* (K. Sun, R. Guo, Y. Liang, J. E. Heger, S. Liu, S. Yin, M. A. Reus, L. V. Spanier, F. Deschler, S. Bernstorff, P. Müller-Buschbaum, *ACS Applied Materials Interface*, **15**, 30342-30349 (2023)) [48], *Unraveling the modification effect at NiO_x/perovskite interfaces for efficient and stable inverted perovskite solar cells* (X. Kang, D. Wang, K. Sun, X. Dong, W. Hui, B. Wang, L. Gu, M. Li, Y. Bao, J. Zhang, R. Guo, Z. Li, X. Jiang, P. Müller-Buschbaum, L. Song, *Journal of Materials Chemistry A*, **11**, 22982-22991 (2023)) [67], and *Deciphering Structure and Charge Carrier Behavior in Reduced-Dimensional Perovskites* (K. Sun, R. Guo, S. Liu, D. Yang, X. Jiang, L. F. Huber, Y. Liang, M. A. Reus, Z. Li, T. Guan, J. Zhou, M. Schwartzkopf, S. D. Stranks, F. Deschler, P. Müller-Buschbaum, *Advanced Functional Materials*, 2411153 (2024)) [68]. Reproduced from [48] with permission from American Chemical Society, Copyright 2023 and reproduced from [67] with permission from Royal Society of Chemistry, Copyright 2023, and reproduced from [68] with permission, Copyright 2024, Wiley-VCH.

3.1 Substrates

The patterned indium doped tin oxide substrates (ITO, high transmittance, 25×25 mm, 15 Ohm/Sq) and the glass (76×26 mm²) were purchased from Yingkou Shangneng Photoelectric Material Co., Ltd, and Carl Roth, respectively. They were sequentially rinsed in Hellmanex III (Hellmanex III: DI water = 2:98), DI water, ethanol (Carl Roth, 70%), acetone (Carl Roth, 99.8%), and isopropanol (Carl Roth, 99.5%) in the ultrasonic bath for 10 min each. The substrates were further cleaned and functionalized with O₂ plasma (0.4 bar, 250 W) for 10 min before spin-coating.

3.2 Materials

This section lists all the chemicals used in this thesis. The materials were used directly without any additional treatment (Table 3.1) unless stated otherwise.

3.3 Electron Blocking Layer

In general, PEDOT:PSS and NiO_x are the materials of electron blocking layer (EBL) used in inverted PSCs (p-i-n). The PEDOT:PSS solution was filtered and spin-coated at 4000 rpm for 30 min on ITO or glass substrates, followed by annealing at 150 °C for 30 min in air. In terms of the fabrication of NiO_x nanoparticle, $\text{Ni}(\text{NO}_3)_2 \cdot 6\text{H}_2\text{O}$ (5.815 g) was dissolved in DI water (20 mL) to get a green solution by stirring for 30 min. An aqueous solution of NaOH (10 mol L⁻¹ in deionized water) was then slowly added to the green solution by stirring for 20 min. DI water was used to wash the colloidal precipitates, which were dried in vacuum freeze dryers for 24 h. The resulting products were finally calcined at 270 °C for 2 h. For fabrication of NiO_x EBL, the nanoparticle ink (10 mg/mL in DI water and IPA = 3:1, v:v) was spin-coated on substrates at 2000 rpm for 30 s and annealed at 130 °C for 50 min.

For the EBL used in n-i-p PSCs, spiro-OMeTAD solutions were made by mixing 72.3 mg spiro-OMeTAD, 17.5 μL LITFSI (520 mg/mL in ACN), and 28.8 μL tBP in 1 mL CB. Then the spiro-OMeTAD solution was dynamically spin-coated on top of perovskite/HBL samples at 3500 rpm for 30 s, followed by storage in a dark desiccator with silica gel overnight.

3.4 Hole Blocking Layer

In terms of fabrication of n-i-p PSCs, SnO_2 was used for HBL, which was achieved by spin-coating diluted tin (IV) oxide solution (SnO_2 :DI water = 1:4) on the ITO or glass substrates at 4000 rpm for 30 min in air. Afterward, the as-prepared samples were annealed in air at 150 °C for 30 min.

The PC_{61}BM solutions used in p-i-n PSCs were prepared by mixing 20 mg PC_{61}BM in 1 mL CB. Subsequently, the solutions were dynamically spin-coated on top of perovskite samples at 3000 rpm for 30 s.

3.4. Hole Blocking Layer

Table 3.1: Materials and solvents

Materials	Formula or Abbreviations	Company	Purity
chlorobenzene	CB	Sigma-Aldrich	99.8%
lead iodide	PbI ₂	Sigma-Aldrich	99.99%
lead bromide	PbBr ₂	Sigma-Aldrich	≥99%
methylammonium bromide	MABr	Sigma-Aldrich	99%
formamidinium iodide	FAI	Sigma-Aldrich	99%
methylammonium iodide	MAI	Sigma-Aldrich	99%
N,N-dimethylformamide	DMF	Sigma-Aldrich	99.8%
dimethyl sulfoxide	DMSO	Sigma-Aldrich	99.9%
4-tert-butylpyridine	tBP	Sigma-Aldrich	96%
bis(trifluoromethane)sulfonimide lithium salt	TFSI	Sigma-Aldrich	99.95%
2,2',7,7'-tetrakis[N,N-di(4-methoxyphenyl)amino]-9,9'-spirobifluorene	sprio-OMeTAD	Sigma-Aldrich	99%
acetonitrile	ACN	Sigma-Aldrich	≥99.8%
tin (IV) oxide	SnO ₂	Alfa Aesar	\
poly(3,4-ethylenedioxythiophene)	PEDOT:PSS	Ossila	\
polystyrene sulfonate	(AI 4083)		
[6,6]-phenyl C ₆₁ butyric acid methyl ester	PC ₆₁ BM	Sigma-Aldrich	≥99.5%
bathocuproine	BCP	Sigma-Aldrich	99%
phenethylammonium iodide	PEAI	Sigma-Aldrich	98%
1,4-phenylenedimethan ammonium	PDMAI ₂	Xi'an Polymer Light Technology Corporation	99.5%
isopropanol	IPA	Sigma-Aldrich	99.8%
cesium iodide	CsI	Sigma-Aldrich	99.9%
2-Iodobenzoic acid	2-IBA	Adamas	98%
2-iodobenzenesulfonic acid	2-IBSA	Adamas	97%
2-iodophenylboronic acid	2-IPBA	Adamas	95%
4-iodophenylboronic acid	4-IPBA	Adamas	95%

3.5 Perovskite Layer

3.5.1 Perovskite Layer Used in Chapter 5

$\text{Cs}_{0.05}(\text{FA}_{0.99}\text{MA}_{0.02})_{0.95}\text{Pb}(\text{I}_{0.98}\text{Br}_{0.02})_3$ was prepared by mixing PbI_2 (725.8 mg), FAI (244.9 mg), MABr_2 (3.3 mg), PbBr_2 (11.2 mg), CsI (19.8 mg) and MACl (16.0 mg) powder in DMF/DMSO (5:1, v/v) with 4 h stirring at room temperature. The mixed-cation perovskite films were obtained by a two-step spin-coating process with 1000 rpm for 10 s and 4000 rpm for 40 s. 150 μL chlorobenzene was then dropped at the 25 s of the second spin-coating step. Finally, the films were annealed at 110 $^\circ\text{C}$ for 20 min.

3.5.2 Perovskite Layer Used in Chapter 6

To prepare the MAFA precursor $[(\text{MAPbBr}_3)_{0.08}(\text{FAPbI}_3)_{0.92}]$, the powder containing methylammonium bromide (10.75 mg), lead bromide (35.23 mg), formamidinium iodide (189.85 mg), lead iodide (530.10 mg) were mixed and added into 800 μL DMF and 200 μL DMSO stirring at 70 $^\circ\text{C}$ for 40 min. The CsMAFA perovskite solution was mixed with cesium iodide (15.59 mg), methylammonium bromide (10.21 mg), lead bromide (33.47 mg), formamidinium iodide (180.36 mg), lead iodide (532.47 mg) into 800 μL DMF and 200 μL DMSO stirring at 70 $^\circ\text{C}$ for 40 min. For the CsI-HBL solution, cesium iodide (15.59 mg) was added into a diluted tin (IV) oxide solution (SnO_2 in 15% H_2O colloid dispersion; SnO_2 : DI water=1:4), after that the solution was stirred overnight at room temperature.

3.5.3 Perovskite Layer Used in Chapter 7

The 2D RP $(\text{PEA})_2\text{MA}_{n-1}\text{Pb}_n\text{I}_{3n+1}$ perovskite and DJ $(\text{PDMA})\text{MA}_{n-1}\text{Pb}_n\text{I}_{3n+1}$ perovskite solutions were prepared by dissolving the appropriate stoichiometric quantities of PbI_2 , MAI, and PEAI or PDMAI₂ in a mixture of DMF and DMSO (9:1, v/v), where the concentration of Pb^{2+} is 0.5 M. The solutions were stirred at 70 $^\circ\text{C}$ until fully dissolved and cooled down to room temperature before use. Subsequently, the perovskite precursor was slot-die-coated on a preheated substrate (70 $^\circ\text{C}$) with a coating speed of 5 mm/s (Figure 3.1). The pumping speed was 110 $\mu\text{L}/\text{min}$, and the gap height was 200 μm . The N_2 knife was set at a 45-degree angle against the printing direction with a pressure of 10 psi. Importantly, the slot-die coating parameters, including the gap height, printing speed, pump speed, substrate temperature, and N_2 flow rate need to be reoptimized since these parameters vary from one solution system to another. For example, solutions with volatile solvents can allow for a relatively higher coating speed and a lower substrate

temperature.

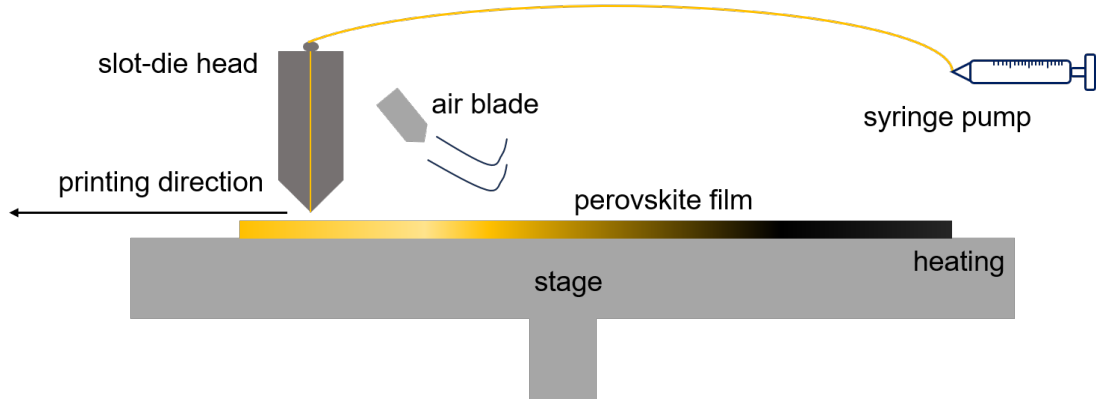


Figure 3.1: Sketch of slot-die coating, including a slot-die head, an air blade, a sample stage, and a syringe pump system.

Afterwards, the samples were annealed at 100 °C for 10 min. Details about the slot-die coater can be found elsewhere [69].

3.6 Metal Electrodes

For n-i-p PSCs, an 80 nm Au film was thermally evaporated on top of the EBL layer under a vacuum pressure of 1×10^{-6} bar at the rate of 0.6 \AA s^{-1} , whereas for p-i-n PSCs, a 100 nm thick Ag was evaporated under a vacuum of 1×10^{-6} bar.

3.7 Devices

The fabrication process of n-i-p devices is presented here (Figure 3.2). The ITO substrates were sequentially rinsed in Hellmanex III, DI water, ethanol, acetone, and isopropanol. After 10 min treatment of O₂ plasma, the diluted tin (IV) oxide solution (SnO₂: DI water=1:4) was spin-coated on the ITO substrate at 4000 rpm for 30 s and followed by annealing at 150 °C for 30 min. Then, the perovskite thin films were deposited onto the SnO₂ layer at 5000 rpm for 35 s in a nitrogen glovebox, and chlorobenzene (150 μL) was applied 10 s before ending. Afterwards, the films were annealed at 150 °C for 20 min. Subsequently, the electron blocking layer (EBL) was deposited on top of the perovskite film at 3500 rpm for 30 s using the spiro-OMeTAD solution, which contains 72.3 mg spiro-OMeTAD, 17.5 μL bis(trifluoroethane)sulfonamide lithium salt (LiTFSI) stock solution (520 mg/mL in acetonitrile), 28.8 μL 4-tertbutylpyridine (tBP) and 1 mL chlorobenzene. Finally, 80 nm Au film was thermally evaporated on top of the EBL layer under a vacuum

pressure of 1×10^{-6} torr at the rate of 0.6 \AA s^{-1} .

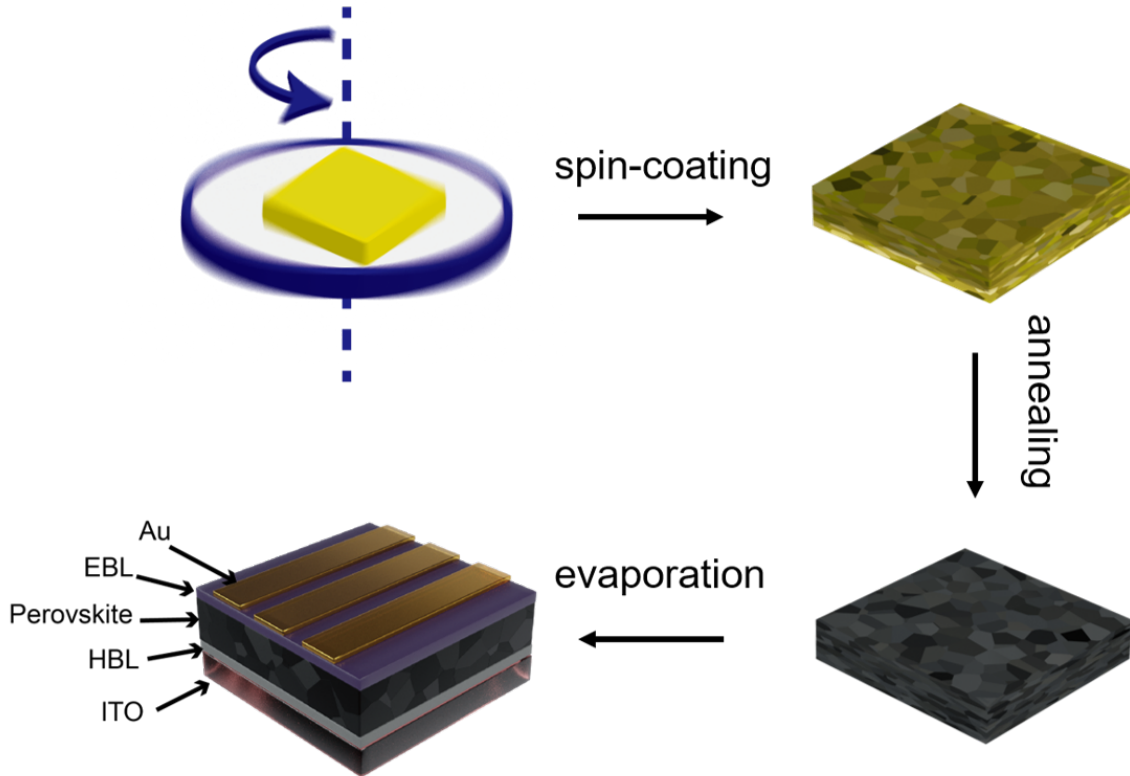


Figure 3.2: Fabrication process of n-i-p PSCs, where the main processes are indicated.

For the p-i-n device in Chapter 7, the description of the fabrication of the active layer is disclosed in Section 3.5.3. The inverted solar cells had a device structure of ITO/PEDOT:PSS/perovskite/PC₆₁BM/BCP/Ag. The PEDOT:PSS was filtered and spin-coated on O₂-plasma treated ITO substrates at 4000 rpm for 30 s and then annealed at 150°C in air for 30 min. Afterwards, the perovskite was deposited as described above. The PC₆₁BM solution (20 mg/mL in CB) was dynamically spin-coated on ITO/PEDOT:PSS/perovskite layers at 3000 rpm for 30 s. Afterward, the BCP (0.5 mg/mL in IPA) solutions were dynamically deposited at 3000 rpm for 30 s. Finally, a 100 nm thick Ag was evaporated under a vacuum of 1×10^{-6} bar.

Sample Characterization

In this chapter, we overview the characterization methods used in this thesis, including spectroscopy, X-ray scattering, and imaging technique, where most of this chapter is based on the publications *Morphological Insights into the Degradation of Perovskite Solar Cells under Light and Humidity* (K. Sun, R. Guo, Y. Liang, J. E. Heger, S. Liu, S. Yin, M. A. Reus, L. V. Spanier, F. Deschler, S. Bernstorff, P. Müller-Buschbaum, *ACS Applied Materials Interfaces*, **15**, 30342-30349 (2023)) [48], *Unraveling the modification effect at NiO_x/perovskite interfaces for efficient and stable inverted perovskite solar cells* (X. Kang, D. Wang, K. Sun, X. Dong, W. Hui, B. Wang, L. Gu, M. Li, Y. Bao, J. Zhang, R. Guo, Z. Li, X. Jiang, P. Müller-Buschbaum, L. Song, *Journal of Materials Chemistry A*, **11**, 22982-22991 (2023)) [67], and *Deciphering Structure and Charge Carrier Behavior in Reduced-Dimensional Perovskites* (K. Sun, R. Guo, S. Liu, D. Guo, X. Jiang, L. F. Huber, Y. Liang, M. A. Reus, Z. Li, T. Guan, J. Zhou, M. Schwartzkopf, S. D. Stranks, F. Deschler, P. Müller-Buschbaum, *Advanced Functional Materials*, 2411153 (2024)) [68]. Reproduced from [48] with permission from American Chemical Society, Copyright 2023, reproduced from [67] with permission from Royal Society of Chemistry, Copyright 2023, and reproduced from [68] with permission from Wiley-VCH, Copyright 2024.

4.1 Scanning Electron Microscopy

A scanning electron microscope (SEM) probes the surface of a sample with a focus beam of electrons since electron wavelengths are much shorter than photon wavelengths in the visual spectrum. The electrons interact with atoms in the sample, giving rise to information about the surface topography and composition of the sample. The electron wavelength λ_C can be extracted from the de Broglie equation:

$$\lambda_C = \frac{h}{p} = \frac{hc}{\sqrt{2m_e V e c^2 + V^2 e^2}} \quad (4.1)$$

where m_0 , e , p , h , and c correspond to the electron rest mass, charge, momentum, Planck's constant, and the speed of light, respectively. With the typical acceleration potential of 5 kV, the λ_C is calculated to be around 17.3 pm. Most SEM measurements are measured at the Zentrum für Nanotechnologie und Nanomaterialien (ZNN) of the Walter-Schottky-Institut (WSI) with a 5-7 mm working distance and an accelerating voltage of 5 kV. To avoid electron beam-induced perovskite degradation, a larger working distance is applied in our case [70]. Line-by-line raster scans with the electron beam generate secondary electrons by inelastic scattering, which are then detected by an InLens detector to capture the surface morphology. The brightness of SEM images is related to the detected electrons; thus, elevated points or areas with positive curvature are brighter. In contrast, materials with high electron density emit electrons, and therefore, dielectric materials that are charged up are darker. To further process SEM images, the open-source software ImageJ was used (<https://imagej.net/ij/docs/install/index.html>).

4.2 Atomic Force Microscopy

Atom force microscopy (AFM) is another powerful technique that can be used to probe the surface topology of materials at atomic resolution without damaging the sample. A detailed setup is depicted in Figure 4.1, including a sample stage, a cantilever with a fine tip, a laser diode, a detector, and an electronic feedback loop, with the tip attached to the flexible cantilever.

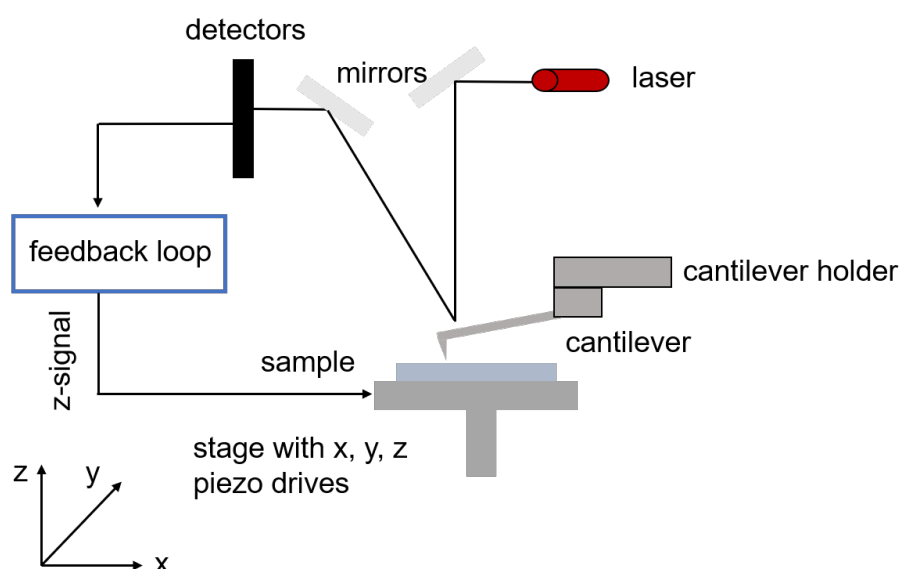


Figure 4.1: Sketch of AFM setup with the main parts indicated.

The basic working principle is the interaction between the tip and the sample surface,

which typically follows the Lennard-Jones potential. There are three modes in AFM: contact, tapping, and non-contact, depending on the distance between the sample surface and the tip. Regarding the contact mode, the tip is pressed to the surface, and the induced deflection of the cantilever measures the interaction between the tip and the sample surface. However, this mode is not always recommended, as this might damage the tip. In terms of tapping and non-contact mode, the tip oscillates close to the resonance frequency just above the surface with the oscillation amplitude as the measurement parameter. Notably, the tip-to-sample distance is monotonous to the oscillation amplitude. Images were obtained using a MultiMode 8 atomic force microscope (Bruker) in ambient conditions. Images were taken in tapping mode at a scan rate below 1 Hz, and the data were further processed by Gwyddion (<http://gwyddion.net/>) to adjust contrast and quantify the surface roughness. NSG30 AFM probes (TipsNano) were utilized for the imaging process, featuring a typical resonance frequency of 320 kHz, a nominal tip radius of 8 nm, and a scan size of $5 \mu\text{m} \times 5 \mu\text{m}$.

4.3 Optoelectronic Characterization

4.3.1 Photoluminescence Spectroscopy

Photoluminescence (PL) is a non-destructive and contactless method of studying material properties of perovskites, e.g., bandgaps, electronic properties, local disorder, phase distribution, and dynamic effects like degradation mechanism or photo-induced phase segregation. When the sample is exposed to light irradiation, a photoexcitation process is initiated, where light is absorbed and imparts the excess energy to the material. This energy can be dissipated by the emission of light or through luminescence. A typical PL setup is depicted in Figure 4.2, where the emitted light is collected by a spherical mirror system and focused on the entrance hall of an optical fiber. This results in the emitted photons being directed to a monochromator and subsequently collected by a photodiode array detector. The reflected laser light is then filtered off by a long-pass filter.

In typical fluorescence, photons are emitted at higher wavelengths compared to the photons absorbed. When incident light aligns with a molecule's absorption wavelength, the molecule transitions from its ground state to a higher excited state, referred to as S_2 here. Subsequently, electrons undergo internal conversion, influenced by vibrational relaxation and heat dissipation to the environment. As depicted in Figure 4.3, the ultimate photoemission transition can occur via either a rapid singlet state (fluorescence, typically in the range of nanoseconds) or a slower triplet state (phosphorescence, typically in microseconds).

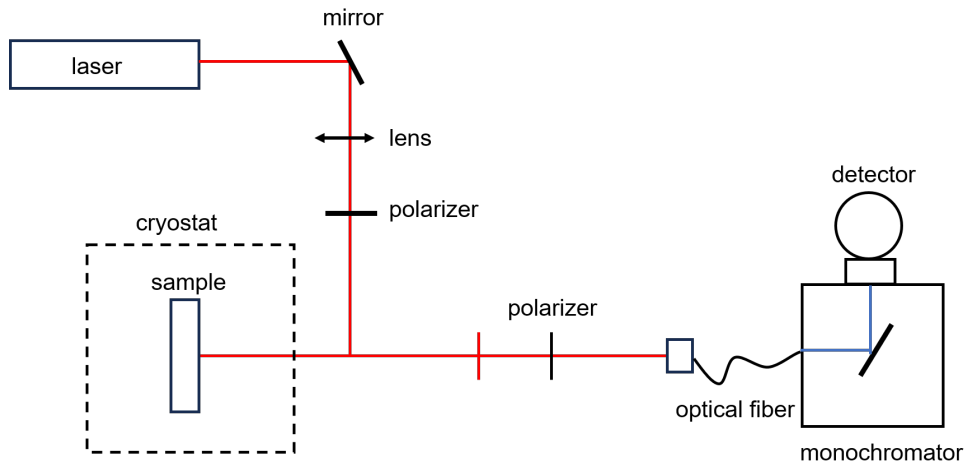


Figure 4.2: Sketch of a PL setup.

Two non-radiative deactivation mechanisms compete with fluorescence: internal conversion from the lowest singlet excited state to the ground state and intersystem crossing from the excited singlet state to the triplet state. This latter process gives rise to phosphorescence. The photoluminescence flux can be used to calculate the quasi-Fermi level splitting (ΔE_f) [71]:

$$\Delta(E_f) = kT \ln \frac{n^2}{n_i^2} \quad (4.2)$$

where n and n_i refer to the concentration of electrons and the equilibrium charge carriers, respectively.

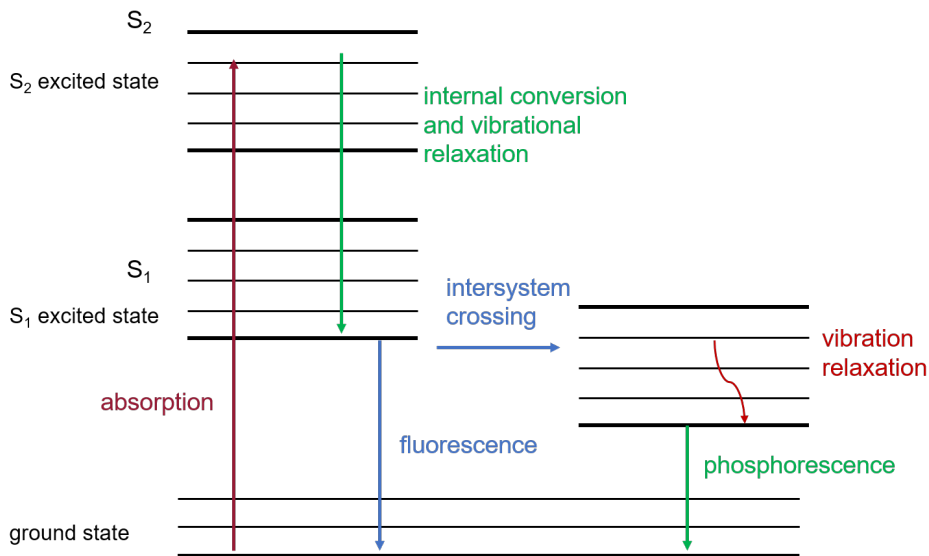


Figure 4.3: Sketch of the Jablonski diagram, showing the absorbance, fluorescence, and phosphorescence.

The charge carrier concentration can be calculated with the effective density of states N_C and N_V (for conductive and valence bands, respectively) and the bandgap (E_g).

$$n_i^2 = N_C N_V \exp\left(\frac{-E_g}{kT}\right) \quad (4.3)$$

Equation 4.2 ensures that for a given generation and recombination rate, materials with larger bandgap (that is, materials with lower n_i according to Equation 4.3) tend to have a higher ΔE_f . Typically, a 405 nm or 450 nm excitation is chosen. However, it is important to select the most suitable excitation energy and slit sizes, as our instrument has a saturation point (maximum intensity of 1000). Typically, scans can be performed from 500 nm to 900 nm, with a slit size typically ranging from 5 to 15 nm.

4.3.2 Confocal Photoluminescence Mapping

Photoluminescence mapping was performed using a confocal time-correlated single-photon counting (TCSPC) setup (PicoQuant, MicroTime 200). A 404 nm pulsed laser with an average power of 100 mW/cm² (0.1 μ J/cm² per pulse), operating at repetition rates of 10 MHz for various perovskite films, was focused onto the sample using a $\times 100$ objective. The resulting data were smoothed by averaging nearby data points spatially and temporally. PL was collected across a region of 10 μ m \times 10 μ m. [72]. Confocal PL and time-resolved photoluminescence (TRPL) measurements in this thesis were performed at Cambridge University. In addition, a time-correlated single photon counting technique is used to record the transient photoluminescence signals, which is typically used to study the charge carrier recombination kinetics in the perovskite field. The typical setup with each component is shown in Figure 4.4. In short, the pulsed laser excites the perovskite sample (which can be either a pure film or a perovskite film with a charge transport layer), and then the luminescence is directed toward a detector. The detection unit measures the time elapsed between the excitation laser pulse and the first photon emitted and recorded. Because photon emission is a statistical process, the measurement is conducted at a high repetition rate (kHz–MHz). This results in the generation of a histogram of photon emission times, which mirrors the luminescence decay observed in the sample. The average radiative lifetime was used as a means to mathematically quantify the lifetime and statistically compare the decay times between samples, but it was stressed that no physical model was involved in this.

4.3.3 UV-Vis Spectroscopy

UV-Vis spectroscopy is a powerful technique to quantify the absorption, transmission, and reflection in ultra-violet and visible range.

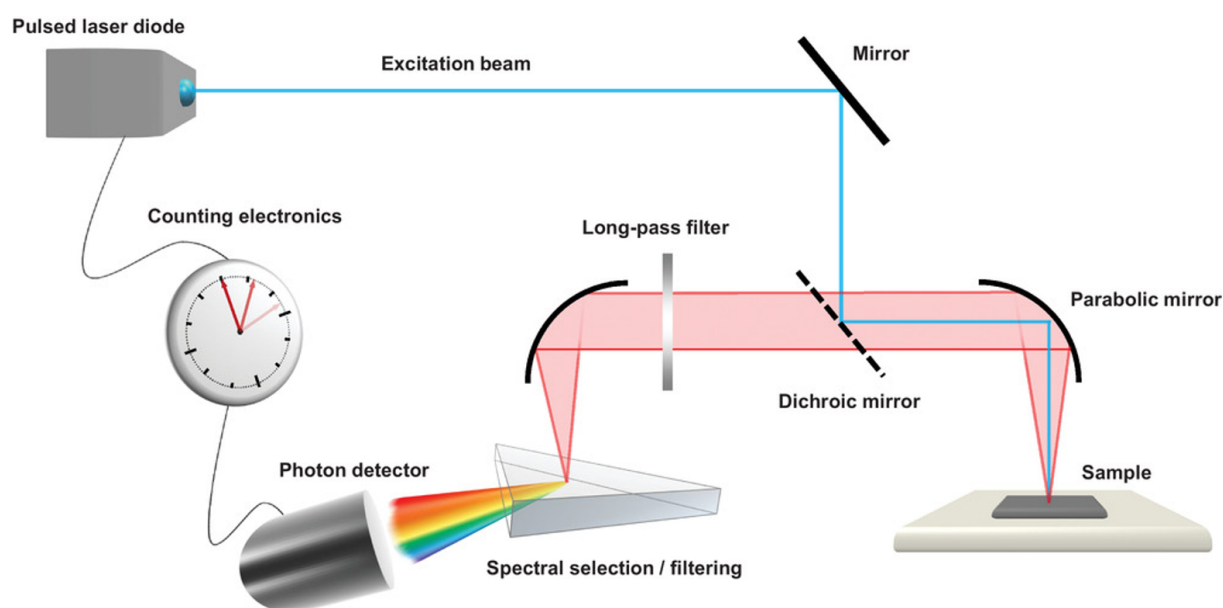


Figure 4.4: Sketch of the TRPL setup, typically consisting of a pulsed laser diode, photodetector, and counting electronics. Reproduced from Ref. [71] with permission. Copyright 2020, Wiley-VCH

Typically, a UV-Vis setup consists of three main components, that is, the light sources for visible light (halogen lamp) and ultraviolet light (deuterium lamp), a monochromator that narrows down the spectrum to a selected wavelength band, and a beam splitter that divides the beam into a sample and a reference beam (Figure 4.5).

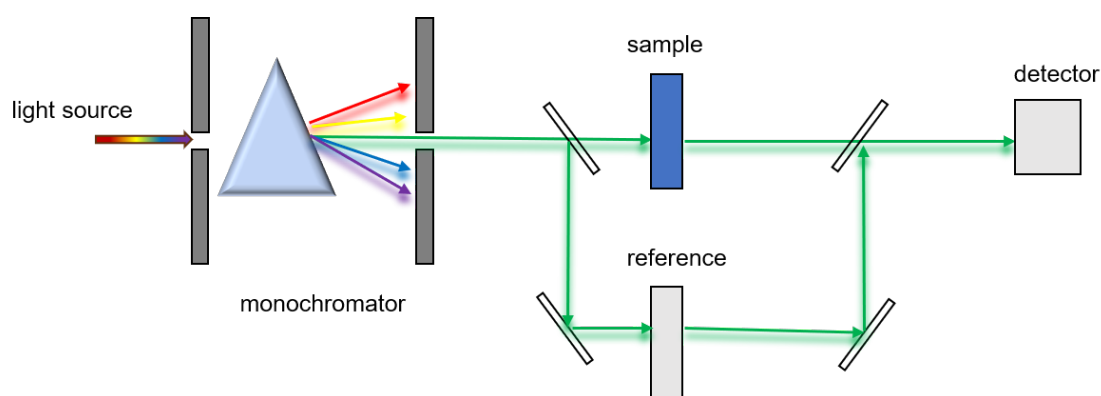


Figure 4.5: Sketch of a UV-Vis setup.

When light passes through the sample, the intensity of the transmitted light, $I_t(\lambda)$, is measured by a photodetector and compared with the incident radiation, $I_0(\lambda)$. The absorbance $A(\lambda)$ of the sample is defined by the Lambert-Beer law:

$$A(\lambda) = -\log_{10} \left(\frac{I_t(\lambda)}{I_0(\lambda)} \right) = L\alpha(\lambda) \log_{10}(e) \quad (4.4)$$

where L and $\alpha(\lambda)$ are the thickness and the absorption coefficient of the material, respectively. Therefore, by including the transparent substrate of the sample in the reference beam, its contributions can be eliminated by logarithmic subtraction. The prerequisite of light absorption for semiconducting materials is that the photon energy E_{ph} is higher than the bandgap energy E_g . In other words, the bandgap of a semiconducting sample can be extracted from UV-Vis spectroscopy using the Tauc equation: [73]

$$(\alpha h\nu)^n = B(h\nu - E_g) \quad (4.5)$$

where B and h refer to a constant and the Planck's constant, respectively. By plotting $(\alpha h\nu)^n$ against photon energy $h\nu$, the bandgap can be extracted from the intersection on the x-axis after linear extrapolation. The exponent n refers to the semiconductor material with indirect bandgaps ($n = 0.5$) or direct bandgaps ($n = 2$). In addition, the Urbach energy, which corresponds to the energetic disorder, can be extracted from the absorption spectrum with a characteristic sharp band edge [74]. In practical measurements, baseline correction typically involves blocking the probe beam entirely to establish 0% transmission and allowing the probe beam to pass freely to establish 100% transmission. Typically, the scan range is set from 500 to 900 nm, with a scan speed of 240 nm/min. The spectral slit width is set to 1 nm, and depending on the sample, either a glass or ITO substrate is used as the reference.

4.3.4 Transient Absorption Spectroscopy

Transient absorption spectroscopy (TAS) is used to unravel the photoexcited charge carriers of perovskite materials. In a TA measurement, a femtosecond pulse (that is pump pulse) initiates the populations of excited states, which are then monitored by another broadband femtosecond pulse (probe) with a varied time delay (Figure 4.6A). This delay is controlled either by a mechanical delay stage for picosecond delay or an electrical delay stage for nanosecond delay. By monitoring the difference in the transmission spectra of the probe with and without pump pulse, time-resolved changes in the absorption of the materials induced by the pump pulse can be retrieved and correlated with the evolution of excited states. Therefore, the signal obtained from TA measurements is the relative transmission change to the probe, given by:

$$\frac{\Delta T}{T} = \frac{T_{pump\ on} - T_{pump\ off}}{T_{pump\ off}} \quad (4.6)$$

The resultant transmission difference spectrum contains three types of signals (Figure 4.6B):

- photoinduced absorption (PIA), $\Delta T < 0$, might be due to a band renormalization, a

self-trapped state, and an excited state absorption (ESA).

- ground state bleach (GSB), $\Delta T > 0$, resulting from the reduction in optical density in the region of the ground state absorption from the depletion of the ground state electronic population and filling of excited states [75].
- stimulated emission (SE), $\Delta T > 0$, due to a pump-induced emission from the sample, which is located at similar energies of the photoluminescence of the sample.

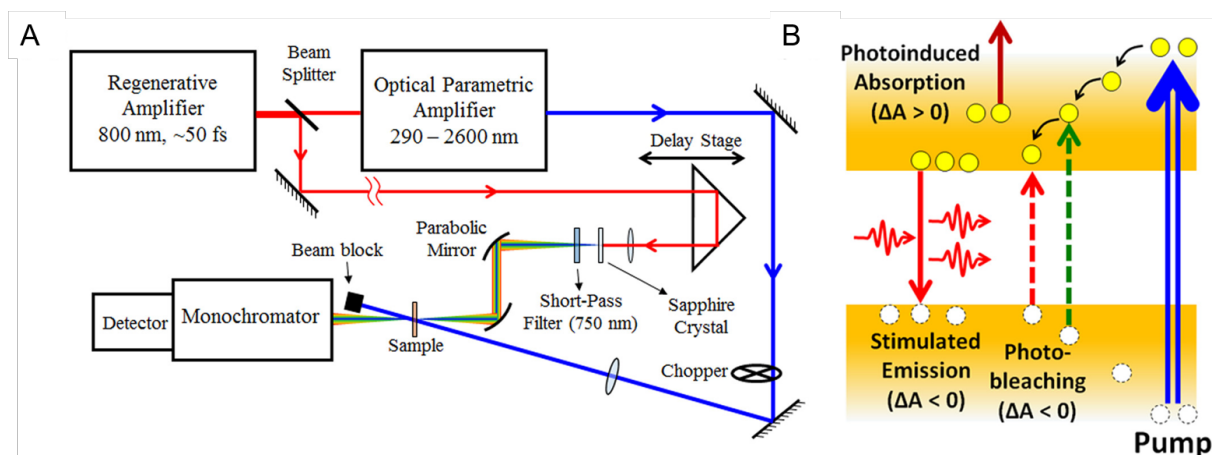


Figure 4.6: (A) Sketch of a typical fs-TAS setup. (B) Illustration of the photobleach (PB), photoinduced absorption (PIA), and stimulated emission (SE) processes. Reproduced from Ref. [75] with permission. Copyright 2016, American Chemical Society.

TA measurements in this thesis were performed at Heidelberg University with commercial TA spectrometers (Ultrafast Systems, HELIOS and EOS). The relative content of the respective phase in RDPs can be quantified by the amplitude of the GSBs peak signal as [76]:

$$p_{ni} = \frac{\int_{ni}^n \Delta A dE}{\int_n^m \Delta A dE} \quad (4.7)$$

where p_{ni} and ΔA are the relative content of the respective phase and the amplitude of the GSBs signal of each phase, respectively. All TA data were collected for photoexcitation at 430 nm with pump fluence of $\sim 200 \mu\text{J}/\text{cm}^2$.

4.4 Solar Cell Characterization

4.4.1 Current density-Voltage measurement

The current density-voltage (J-V) was characterized using a Keithley 2611B source meter under 1.5G illumination (class ABA, LOT-Quantum design GmbH, $100 \text{ W}/\text{m}^2$). The light

intensity was calibrated by a Si reference cell (Fraunhofer ISE019-2015). The Si reference cell should give rise to a short circuit current of 47.95 mA under AM 1.5G illumination. The PSCs were measured with a scan step of 10 mV, a scan speed of 50 mV s⁻¹, and an integration time of 100 ms. If not stated otherwise, the forward scan and reverse scan are operated from -0.2 V to 1.2 V and from 1.2 V to -0.2 V in the case of n-i-p PSCs. There are 6 solar cells per substrate with a substrate dimension of 2.5 cm × 2.5 cm. The active area was defined by a metal aperture (0.079 cm²). All devices were measured without encapsulation. The solar cell performance was calculated based on Python codes (available at [https://collab.dvb.bayern/display/TUMe13/Batch processing](https://collab.dvb.bayern/display/TUMe13/Batch+processing)).

4.4.2 External Quantum Efficiency

The external quantum efficiency (EQE) is defined as the flux of electrons extracted from a solar cell under operation divided by the incident photon flux. Measurements of EQE spectra were made using a QTEST HIFINITY 5 (Crowntech Inc., USA) at room temperature in the air. A standard Si single-crystal photovoltaic cell was used to calibrate the light intensity.

4.5 Experimental Setups for X-ray Scattering

This section describes the experimental setups using synchrotron sources, the detailed technical parameters, and data correction and processing.

***Operando* GISAXS/GIWAXS During Device Operation**

Operando GISAXS/GIWAXS measurements are performed at the Austrian SAXS beamline (ELETTRA, Trieste, Italy) and the beamline P03 MiNaXS of the storage ring PETRA III (DESY, Hamburg, Germany), respectively [77].

Regarding the *operando* experiment at ELETTRA, the X-ray wavelength is 1.550 Å, corresponding to a photon energy of 8 keV. The scattering data were collected by a Pilatus 1M detector (Detrics, pixel size of 172 μm) at an incidence angle of 0.4°. The sample-to-detector distance (SDD) was set to 1577.5 mm.

In terms of the *operando* setup at ELETTRA (Figure 4.7), the whole setup consists of a home-made gas-flow setup, a solar simulator, a Keithley, a water-cooling system, and a chamber with two attached Kapton windows on both front and back side. The working temperature of the perovskite solar cell chamber was set to 25 °C by a water-cooling system in order to eliminate the potential structure change induced by temperature. A homemade gas-flow setup was applied to control the humidity of the whole device. The

solar cell performance as a function of time was simultaneously obtained by a source meter (Keithley 2600) at 120 s intervals. Notably, the relative humidity was set to 75 % ramping up from the start.

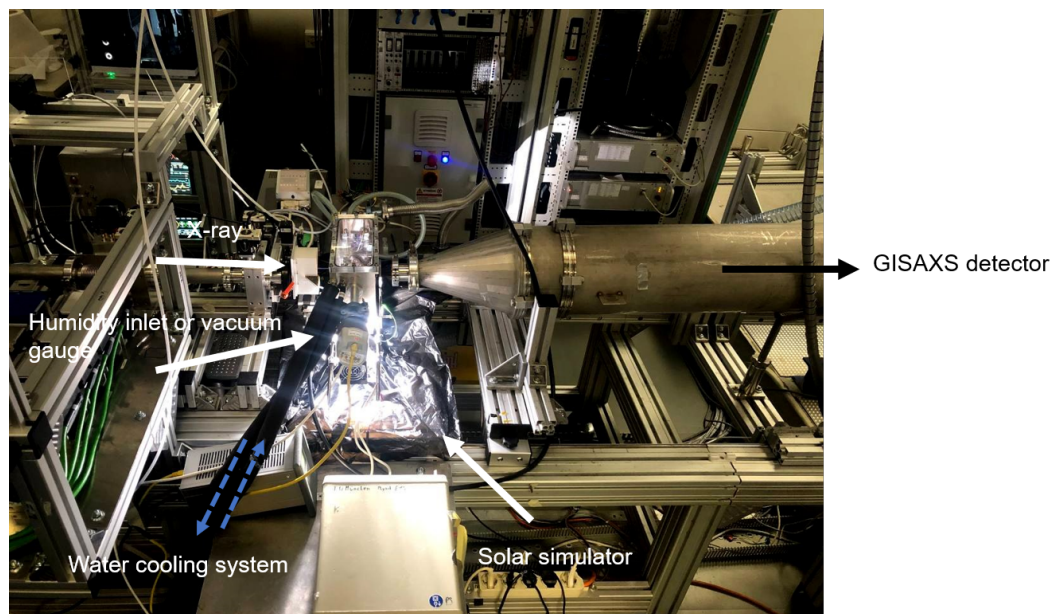


Figure 4.7: Operando setup at ELETTRA, consisting of a pocket solar, a Julabo, and a solar simulator.

In addition, static GIWAXS measurements (Chapter 6) were carried out with a Ganesha 300XL SAXS-WAXS instrument at a beam energy of 8.047 keV. The GIWAXS data was recorded by a Pilatus 300 K (Dettrics, pixel size of 172 μm) at a SDD of 95.67 mm, and the incident angle was 0.6 $^\circ$.

All GIWAXS data (in and ex situ) in Chapter 7 were collected at beamline P03 at PETRA III synchrotron (DESY, Hamburg) [77]. In situ 2D GIWAXS data was collected under an incidence angle of 0.4 $^\circ$ with an X-ray beam energy of 11.8 keV and recorded on a LAMBDA 9M detector (X-Spectrum), where the SDD was 243 mm. In the kinetic study of the film growth, the data was recorded with an exposure time of 0.2 s. Operando GIWAXS data was collected under an incident angle of 0.6 $^\circ$ with an electron X-ray beam energy of 11.83 keV and a SDD of 354 mm, whereas an exposure time of 1 s was used. Angular-dependent X-ray scattering data was collected with an X-ray beam energy of 12.92 keV and a SDD of 279.25 mm. The scattering depth is calculated in <https://gixa.ati.tuwien.ac.at/tools/penetrationdepth.xhtml> [78].

The in-situ printing setup is depicted in Figure 4.8, where a portable photoluminescence setup and atmosphere control can be integrated. The operando GIWAXS measurement on the quasi-2D perovskite solar cells was done via the ISOS-L-1I protocol (i.e., under the continuous bias scan and light illumination), using the same setup as mentioned earlier

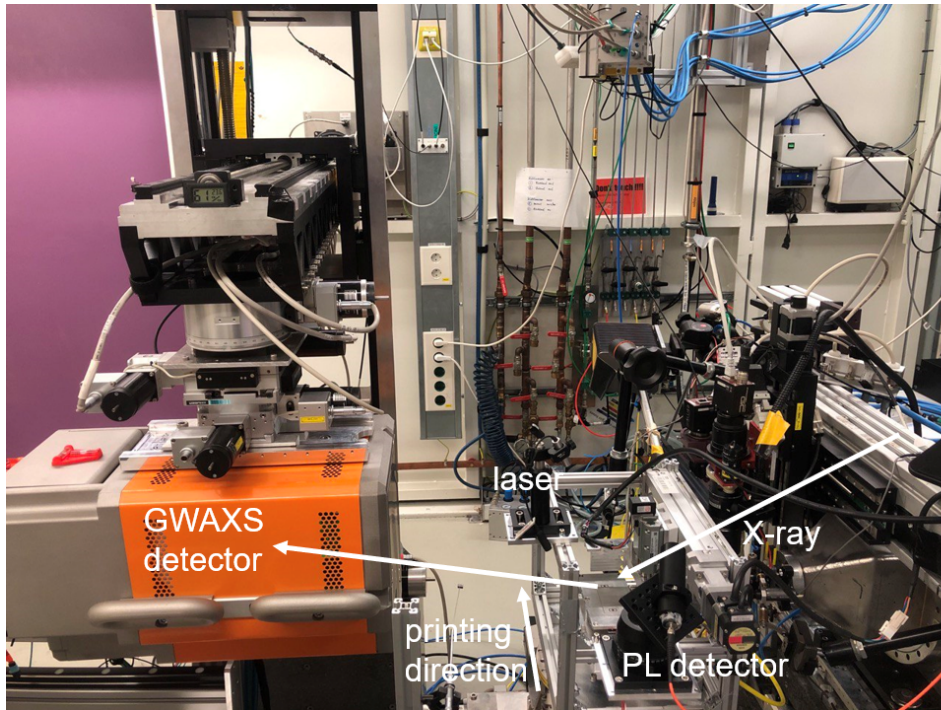


Figure 4.8: In-situ printing setup at DESY, Hamburg, with the main parts labeled.

at ELETTRA. In addition, the entire chamber was connected with cooling water (25 °C) to preclude the temperature-induced degradation.

The positions of the beam center and SDD in all measurements were calibrated by fits to the patterns of LaB_6 and CeO_2 with the DPDAK package [79]. The reshaped 2D GIWAXS data, the line cuts, and the azimuthal integration of the scattering data were processed with the Python tool INSIGHT [66]. The correction of SDD was done by calibrating the ITO peak to $q = 2.132 \text{ \AA}^{-1}$. The GIWAXS data in Chapter 7 was indexed according to literature [80, 81].

A proper *operando* experiment should adhere to these protocols: conducting an X-ray radiation damage test to determine the maximum exposure time of the sample; aligning the sample, which includes determining the sample movement limit (especially crucial for GISAXS measurements) and correcting for tilt; periodically checking the alignment due to heat expansion. Notably, the sample holder is moved in tiny steps by the hexapod before each individual X-ray measurement to minimize beam-induced damage.

Unraveling the Modification Effect at NiO_x/Perovskite Interfaces

The results shown in this chapter are retrieved from the publication: *Unraveling the modification effect at NiO_x/perovskite interfaces for efficient and stable inverted perovskite solar cells* (X. Kang, D. Wang, K. Sun, X. Dong, W. Hui, B. Wang, L. Gu, M. Li, Y. Bao, J. Zhang, R. Guo, Z. Li, X. Jiang, P. Müller-Buschbaum, L. Song, *Journal of Materials Chemistry A*, **11**, 22982-22991 (2023)), reproduced from [67] with permission, copyright 2023, Royal Society of Chemistry. Kang *et al.*, contributed to device fabrication and performed SEM, FTIR, KPFM, and SEM characterizations.

Due to low costs and high light transmittance, solution-processed NiO_x nanocrystals as the hole transport layer (HTL) for inverted perovskite solar cells (PSCs) have attracted great attention recently. Nevertheless, the intrinsic defects (Ni vacancies) in the NiO_x film and the I vacancies at the buried interface of the perovskite limit the performance of PSCs. Thus, in this work, iodine-substituted phenyl acids are used to modify the NiO_x/perovskite layer interface. The results show that the acid functional groups have strong coordination with Ni vacancies in the NiO_x film, giving rise to a high conductivity of NiO_x films and thereby an improved hole transport capacity. The para-iodine gives the molecule a larger dipole moment, leading to a better energy level alignment between NiO_x and the perovskite and thereby a favorable hole transfer through the NiO_x/perovskite interface. As a result, the PSC based on 4-iodophenylboronic acid yields a champion power conversion efficiency (PCE) of 22.91% and an improved fill factor of 86.18%. The non-encapsulated device maintains above 80% of its initial PCE after storing in N₂ for 3000 h, under heating at 60 °C for 1000 h and in air with a relative humidity (RH) of 50–70% for 1000 h.

5.1 Preface

Taking advantage of high efficiency, low costs, solution processability and long term operational stability, PSCs have been identified as one of the most promising photovoltaic technologies [82, 83, 84, 85, 86]. Among the device configurations, inverted PSCs have attracted great attention in recent years due to their excellent operating stability, low hysteresis, and low temperature processability [87, 88]. Particularly, PCEs underwent a rapid increase, which have been pushed well beyond 25% [89]. The hole transport layer (HTL) plays a critical role in inverted PSCs because it determines the hole conductivity and crystallization of perovskites. Poly(triarylamine) (PTAA) hinders the commercialization of PSCs due to its strong hydrophobicity and poly(3,4-ethylenedioxythiophene):polystyrene sulfonate (PEDOT:PSS) is substituted due to the energy level mismatch between the HTL/perovskite layer and the carrier recombination at the interface [90, 91, 92, 93]. Other than that, self-assembled monolayers (SAMs) emerging in recent years typically require complex synthesis and high costs and are unsuitable for large area deposition [94, 95, 96, 97]. Moreover, the intrinsic hole mobility is low. To address this issue, various dopants featuring hygroscopicity and corrosivity are used to modify the electronic properties of organic HTMs. However, the obtained device stability will be negatively affected [98, 99, 100, 101, 102, 103, 104].

Owing to superior physical and chemical stability, high light transmittance, ease of production and low costs, the inorganic counterparts have gained significant research interest in inverted PSCs [105, 106, 107, 108, 109, 110, 111, 112]. Among various species, NiO_x is an attractive and promising alternative with the additional merits of having an appropriate energy level alignment with perovskites and a low hysteresis in device operation [113, 114, 115]. The intrinsic defects (Ni vacancies) in NiO_x films are essential for hole conductivity, but they simultaneously cause the generation of defect energy levels and perovskite degradation [116, 117, 118, 119]. Therefore, a proper modification at the NiO_x/perovskite interface is necessary. Halogen-substituted benzoic acids have been reported to modify NiO_x films, which could lower charge carrier recombination and achieve stable and efficient inverted PSCs [120, 121]. On the one hand, acid groups were found to passivate oxygen defects at the NiO_x surface. On the other hand, halogen bonding allowed for a strong reaction between the used molecules and perovskites, which was beneficial to passivate defects and suppress ion migration in the perovskite films [120]. Therefore, the modification molecules served as bridging agents at the interface as they had chemical bonding with both NiO_x and perovskite.

Inspired by these approaches, a series of iodine-substituted phenyl acids are used to modify the NiO_x/perovskite interface and present a systematic study on how the acid functional groups and iodine locations at the benzene ring impact the photovoltaic performance

of inverted PSCs. Different acid groups feature different coordination effects with the NiO_x film, consequently giving different degrees of modification on the semiconductor properties of the NiO_x . Among the used modifiers, 2-iodophenylboronic acid (2-IPBA) is optimal due to the strongest coordination with Ni vacancies. In addition, the influence of iodophenyl functional groups by varying the iodine locations at the benzene ring is further explored. The para-substituent gives a larger dipole moment than the ortho-iodine, engendering a better energy level alignment between the NiO_x and perovskite and thereby a favorable hole transfer through the NiO_x /perovskite interface. Moreover, the halogen bonding between the 4-iodophenylboronic acid (4-IPBA) with perovskite is stronger than for the 2-IPBA-perovskite interaction, leading to a decreased density of trap states at the buried surface of the perovskite film. As a result, the 4-IPBA-based inverted $\text{Cs}_{0.05}(\text{FA}_{0.98}\text{MA}_{0.02})_{0.95}\text{Pb}(\text{I}_{0.98}\text{Br}_{0.02})_3$ PSCs exhibited a champion PCE of 22.91% and a fill factor (FF) of 86.18%. The nonencapsulated devices retain 81.1%, 80.6% and 80.1% of their initial PCEs after storing in N_2 for 3000 h, in air with a relative humidity (RH) of 50–70% and heating at 60 °C for 1000 h, respectively.

5.2 Solar Cell Performance and Morphology

The perovskite studied in this work is $\text{Cs}_{0.05}(\text{FA}_{0.98}\text{MA}_{0.02})_{0.95}\text{Pb}(\text{I}_{0.98}\text{Br}_{0.02})_3$. It has been demonstrated that halogenated phenyl acids could efficiently modify NiO_x layer surfaces, leading to stable and efficient inverted perovskite solar cells [120, 121]. For a systematic study, the influence of acid groups on the modification properties of NiO_x thin films is discussed. Following this concept, 2-iodobenzoic acid (2-IBA), 2-iodobenzenesulfonic acid (2-IBSA), and 2-IPBA are selected to modify the NiO_x layers (Figure 5.1).

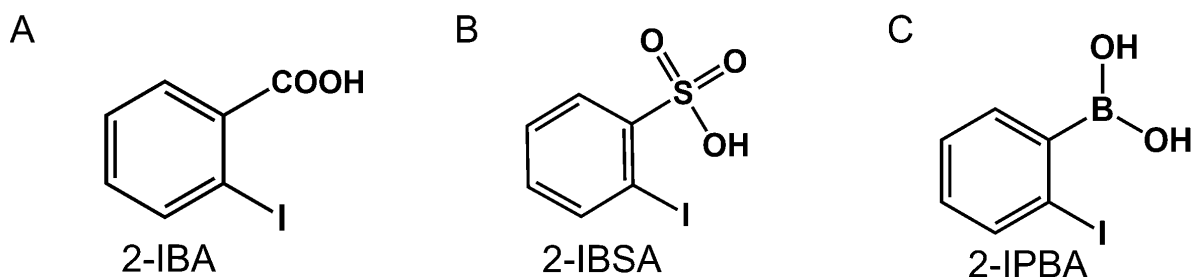


Figure 5.1: Chemical structures of (A) 2-IBA, (B) 2-IBSA, and (C) 2-IPBA. Reproduced from Ref. [67] with permission. Copyright 2023, Royal Chemistry of Society.

Figure 5.2A compares the current–voltage ($J - V$) characteristics of the best-performing PSCs without (control) and with different modifiers.

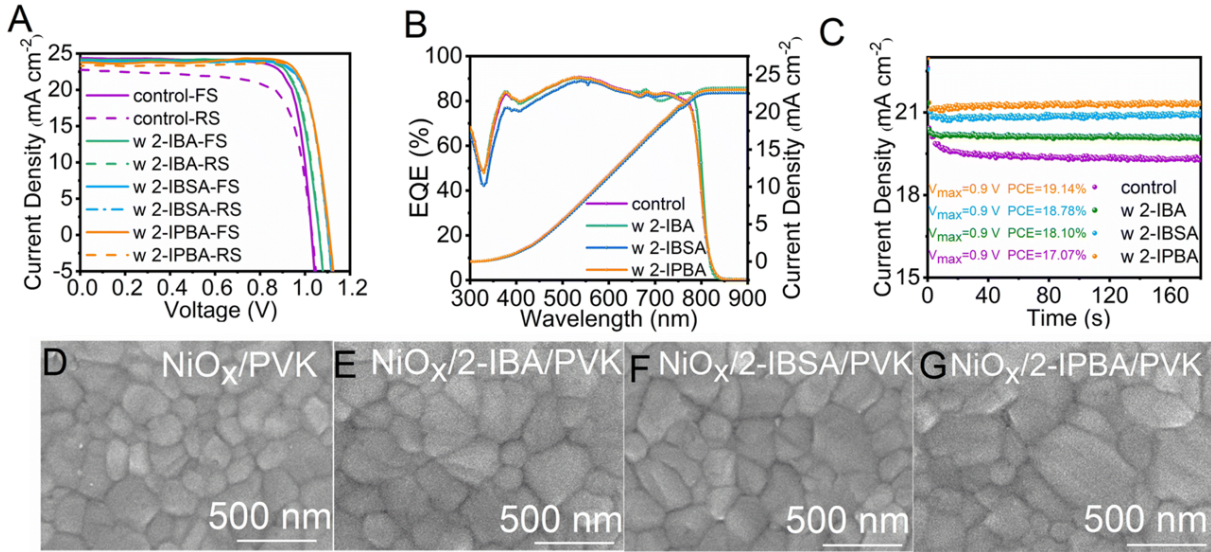


Figure 5.2: (A) J - V curves of PSCs measured in both reverse and forward directions. (B) EQE spectra with integrated J_{sc} curves and (C) steady-state photocurrents at maximum power points of the control, 2-IBA-, 2-IBSA- and 2-IPBA-modified devices, respectively. SEM images of perovskite films deposited on (D) NiO_x , (E) $\text{NiO}_x/2\text{-IBA}$, (F) $\text{NiO}_x/2\text{-IBSA}$, and (G) $\text{NiO}_x/2\text{-IPBA}$, respectively. Reproduced from Ref. [67] with permission. Copyright 2023, Royal Chemistry of Society.

Table 5.1: Extracted champion photovoltaic parameters from J - V curves

samples	scan direction	V_{OC} (V)	J_{SC} ($\text{mA} \cdot \text{cm}^{-2}$)	FF (%)	PCE (%)
control	forward	1.03	24.35	80.04	20.04
control	reverse	1.02	23.50	75.82	18.23
W 2-IBA	forward	1.06	24.20	80.81	20.77
W 2-IBA	reverse	1.06	24.16	80.77	20.76
W 2-IBSA	forward	1.10	23.95	80.97	21.37
W 2-IBSA	reverse	1.10	23.84	81.09	21.28
W 2-IPBA	forward	1.10	23.76	82.90	21.81
W 2-IPBA	reverse	1.10	23.30	84.25	21.68

The extracted photovoltaic parameters are summarized in Table 5.1. It is noted that the control device exhibits a champion PCE of 20.04%. With the introduction of iodine-substituted phenyl acids, the obtained PCEs increased, reaching 20.77%, 21.37% and 21.81% for the 2-IBA-based, 2-IBSA-modified and 2-IPBA-treated devices, respectively.

5.2. Solar Cell Performance and Morphology

To verify the performance reliability, the PCE distributions are obtained out of 35 devices for each type individually (Figure 5.3).

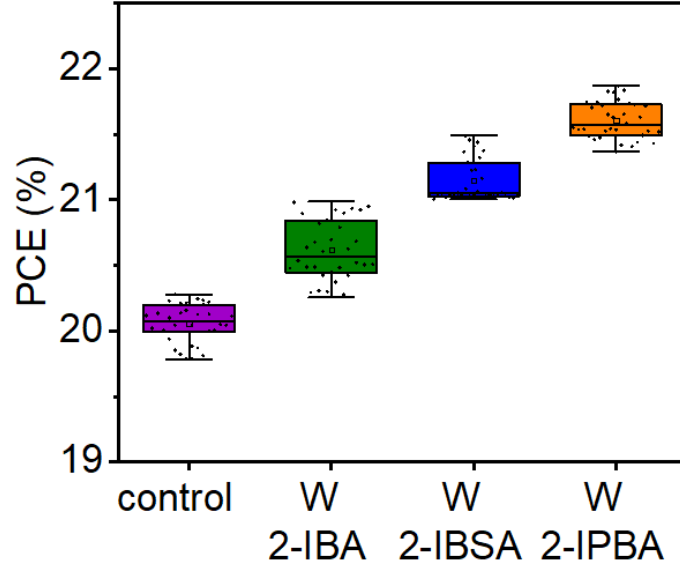


Figure 5.3: PCE statistics obtained from 35 individual control, 2-IBA, 2-IBSA, and 2-IPBA modified PSCs. Reproduced from Ref. [67] with permission. Copyright 2023, Royal Chemistry of Society.

Table 5.2: The average data collected out of 35 cells

samples	V_{OC} (V)	J_{SC} ($mA\ cm^{-2}$)	FF (%)	PCE (%)
control	1.03 ± 0.01	24.23 ± 0.27	79.89 ± 1.32	20.06 ± 0.15
W 2-IBA	1.06 ± 0.01	24.19 ± 0.16	80.93 ± 0.14	20.61 ± 0.24
W 2-IBSA	1.10 ± 0.01	23.95 ± 0.19	80.32 ± 0.21	21.20 ± 0.17
W 2-IPBA	1.10 ± 0.01	23.57 ± 0.33	82.08 ± 0.71	21.70 ± 0.14

The average data collected out of 35 cells are summarized in Table 5.2 and the value is the highest for the 2-IPBA-treated cells as well. Figure 5.2B displays the external quantum efficiency (EQE) spectra of these four types of PSCs, in which the integrated J_{SC} values agree well with the values obtained from $J - V$ sweeps. The observed PCE improvement mainly originates from the enhancement of FF and V_{OC} (Table 5.1). The steady-state photocurrent outputs at the maximum power points show higher photocurrents over time in the device based on $NiO_x/2-IPBA$ (Figure 5.2C) among other types of PSCs. The differences in the device performance induced by different acid groups are discussed in detail regarding their interaction with NiO_x in the following.

To investigate the influence of 2-IBA, 2-IBSA and 2-IPBA treatments on the morphology of the perovskite films, plan view scanning electron microscope (SEM) measurements are carried out and the obtained results are displayed in Figure 5.2D–G. All films present a dense structure composed of closely packed perovskite crystals. However, the grain sizes differ. The control sample features an average size of about 200 ± 44.76 nm. With the modification at the NiO_x /perovskite interface, an increase in the average grain size is observed, reading 278 ± 65.66 nm for the 2-IBA-modified perovskite film, 267 ± 49.60 nm for the 2-IBSA-modified perovskite sample and 290 ± 54.58 nm for the 2-IPBA-modified perovskite film (Figure 5.4).

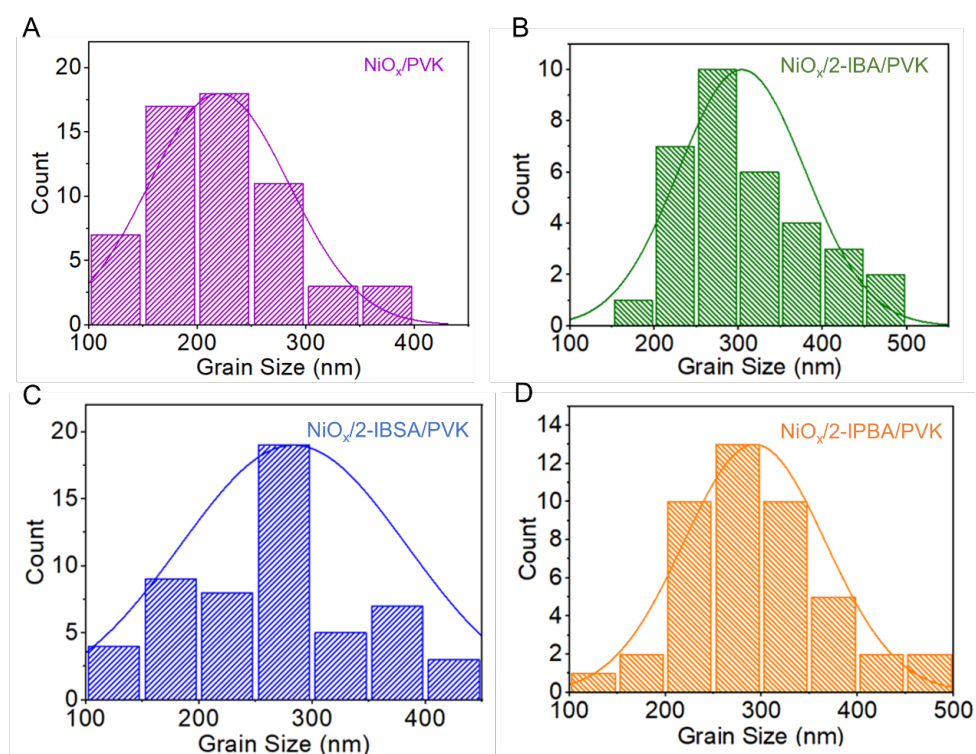


Figure 5.4: Size distributions of the perovskite grains deposited on (A) NiO_x , (B) $\text{NiO}_x/2\text{-IBA}$, (C) $\text{NiO}_x/2\text{-IBSA}$, and (D) $\text{NiO}_x/2\text{-IPBA}$, respectively. Reproduced from Ref. [67] with permission. Copyright 2023, Royal Chemistry of Society.

The increased grain size is ascribed to the improved hydrophobicity of the NiO_x film after modification, which is verified by contact angle measurements (Figure 5.5). It is found that all modified NiO_x films are more hydrophobic than the control sample. A similar observation was reported by Su *et al.*, who found that an improved hydrophobicity of the deposited substrate gave rise to an increased perovskite-grain size due to the reduced nucleation sites induced by the higher surface energy [122]. From the cross-sectional SEM images, the thicknesses of all perovskite films are determined to be about 700 nm (Figure 5.6).



Figure 5.5: Contact angle testing for (A) the NiO_x , (B) $\text{NiO}_x/2\text{-IBA}$, (C) $\text{NiO}_x/2\text{-IBSA}$, and (D) $\text{NiO}_x/2\text{-IPBA}$ substrates. Reproduced from Ref. [67] with permission. Copyright 2023, Royal Chemistry of Society.

5.2.1 Crystallinity and Orientation

Grazing-incidence wide-angle X-ray scattering (GIWAXS) measurements give crystalline information about the whole film. The reshaped 2D-GIWAXS data are shown in Figure 5.7A–D. The perovskite films deposited on NiO_x , $\text{NiO}_x/2\text{-IBA}$, $\text{NiO}_x/2\text{-IBSA}$ and $\text{NiO}_x/2\text{-IPBA}$ display characteristic diffraction rings at $q \sim 1, 2, \text{ and } 2.2 \text{ \AA}^{-1}$, which correspond to the (110), (220), and (310) crystal planes, suggesting that 2-IBA, 2-IBSA and 2-IPBA treatments do not alter the crystal phase (the signal at $q \sim 0.5 \text{ \AA}^{-1}$ is from

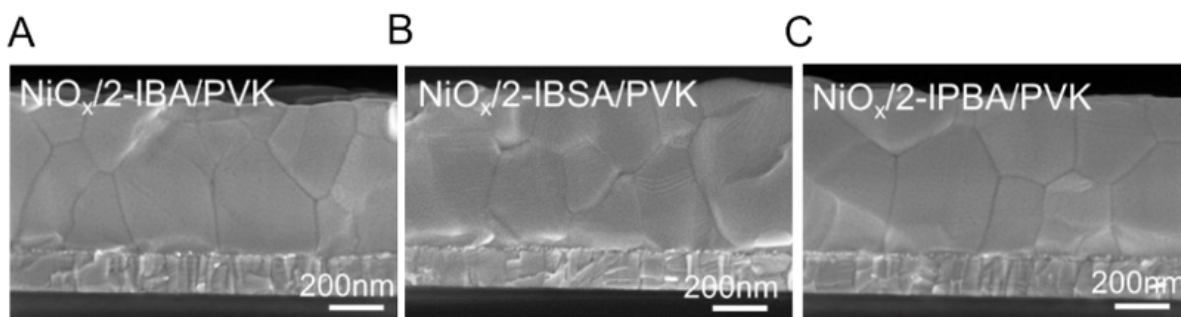


Figure 5.6: Cross-sectional SEM images of the perovskite films deposited on the (A) $\text{NiO}_x/2\text{-IBA/PVK}$, (B) $\text{NiO}_x/2\text{-IBSA/PVK}$, and (C) $\text{NiO}_x/2\text{-IPBA/PVK}$ substrates. Reproduced from Ref. [67] with permission. Copyright 2023, Royal Chemistry of Society.

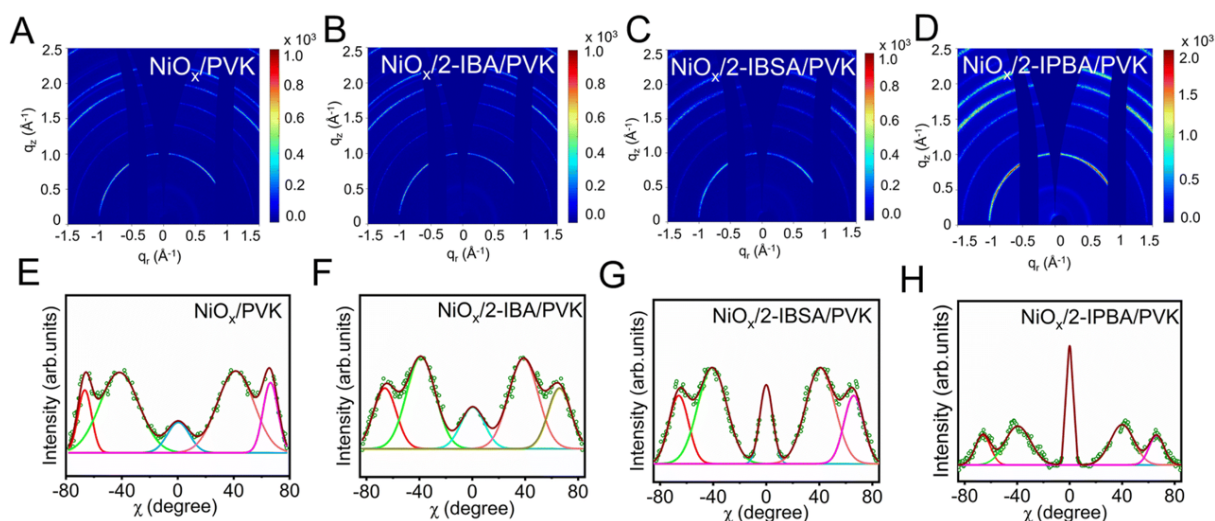


Figure 5.7: Reshaped 2D GIWAXS data obtained from the perovskite films deposited on (A) NiO_x, (B) NiO_x/2-IBA, (C) NiO_x/2-IBSA, and (D) NiO_x/2-IPBA, respectively. The vertical black stripes at $q_r = -0.5$ – 0.2 \AA^{-1} and $q_r = 0.8$ – 1.1 \AA^{-1} are due to the inter-module detector gaps. Azimuthal tube integrals are performed on (110) diffraction rings with an angular width of $q_r = 0.97$ – 1.02 \AA^{-1} of perovskite films deposited on (E) NiO_x, (F) NiO_x/2-IBA, (G) NiO_x/2-IBSA, and (H) NiO_x/2-IPBA, respectively. Reproduced from Ref. [67] with permission. Copyright 2023, Royal Chemistry of Society.

Kapton windows at the beamline, which consequently is not related to perovskite films). From the sector-averaged integrals of the 2D-GIWAXS data, the position of the diffraction peak was not shifted in the perovskite layer deposited on all modified NiO_x films compared to the control sample, indicating that the halogenated benzoic acid did not affect the crystal structure of the perovskite (Figure 5.8). To further study the crystal orientation induced by the modification molecules, azimuthal tube cuts are performed on the (110) peaks of the 2D-GIWAXS data with an angular width of $q_r = 0.97$ – 1.02 \AA^{-1} (Figure 5.7E–H). The perovskite crystals in all samples have preferred orientations at $\chi \sim 0^\circ$, 40° and 65° , but the full width at half maximum (FWHM) and degree of orientation (DoO) of the corresponding peaks differ (Table 5.3). In detail, the FWHM values decrease and the DoO values increase for the peak at $\chi \sim 0^\circ$. However an opposite trend is shown in the peak at $\chi \sim 65^\circ$, in which the FWHM values increase but the DoO values reduce. This observation indicates that the interfacial molecules shift the orientation of the (110) crystal plane from $\chi \sim 65^\circ$ to normal to the substrate and increase the grain size. This is expressed remarkably in the perovskite sample based on the NiO_x/2-IPBA, in which the smallest FWHM and the largest DoO are present for the peak at $\chi \sim 0^\circ$.

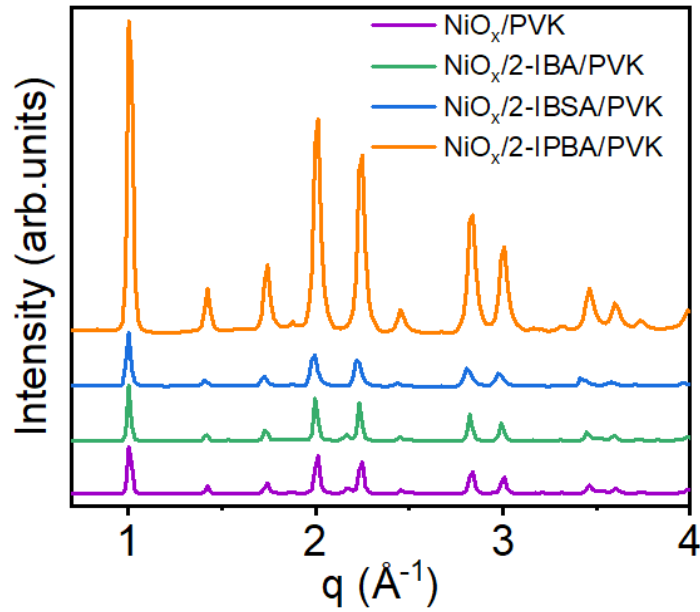


Figure 5.8: The sector-averaged integrals obtained from the 2D GIWAXS data for the perovskite films deposited on the NiO_x , $\text{NiO}_x/2\text{-IBA}$, $\text{NiO}_x/2\text{-IBSA}$ and $\text{NiO}_x/2\text{-IPBA}$ substrates. Reproduced from Ref. [67] with permission. Copyright 2023, Royal Chemistry of Society.

Table 5.3: FWHM and DoO parameters from Figure 5.7E-H

samples		$\chi \sim 0^\circ$	$\chi \sim 40^\circ$	$\chi \sim 65^\circ$
NiO_x/PVK	FWHM	52.18	48.24	17.68
NiO_x/PVK	DoO	2.34%	28.06%	11.20%
$\text{NiO}_x/2\text{I-BA}/\text{PVK}$	FWHM	34.41	31.81	41.76
$\text{NiO}_x/2\text{I-BA}/\text{PVK}$	DoO	5.58%	30.38%	15.62%
$\text{NiO}_x/2\text{I-BSA}/\text{PVK}$	FWHM	20.57	41.14	36.91
$\text{NiO}_x/2\text{I-BSA}/\text{PVK}$	DoO	6.21%	22.48%	10.64%
$\text{NiO}_x/2\text{I-PBA}/\text{PVK}$	FWHM	8.37	43.66	242.76
$\text{NiO}_x/2\text{I-PBA}/\text{PVK}$	DoO	8.02%	18.58%	8.28%

According to the literature, the growth of perovskite crystals is closely related to the substrate surface [122], and an ordered crystal orientation with a large grain size along the (110) direction is believed to have a positive effect on the charge carrier transport.

5.3 Optoelectronic Properties and Chemical Reaction

The UV/Vis absorption spectra of the perovskite films are shown in Figure 5.9A.

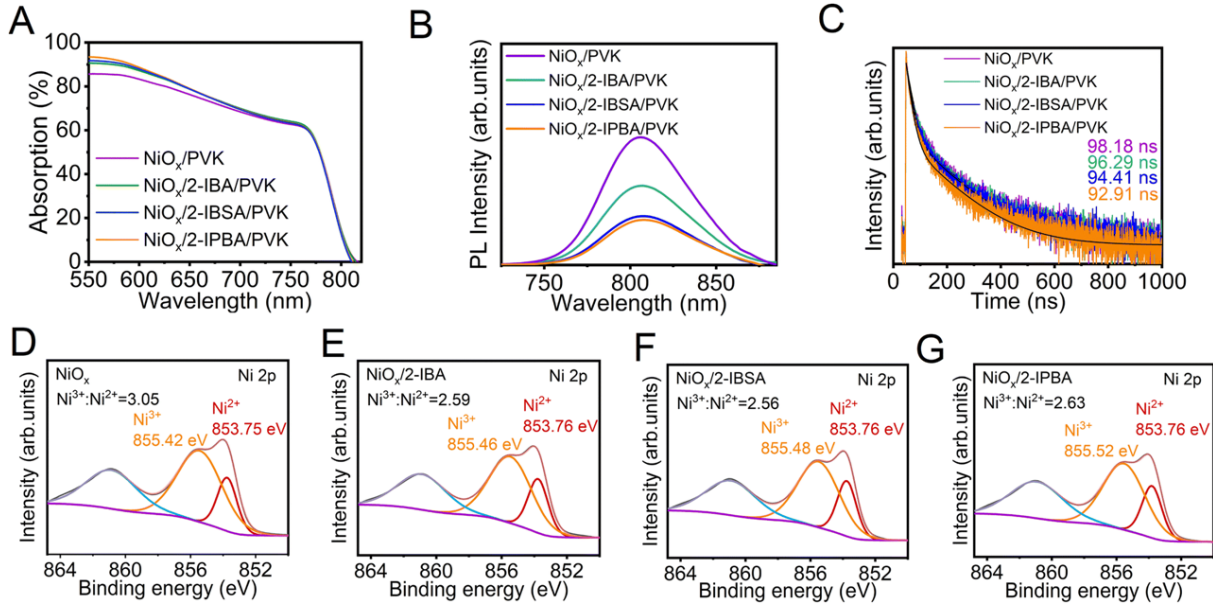


Figure 5.9: (A) UV-vis absorption spectra, (B) steady-state PL spectra, and (C) TRPL spectra of perovskite films deposited on the NiO_x, NiO_x/2-IBA, NiO_x/2-IBSA, and NiO_x/2-IPBA substrates, respectively. XPS spectra of the Ni 2p region for (D) NiO_x, (E) NiO_x/2-IBA, (F) NiO_x/2-IBSA, and (G) NiO_x/2-IPBA films, respectively. Reproduced from Ref. [67] with permission. Copyright 2023, Royal Chemistry of Society.

Generally, higher absorption is observed in the whole visible range for the modified samples than the control film, which is due to the larger grains induced by the halogenated phenyl acids. The photoluminescence (PL) curves show a reduced PL intensity in the modified films compared to the control sample (Figure 5.9B), indicating that the charge carrier transfer is more efficient in the presence of halogenated phenyl acids. This phenomenon is the most significant in the 2-IPBA-modified sample. Time-resolved PL (TRPL) spectra further confirm this conclusion (Figure 5.9C). Biexponential decay functions are used to fit these TRPL data and the obtained parameters are summarized in Table 5.4.

Table 5.4: Fitted TRPL parameters from Figure 5.9C

samples	τ_1 (ns)	τ_2 (ns)	A_1	A_2	ave. (ns)
NiO _x /PVK	20.75	149.46	39.84%	60.16%	98.18
NiO _x /2I-BA/PVK	20.14	144.81	40.43%	59.57%	94.41
NiO _x /2I-BSA/PVK	19.76	143.88	38.34%	61.66%	96.29
NiO _x /2I-PBA/PVK	19.38	136.86	37.41%	62.59%	92.91

The fast decay process is associated with the transfer of photogenerated charge carriers

5.3. Optoelectronic Properties and Chemical Reaction

from the perovskite film to the NiO_x substrate. For the control sample, the fast decay lifetime (τ_1) is about 20.8 ns. After the modification of the NiO_x /perovskite interface, τ_1 decreases and the 2-IPBA-modified sample exhibits the smallest value of 19.4 ns. This occurrence suggests that the charge carrier transfer to the modified NiO_x layers is more efficient. In order to clarify the difference in the morphology and optoelectronic properties of these samples, the interaction between the halogenated phenyl acids and NiO_x is investigated with X-ray photoelectron spectroscopy (XPS) measurements (Figure 5.9D–G). It can be seen that Ni 2p signals for the control sample demonstrate two peaks located at binding energies of 853.75 and 855.42 eV, which originate from Ni^{2+} and Ni^{3+} (Ni vacancies) in NiO_x , respectively, according to the reported literature [123]. Based on the integral area of both peaks, the ratio of $\text{Ni}^{3+}/\text{Ni}^{2+}$ is determined to be 3.05. For all modified samples, the Ni^{2+} peaks remain almost unchanged but the Ni^{3+} peaks shift towards higher binding energies. This occurrence implies that the acid functional groups of the used halogenated phenyl acids interact with Ni vacancies in the NiO_x films. Because of the presence of an unoccupied orbital in boron, the borate groups exhibit the strongest ability to accept electron pairs, while the carboxylate groups demonstrate the weakest ability. As a result, the relative shift observed is the largest for the 2-IPBA-modified NiO_x and the smallest for the 2-IBA-treated sample. Moreover, the ratio of $\text{Ni}^{3+}/\text{Ni}^{2+}$ decreases after modification as compared to the control sample, reading 2.59, 2.56 and 2.63 for the 2-IBA-, 2-IBSA- and 2-IPBA-treated NiO_x . To study the difference in the $\text{Ni}^{3+}/\text{Ni}^{2+}$ ratio, the NiO_x film before thermal annealing is investigated with XPS measurements as well (Figure 5.10). The ratio is determined to be 2.52 in this sample. The

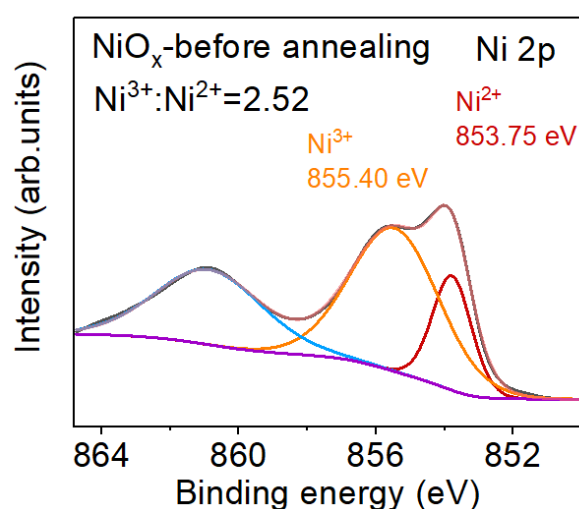


Figure 5.10: XPS spectra of Ni 2p for the NiO_x film before thermal annealing. Reproduced from Ref. [67] with permission. Copyright 2023, Royal Chemistry of Society.

similar ratio values in the NiO_x samples after modification and before annealing indicate that the deposited halogenated phenyl acids could seclude NiO_x from oxygen to further inhibit the expansion of Ni vacancies during thermal annealing.

However, the conductivity of the modified NiO_x is better than that of the control sample (Figure 5.11), which seems to contradict the fact that the higher Ni³⁺ concentration typically gives a higher conductivity of NiO_x films [124].

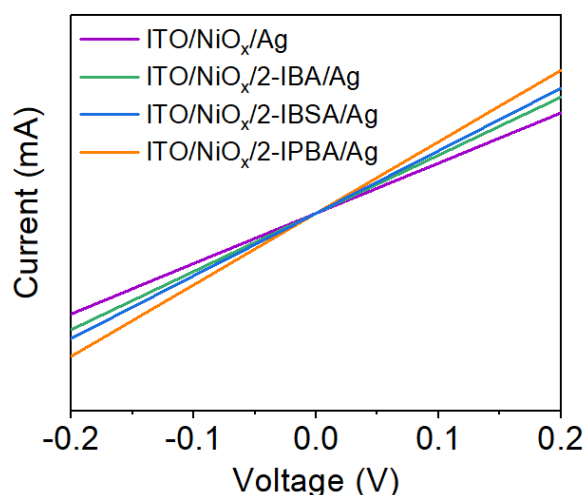


Figure 5.11: *I–V* curves of the NiO_x, NiO_x/2-IBA, NiO_x/2-IBSA and NiO_x/2-IPBA films, respectively. Reproduced from Ref. [67] with permission. Copyright 2023, Royal Chemistry of Society.

This is because the ability to accept electron pairs of the used halogenated phenyl acids allows for the decrease of minority electron density in the p-type NiO_x films, leading to a decreased charge carrier recombination probability and thereby an increased hole transport ability. As a result, *FF* improvement occurs with the modification of NiO_x films and the 2-IPBA device gives the highest *FF*. Furthermore, the decreased content of Ni vacancies will introduce fewer defect energy levels in the NiO_x film, which contributes to a higher *V_{OC}* for the modified devices than the control one. In addition, the O 1s spectra show a decreased peak intensity of the –OH groups (located at 532.44 eV) in the NiO_x film after modification (Figure 5.12). This occurrence is due to the fact that the acid radical groups could react with the –OH groups in the NiO_x films as well. This conclusion is further verified with Fourier transform infrared (FTIR) spectroscopy (Figure 5.13), in which the $\nu(\text{O–H})$ peaks located at $\sim 3500\text{ cm}^{-1}$ decrease in intensity after the modification. The reduced –OH groups contribute to the improved hydrophobicity of the modified films, which is in line with the results from the aforementioned contact angle measurements (Figure 5.5).

5.4. Impact of Iodine Locations on the Optoelectronic Properties.

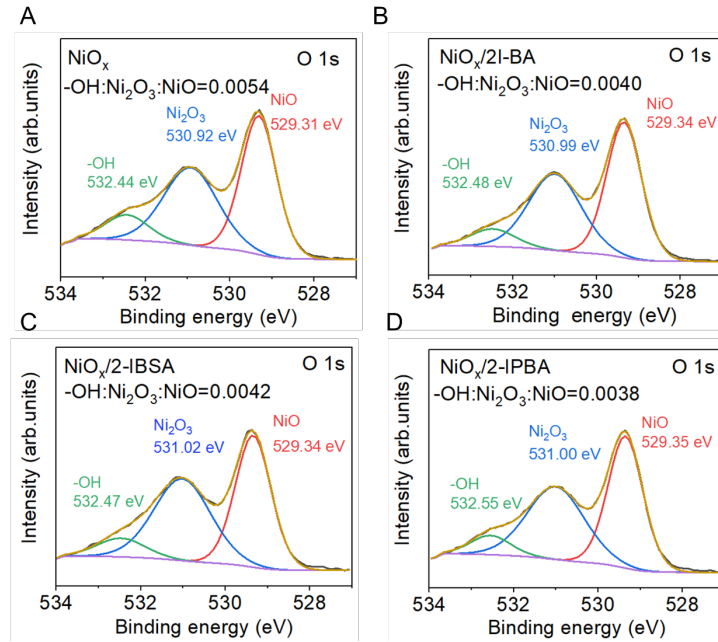


Figure 5.12: XPS spectra of O 1s for (A) the NiO_x, (B) NiO_x/2-IBA, (C) NiO_x/2-IBSA, and (D) NiO_x/2-IPBA films. Reproduced from Ref. [67] with permission. Copyright 2023, Royal Chemistry of Society.

Furthermore, it has been reported that –OH groups at the NiO_x surface could trigger a deprotonation reaction with the deposited perovskite layer, which could cause perovskite degradation [125, 126]. Thus, the chemical reaction between the used acids and –OH groups is conducive to the device stability in this work.

5.4 Impact of Iodine Locations on the Optoelectronic Properties.

In general, the used iodine-substituted phenyl acids are efficient in modifying the NiO_x film regarding the performance improvement of inverted PSCs. Among others, the 2-IPBA is optimal. Its borate group is found to have the strongest coordination with Ni vacancies in the NiO_x films, which also inhibit the increase of Ni³⁺ density. This results in the highest conductivity and reduced defects in the modified NiO_x film, giving an enhanced FF and V_{OC} for the final photovoltaic devices. In addition to the acid functional groups, the influence of the iodophenyl functional groups on the performance of PSCs with respect to the iodine locations at the benzene ring is further explored.

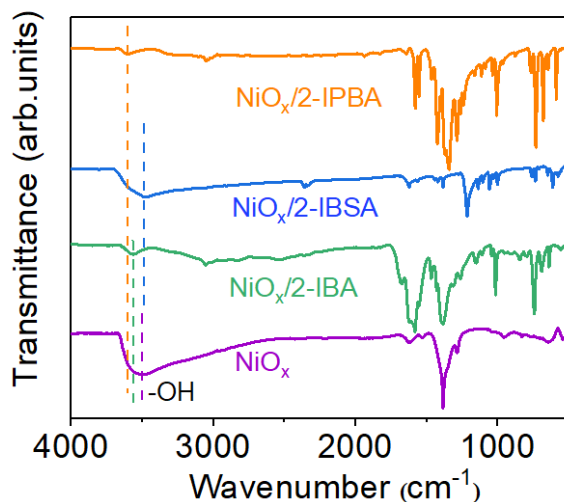


Figure 5.13: FT-IR spectra of the NiO_x, NiO_x/2-IBA, NiO_x/2-IBSA, and NiO_x/2-IPBA films. Reproduced from Ref. [67] with permission. Copyright 2023, Royal Chemistry of Society.

Since the inverted PSCs with iodophenylboronic acids exhibit the best performance from the above research, 2-IPBA and 4-IPBA are selected as the candidates to understand why different iodine locations at the benzene ring produce different modification effects at the NiO_x/perovskite interfaces. Thus, the following studies focus on the impact of the iodine locations on the device performance. The energy band structures of the modified NiO_x films are studied with ultraviolet photoelectron spectroscopy (UPS) measurements. From the secondary electron cut-off (E_{cutoff}) spectra (Figure 5.16A), the Fermi level (EF) values are determined to be 4.54 eV, 4.63 eV, 4.67 eV for the control, 2-IPBA-treated and 4-IPBA-modified NiO_x films, respectively. Furthermore, Kelvin probe force microscopy (KPFM) is used to gain an overview of the surface potential of the NiO_x films (Figure 5.14). The surface potential of NiO_x/4-IPBA is larger than that of NiO_x/2-IPBA, suggesting an increased work function (WF) after 4-IPBA treatment, which is consistent with the UPS results. Figure 5.15 demonstrates the dipole moments of the used molecules, in which the 4-IPBA has a larger dipole moment (4.55 D) than the 2-IPBA (2.85 D). The dipole moments of the used molecules are calculated using density functional theory (DFT) and the molecular structure is optimized at the B3LYP/6-31G (d, p) level with the program Gaussian 09. Since acid groups attach to the NiO_x-film surface, the negative end of the dipole moment points toward the NiO_x substrate and the positive end points upward. In this way, a shift of the vacuum level of the electron energy band at the interface occurs [127, 128], which causes the E_{cutoff} shift of the modified NiO_x films in Figure 5.16A and the shift is much larger for the 4-IPBA-treated film.

5.4. Impact of Iodine Locations on the Optoelectronic Properties.

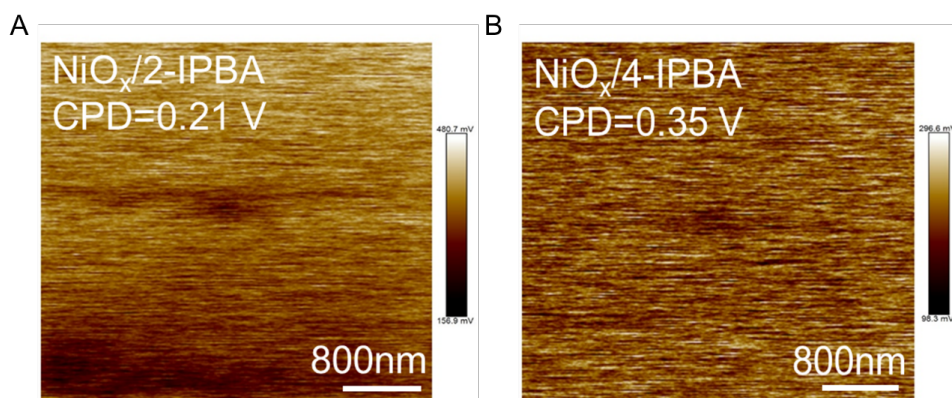


Figure 5.14: KPFM images of (A) the NiO_x/2-IPBA and (B) NiO_x/4-IPBA films. Reproduced from Ref. [67] with permission. Copyright 2023, Royal Chemistry of Society.

From the valence band curves (Figure 5.16B), the energy gaps between E_F and valence band maximum (VBM) are determined, reading 0.67 eV, 0.80 eV and 0.85 eV for the control, 2-IPBA-treated and 4-IPBA-modified samples. This observation can be interpreted by the XPS results in Figure 5.9D–G as the gap values are related to the content of Ni vacancies, in which the higher Ni³⁺ density leads to a stronger p-type semiconductor. Moreover, the VBM levels of the control, 2-IPBA-treated and 4-IPBA-modified samples are calculated to be -5.21 eV, -5.43 eV and -5.52 eV, respectively. Based on the UPS results, a schematic band diagram of the NiO_x/perovskite interface is pictured in Figure 5.16. It is noted that the energy level offset between the VBM and perovskite is the smallest for the 4-IPBA-modified sample, which facilitates hole transfer from perovskite to NiO_x. This conclusion is verified by PL and TRPL measurements on the perovskite films with the modified NiO_x substrates.

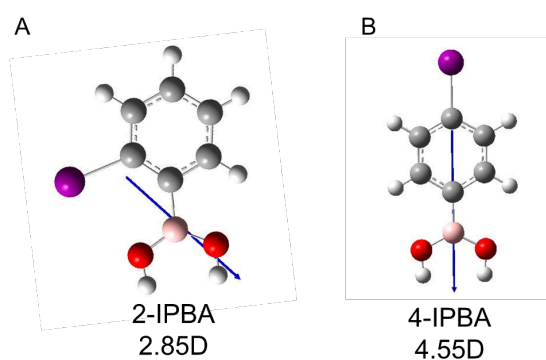


Figure 5.15: Molecular structures and dipole moments of (A) 2-IPBA and (B) 4-IPBA molecules. Reproduced from Ref. [67] with permission. Copyright 2023, Royal Chemistry of Society.

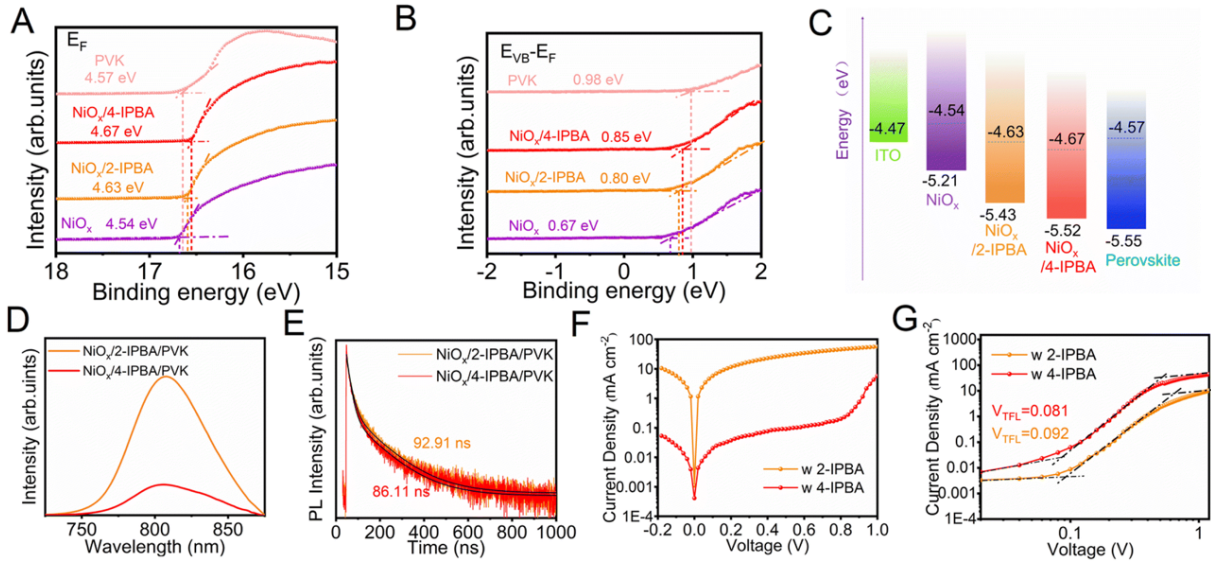


Figure 5.16: UPS spectra of (A) secondary electron cut-off and (B) valence band for the NiO_x , $\text{NiO}_x/2\text{-IPBA}$, $\text{NiO}_x/4\text{-IPBA}$ and perovskite samples, respectively. (C) The corresponding energy level diagram. (D) Steady-state PL spectra and (E) TRPL spectra of perovskite films deposited on the $\text{NiO}_x/2\text{-IPBA}$ and $\text{NiO}_x/4\text{-IPBA}$ films, respectively. (F) Dark J - V and (G) SCLC curves of the devices based on $\text{NiO}_x/2\text{-IPBA}$ and $\text{NiO}_x/4\text{-IPBA}$ substrates, respectively. Reproduced from Ref. [67] with permission. Copyright 2023, Royal Chemistry of Society.

In Figure 5.16D, a reduced PL intensity is observed in the 4-IPBA/perovskite sample than the 2-IPBA-based film, suggesting more efficient hole extraction in the presence of larger dipole moments. From the modeling of TRPL data (Figure 5.16E), t_1 is extracted to be 16.41 ns for the 4-IPBA/perovskite film (Table 5.5).

Table 5.5: Fitted TRPL parameters from Figure 5.16E

samples	τ_1 (ns)	τ_2 (ns)	A_1	A_2	ave. (ns)
$\text{NiO}_x/4\text{-IPBA/PVK}$	16.41	137.80	42.58%	57.42%	86.11

Compared to the 2-IPBA/perovskite sample (Figure 5.9C), the decreased t_1 implies that larger dipole moments at the interface benefit the hole transfer from the perovskite to NiO_x . This is verified by the dark-current measurements. Figure 5.16F shows that the dark current of the 4-IPBA-modified device is lower than that of the control PSC over the applied bias, depicting a reduced trap-mediated recombination. To quantitatively analyze the density of trap states, the space charge-limited current (SCLC) measurements are performed on the hole-only devices (Figure 5.16G). The trap-filled limit voltage (V_{TFL}) values are determined to be 0.092 and 0.081 V for the 2-IPBA- and 4-IPBA-modified

5.4. Impact of Iodine Locations on the Optoelectronic Properties.

devices, which correspond to densities of trap states (N_t) of 1.29×10^{15} and $1.13 \times 10^{15} \text{ cm}^{-3}$, respectively. The light-intensity dependent V_{oc} is displayed in Figure 5.17A. For the $\text{NiO}_x/4\text{-IPBA}$ device, the linear slope ($1.27 k_B T/q$) is smaller than that of the $\text{NiO}_x/2\text{-IPBA}$ device ($1.45 k_B T/q$), where k_B , T , and e represent the Boltzmann constant, temperature, and elementary charge, respectively. The reduction in ideality factor demonstrates that a significant amount of defect-assisted recombination has been suppressed in the $\text{NiO}_x/4\text{-IPBA}$ device. The power-law equation describes how J_{sc} and light intensity are related: $J_{sc} \propto I^a$, (where I and a , respectively, stand for light intensity and the exponential factor). The corresponding plot is shown in Figure 5.17B.

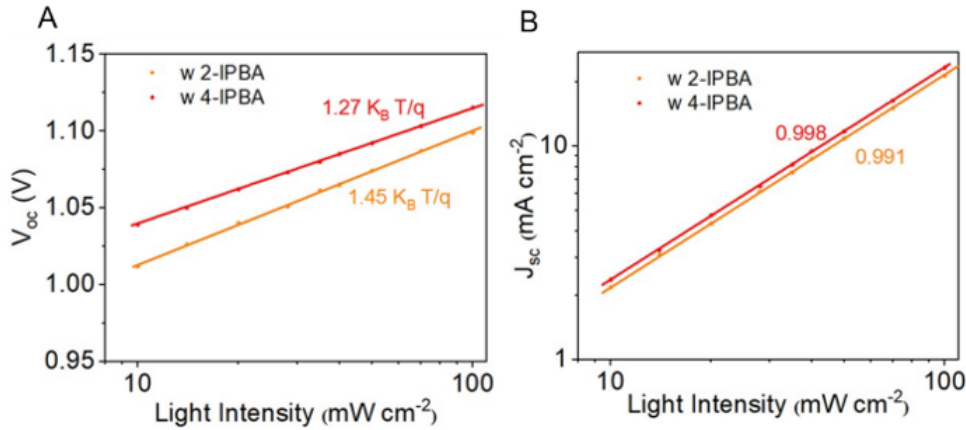


Figure 5.17: (A) V_{OC} and (B) J_{SC} versus light intensity of PSCs with the 2-IPBA and 4-IPBA modification. Reproduced from Ref. [67] with permission. Copyright 2023, Royal Chemistry of Society.

The a value of the device based on $\text{NiO}_x/4\text{-IPBA}$ ($a = 0.998$) is closer to 1 as compared to that of the $\text{NiO}_x/2\text{-IPBA}$ device ($a = 0.991$), indicating the reduced trap-assisted recombination. The larger dipole moments lower the hole transport barrier and suppress charge carrier recombination, which consequently facilitates the extraction of holes from perovskites and hole transfer to the anode. This may lead to a higher FF in the photovoltaic device. To clarify the difference in the density of trap states, the interaction between iodophenylboronic acids and perovskite is investigated with XPS measurements (Figure 5.18A). For the perovskite sample, the I 3d core level exhibits two main peaks located at 630.31 and 618.81 eV, corresponding to I 3d_{3/2} and I 3d_{5/2}, respectively. However both peaks shift towards higher binding energies in the modified films. I atoms in iodophenylboronic acid (Lewis acid) can coordinate with the uncoordinated I⁻ (Lewis base) in perovskites through halogen bonds, which are stronger in the 4-IPBA/perovskite sample. Halogen bonds have been demonstrated to passivate the perovskite buried interface efficiently [120]. The stronger coordination leads to larger sized perovskite grains with

the 4-IPBA treatment, which is visible in plan-view (Figure 5.18B) and cross-sectional SEM images (Figure 5.18C and Figure 5.6C). The 2D-GIWAXS data and the sector-averaged integrals show no obvious changes in peak positions for the 4-IPBA-modified perovskite film compared to the 2-IPBA-treated one (Figure 5.18D–E). However, the azimuthal tube cuts based on the (110) peak depict a slight change (Figure 5.18F), in which a smaller FWHM (8.17) and a larger DoO are observed for the peak at $\chi \sim 0^\circ$ (10.46%). This observation indicates that the para-substituents further induce larger crystals with a preferred orientation normal to the substrate.

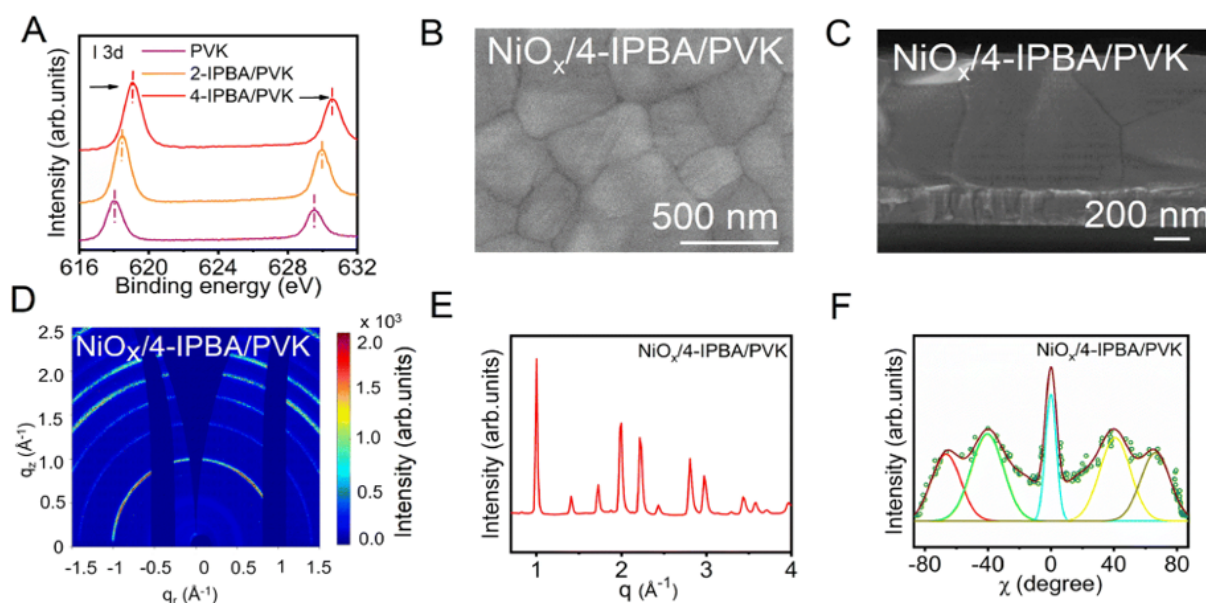


Figure 5.18: (A) XPS of the I 3d core level of the perovskite thin films without treatment, with 2-IPBA and 4-IPBA, respectively. (B) Plan-view SEM of the perovskite thin film deposited on NiO_x/4-IPBA. (C) Cross-sectional SEM images of the perovskite thin films deposited on NiO_x/4-IPBA. (D) 2D GIWAXS data of perovskite thin films deposited on NiO_x/4-IPBA. (E) The sector-averaged integrals of the 2D-GIWAXS data of perovskite deposited on NiO_x/4-IPBA. (F) Azimuthal tube integrals are performed on (110) diffraction rings with an angular width of $q_r = 0.97\text{--}1.02 \text{ \AA}^{-1}$ of perovskite films deposited on NiO_x/4-IPBA. Reproduced from Ref. [67] with permission. Copyright 2023, Royal Chemistry of Society.

5.5 Long-term Stability

The $J - V$ characteristics of the 4-IPBA-based inverted PSCs are depicted in Figure 5.19A. The best-performing PSC is examined to have a champion PCE of 22.91% with a V_{OC} of 1.08 V, a J_{SC} of 24.42 mA/cm², and a FF of 86.18%, which are superior to the performance of other devices with the halogenated phenyl acid-modified NiO_x HTLs.

5.5. Long-term Stability

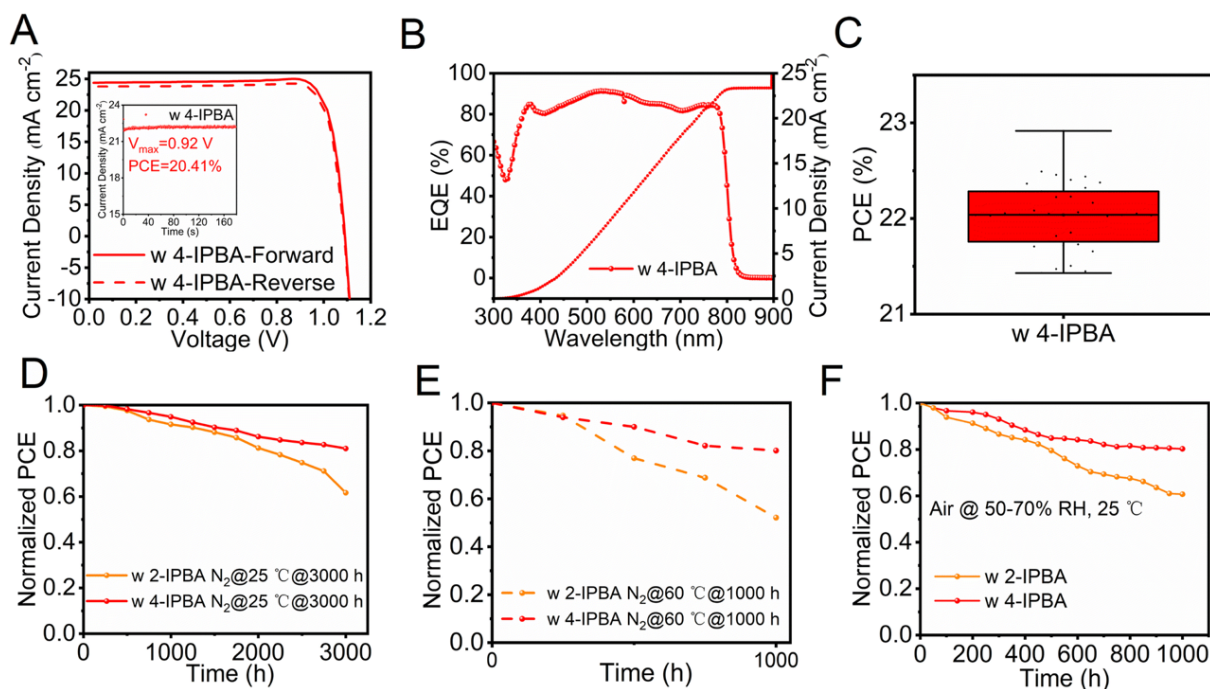


Figure 5.19: (A) J - V curves of the 4-IPBA-based PSC measured in the reverse and forward directions and the steady-state photocurrent output at the maximum power point (inset). (B) EQE spectrum and the corresponding integrated J_{SC} curve. (C) PCE statistics obtained from 35 4-IPBA-treated PSCs. Storage stability in (D) N_2 atmosphere at 25 °C for 3000 h, (E) 60 °C for 1000 h and (F) air (RH of 50–70%, 25 °C) for 1000 h. PCEs are normalized to their initial values. Reproduced from Ref. [67] with permission. Copyright 2023, Royal Chemistry of Society.

The steady-state photocurrent output at the maximum power point shows that the device based on the $NiO_x/4$ -IPBA substrate exhibits a higher photocurrent (22.18 mA/cm^2) over time than the $NiO_x/2$ -IPBA-based device (21.28 mA/cm^2) (Figure 5.19A and Figure 5.2C). EQE measurements are carried out to verify the J_{SC} reliability (Figure 5.19B). By integrating the EQE data over the whole measured spectrum, the J_{SC} is calculated to be 23.45 mA cm^{-2} , which is line with the value extracted from the $J - V$ curve. A PCE statistical plot is given in Figure 5.19C, demonstrating good device reproducibility. Other photovoltaic parameters are displayed in Figure 5.20. Furthermore, the durability test against elevated temperatures and moisture is carried out on both inverted PSCs. After storage in a nitrogen glovebox at room temperature under ambient light illumination for 3000 h, the 2-IPBA- and 4-IPBA-based devices retain 61.5% and 81.0% of their initial PCEs, respectively (Figure 5.19D).

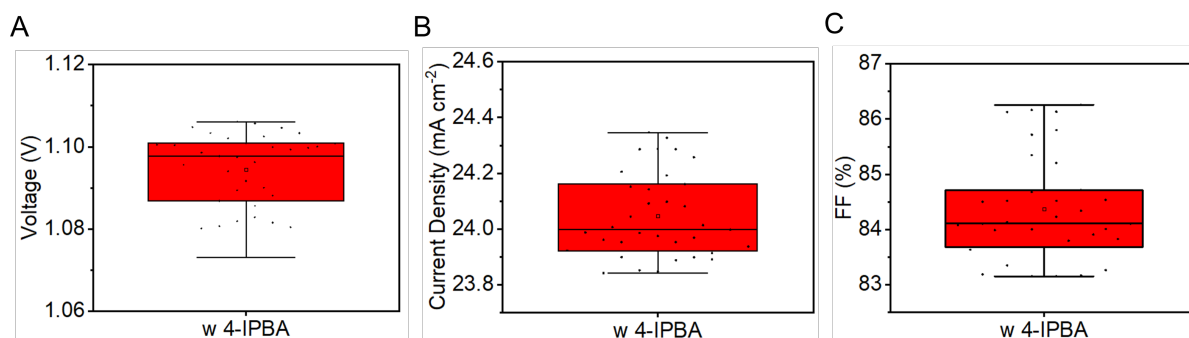


Figure 5.20: (A) V_{OC} , (B) J_{SC} , and (C) FF statistics obtained from 35 PSCs with the 4-IPBA modification. Reproduced from Ref. [67] with permission. Copyright 2023, Royal Chemistry of Society.

For thermal stability, both cells are aged at an elevated temperature of 60 °C in a nitrogen glovebox under ambient light illumination for 1000 h, 47.2% and 19.9% PCE losses are found in the 2-IPBA- and 4-IPBA-based PSCs, respectively (Figure 5.19E). For the water-vapor stability, the 2-IPBA- and 4-IPBA-modified cells are exposed to air with a RH of 50–70% under ambient light illumination at room temperature for 1000 h, showing the remaining PCEs of 60.6% and 80.6%, respectively (Figure 5.19F). It is noted that 4-IPBA-based PSCs exhibit a better device stability than the 2-IPBA-modified devices regarding storage in a N₂ atmosphere, thermal aging, and moisture resistance. Moreover, the modified inverted PSCs generally demonstrate much better device stability than those control cells as they undergo severe performance decay under the same aging conditions (Figure 5.21).

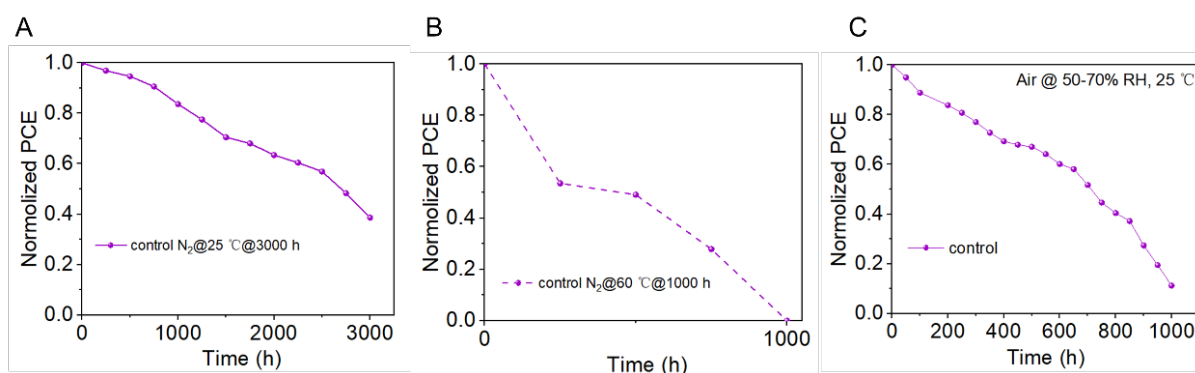


Figure 5.21: Normalized PCEs of the control device stored in (A) N₂ atmosphere at 25 °C for 3000 h, (B) 60 °C for 1000 h, and (C) air (RH of 50–70%, 25 °C) for 1000 h. Reproduced from Ref. [67] with permission. Copyright 2023, Royal Chemistry of Society.

Firstly, the interaction between the used molecules and the NiO_x is verified to inhibit the expansion of Ni vacancies and to reduce the density of –OH groups at the film surface,

leading to improved device stability. It has been demonstrated that Ni vacancies had a strong oxidation ability, in which iodide ions could be oxidized to iodine [116]. And $-\text{OH}$ groups were found to degrade the perovskite by introducing positive charge defects [126]. Secondly, I atoms in iodophenylboronic acids can coordinate with the uncoordinated I- (Lewis base) at the perovskite buried interface via halogen bonding to strengthen the structural stability of the device. Han *et al.* verified that the halogen bonds inhibited the formation of the voids at the NiO_x /perovskite interface under a light soaking aging test with 1-sun illumination and the voids were the trigger of the perovskite degradation [120]. The strongest coordination effect between the 4-IPBA and perovskite accounts for the best device stability.

5.6 Conclusion

A systematic study on the modification of NiO_x /perovskite interfaces with iodine-substituted phenyl acids for inverted perovskite solar cells is performed. First, the influence of different acid groups on the photovoltaic performance is investigated. Generally, the modified devices achieve a better performance than the control cells. It is found that the iodine-substituted phenyl acids can seclude NiO_x from oxygen to further inhibit the Ni vacancy expansion during thermal annealing, which results in fewer defect energy levels in the NiO_x film. This occurrence interprets higher V_{OC} values in the modified devices. Moreover, the acid groups are found to coordinate with Ni vacancies in the NiO_x films, leading to a decreased charge carrier recombination probability and thereby an increased hole transport ability. Among the studied iodine-substituted phenyl acids, the modification with 2-IPBA is optimal, which exhibits a champion PCE of 21.81%. The influence of iodophenyl functional groups on the device performance from the aspect of iodine locations at the benzene ring is also investigated. Owing to a larger dipole moment, the 4-IPBA-modified NiO_x film has a better energy level alignment with the perovskite, which consequently facilitates the hole extraction from perovskites and hole transfer to the anode. Furthermore, the stronger coordination between 4-IPBA and perovskite via halogen bonding leads to larger sized perovskite grains and a reduced density of trap states. As a result, the 4-IPBA-based inverted PSC shows a champion PCE of 22.91% with negligible hysteresis. The device demonstrates excellent long-term stability, which retains 81.04%, 80.56% and 80.07% of the initial PCE values after storage in N_2 for 3000 h, at an elevated temperature of 60 °C and in air with relative humidity (RH) of 50–70% for 1000 h, respectively. This work illustrates a basic understanding of how iodine-substituted phenyl acids improve the NiO_x /perovskite interface, providing general guidance to design interfacial modification molecules for efficient and stable inverted PSCs.

Degradation of Perovskite Solar Cells under Light and Humidity

The results shown in this chapter are extracted from the publication: *Morphological Insights into the Degradation of Perovskite Solar Cells under Light and Humidity* (K. Sun, R. Guo, Y. Liang, J. E. Heger, S. Liu, S. Yin, M. A. Reus, L. V. Spanier, F. Deschler, S. Bernstorff, P. Müller-Buschbaum, *ACS Applied Materials & Interfaces*, **15**, 30342-30349 (2023)), reproduced from [48] with permission, copyright 2023, American Chemical Society.

Perovskite solar cells have achieved competitive power conversion efficiencies compared with established solar cell technologies. However, their operational stability under different external stimuli is limited, and the underlying mechanisms are not fully understood. In particular, an understanding of degradation mechanisms from a morphology perspective during device operation is missing. Herein, I investigate the operational stability of PSCs with CsI bulk modification and a CsI-modified buried interface under AM 1.5G illumination and $75 \pm 5\%$ relative humidity, respectively, and concomitantly probe the morphology evolution with grazing-incidence small-angle X-ray scattering. I find that volume expansion within perovskite grains, induced by water incorporation, initiates the degradation of PSCs under light and humidity and leads to the degradation of device performance, in particular, the fill factor and short-circuit current. However, PSCs with modified buried interface degrade faster, which is ascribed to grain fragmentation and increased grain boundaries. In addition, a slight lattice expansion and PL redshifts in both PSCs after exposure to light and humidity are revealed. The detailed insights from a buried microstructure perspective on the degradation mechanisms under light and humidity are essential for extending the operational stability of PSCs.

6.1 Preface

Organic–inorganic hybrid perovskites with intriguing properties like long charge carrier diffusion length and large absorption coefficient are attracting tremendous attention as one of the most promising next-generation photovoltaic materials [129, 130]. The power conversion efficiency (*PCE*) of state-of-the-art perovskite solar cells (PSCs) has risen to 25.6% with the help of composite engineering [129, 131, 132], surface passivation, and interface engineering [133, 134]. In contrast to the significant improvement in *PCE* recently achieved, the operational stability with respect to different stresses, however, remains a major drawback toward the commercialization of PSCs. Therefore, understanding degradation mechanisms under operation conditions with the presence of different stresses is the prerequisite to further improve the operation stability and longevity of PSCs.

Previous works have shown that mixed halide perovskites undergo phase segregation when consecutively exposed to 1 sun illumination (AM 1.5G), resulting in the formation of halide-rich domains and localized variations in the materials bandgap [135, 136, 137]. This change would further cause the reduction of the open circuit voltage (V_{OC}) and charge carrier mobility, which is detrimental to the device performance [138, 139, 140, 141]. Additionally, direct evidence shows that in the presence of moisture, particularly under high humidity, perovskites form phase segregation during the operation [50] and decompose to hydrate products and, eventually, lead iodide (PbI_2) [142, 143, 47]. In addition to hydrate phases, when water penetrates perovskite solar cells, it also leads to enhanced ion migration and further deteriorates the solar cell performance [49].

However, it was also reported that upon exposure to either light or moisture alone, no decomposition or spatial changes can be found in the case of $Cs_{0.15}FA_{0.85}PbI_3$, where FA and Cs are formamidinium (FA) and cesium (Cs), respectively [144]. In addition to the aforementioned circumstances, a lower level of humidity has limited impacts on the perovskite stability [145, 33, 146].

Thus, understanding the operational stability of PSCs under light and high humidity should be prioritized. Moreover, a study of the buried microstructure evolution of PSCs during operation, particularly the buried interface, where the deep-level trap states are accumulated [147], is still lacking, mainly due to their non-easily accessible characteristics. Grazing-incidence small-angle X-ray scattering (GISAXS) featuring high statistics via a large probing area, has proven to be a powerful and non-destructive tool for tracking buried structures in real time during device operation [62, 148, 149, 150, 151]. In addition, GISAXS can differentiate changes through different scattering length densities of different materials, which enables tracking changes of the active layer during device operation.

To the best of our knowledge, there is no study monitoring the real-time evolution of PSCs' buried structures under high humidity and light during device operation. There-

fore, it is of particular interest to investigate the operational stability through GISAXS in the presence of light and high humidity from a morphological and optoelectronic perspective.

Composition engineering and interface engineering, particularly buried interface modification, have already been successfully applied to increase the PSC performance [129, 152, 153, 154]. In this regard, I use the component of $(\text{MAPbBr}_3)_{0.08}(\text{FAPbI}_3)_{0.92}$ as MAFA solar cells and dope cesium iodide (CsI) in the perovskite precursor, hereby denoted as CsMAFA. In the second case, to form a strengthened buried interface, CsI is added in the hole-blocking layer (HBL) to interact with the excess lead iodide (PbI_2) in the perovskite layer, hereby denoted as CsI-HBL.

In the present work, I concomitantly investigate the evolution of different PSC performances and related morphological changes under AM 1.5G illumination and $75 \pm 5\%$ relative humidity. I find that the CsI-HBL PSCs experience a faster decay, while CsMAFA PSCs show great potential in their stability against light and humidity. Notably, device degradation is highly related to the morphology change of the perovskite layer. Operando GISAXS measurements show that volume expansion drives the PSCs degradation under light and humidity independent of the modification method, whereas grain fragmentation along with increased grain boundaries (GBs) in CsI-HBL devices after aging causes the deterioration of the solar cell performance. Moreover, a slight lattice expansion and photoluminescence redshift are disclosed by ex situ grazing-incidence wide-angle X-ray scattering (GIWAXS) and photoluminescence (PL), respectively. As such, I highlight the importance of bulk defect passivation and the reduction of small grains and grain boundaries in terms of enhancing the longevity of PSCs against external stimuli.

6.2 Solar Cell Evolution under Light and Humidity

The PSCs were fabricated using a one-step deposition method with the architecture of indium tin oxide (ITO)/ SnO_2 /perovskite/spiro-OMeTAD/Au, as illustrated in Figure 6.1A. Details of the fabrication process can be found in Chapter 3. A blueshift in both the absorption and PL spectra is observed (Figure 6.2A), manifesting the incorporation of CsI in the perovskite components. In addition, smooth and pinhole-free MAFA and CsMAFA films are displayed in Figure 6.2B,C. The transmittance (Figure 6.3) of the HBL is found to decrease by $\sim 4.5\%$ in the visible light region (400–800 nm) after the addition of CsI. However, the absorbance of different HBL-based perovskite films is rather similar in the whole absorption range (Figure 6.4A). The CsI-HBL sample exhibits a faster PL quenching, indicating a faster electron transfer compared to the MAFA sample.

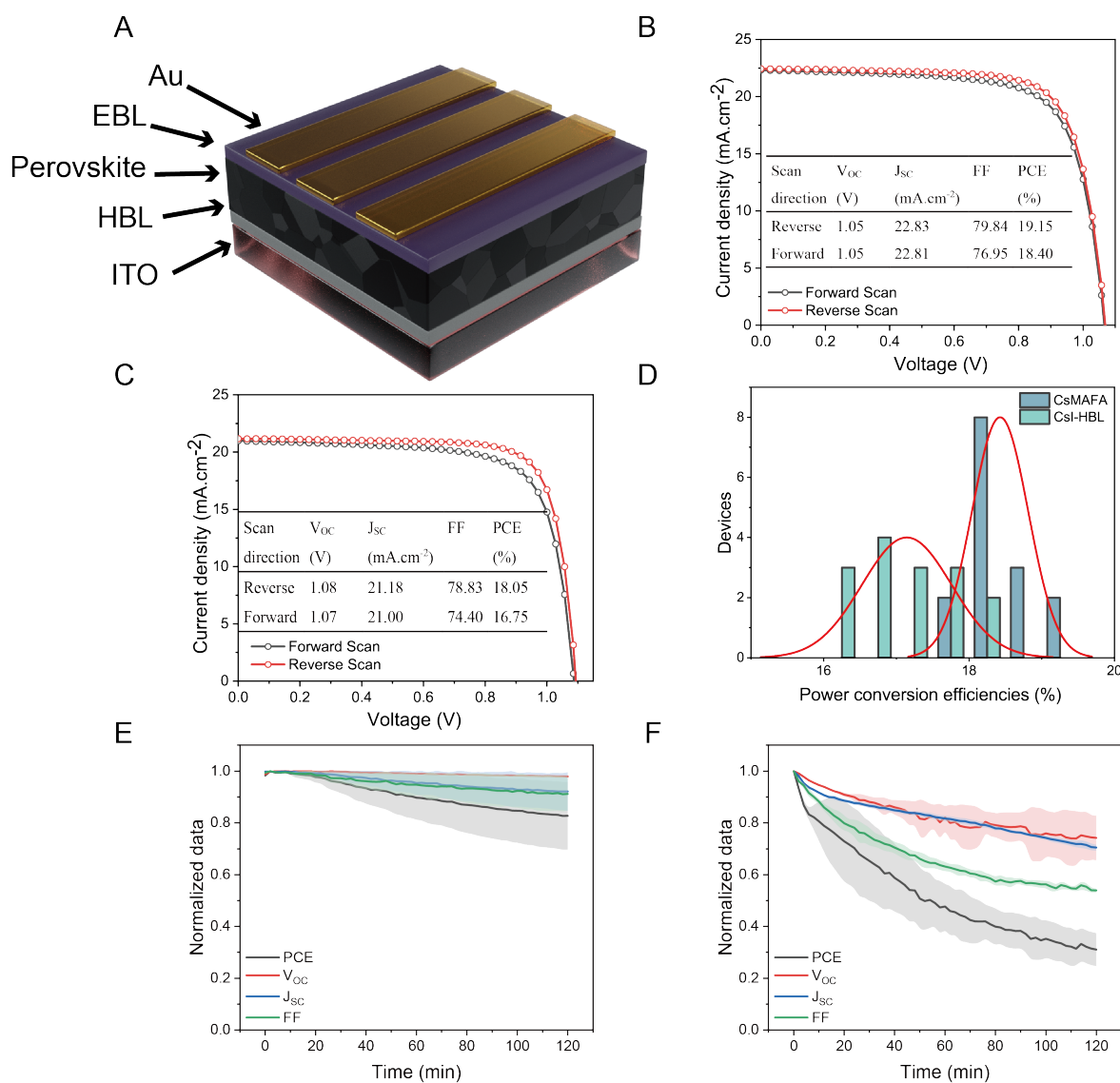


Figure 6.1: (A) Schematic illustration of the used device architecture. Champion performance of (B) CsMAFA device and (C) CsI-HBL device. d) PCE histograms of respective devices acquired from 15 devices, where red lines show the respective Gaussian fit. Device performance under AM 1.5G illumination and $75 \pm 5\%$ relative humidity as a function of time measured by reverse scans for (E) CsMAFA devices and (F) CsI-HBL devices. Reproduced from Ref. [48] with permission. Copyright 2023, American Chemical Society.

In addition, the histograms of the PCE data collected from CsMAFA and CsI-HBL are displayed in Figure 6.1D, with the PCE values of the champion devices (Figure 6.1B,C) of CsMAFA and CsI-HBL reaching 19.15 and 18.05%, respectively.

6.2. Solar Cell Evolution under Light and Humidity

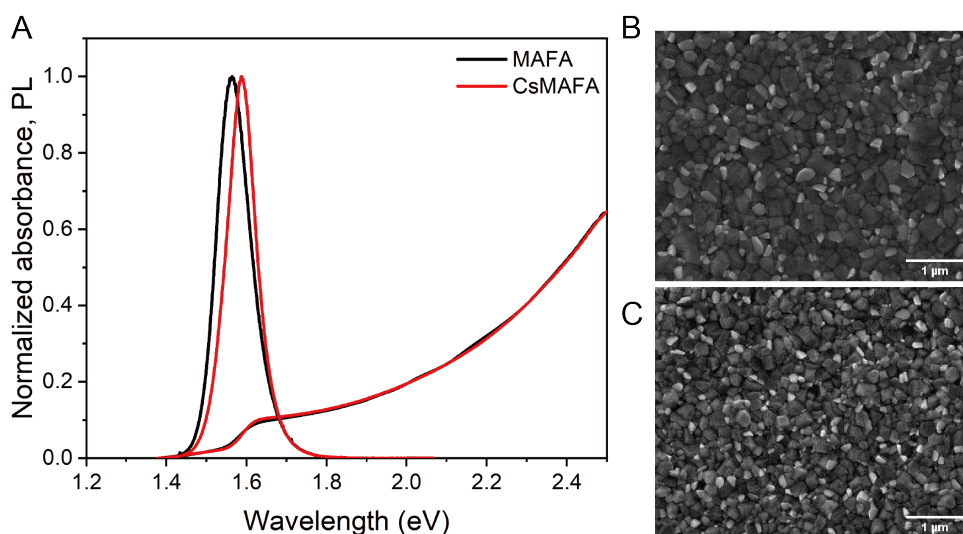


Figure 6.2: (A) Normalized light absorption and photoluminescence spectra of pure MAFA (black) and CsMAFA films (red). SEM images of (B) MAFA and (C) CsMAFA films. Reproduced from Ref. [48] with permission. Copyright 2023, American Chemical Society.

The respective solar cell parameters are shown in Figure 6.5, where the CsMAFA devices demonstrate better performance in comparison to the other devices. Notably, the average FF and V_{OC} values of the CsI-HBL cells are enhanced compared to those of the MAFA cells, which can be presumably ascribed to the defect passivation at the buried interface by CsI modification. In terms of device stability, I use these PSCs in *operando* setup under continuous light illumination for 2 h to verify their stability (Figure 6.6).

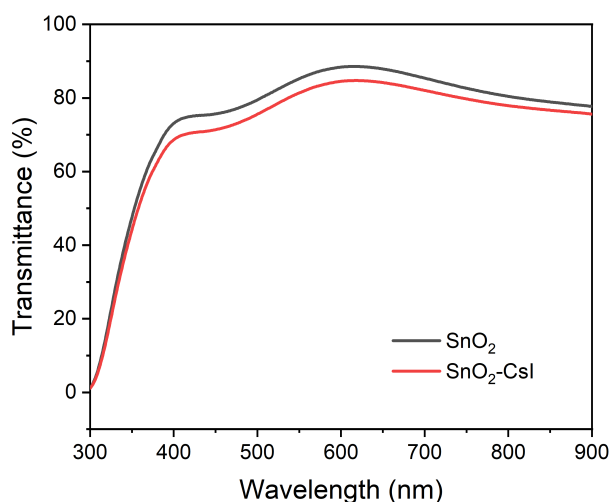


Figure 6.3: Transmittance spectra of pristine SnO₂ film (black) and CsI doped SnO₂ film (red). Reproduced from Ref. [48] with permission. Copyright 2023, American Chemical Society.

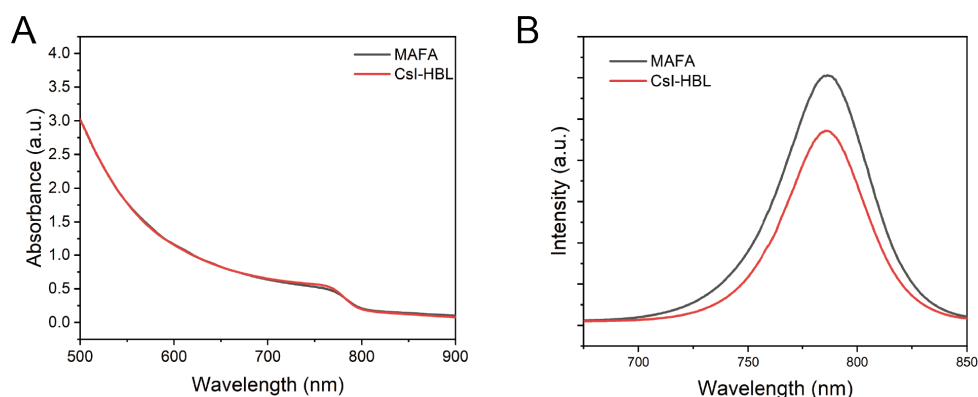


Figure 6.4: (A) Absorbance of perovskite film deposited on pristine SnO_2 (MAFA, black line) and SnO_2 -CsI (red line) films on glass. (B) PL spectra of MAFA deposited on SnO_2 (black) and SnO_2 -CsI (red) films on glass. Reproduced from Ref. [48] with permission. Copyright 2023, American Chemical Society.

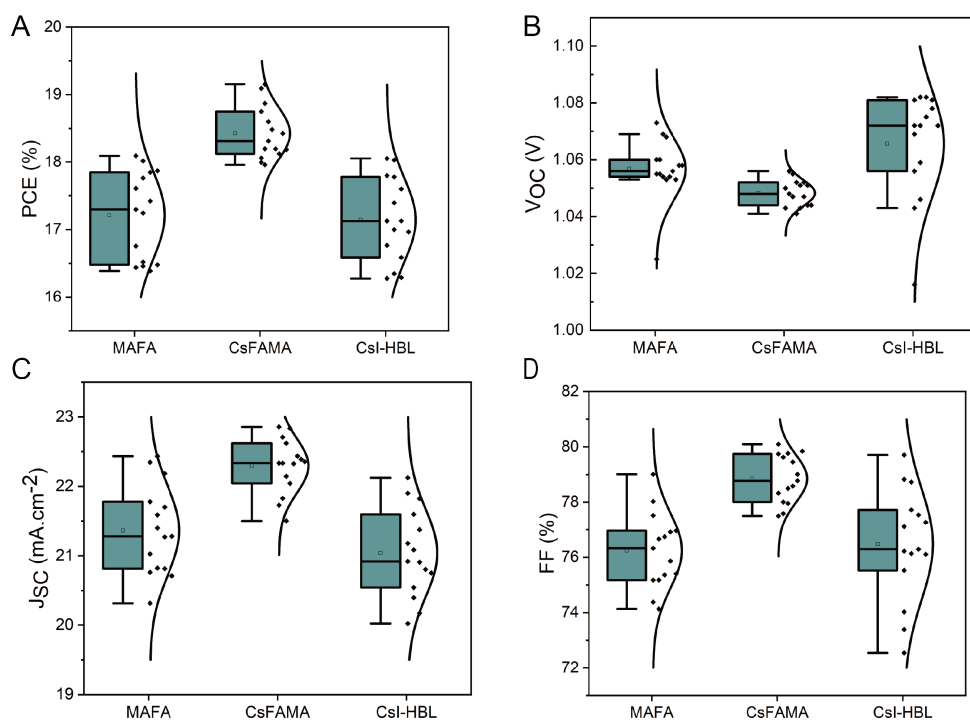


Figure 6.5: Statistic distribution of solar cell parameters of 15 MAFA, CsMAFA and CsI-HBL devices: (A) PCE, (B) V_{OC} , (C) J_{SC} , and (D) FF. Reproduced from Ref. [48] with permission. Copyright 2023, American Chemical Society.

The operando setup, which has been already successfully used in previous work, is pictured in Figure 4.7, in which a cooling water system is applied to rule out any temperature-induced degradation [148, 155, 156].

6.2. Solar Cell Evolution under Light and Humidity

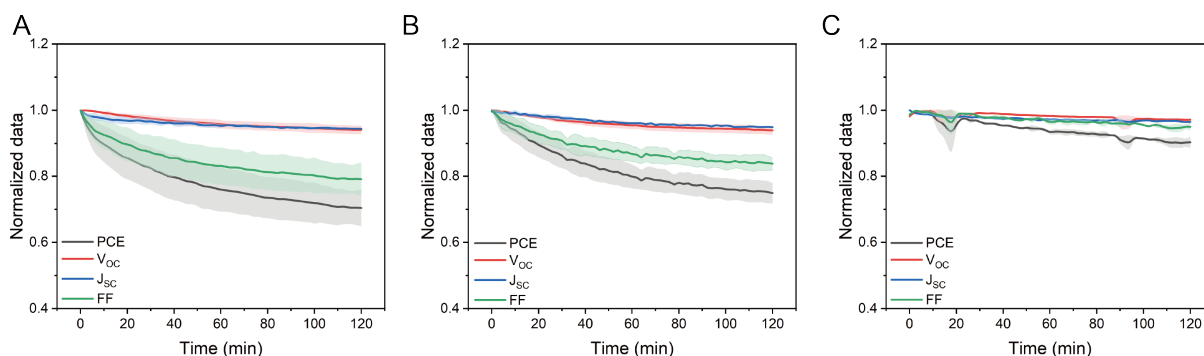


Figure 6.6: Solar cell performance evolution of devices under 1-sun illumination measured by reverse scans of (A) MAFA device, (B) CsI-HBL device, suggesting that the enhanced stability of CsI-HBL compared to MAFA, and (C) CsMAFA device. Reproduced from Ref. [48] with permission. Copyright 2023, American Chemical Society.

A decrease in PCE after aging of 30% for the MAFA devices, 10% for the CsMAFA devices, and 25% for the CsI-HBL devices is observed, suggesting the intrinsic stability of the CsMAFA device against light, which coincides with the work of Saliba *et al.* [157]. In the case of being exposed to light and humidity, the solar cells are placed in the operando setup connected with a gas-flow setup. In detail, the whole setup consists of a homemade gas-flow setup, a solar simulator, a Keithley, a water-cooling system, and a chamber with two attached Kapton windows on both the front and backside. The working temperature of the perovskite solar cell chamber was set to 25 °C by a water-cooling system in order to eliminate the potential structure change induced by temperature. A homemade gas-flow setup was applied to control the humidity of the whole device. The solar cell performance as a function of time was simultaneously obtained by a source meter (Keithley 2600) at 120 s intervals. Notably, the relative humidity was set to 75% ramping up from the start. The solar cell performances of different devices as a function of time is shown in Figure 6.1E,F. If it is not stated elsewhere, the aging test is performed under AM 1.5G light illumination and 75% humidity at a temperature of 25 °C. I observe that the PCEs of the CsMAFA and CsI-HBL devices drop by ~ 17 and 66%, respectively, mainly originating from the loss in the FF and J_{SC} . This observation shows that the solar cell performance is critically deteriorated in the presence of high humidity, in accordance with theoretical calculation in the work of Lu *et al.*[158]. Low FF values result from high parasitic resistance (shunt and series resistance) losses, whereas in practice, a non-dense and non-uniform perovskite layer may give rise to a lower shunt resistance [159]. Thus, the degradation of solar cells is highly related to the morphology evolution of the perovskite active layer, which is discussed in the GISAXS results part. On the other hand, the evolution of the photovoltaic performance also manifests that the CsMAFA devices are

more stable against light and moisture compared to the CsI-HBL devices, corroborating that perovskites with CsI distributed evenly in the bulk are more durable against light and moisture.

6.3 Structural Evolution during Device Operation

Prior to the GISAXS results, the microscopic surface morphologies of the samples before (Figure 6.7) and after aging are shown in Figure 6.11A,B.

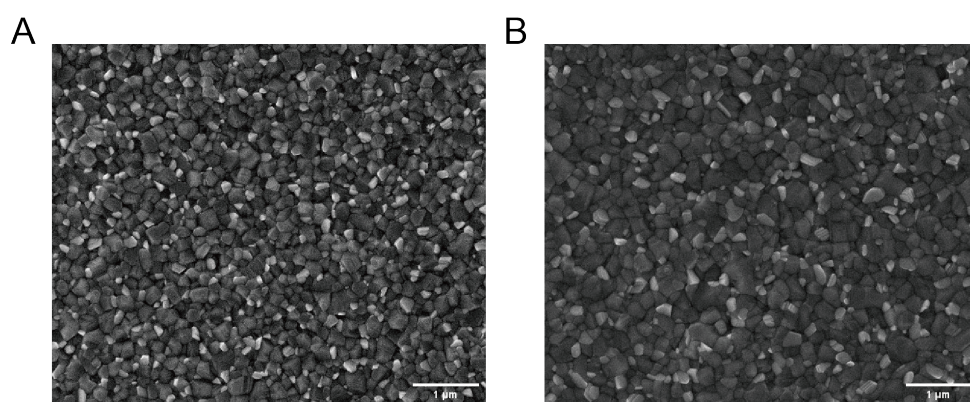


Figure 6.7: SEM images of (A) CsMAFA/HBL film before aging and (B) CsI-HBL/HBL before aging. Reproduced from Ref. [48] with permission. Copyright 2023, American Chemical Society.

There is no formation of needle-shaped crystals during device operation, which are often observed after aging [160]. In contrast, round-shaped crystals (highlighted by the red frame), with which water ingresses into the perovskite crystals, are easily seen after aging. However, scanning electron microscopy (SEM) is restricted to probing the surface morphology and insufficient to probe the inner morphology, while GISAXS, featuring a high photon flux and large sample probe area, is ideal for tracking the buried structure evolution at a high time resolution. Thus, GISAXS is selected to investigate the structural changes under AM 1.5G illumination and humidity during device operation. The 2D GISAXS data of the PSCs are acquired with a time interval of 2 min in the initial 36 min and a time interval of 4 min for the remaining 84 min, and each frame is recorded at a 1 s acquisition time to avoid any beam damage on the sample. Detailed technical information is present in the following text. Operando GISAXS experiments were carried out at the Austrian SAXS beamline of the Elettra Synchrotron at Trieste, with a beam energy of 8 keV. The scattering data were collected by a Pilatus 1M detector (Detrics, pixel size of $172 \mu\text{m}$) at an incidence angle of 0.4° . The sample-to-detector distance (SDD) was set to 1577.5 mm. The GISAXS images were further analyzed via DPDAK software

6.3. Structural Evolution during Device Operation

[79]. Notably, Figure 6.8 shows that no morphological damage can be found after 100 s of exposure to the X-ray beam.

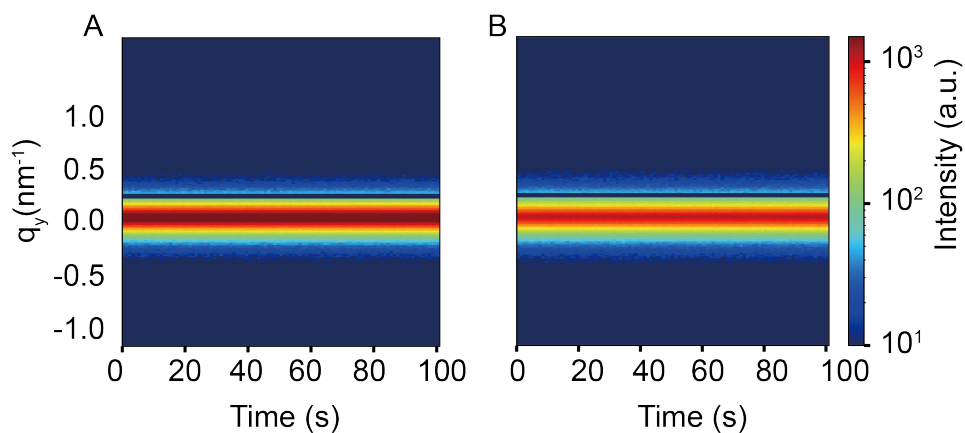


Figure 6.8: X-ray beam irradiation damage tests acquired from horizontal line cuts of 2D GISAXS data of (A) CsMAFA device and (B) CsI-HBL device. Reproduced from Ref. [48] with permission. Copyright 2023, American Chemical Society.

Selected 2D GISAXS data of each sample measured at different operation times are presented in Figures 6.9 and 6.10, corroborating the relatively stable structure of the PSCs against light soaking and humidity. Additionally, the 2D GISAXS data of the CsMAFA device (Figure 6.9) shows that a more uniform structure can be obtained with the introduction of CsI in the perovskite precursor, in good agreement with the SEM images (Figure 6.2C).

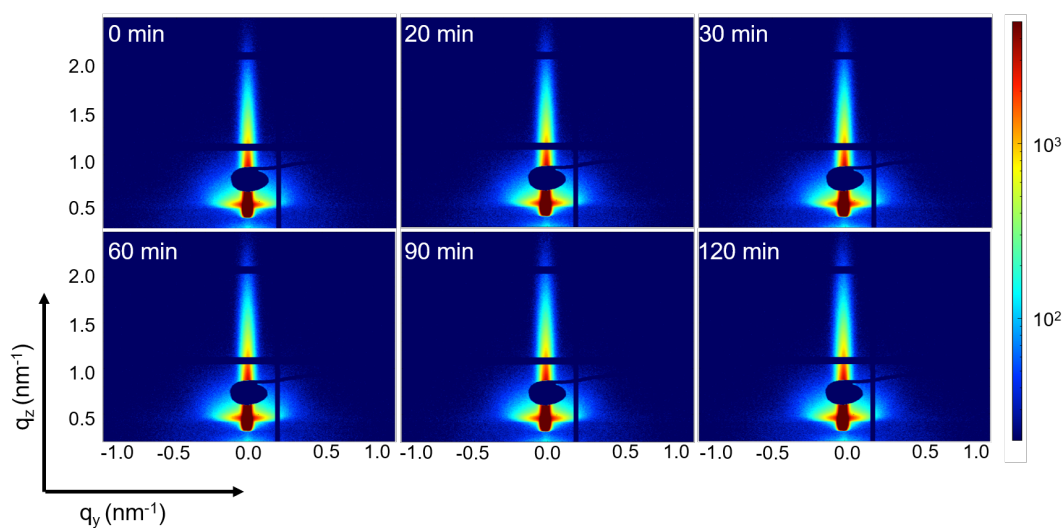


Figure 6.9: Selected 2D GISAXS data of CsMAFA device at different operation time as indicated. Reproduced from Ref. [48] with permission. Copyright 2023, American Chemical Society.

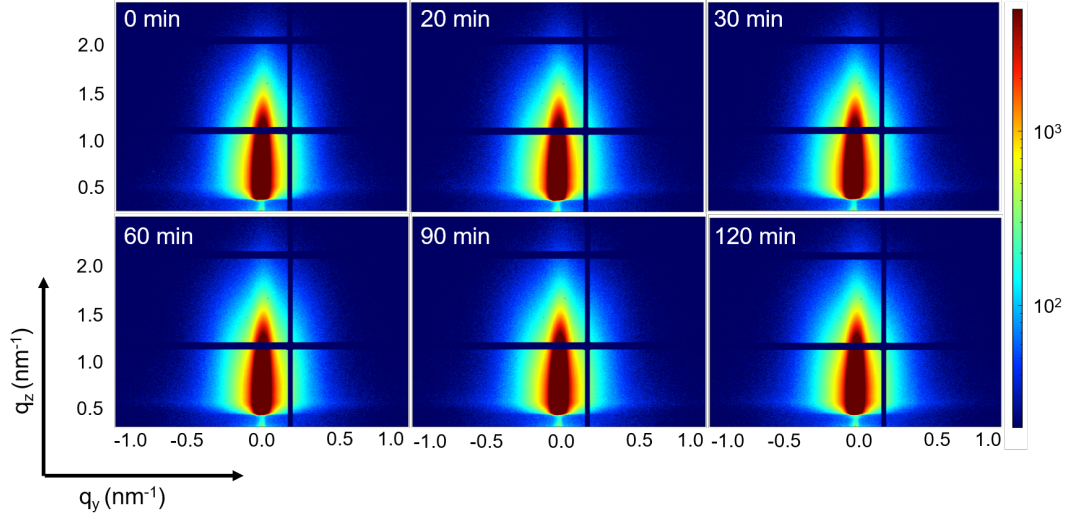


Figure 6.10: Selected 2D GISAXS data of CsI-HBL device at different operation time as indicated. Reproduced from Ref. [48] with permission. Copyright 2023, American Chemical Society.

To quantitatively analyze the morphology changes during device operation, horizontal line cuts of the 2D GISAXS data are performed at the respective Yoneda regions. Afterward, the corresponding GISAXS data are modeled with a 1D paracrystal model (Figure 6.11C,D) [161]. Details about the GISAXS modeling are displayed below. The critical angle of each material with respect to each layer was calculated. A vertical line cut was performed to identify the respective Yoneda peak position and afterwards a horizontal line cut was done by cutting at the Yoneda peak position of the perovskite material [62]. Then the horizontal line cut data were modelled in the framework of the distorted wave Born approximation (DWBA). Additionally, local monodisperse approximation (LMA) in combination with the effective interface approximation (EIA) were used. Thus, the total scattering intensity depended linearly on the number of scattering centers N , the square of form factor $F(\vec{q})$ and structure factor $S(\vec{q})$ and can be described as [162]:

$$I(q) \propto N \cdot \langle |F(\vec{q}, R_i)|^2 \rangle \cdot S(q, R_i) \quad (6.1)$$

Given that perovskite crystals were positioned with uncorrelated distances between the crystals, as evidenced by the SEM images, thereafter the structure factor was neglected. The scattering signal constituted of rotation-symmetric averages over the scattering centers in the plane of the substrate, while the substrate and film surface act as vertical confinement. Therefore, a cylinder model was used regardless of the real perovskite grain shape [163]. In terms of detailed crystal size distribution modeling, I refer readers to the literature [163].

6.3. Structural Evolution during Device Operation

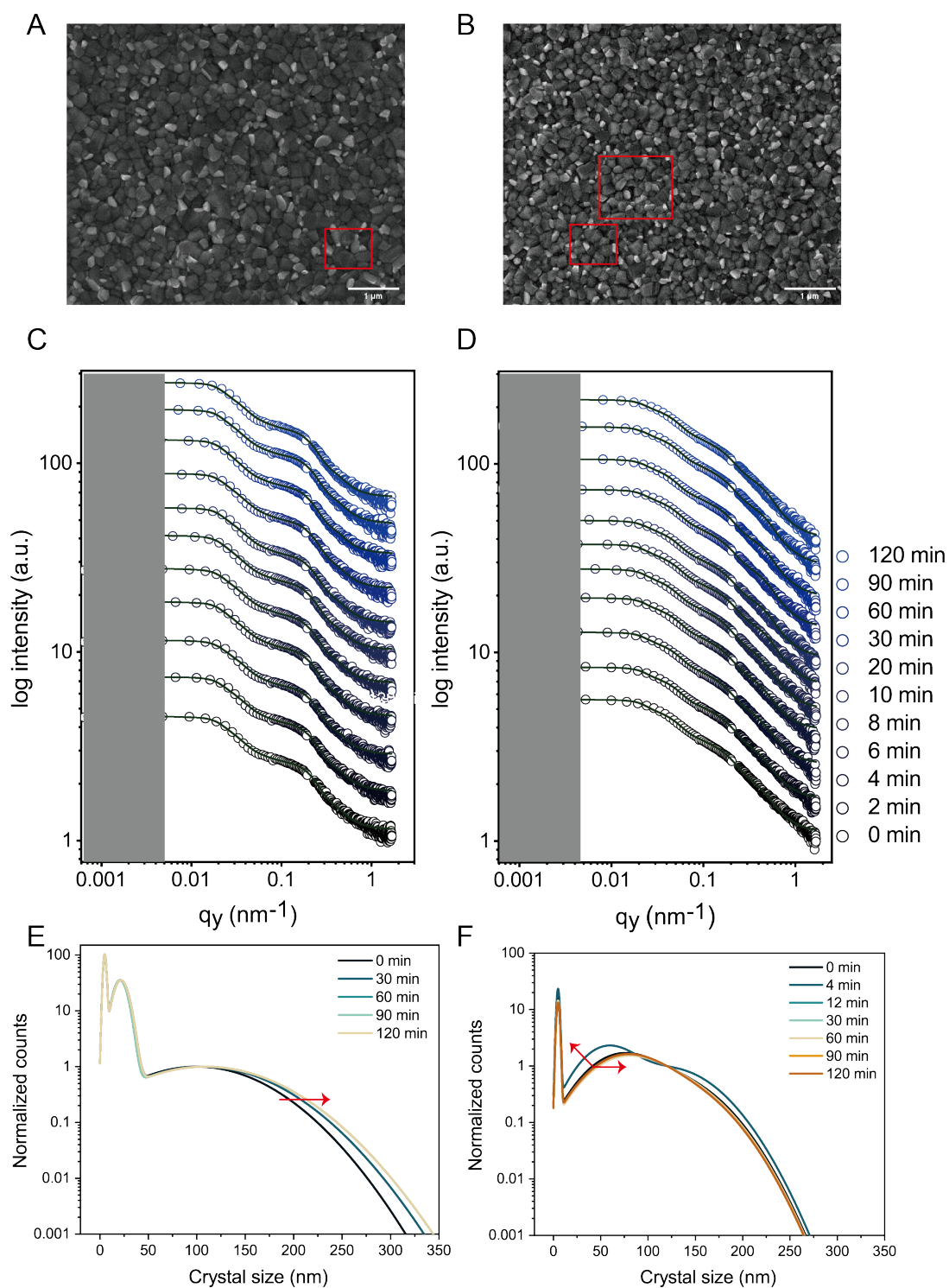


Figure 6.11: SEM images of (A) CsMAFA and (B) CsI-HBL film after aging. Horizontal line cuts of 2D GISAXS data (symbols) shown with fits (lines), where the grey rectangular area illustrates the resolution: (C) CsMAFA and (D) CsI-HBL devices. The data is shifted along the y-axis for data readability. Crystal size evolution extracted from GISAXS fits over time under device operation: e) CsMAFA and f) CsI-HBL devices. Reproduced from Ref. [48] with permission. Copyright 2023, American Chemical Society.

Moreover, the crystal size distributions from the GISAXS fits [163] are derived. Figure 6.11E,F shows the distributions with the counts normalized to the number of large crystals. The crystal sizes, which refer to as the volumes of perovskite grains, increase in the end, manifesting the integration of small grains with water molecules for both samples, in accordance with the SEM results. Thus, I infer that a volume expansion where water is incorporated within the perovskite grains results in the degradation of both PSCs. In contrast to the crystal evolution in CsMAFA devices, the crystal size (~ 70 nm) of the CsI-HBL device decreases and reaches ~ 56.4 nm at 4 min (Figure 6.11F), suggesting grain fragmentation during operation. Moreover, the intensity increases in the CsI-HBL devices (Figure 6.11F), indicating an increase in the number of perovskite crystals during the device operation, while there is no such increase in the CsMAFA devices. Small perovskite grains might be deemed as recombination hot spots, leading to a stronger recombination loss and limiting the V_{OC} [164, 165, 166, 167]. Such an increase in the quantity of the perovskite crystals would introduce an increasing number of grain boundaries, which accelerates the moisture degradation and decreases the shunt resistance (Figure 6.12), therefore reducing the J_{SC} and FF [168, 169].

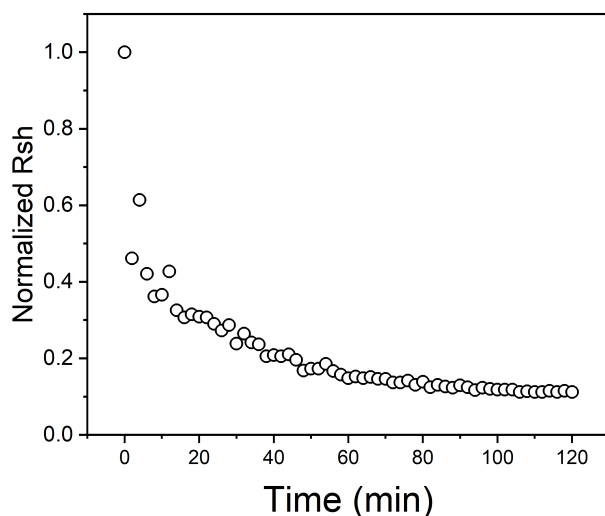


Figure 6.12: Normalized shunt resistance of CsI-HBL device under light and humidity as a function of time. Reproduced from Ref. [48] with permission. Copyright 2023, American Chemical Society.

In addition, to exclude that such grain fragmentation is peculiar in CsI-HBL devices, an operando GISAXS measurement of MAFA is also performed (Figure 6.13), which manifests that no grain fragmentation is found in the MAFA samples. The morphology evolution of the said device is in line with the evolution of the device performance.

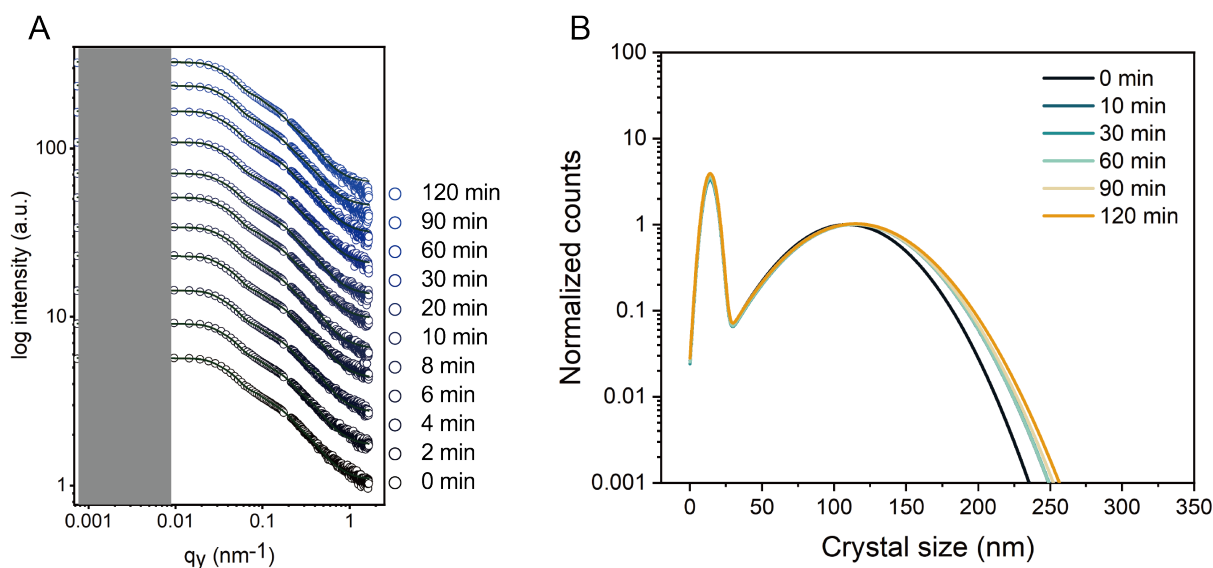


Figure 6.13: (A) Horizontal line cuts of 2D GISAXS data (symbols) shown with fits (lines), where the grey rectangle represents the resolution. (B) Crystal size evolution extracted from GISAXS fits over time under device operation, indicating only minor changes in the large-size tail of the size distribution. Reproduced from Ref. [48] with permission. Copyright 2023, American Chemical Society.

As such, I deduce that the degradation of CsMAFA PSCs under light and humidity is initiated by the volume expansion, whereas the degradation of PSCs with modified buried interfaces is initiated by the grain fragmentation as well as the increased GBs and exacerbated by volume expansion. In addition, there might be a partial interaction between perovskite and water molecules, which may not be captured without suitable in situ techniques.

6.4 Crystallinity Evolution

In addition to the GISAXS measurements, I also perform ex situ GIWAXS to gain insights on the change of the crystalline structure. Figure 6.16A-D shows the 2D GIWAXS data of respective sample before and after aging, where the prominent Debye–Scherrer-ring ($\sim 1.0 \text{ \AA}^{-1}$) and a halo at $\sim 0.9 \text{ \AA}^{-1}$ correspond to the (100) Bragg peak of the perovskite and the PbI_2 peak [65]. In contrast to the CsMAFA devices, the halo ring in Figure 6.16C is invisible, corroborating the reaction between CsI-doped HBL and the excess PbI_2 in the active layer. The azimuthal cake cuts integrated from the 2D GIWAXS data are seen in Figure 6.14, in which no split or additional peak can be observed. This finding indicates that no phase segregation and phase transformation occurred during device operation. Also, these results illustrate that there is no perovskite decomposition after aging.

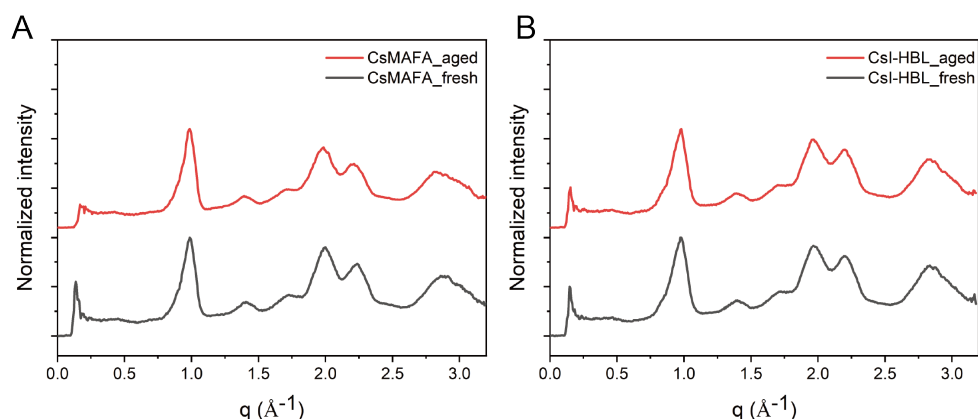


Figure 6.14: Azimuthal integration of 2D GIWAXS data before and after aging, obtained from cake cuts: (A) CsMAFA device and (B) CsI-HBL device. Reproduced from Ref. [48] with permission. Copyright 2023, American Chemical Society.

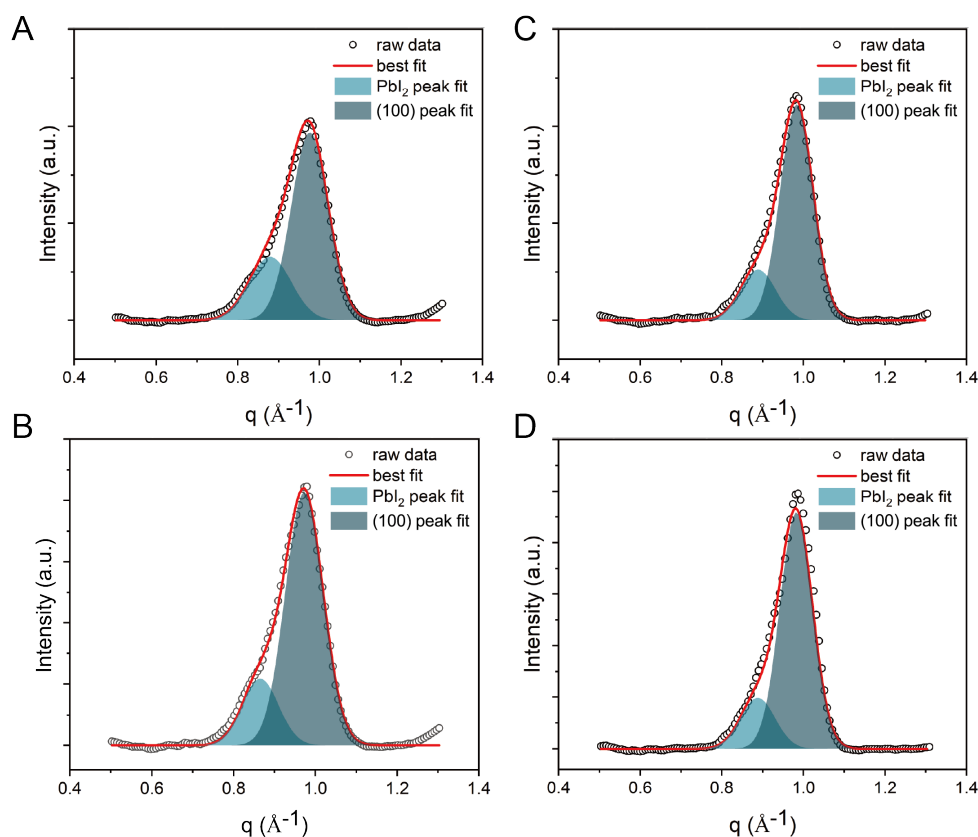


Figure 6.15: Zoom in and fits of azimuthal integration of 2D GIWAXS data: (A) CsMAFA before aging, (B) CsI-HBL before aging, (C) CsMAFA after aging, and (D) CsI-HBL after aging. The Bragg peak position of PbI_2 (0.89 \AA^{-1}) was unchanged after aging. Reproduced from Ref. [48] with permission. Copyright 2023, American Chemical Society.

6.4. Crystallinity Evolution

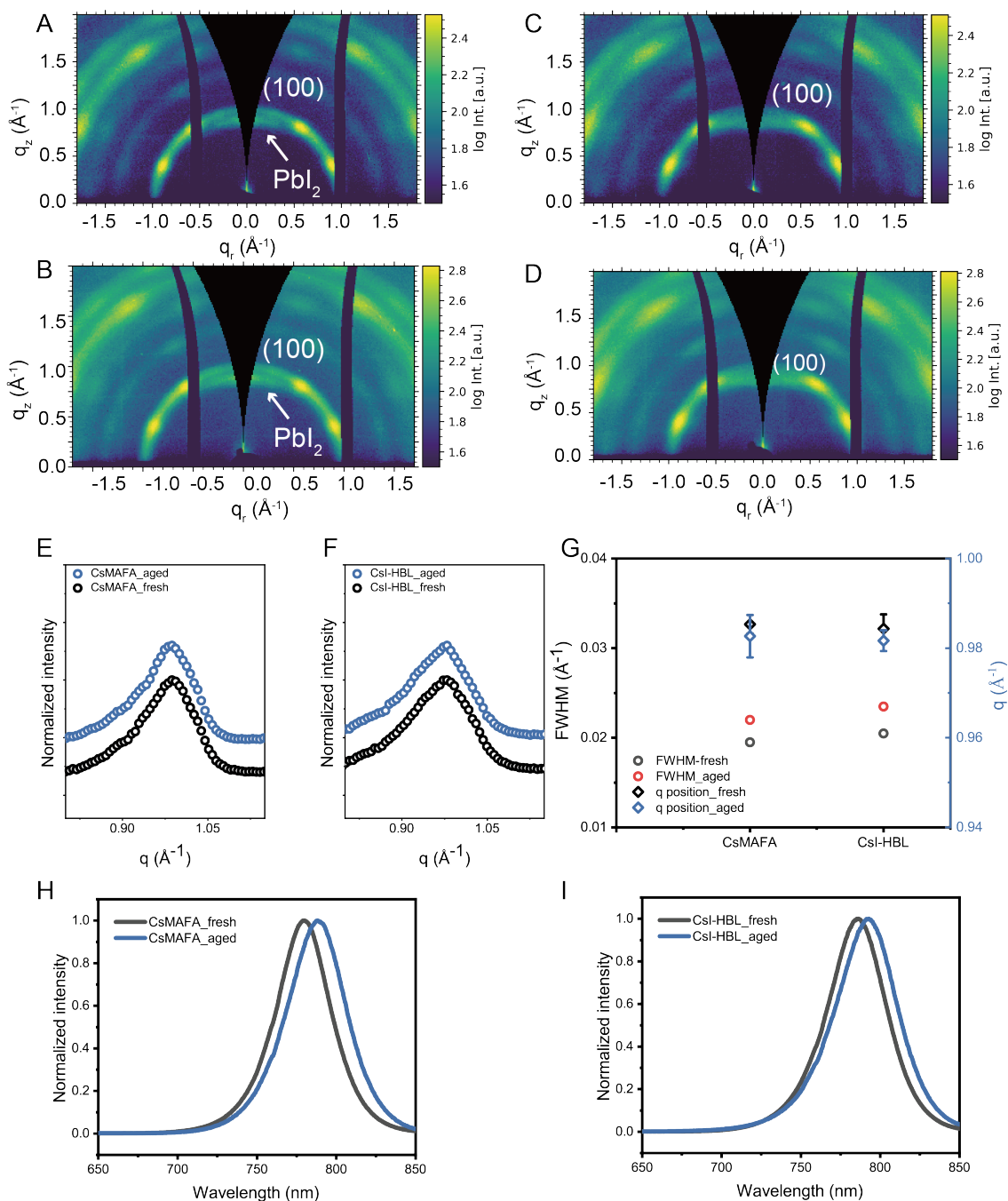


Figure 6.16: Reshaped 2D GIWAXS data of (A) fresh CsMAFA device, (B) aged CsMAFA device, (C) fresh CsI-HBL device, and (D) aged CsI-HBL device. Enlarged pseudo-XRD data, obtained from the azimuthal cake cuts of (E) CsMAFA and (F) CsI-HBL device data. (G) Peak positions and FWHM of the perovskite (100) peak before and after aging, where the circles and rhombus denote the FWHM and q position, respectively. The error bars are calculated through three-times fits of the perovskite (100) peak with Gaussian profiles. Normalized PL data of respective film before and after aging: (H) CsMAFA and (I) CsI-HBL. Reproduced from Ref. [48] with permission. Copyright 2023, American Chemical Society.

Therefore, the ex situ GIWAXS experiments manifest that water molecules are not interacting with perovskite absorbers during this aging period; however, longer exposure to light and high humidity would lead to the hydration and even decomposition of the perovskites [41]. In order to track the evolution of the crystal lattice, the (100) peak is fitted with Gaussian functions as illustrated in Figure 6.16E,F. The fit data is displayed in Figure 6.15. It is worth noticing that the (100) peaks with respect to all samples shift toward lower values (Figure 6.16G), indicating a slight lattice expansion after aging. This slight lattice expansion can further lead to defect formation and even non-radiative recombination, which are detrimental to solar cell performance [170, 171, 172, 173]. Moreover, the full width at half maximum (FWHM) of the respective perovskite (100) peak increases, suggesting the reduced crystallinity after 120 min aging [174]. Apart from the GIWAXS measurements, Figure 6.16H,I shows the PL data before and after aging. From fits with Gaussian functions, I find that the PL signal positions of the CsMAFA and CsI-HBL samples are shifted 20 and 10 meV to lower values (redshift), respectively. This phenomenon can be attributed to an enlarged unit cell or the enrichment of FA^+ since an FA-based perovskite has a larger crystal lattice and a smaller bandgap with respect to other A-site-based perovskites [141, 174, 175]. Figure 6.17 demonstrates relatively similar absorption in the range of 500–800 nm after being exposed to light soaking and humidity, whereas the light absorption of CsI-HBL drops at around 500 nm (Figure 6.14C).

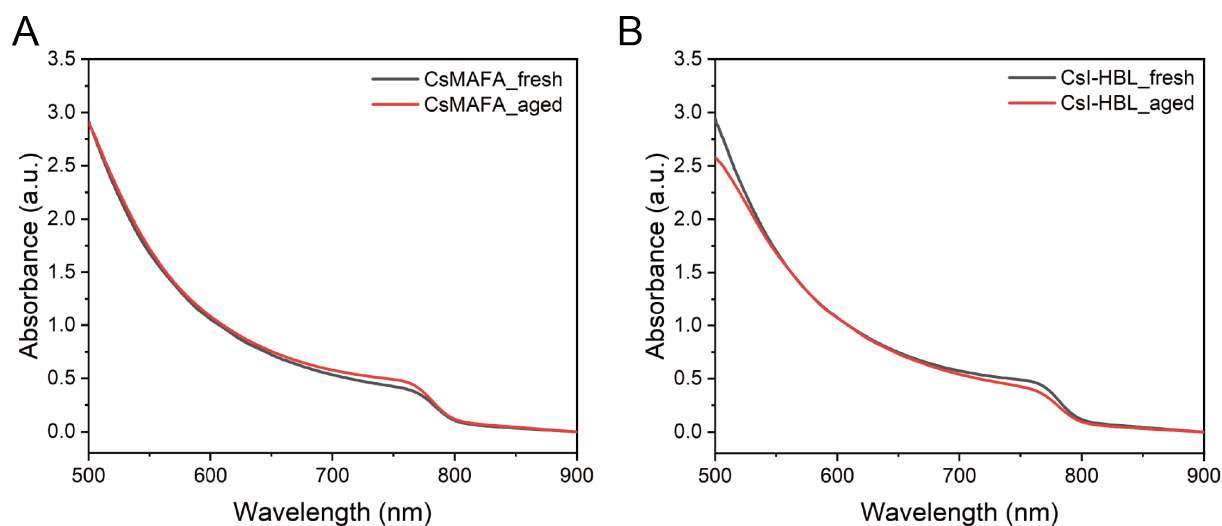


Figure 6.17: Light absorption spectral of ITO/HBL/perovskite films before and after aging: (A) CsMAFA and (B) CsI-HBL. Reproduced from Ref. [48] with permission. Copyright 2023, American Chemical Society.

Taken together, a slight lattice expansion is observed after aging under light and humidity regardless of the CsI modification method. To wrap up, I find that water incorporation into perovskite grains results in volume expansion, as evidenced by the GISAXS results.

However, PSCs with CsI-modified buried interfaces experience grain fragmentation with water molecule invasion, leading to a faster decay of the device performance under external stimuli. These morphology changes result in the deterioration of FF and J_{SC} , exacerbating the degradation of the solar cell performance under light and humidity. In addition, GIWAXS data suggest that no chemical decomposition occurs and a minor lattice expansion is discovered after aging.

6.5 Conclusion

To conclude, I concurrently study the device performance and morphology evolution of different PSCs during operation under AM 1.5G illumination and $75 \pm 5\%$ humidity by GISAXS. I find that the solar cells undergo severe degradation when continuously exposed to light and humidity, particularly FF and J_{SC} , which is induced by the morphology change of the active layer. Such morphology change originates from the volume expansion with water molecule incorporation into the perovskite grains. In addition, I also find a slight lattice expansion and PL redshift in both types of PSCs after aging. At the same time, devices with bulk component modification show a better stability against both light and humidity, while the grain fragmentation and increased grain boundaries in PSCs with modified buried interfaces after aging lead to a faster decay of the device performance. This work demonstrates the evolution of the microscopic morphology during the operation of chemically engineered perovskite solar cells under light and humidity exposure. Specifically, I find that a bulk modification effectively suppresses moisture-induced degradation under operation conditions. This understanding contributes to identifying the degradation mechanism and guiding the fabrication of stable PSCs.

Structure and Charge Carrier Behavior in Reduced-Dimensional Perovskites

The results shown in this chapter are retrieved from the publication: *Deciphering Structure and Charge Carrier Behavior in Reduced-Dimensional Perovskites* (K. Sun, R. Guo, S. Liu, D. Yang, X. Jiang, L. F. Huber, Y. Liang, M. A. Reus, Z. Li, T. Guan, J. Zhou, M. Schwartzkopf, S. D. Stranks, F. Deschler, P. Müller-Buschbaum, *Advanced Functional Materials*, 2411153 (2024)), reproduced from [68] with permission, copyright 2024, Wiley-VCH.

Reduced-dimensional perovskites (RDPs) have advanced perovskite optoelectronic devices due to their tunable energy landscape, structure, and orientation. However, the origin of structural and photophysical property changes when moving from low-dimensional to high-dimensional RDPs remains to be understood. This study systematically reveals structural and photophysical properties of slot-die-coated Dion-Jacobson (DJ) and Ruddlesden-Popper (RP) RDPs with different dimensionalities. RP RDPs with lower dimensionality ($n=2$) exhibit a dominant $n=2$ phase, preferential out-of-plane orientation, and longer charge carrier lifetime compared with DJ RDPs. In addition, the formation kinetics of RDPs with higher dimensionality ($n=4$) are unraveled by in situ X-ray scattering, showing the favorable formation of the lower- n phase in RP RDPs. The formation of these lower- n phases is thermodynamically and stoichiometrically favored, while these phases are likely in the form of an “intermediate phase” which bridges the 3D-like and lower- n phases in DJ RDPs. DJ RDPs with higher dimensionality demonstrate comparable phase purity, preferential orientation, spatially vertical phase homogeneity, and longer charge carrier lifetime. As such, DJ-based perovskite solar cells (PSCs) ($n=4$) demonstrate better photostability under operational conditions than RP-based PSCs. Thus, the work paves the way for the utilization of RDPs to upscale PSCs.

7.1 Preface

Reduced-dimensional (2D and quasi-2D) perovskites (RDPs) with intriguing physical and structural properties [31, 12], have emerged as promising candidates in photovoltaics (PV) [176, 177, 178, 179], light-emitting devices [180], and next-generation optoelectronics devices [181]. RDPs are perovskite quantum wells (QWs) separated by bulky organic cations, in which the width (n) of the RDPs is determined by the thickness of the PbI_6 octahedra. Two typical RDPs, i.e., Dion-Jacobson (DJ) and Ruddlesden-Popper (RP) perovskites have the chemical formulas of $\text{LA}_{n-1}\text{Pb}_n\text{I}_{3n+1}$ and $\text{L}'_2\text{A}_{n-1}\text{Pb}_n\text{I}_{3n+1}$, where L, L', and A refer to the divalent, monovalent organic spacer cations, and monovalent cations, respectively.

In general, a number of factors, e.g., the stoichiometry of the perovskite precursor [11], ligand type and size [182, 183], additives [184, 185], fabrication methods [186, 187], jointly affect the phase distributions of RDPs. A mixture of multiple dimensionalities of RDPs with random crystal orientation is expected to build up during the film formation process [177, 188, 189]. Such phase impurities may introduce an inhomogeneous energy landscape and impede charge transport [183, 190, 191]. Therefore, it is imperative to investigate the phase distribution and crystal orientation of RDPs, which necessitates studying their growth kinetics, as these characteristics are determined during film growth. However, despite some pioneering work on the growth kinetics of RP RDPs [35, 192], a comprehensive study combining the growth mechanisms of both, RP and DJ RDPs in a large-scale deposition is still missing.

In addition to the growth kinetics, the organic cations heavily influence the structural distortion and interlayer screening, resulting in their different photophysical properties, e.g., binding energy and charge carrier mobility [193]. In particular, the coupling of inorganic anions and organic spacers in RDPs facilitates the electron-phonon reaction, resulting in high non-radiative charge recombination and shorter charge carrier lifetimes [194]. Therefore, understanding the function of organic ligands on the phase purity, growth mechanism, and charge carrier dynamics is beneficial for directing the usage of RDPs in 2D/3D heterojunction and quasi-2D solar cell applications.

To fill this gap and enable the advancement of large-scale deposition of RDPs, I focus on the slot-die coated RP and DJ RDPs with varying dimensionalities ($n=2$ or 4), i.e., $(\text{PEA})_2\text{MA}_{n-1}\text{Pb}_n\text{I}_{3n+1}$ (PEA: phenethylammonium) and $(\text{PDMA})\text{MA}_{n-1}\text{Pb}_n\text{I}_{3n+1}$ (PDMA: 1,4-phenylenedimethan ammonium), owing to their chemical similarities and extensive applications in the field [186, 195]. Using grazing incidence wide-angle X-ray scattering (GIWAXS), the phase distribution and orientations of respective RDPs is determined, highlighting the different phase composition in RDPs with higher dimensionality. The film growth of RDPs ($n=4$) is further monitored during slot-die coating with in situ

scattering techniques, showing the stoichiometry-determined phase formation. With the help of transient absorption (TA) spectroscopy, I unravel the phase purity, charge carrier behavior, and energy transfer in respective RDPs. I further test the intrinsic stability of perovskite solar cells (PSCs) based on RP and DJ ($n=4$) RDPs under the protocol of ISOS-L-1I with operando GIWAXS, showcasing the overall better stability of DJ-based PSCs. This work leverages the understanding of structural-photophysical properties in RP and DJ materials with different dimensionalities, thus advancing the utilization of 2D perovskites as passivation layers and promoting the fabrication of efficient quasi-2D PSCs.

7.2 Phase Purity and Spatially Vertical Homogeneity

Multiple n -value phases of RDPs are naturally formed during the crystallization, resulting in an inhomogeneous energy landscape and inefficient energy transfer [176, 76]. Identifying the phase distributions and their orientations enables a deeper understanding of the charge carrier dynamics. Therefore, the depth-dependent GIWAXS measurements at different incident angles (α_i , 0.2 - 0.6°) are performed to investigate the vertically spatial phase distribution (Figure 7.6; Figure 7.1).

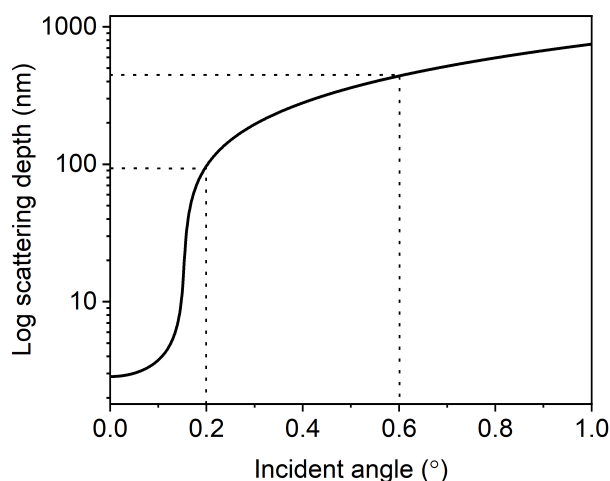


Figure 7.1: Scattering depth of the X-ray beam versus incident angle. The scattering depth is 441.2 nm at the incident angle of 0.6° . Reproduced from Ref. [68] with permission. Copyright 2024, Wiley-VCH.

I find that the lower- n phases (normally below 1 \AA^{-1}) and 3D-like phase ($\sim 1 \text{ \AA}^{-1}$) of RP and DJ RDPs ($n=2$) present with the increase α_i , indicating that these phases are distributed homogeneously throughout the film.

The reshaped 2D GIWAXS data at $\alpha_i=0.6^\circ$ (Figure 7.2) illustrate that the RP RDPs exhibit a preferential orientation (Bragg peaks) along the out-of-plane direction. In contrast, DJ RDPs appear to be predominantly isotropic with a partially vertical orientation.

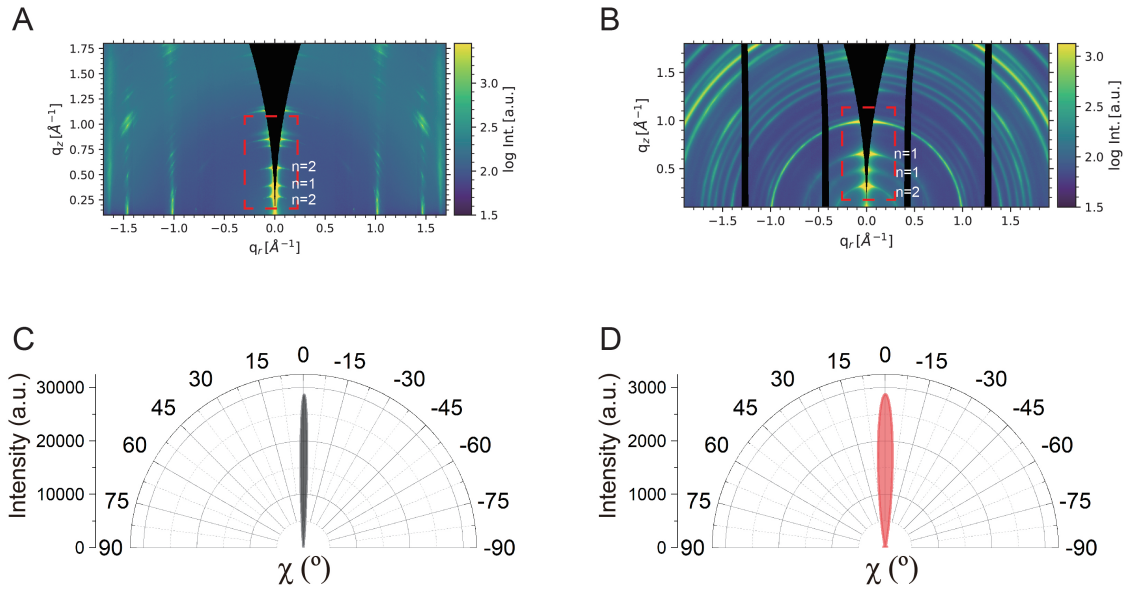


Figure 7.2: Reshaped 2D GIWAXS data of RDPs ($n=2$) at incident angle (α_i) of 0.6° with the main phases indicated. (A) RP RDPs and (B) DJ RDPs. The Bragg spots in (A) demonstrate the preferential orientation along the out-of-plane direction, whereas DJ RDP is overall isotropic with partially vertical orientations (highlighted in the red framework). Azimuthal tube cuts as a function of polar angle, extracted from the cut along (C) $q \sim 0.56 \text{ \AA}^{-1}$ of RP RDPs and (D) $q \sim 0.66 \text{ \AA}^{-1}$ of DJ RDPs, where the data was corrected by subtracting the local background near the selected q range such that the data only shows the highly-oriented area. Reproduced from Ref. [68] with permission. Copyright 2024, Wiley-VCH.

In terms of high-dimensional RDPs, with an increased scattering depth, the peak of lower- n phases in RP RDPs ($n=4$) becomes more prominent (Figure 7.6E; Figure 7.3, A-C), corroborating that lower- n phases are prone to be present in the interior of the RP film and their phase heterogeneity along the vertical direction. In contrast, the signals of lower- n phases in DJ RDPs ($n=4$) are indiscernible (Figure 7.6F; Figure 7.3, D-F), meaning an insufficient presence of lower- n phases in DJ RDPs and their spatially vertical phase homogeneity. This structure variance in RP and DJ RDPs illustrates that DJ with higher dimensionality are prone to form phase-pure perovskite. On the other hand, the signals at lower α_i in both RP and DJ RDPs ($n=4$) are predominantly 3D-like phases, manifesting that the 3D-like phase tends to stack at the air-substrate interface.

7.2. Phase Purity and Spatially Vertical Homogeneity

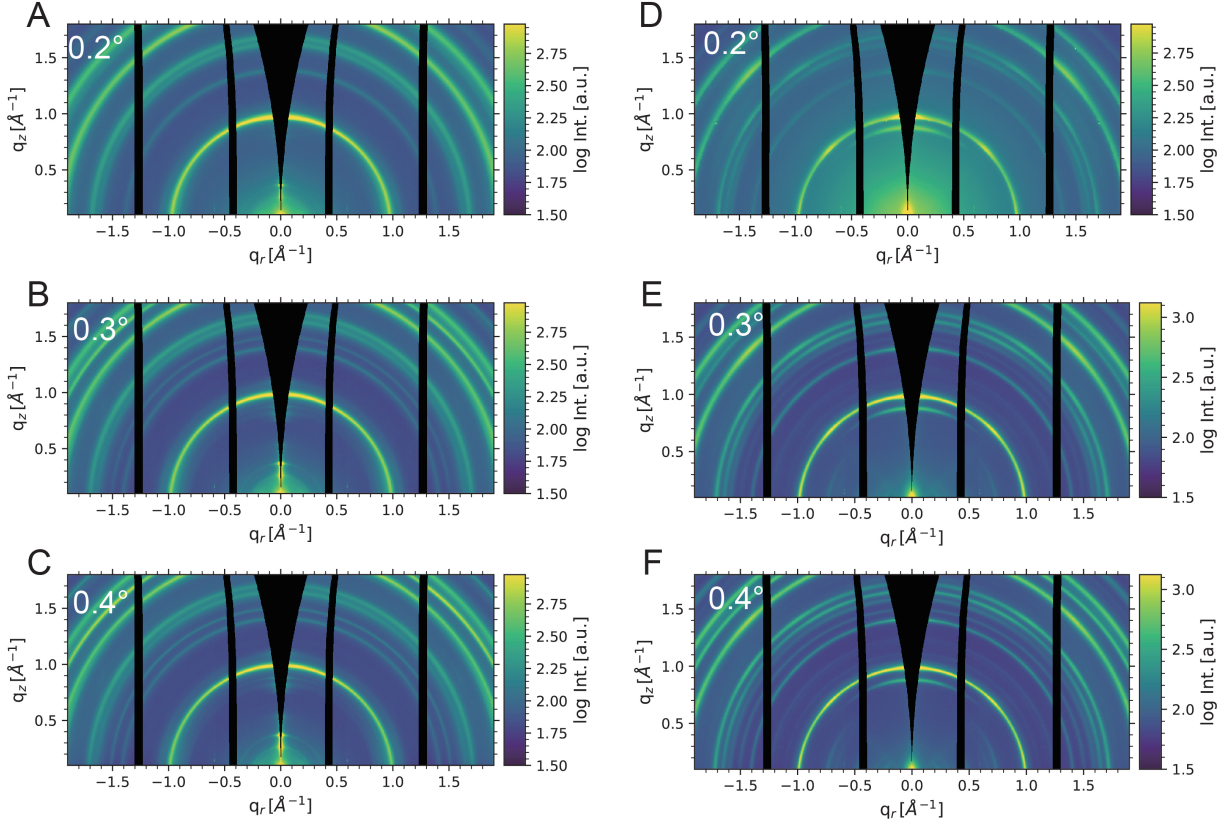


Figure 7.3: Reshaped 2D GIWAXS data of RDPs ($n=4$) with different incident angles (α_i). RP RDPs at (A) $\alpha_i=0.2^\circ$, (B) $\alpha_i=0.3^\circ$, and (C) $\alpha_i=0.4^\circ$. DJ RDPs at (D) $\alpha_i=0.2^\circ$, (E) $\alpha_i=0.3^\circ$ and (F) $\alpha_i=0.4^\circ$. Reproduced from Ref. [68] with permission. Copyright 2024, Wiley-VCH.

In addition, the PL spectra (Figure 7.4) excited from front and back (glass side) show that the intensities at peak ~ 570 nm (back) are higher, implying that the lower- n phases are mainly located at the bottom of the films, in agreement with GIWAXS data.

In light of the favorable formation of 3D-like phase and phase distribution along the vertical direction [52], I can deduce that the nucleation of RDPs ($n=4$) starts at the air-precursor interface. Knowing where the nucleation and crystallization take place and locating these n -value phases enable suppressing the lower- n phase and realizing a homogenous energy landscape.

Furthermore, with the increased dimensionality, the orientation of perovskite crystals becomes less pronounced, shifting from a predominantly vertical or partially vertical alignment to a more isotropic orientation. Notably, DJ RDPs show distinct orientations at $\chi=0^\circ$, 45° and 80° (Figure 7.5) compared to RP RDPs (oriented mainly at $\chi=0^\circ$). In addition, to retrieve the crystal orientation distribution, the material quantity (MQ) is calculated by correcting the intensity with a factor of $\sin\chi$ (Figure 7.5) [65].

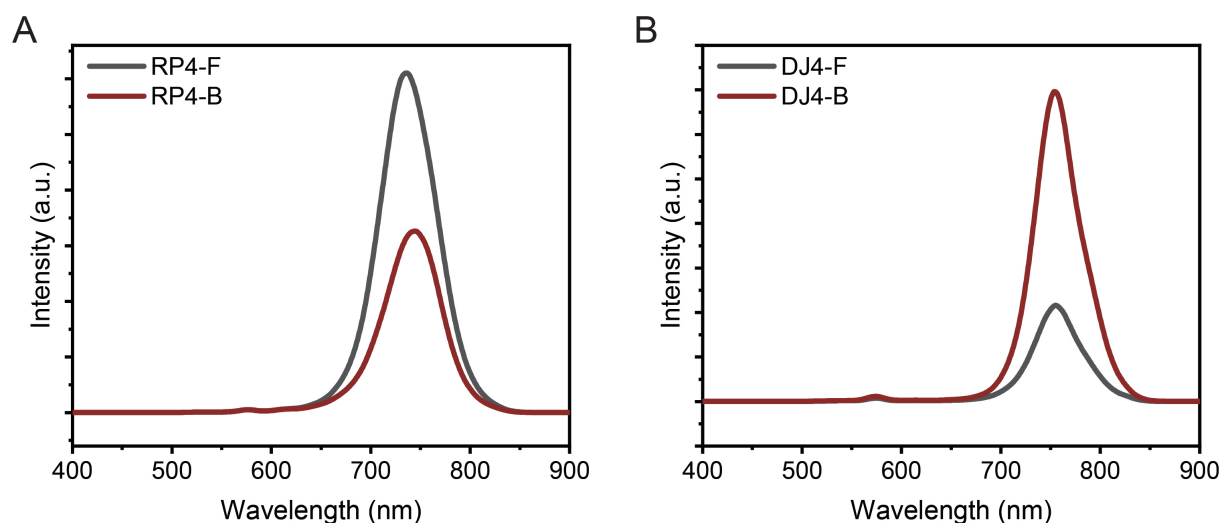


Figure 7.4: Steady-state photoluminescence spectra of (A) RP RDPs ($n=4$) film on glass and (B) DJ RDPs ($n=4$) film on glass, where black and red curves represent PL data acquired from front and back (glass side) excitation, respectively. Reproduced from Ref. [68] with permission. Copyright 2024, Wiley-VCH.

I notice an increase in oriented crystal contribution in DJ RDPs (43%) in comparison to RP RDPs (23%), suggesting their preferential orientation and potentially higher efficiency for charge transport.

Taken together, the schematic illustration of the respective RDPs is depicted in Figure 7.6, C, D, G, and H. In short, the 3D-like phase and lower- n phases of RP and DJ ($n=2$) are homogeneously distributed throughout the film, where the RP and DJ crystals are vertically oriented and partially vertically oriented, respectively. With increasing dimensionality, the texture becomes weaker in both RP and DJ RDPs. Moreover, I notice multiple n -values phases coexist in RP film ($n=4$), with stacking of substrate/lower- n phase/3D-like phase, whereas the lower- n phase is invisible in DJ RDPs. These results indicate that RP RDPs with lower dimensionality have a preferential orientation along the out-of-plane direction compared to DJ, which facilitates charge transport. In contrast, DJ RDPs ($n=4$) demonstrate an improved phase purity and a more pronounced orientation distribution (43%) compared to RP RDPs (23%).

7.2. Phase Purity and Spatially Vertical Homogeneity

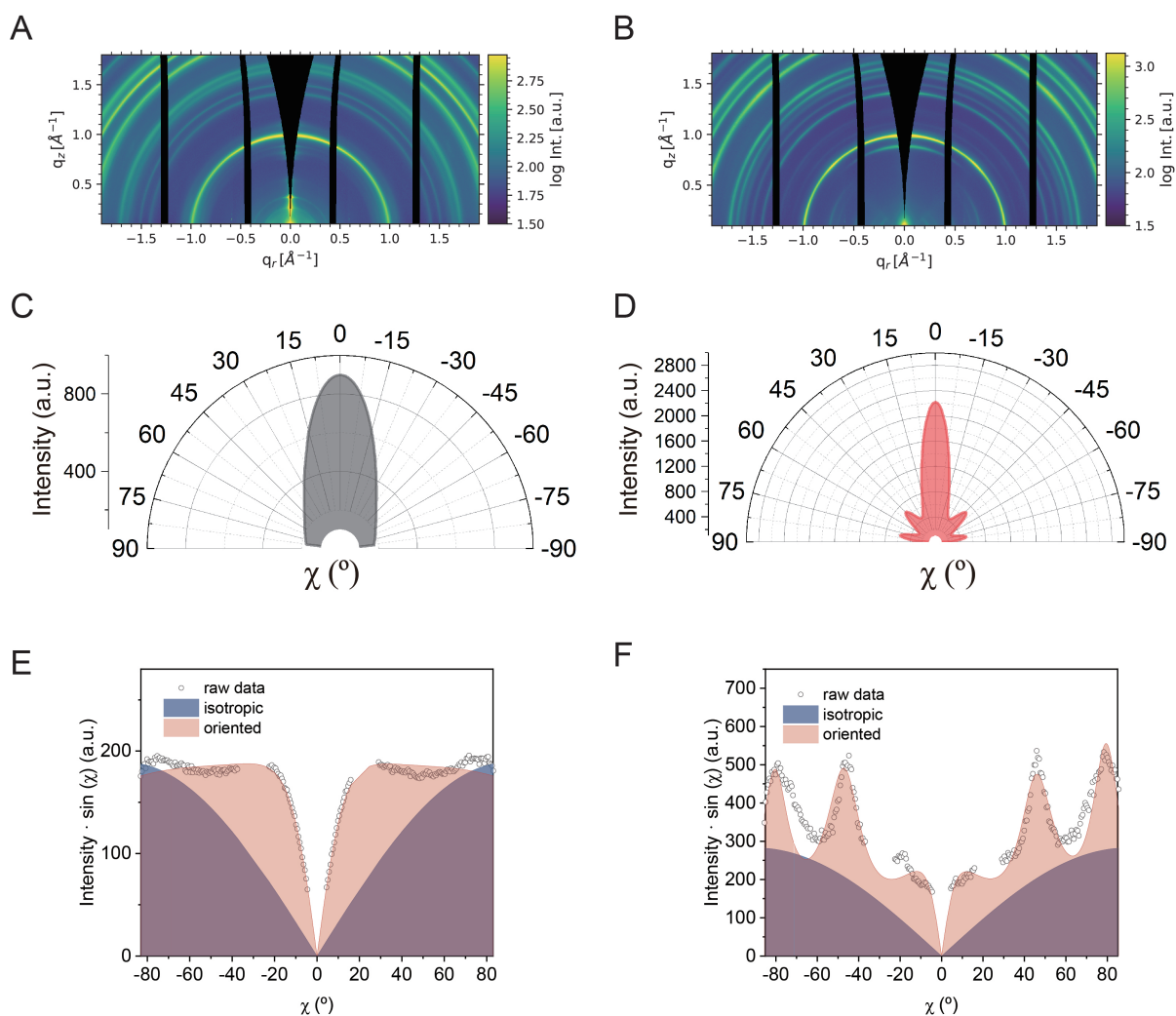


Figure 7.5: Reshaped 2D GIWAXS data of RDPs ($n=4$) at incident angle (α_i) of 0.6° . (A) RP RDPs and (B) DJ RDPs. Azimuthal tube cuts as a function of polar angle, extracted from the cut along (C) $q \sim 1.0 \text{ \AA}^{-1}$ of RP RDPs and (D) $q \sim 1.0 \text{ \AA}^{-1}$ of DJ RDPs, where the data was corrected by subtracting the local background near the selected q range such that the data only shows the highly-oriented area. This demonstrates that the DJ RDPs have a more pronounced orientation distribution compared to RP RDPs, particularly at $\chi = 45^\circ, 80^\circ$. Pole figures of (E) RP RDPs and (F) DJ RDPs, where light red and light blue shaded areas refer to the oriented contributions and isotropic orientations, respectively. The intensity was corrected using the Lorenz factor $\sin\chi$, and the orientation distributions were calculated based on the integration ratio of the respective shaded areas. Reproduced from Ref. [68] with permission. Copyright 2024, Wiley-VCH.

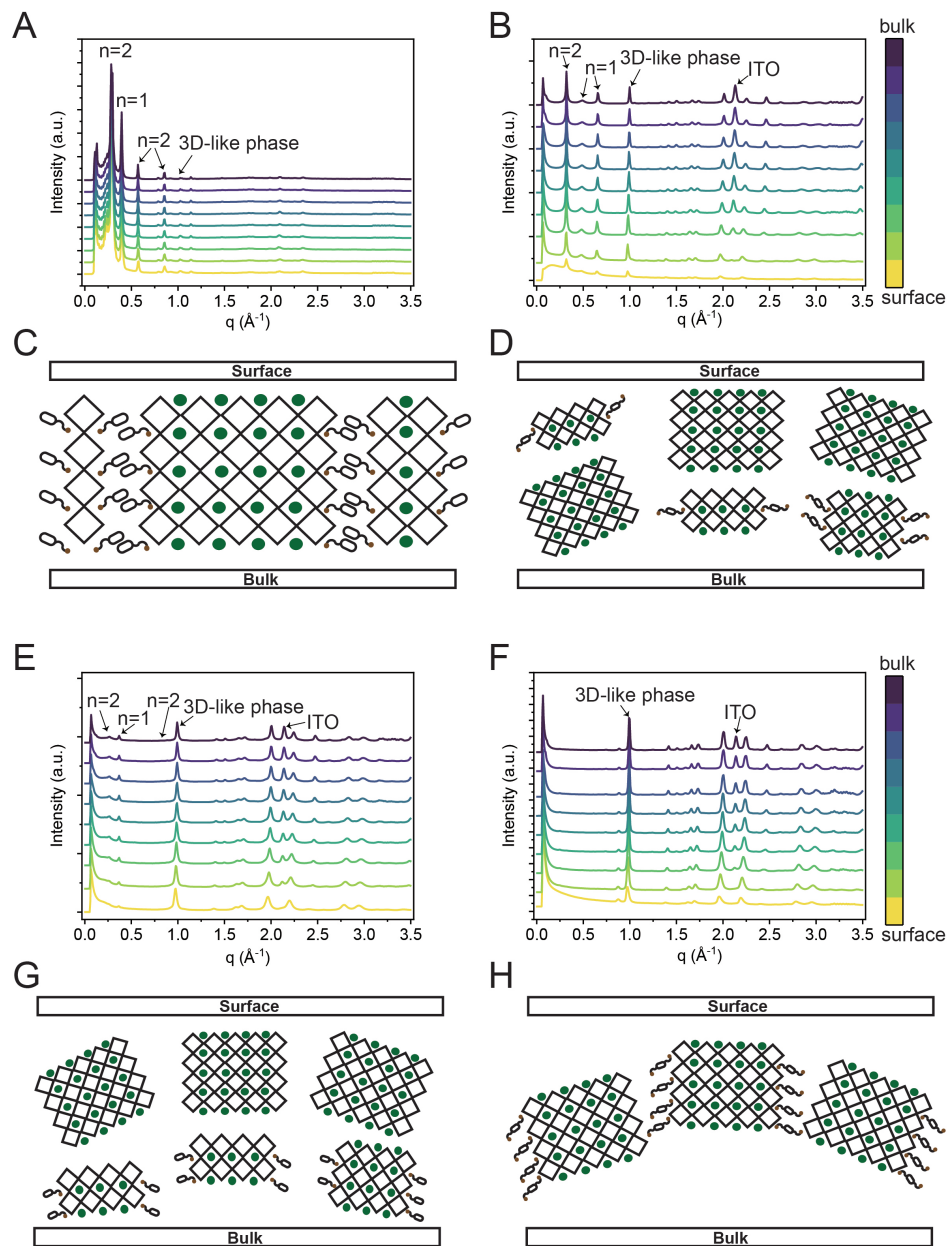


Figure 7.6: Phase distributions and schematic illustration of RDPs film. Angular-dependent pseudo-XRD was extracted from 2D GIWAXS data with varying incident angles, in which the different phases of RDPs and the ITO peak are indicated. (A) RP RDPs ($n=2$) and (B) DJ RDPs ($n=2$). Schematic illustration of the structures of RDPs ($n=2$). (C) RP RDPs, where the crystals are vertically oriented, and (D) DJ RDPs, in which the 3D-like phase and lower- n phase are partially vertically oriented. Angular-dependent pseudo-XRD of (E) RP RDPs ($n=4$), showing the increased quantity of lower- n phases with increasing depth, and (F) DJ RDPs ($n=4$). Schematic illustration of the structures of RDPs ($n=4$). (G) RP RDPs, showing that the majorities are randomly oriented and the lower- n phase is distributed in the interior of the film, and (H) DJ RDPs, exhibiting their phase purity and orientations at $\chi = 0^\circ$ and 45° . Reproduced from Ref. [68] with permission. Copyright 2024, Wiley-VCH.

7.3 Growth Mechanisms of RDPS

To disclose the structural and orientational disparities in RDPs ($n=4$), in situ GIWAXS measurements (Figure 7.7, A and B) are performed to monitor the growth kinetics during film growth.

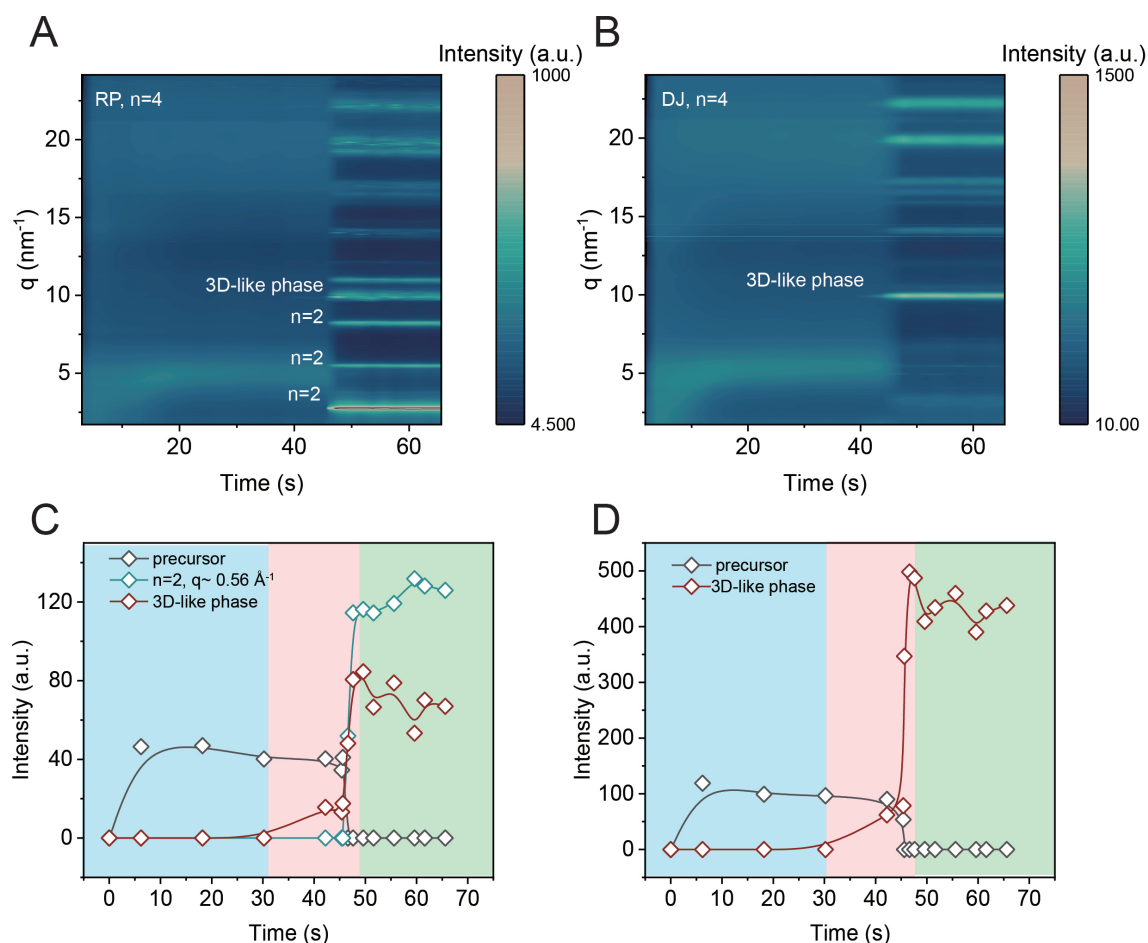


Figure 7.7: Growth kinetics of RP and DJ RDPs ($n=4$) on ITO substrates. 2D color plots of radially integrated line profiles of in situ GIWAXS data, where the prominent peaks are indicated. (A) RP RDPs film and (B) DJ RDPs film. The normalized integrated intensity of the selected Bragg peaks as a function of time for (C) RP and (D) DJ RDPs. This shows the conversion of precursor (broad peak at $q \sim 0.5 \text{ \AA}^{-1}$) to the final quasi-2D perovskite film, where the Bragg peaks of $q \sim 0.56 \text{ \AA}^{-1}$ and $q \sim 1.0 \text{ \AA}^{-1}$ represent the lower- n phase (040) and 3D-like phase of RDPS. The background color indicates the different regimes of growth of RDPS. Reproduced from Ref. [68] with permission. Copyright 2024, Wiley-VCH.

I observe two broad isotropic rings at $\sim 0.5 \text{ \AA}^{-1}$ and $\sim 1.9 \text{ \AA}^{-1}$ in both RP and DJ RDPS ($n=4$, Figure 7.8A and Figure 7.8A) for the first 40 s, representing the colloidal precursor sol-gels. Selected 2D reshaped GIWAXS data (Figure 7.8 and Figure 7.9) of RP and DJ

RDPs show the representative features at different timescales during film growth.

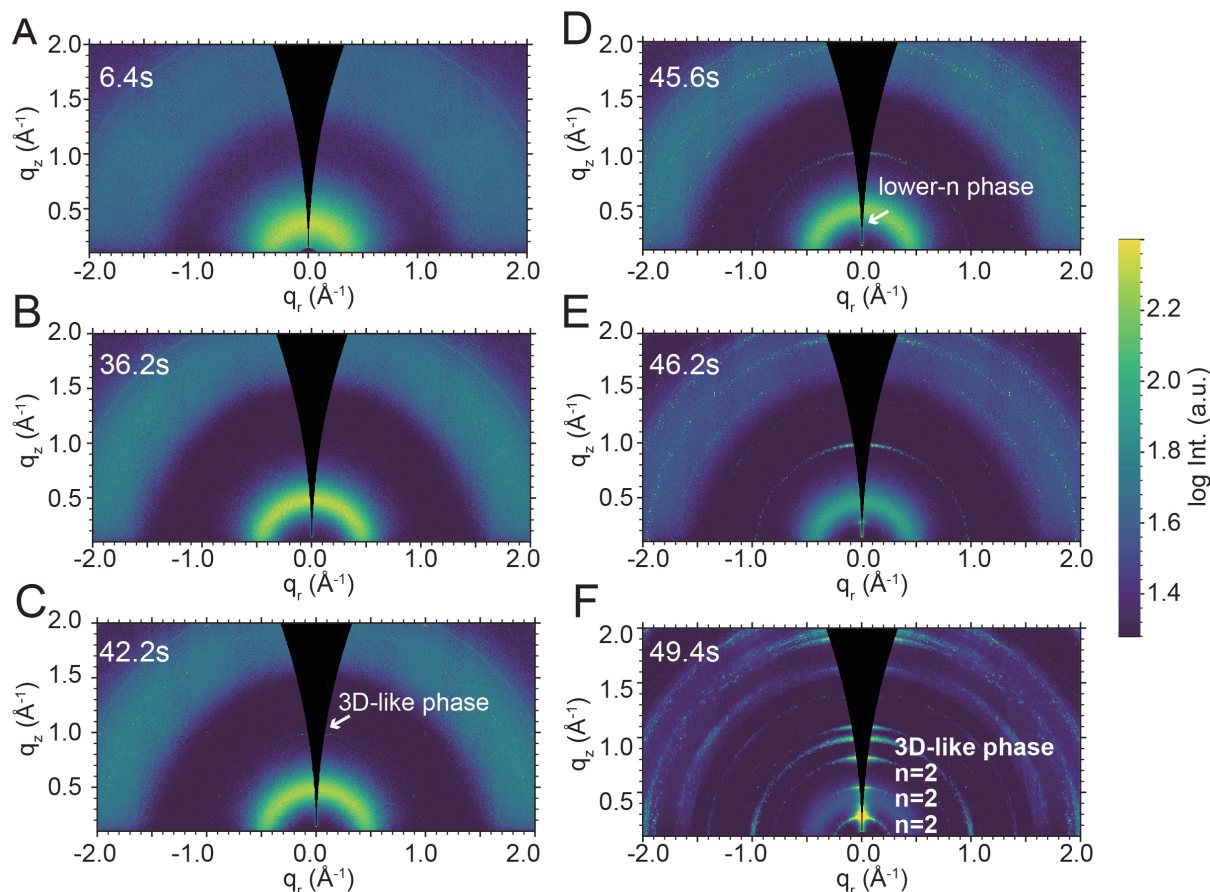


Figure 7.8: Selected reshaped 2D GIWAXS data of RP RDPs ($n=4$) during film growth, where the time scale and main phases are indicated. These data indicate that the formation of 3D-like phases is prior to the formation of lower- n phases in RP. In terms of orientation, the RP perovskites start growth along the out-of-plane direction, reorient, and ultimately become less oriented, i.e., shifting from Bragg spots to Debye–Scherrer rings. (A) 6.4s, (B) 36.2 s, (C) 42.2 s, (D) 45.6 s, (E) 46.2 s, and (F) 49.4 s. Reproduced from Ref. [68] with permission. Copyright 2024, Wiley-VCH.

After 40 s, the broad rings start to diminish, and the 3D-like phase appears. I do not observe any intermediate phase (e.g., $2\text{MAI} \cdots \text{PbI}_2 \cdots 2\text{DMF}$) during film growth, likely due to the higher substrate temperature, which suppresses the formation of an intermediate phase [196].

To quantify the conversion of the precursor and the formation of RDPs, the peak intensities of the precursor, 3D-like phase, and $n=2$ phase ($q \sim 0.56 \text{ \AA}^{-1}$) are extracted and plotted (Figure 7.7, C and D).

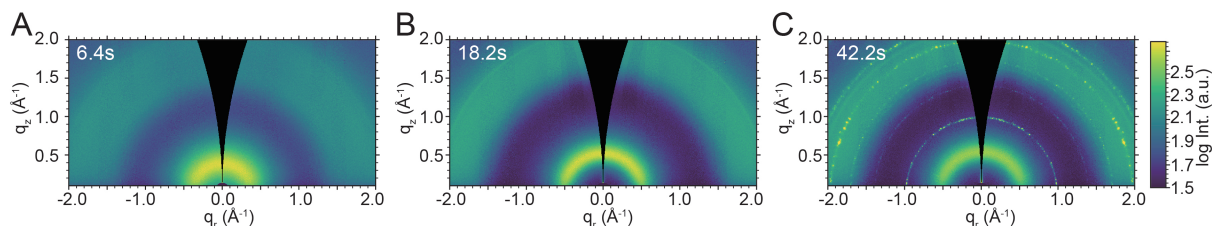


Figure 7.9: Selected reshaped 2D GIWAXS data of DJ RDPS ($n=4$) during film growth at different time scales. (A) 6.4 s, (B) 18.2 s, and (C) 42.2 s. Reproduced from Ref. [68] with permission. Copyright 2024, Wiley-VCH.

The conversion rate of the precursor peak mirrors the formation of the 3D-like phase, indicating a direct transition from precursor to RDPS in both studied cases. Interestingly, the emergence of the 3D-like phase (at ~ 40.2 s) precedes the formation of the $n=2$ phase in RP RDPS (~ 45.6 s). This difference is related to the stoichiometry and formation energy, i.e., the formation of the 3D-like phase is more thermodynamically favored compared with lower- n phases [197].

In addition, I find that many lower- n phases coexist in RP, while these signals are indiscernible in DJ RDPS, in accordance with depth-dependent GIWAXS data. Such phenomena are correlated with three factors: a) The stoichiometries of RDPS ($n=4$), particularly the concentration of long ligands in relation to MA^+ , determine the formation of lower- n phase such that the formation of lower- n phases in RP RDPS is more favorable compared to DJ RDPS. To test this, the growth of RP RDPS ($n=2$) is monitored under the same condition with in situ GIWAXS (Figure 7.10).

It is found that lower- n phases ($q \sim 0.28 \text{ \AA}^{-1}$) are formed prior to the formation of 3D-like phase, which is ascribed to the higher concentration of long ligands than that of MA^+ ; b) I infer that there might be an insufficient presence of lower- n phase or some “intermediate phases” bridging the 3D-like phase and lower- n phases in DJ RDPS, likely not yielding the signal of lower- n phase in GIWAXS (15); c) The lower formation energies of the lower- n phases in RP RDPS facilitate their formation in comparison to their DJ analogs [198, 199, 191].

The schematic illustrations (Figure 7.11) summarize the formation kinetics of RP and DJ RDPS ($n=4$), showing the individual events that occur during the film growth. In terms of RP formation, first, the solvent-perovskite complex provides the scaffold that can facilitate the nucleation and the construction of the QWs [200], followed by the formation of a weakly-textured 3D-like phase at the air-film interface. Continuous nucleation leads to the formation of lower- n phases that consume a large portion of long ligands, which in turn leave the short-chain precursors and promote the further growth and reorientation of the 3D-like phase.

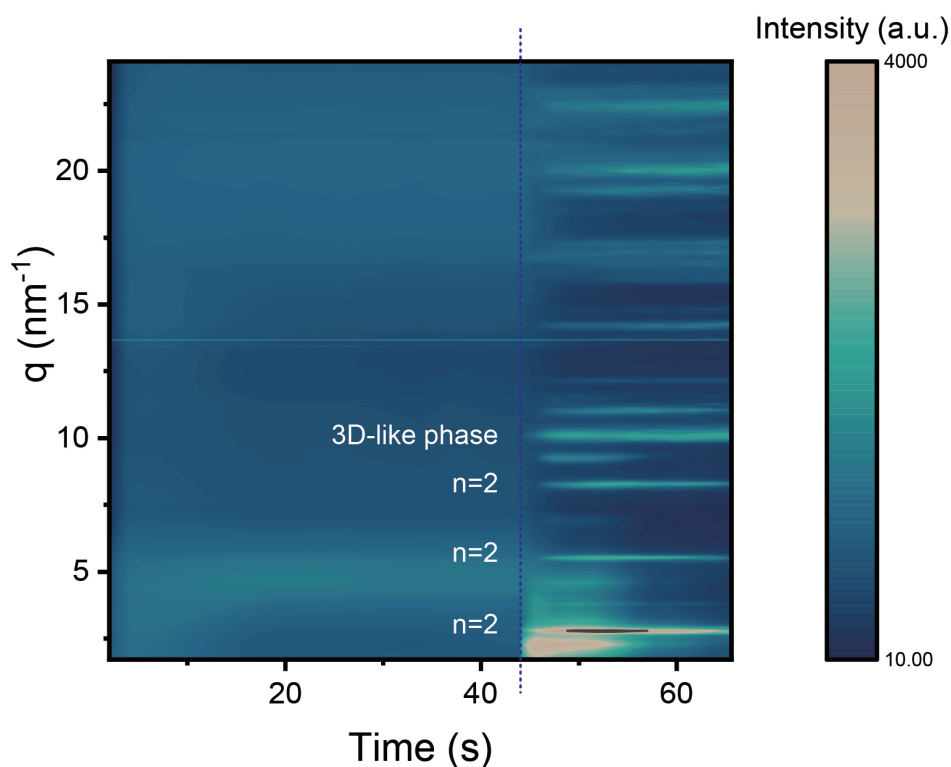


Figure 7.10: 2D color plot of radically integrated line profiles of in situ 2D GIWAXS data of RP RDPs ($n=2$), showing the main phases and the formation of lower- n phase ahead of the formation of 3D-like phase. Reproduced from Ref. [68] with permission. Copyright 2024, Wiley-VCH.

Considering the different formation rates of lower- n and 3D-like phases in RP and the location of these lower- n phases (i.e., the interior of the film), further efforts should be devoted to employing buried interface engineering, e.g., using ligands that can anchor lower- n phases to achieve controllable the growth and the orientation of these phases. In contrast, DJ RDPs undergo a direct transformation from precursor to 3D-like phase and “intermediate phase.” It is also worth mentioning that the film formation processes of slot-die coating and one-step spin-coating for RDPs are quite similar, as they both involve three stages: sol-gel, 3D-like perovskite, and 2D perovskite formation [35].

7.4 Charge Carrier Behavior

To further determine the phase purity and the charge carrier behavior of RDPs with different dimensionalities, I utilize ultraviolet-visible (UV-vis) and ultrafast TA spectroscopy. Multiple absorption features of respective RDPs are disclosed in Figure 7.12.

7.4. Charge Carrier Behavior

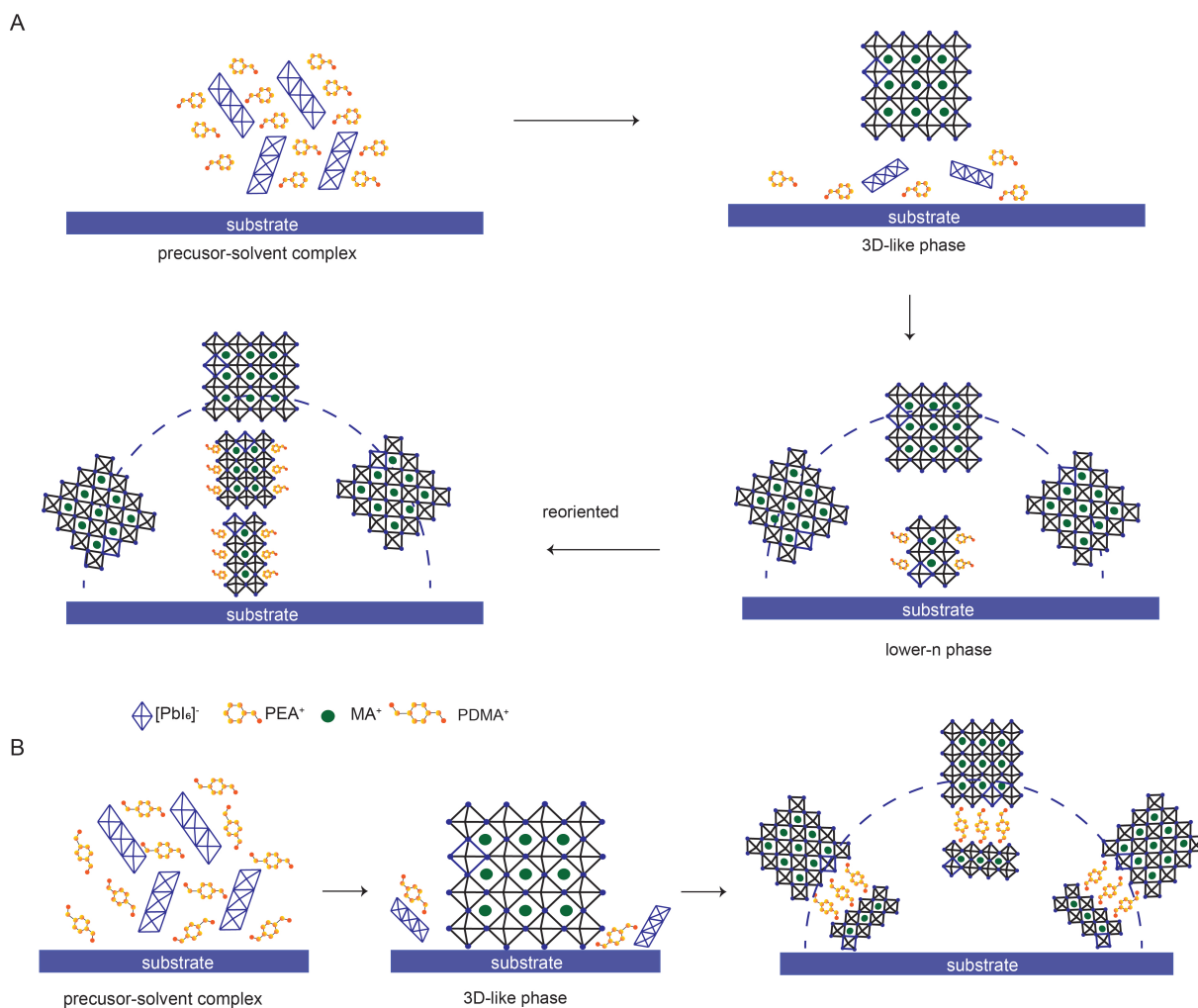


Figure 7.11: Schematic illustration of the growth mechanism. (A) RP RDPs ($n=4$) and (B) DJ RDPs ($n=4$). In both cases, the film starts in the sol-gel stage, followed by the nucleation at the air-substrate interface. Then, in RP, weakly-textured perovskites are formed, accompanied by the formation of preferentially oriented lower- n phases. Further growth leads to the perovskite reorientation and, thus, a broader orientation distribution. While DJ RDPs exhibit a direct transition from sol-gel to 3D-like phase and pronounced orientations at $\chi=0^\circ$, 45° and 85° , respectively. Reproduced from Ref. [68] with permission. Copyright 2024, Wiley-VCH.

Interestingly, DJ RDPs ($n=4$) show only small signals of lower- n phases, corroborating the minor presence of lower- n phases compared to the predominant 3D-like phase. Figure 7.13A-D shows TA contour plots as a function of pump-probe delay time. For RP RDPs, distinct ground state bleach peaks (GSBs) at ~ 567 nm, 607 nm, 640 nm, and 718 nm correspond to the $n=2$, 3, 4, and 3D-like phases ($GSB_{n=\infty}$), whereas for DJ RDPs, the GSBs peaks of $n=2$, 3, and 3D-like phases are located at 564 nm, 609 nm, and 746 nm, respectively.

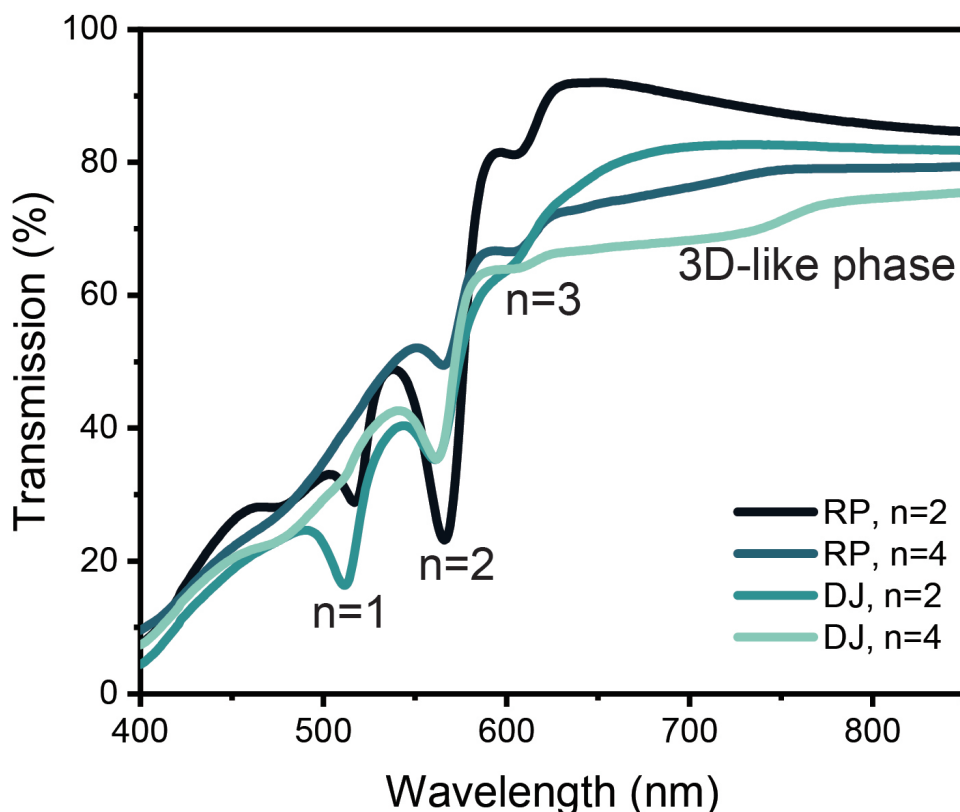


Figure 7.12: Transmittance data of respective RDPs film on glass substrate with characteristic peaks indicated. Reproduced from Ref. [68] with permission. Copyright 2024, Wiley-VCH.

The temporal evolution of TA spectra shows GSBs features with high-energy tails near the band edge as well as the photo-induced absorption (PIA) signals [201].

As shown in Figure 7.13E,F, RP RDPs ($n=2$) have a dominant $\text{GSB}_{n=2}$ peak, whereas DJ RDPs ($n=2$) have a broad phase distribution. In addition, in comparison to DJ RDPs ($n=4$), which have a relatively uniform phase distribution, features with lower n phase in RP RDPs ($n=4$) are enhanced (Figure 7.13G and H).

I also notice a redshift of the 3D-like phase in both RP and DJ with higher dimensionality, which might be caused by hot carrier cooling or energy transfer from the “intermediate phase” to a 3D-like phase [20, 25].

To quantitatively evaluate the relative contents of each phase, the respective GSB peak at a time delay of 1 ps is integrated and normalized to the maximum value (Figure 7.13I, detailed analysis in Table 7.1).

Notably, I find that the RP RDPs with lower dimensionality demonstrate a dominant $n=2$ phase (85%) compared with DJ RDPs (40%), suggesting their phase purity. RDPs with higher dimensionality show an opposite trend, where DJ RDPs consist of a large population of larger- n phases ($n > 3$, 60%) compared to RP RDPs.

7.4. Charge Carrier Behavior

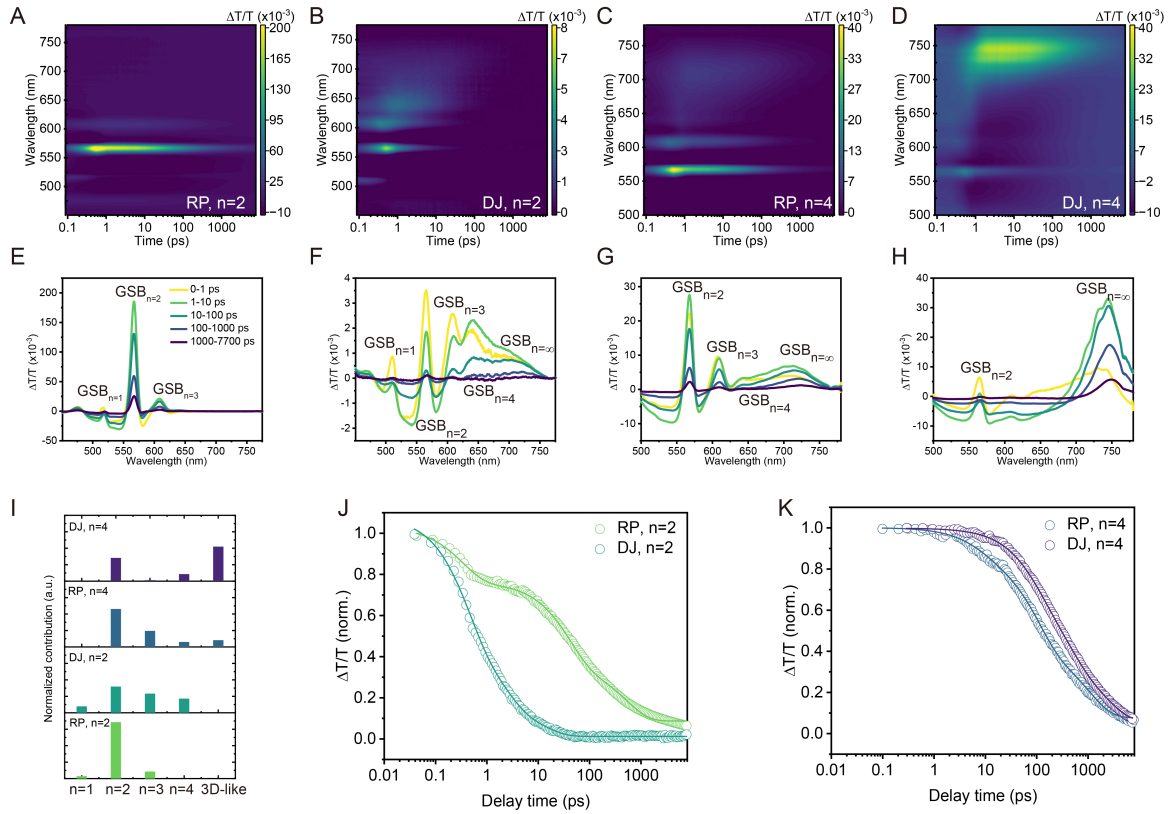


Figure 7.13: Charge carrier behavior of RDPs. Transient absorption maps of (A) RP RDPs ($n=2$), (B) DJ RDPs ($n=2$), (C) RP RDPs ($n=4$), and (D) DJ RDPs ($n=4$), where the RDPs were deposited on glass substrates. TA spectra at selected time delays after excitation of (E) RP RDPs ($n=2$), (F) DJ RDPs ($n=2$), (G) RP RDPs ($n=4$), and (H) DJ RDPs ($n=4$). TA spectra were collected following photoexcitation at 430 nm with pump fluence of $\sim 200 \mu\text{J}/\text{cm}^2$. (I) The relative contribution from different phases of respective RDPs to the TA signal, as calculated from the amplitudes of the respective GSBs in TA spectra at 1 ps. Recombination dynamics at (J) $\text{GSB}_{n=2}$ of RDPs ($n=2$) and (K) $\text{GSB}_{n=\infty}$ of RDPs ($n=4$). Reproduced from Ref. [68] with permission. Copyright 2024, Wiley-VCH.

To compare the charge carrier dynamics in the respective RDPs, I take the TA kinetics of the representative GSBs (i.e., the $\text{GSB}_{n=2}$ peak for RDPs with lower dimensionality and $\text{GSB}_{n=\infty}$ for RDPs with higher dimensionality) and plot them against delay time (Figure 7.13J,K). I find that the TA decay in the $\text{GSB}_{n=2}$ region of DJ ($n=2$) RDPs is faster than that of RP RDPs, whereas the decay of GSBs (3D-like phase) of RP ($n=4$) RDPs is faster than that of DJ RDPs. The complex charge carrier dynamics between different phases can be only fitted qualitatively, i.e., without a firm physical model (detailed analysis in Table 7.2).

Table 7.1: Relative content of respective phases in RDPs, where the data was extracted from the integration of respective GSBs peaks and normalized.

Sample	Phases	Relative content (%)
RP, $n=2$	$n=1$	4%
	$n=2$	85%
	$n=3$	11%
	$n=4$	0%
	3D-like phase	0%
DJ, $n=2$	$n=1$	8%
	$n=2$	40%
	$n=3$	29%
	$n=4$	21%
	3D-like phase	0%
RP, $n=4$	$n=1$	0%
	$n=2$	58%
	$n=3$	24%
	$n=4$	8%
	3D-like phase	10%
DJ, $n=4$	$n=1$	0%
	$n=2$	35%
	$n=3$	1%
	$n=4$	11%
	3D-like phase	53%

In the case of $\text{GSBs}_{n=2}$ of RDPs ($n=2$), RP RDPs exhibit an average lifetime of 167.6 ps, which is higher than that of DJ RDPs (11.91 ps). The faster decay in DJ might relate to energy transfer from lower- n phases to higher- n phases and the non-radiative recombination, arising from the large population of isotropic lower- n phases [202].

Contrary to $\text{GSBs}_{n=2}$, the average lifetime of $\text{GSBs}_{n=\infty}$ in DJ RDPs ($n=4$) is 893.21 ps, which is two times higher than that of RP RDPs (391.86 ps) and likely related to their larger population of radiative recombination channels.

Table 7.2: Fit results of the decay kinetics in the GSBs region of respective RDPs.

Sample	Amplitude	Decay lifetimes (ps)
RP, n=2	0.287	$\tau_1 = 0.34$
	0.426	$\tau_2 = 39.77$
	0.288	$\tau_3 = 523.10$
DJ, n=2	0.043	$\tau_1 = 0.40$
	0.025	$\tau_2 = 2.14$
	0.932	$\tau_3 = 12.70$
RP, n=4	0.226	$\tau_1 = 0.12$
	0.455	$\tau_2 = 101.45$
	0.319	$\tau_3 = 1094.30$
DJ, n=4	0.314	$\tau_1 = 0.30$
	0.385	$\tau_2 = 468.41$
	0.301	$\tau_3 = 2670.08$

In addition, the GSBs peaks of lower- n phases undergo fast decay accompanied by a rising signal of larger- n phases (Figure 7.14), indicating charge carrier transfer and accumulation in larger- n phases [203, 204, 205].

In addition to examining the structure and charge carrier behaviors of RDPs with different dimensionalities, confocal-PL measurements (Figure 7.15) are utilized to map out the lifetime and film heterogeneity of respective RDPs.

Prior to showing the confocal PL results, the surface morphology and roughness of the respective RDPs are examined to rule out the effects of morphology defects (Figure 7.16). The root-mean-square roughness (RMS) of lower-dimensional RP RDPs (26.9 nm) is lower than that of DJ RDPs (31.9 nm). For RDPs with increasing dimensionality, RP ($n=4$) exhibits an RMS of 12.3 nm compared to DJ RDPs (17.4 nm).

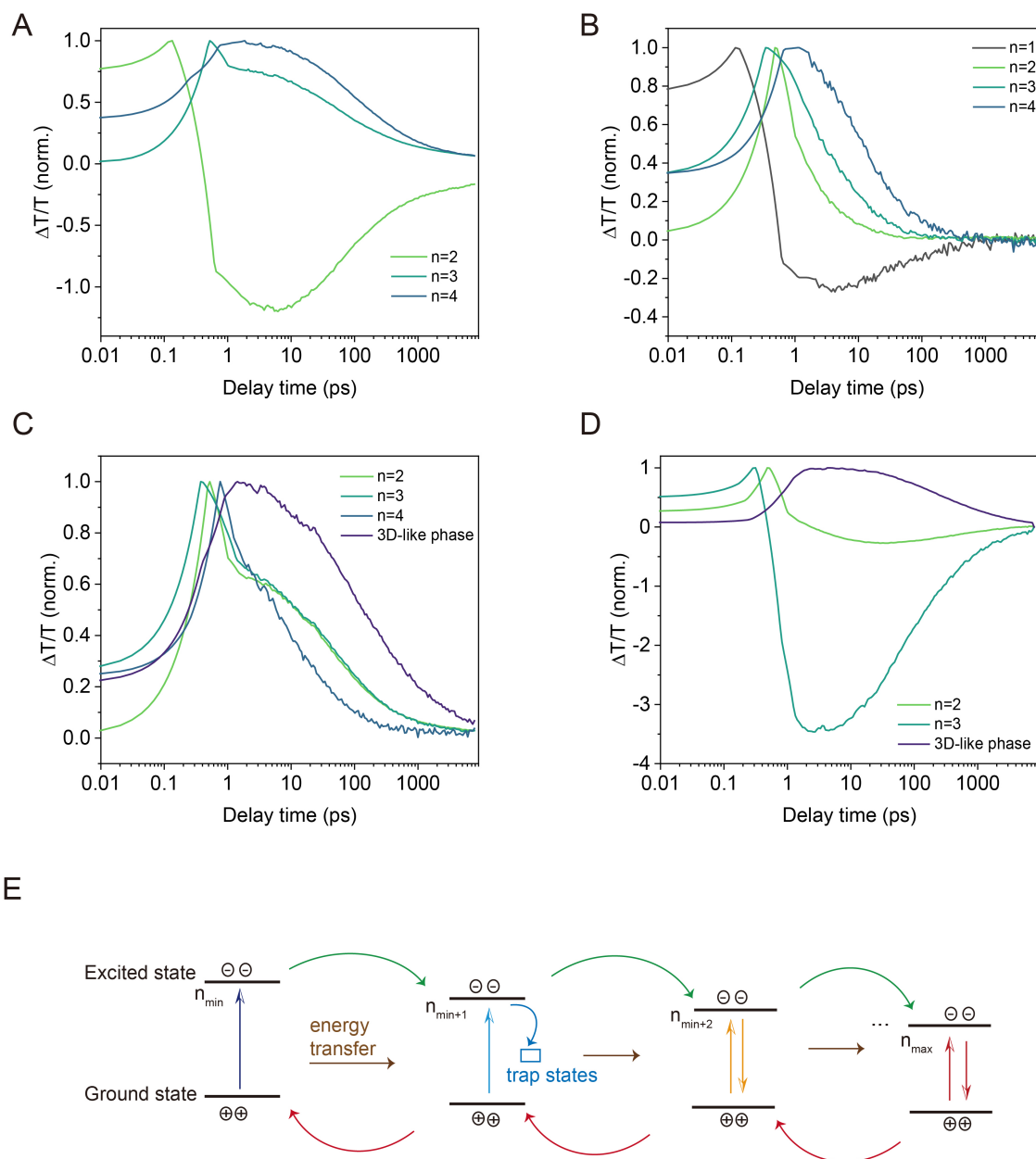


Figure 7.14: TA kinetics extracted from respective phases of (A) RP RDPs ($n=2$), (B) DJ RDPs ($n=2$), (C) RP RDPs ($n=4$), and (D) DJ RDPs ($n=4$), respectively, where the depopulation of lower- n phases and the buildup of higher- n phases indicate the energy funneling in the respective RDPs. (E) Schematic illustration of charge carrier transport in RDPs, showing the electrons transferring from lower- n phases to larger n -phases and the holes transferring from larger n -phases to lower- n phases. This likely results in a spatial charge separation that forms populations of longer-lived charge carriers. Recombination dynamics at (J) $\text{GSB}_{n=2}$ of RDPs ($n=2$) and (K) $\text{GSB}_{n=\infty}$ of RDPs ($n=4$). Reproduced from Ref. [68] with permission. Copyright 2024, Wiley-VCH.

7.4. Charge Carrier Behavior

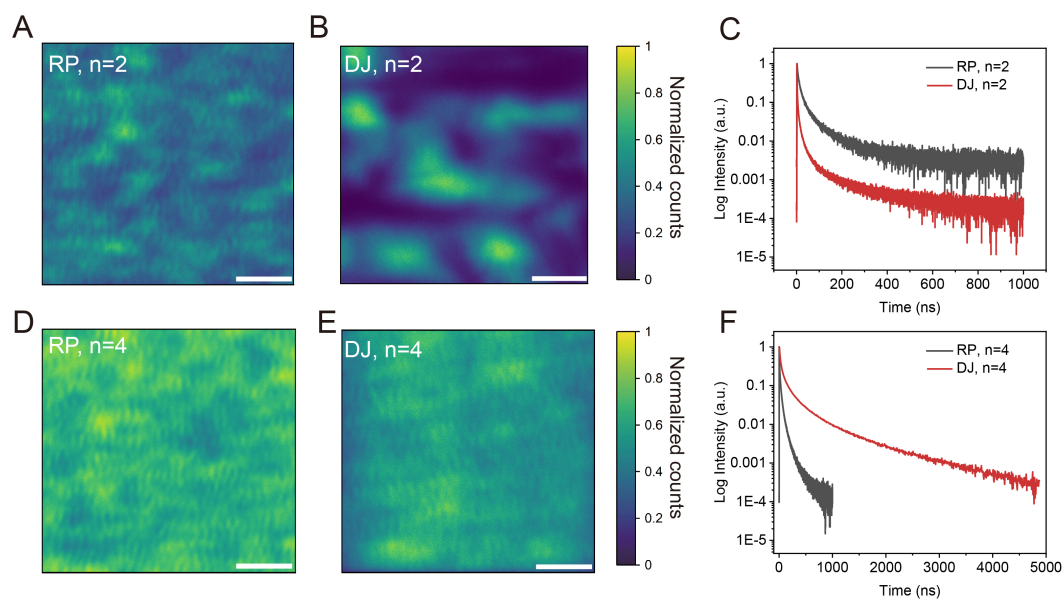


Figure 7.15: Film homogeneity and average radiative lifetime of RDPs. Confocal PL maps of encapsulated perovskite films with a 404 nm excitation (10 MHz; $0.1 \mu\text{J}/\text{cm}^2$ per pulse), with scale bars ($2 \mu\text{m}$). (A) RP RDPs ($n=2$), (B) DJ RDPs ($n=2$), (D) RP RDPs ($n=4$), and (E) DJ RDPs ($n=4$). Statistics of average photoluminescence lifetime of (E) RDPs ($n=2$) and (F) RDPs ($n=4$). Time-resolved PL measurements of (C) RDPs ($n=2$) and (F) RDPs ($n=4$) using a 404 nm excitation. Reproduced from Ref. [68] with permission. Copyright 2024, Wiley-VCH.

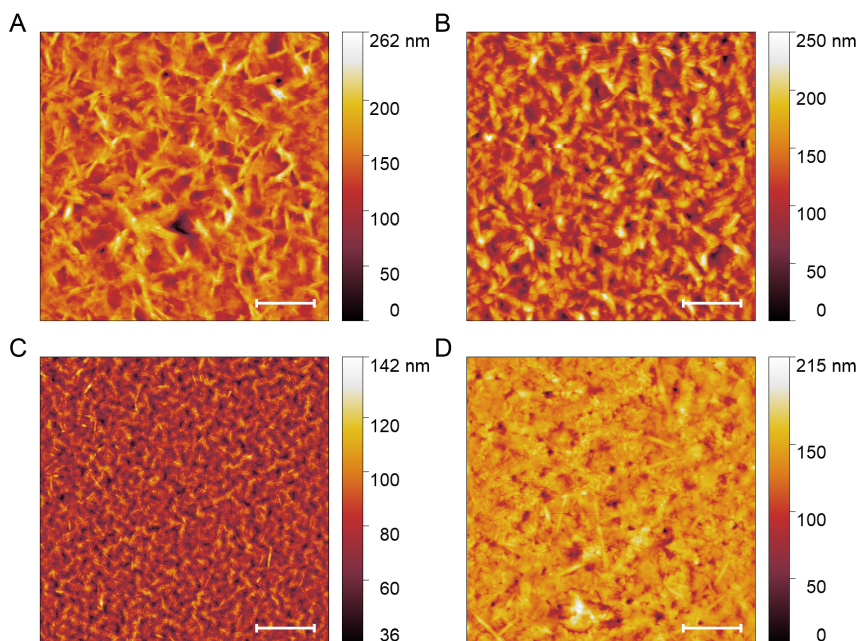


Figure 7.16: AFM images of (A) RP RDP films ($n=2$), (B) DJ RDP film ($n=2$), (C) RP RDP film ($n=4$), and (D) DJ RDP film ($n=4$), where the scale bar is $2 \mu\text{m}$. Reproduced from Ref. [68] with permission. Copyright 2024, Wiley-VCH.

Unlike RDPs ($n=4$), those with lower dimensionality, particularly DJ RDPs, exhibit distinct film heterogeneity (Figure 7.15A and B). The dark regions in Figure 7.15B correspond to reduced average PL lifetime, indicating a higher concentration of defects serving as non-radiative recombination centers over micrometer length scales [206].

In contrast, I observe film homogeneity in RDPs ($n=4$, Figure 7.15D and E). In addition, the average radiative lifetime of respective RDPs is extracted (Figure 7.15C and F), where RP RDPs ($n=2$) exhibit a longer average radiative lifetime (10.6 ns) compared to DJ RDPs (3.0 ns), indicating a decrease in the non-radiative recombination loss of RP RDPs with lower dimensionality.

Interestingly, when increasing the dimensionality, a different trend is observed, that is, DJ RDPs ($n=4$) reveal a longer average radiative lifetime of 37.6 ns, which is four times higher than that of RP RDPs. This indicates that DJ RDPs ($n=4$) exhibit a reduced non-radiative recombination compared with RP RDPs. It should be noted that due to differences in detected spectral ranges, applied excitation fluences, and local diffusion effects [207], direct comparison of charge carrier lifetimes obtained from confocal PL and TA spectra measurements is less feasible.

7.5 Solar Cell Performance and Stability

Collectively, a systematic study of structural and photophysical properties of RDPs with representative dimensionalities ($n=2, 4$) would contribute significantly to the utilization of RDPs in solar cell applications. RP RDPs with lower dimensionality exhibit a dominant $n=2$ phase, vertical orientation, longer charge carrier lifetime, and homogeneity, as confirmed by GIWAXS and TA. These characteristics could potentially make them more suitable as passivation layers in 2D/3D PSCs.

Conversely, DJ RDPs with higher dimensionality demonstrate phase purity, a higher contribution of oriented crystals, spatially vertical phase homogeneity, and longer charge carrier lifetimes, rendering them more suitable for PSCs compared to RP RDPs.

In addition, based on the optoelectronic properties of RP and DJ RDPs with higher dimensionality along with the band structures retrieved from literature [177, 208, 209], an energy level diagram is proposed (Figure 7.17). I observe an energy alignment mismatch between the $n < 3$ phase and hole transport layer (HTL), resulting in inefficient hole extraction. Therefore, reducing the contribution of the lower n phase can facilitate the hole transport in inverted quasi-2D PSCs.

I further use PL to investigate the intrinsic stability of RDPs ($n=4$) under light illumination (Figure 7.18A and B).

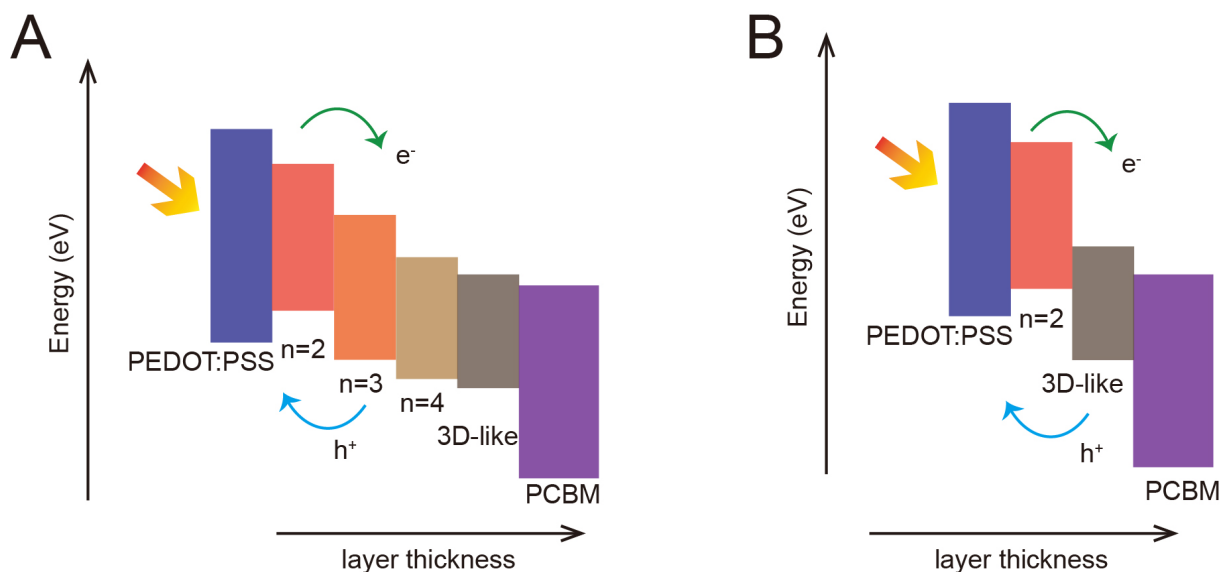


Figure 7.17: Schematic energy band alignment of inverted (A) RP-based PSCs and (B) DJ-based PSCs, showing the energy alignment mismatch of lower- n phases ($n < 3$) and PEDOT:PSS. Reproduced from Ref. [68] with permission. Copyright 2024, Wiley-VCH.

The peak corresponding to the 3D-like phase shows a redshift in both cases along with brightening for the first 30 min, indicative of a decrease in trap density [210]. After illuminating for 60 min, a blueshift in RP RDPs from 752.2 nm to 749.7 nm (Figure 7.18C) and a slight blueshift in DJ RDPs from 771.2 nm to 770.3 nm are observed, suggesting that the population fraction of “intermediate phase” is increasing.

To evaluate the device stability under light illumination, I monitor devices under the protocol of ISOS-L-11 and concurrently track the phase evolution of reduced-dimensional perovskites with operando GIWAXS [6]. The devices are fabricated with an inverted architecture of ITO/PEDOT:PSS/RDPs/PC61BM/BCP/Ag. The detailed fabrication process of inverted perovskite solar cells can be found in Chapter 3.

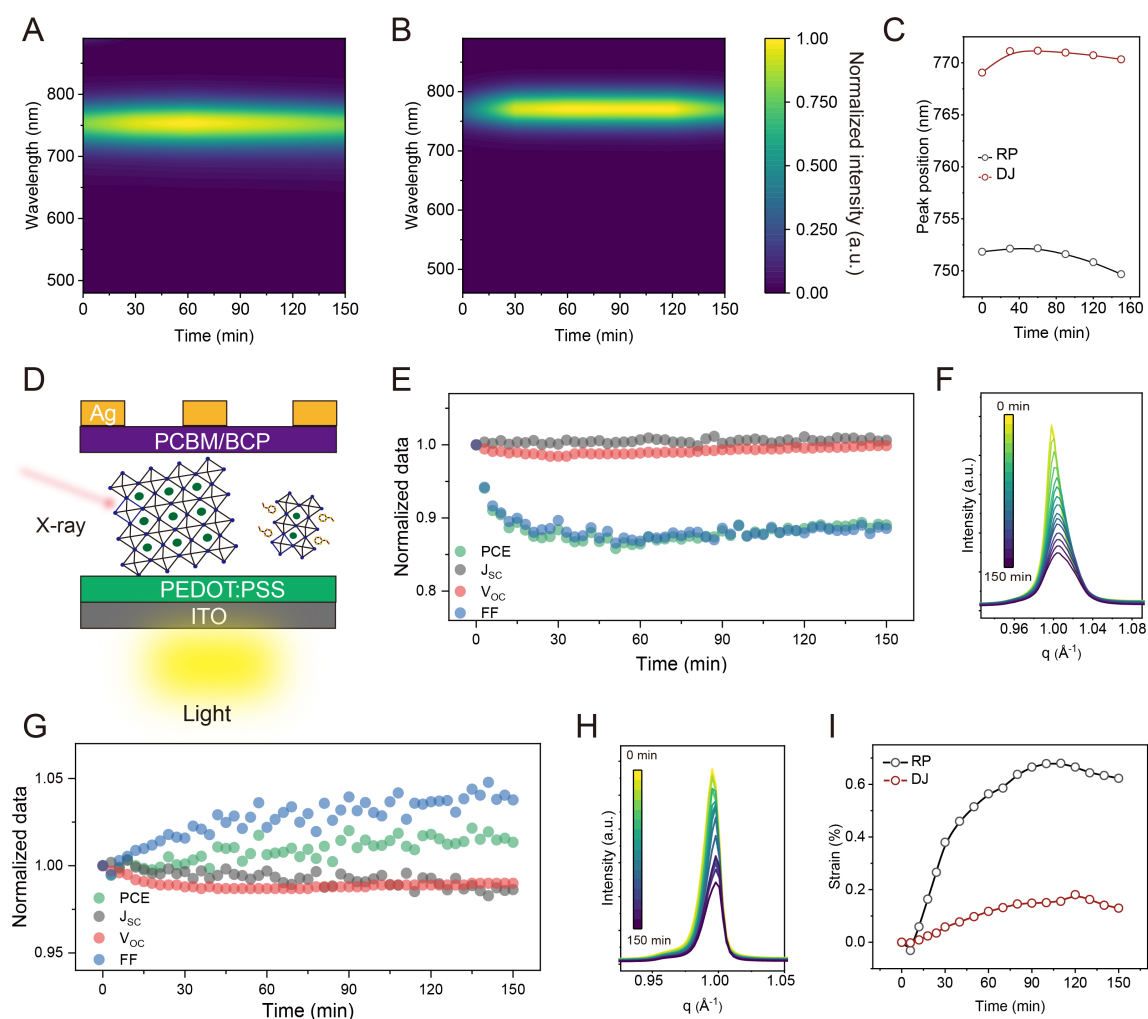


Figure 7.18: Stability of RDPs ($n=4$) films and their device under continuous light illumination. 2D contour plots of normalized photoluminescence as a function of time for (A) RP RDPs, (B) DJ RDPs, and (C) peak positions of the 3D-like phase of RP and DJ RDPs versus time. (D) A schematic illustration of devices operated under AM 1.5 G illumination with concomitant GIWAXS measurement. The solar cell performance as a function of time under 1-sun AM 1.5 G illumination of (E) RP-based PSCs and (G) DJ-based PSCs. (F) Zoom-in pseudo-XRD acquired from 2D GIWAXS data of (F) RP-based device and (H) DJ-based device as a function of time. Notably, the azimuthal cake cuts were cut over the full azimuthal angles, i.e., from 0 to 180°. (I) Evolution of strain derived from (F) and (H). The strain is defined by the q shift relative to the original q value, i.e., calculated by $(q_t - q_0)/q_0$, where t and q_0 represent the time of light illumination and the initial q value, respectively. Reproduced from Ref. [68] with permission. Copyright 2024, Wiley-VCH.

7.5. Solar Cell Performance and Stability

The champion device performance of RP and DJ are shown in Figure 7.19A, in which the champion device of RP exhibits a power conversion efficiency (PCE) of 8.84%, a short-circuit current (J_{SC}) of $13.67 \text{ mA}\cdot\text{cm}^{-2}$, an open-circuit voltage (V_{OC}) of 0.92 V, and a fill factor (FF) of 70.02%.

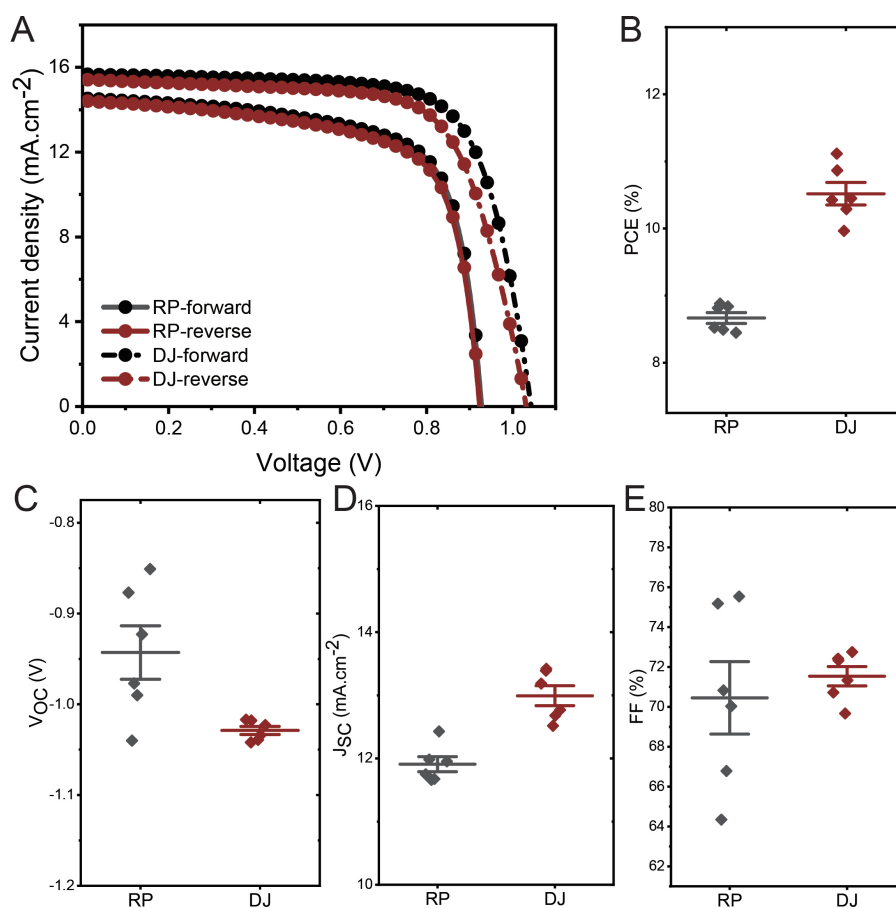


Figure 7.19: Solar cells performance of (A) champion device performance of RP and DJ-based PSCs. Statistics distribution of device performance, collected from the forward scans. (B) PCE, (C) V_{OC} , (D) J_{SC} , and (E) FF . Reproduced from Ref. [68] with permission. Copyright 2024, Wiley-VCH.

The DJ-based device displays a PCE of 11.16%, a J_{SC} of $14.73 \text{ mA}\cdot\text{cm}^{-2}$, a V_{OC} of 1.04 V, and a FF of 72.42%. I notice that DJ-based devices exhibit excellent reproducibility and narrow performance distributions (Figure 7.19B-E) in comparison to RP-based devices. Together with GWIAXS and TA data, three main factors that lead to the variations in device performances are identified, i.e., phase purity, crystal orientation, and energy transfer. On the one hand, the prevalence of lower- n phases in RP RDPs, particularly the isotropic ones, are detrimental to charge transport, resulting in charge recombination and the loss of short-current density [20]. On the other hand, the inhomogeneous energy

landscape caused by the phase impurities leads to inefficient energy transfer from lower- n phases to 3D-like phases. The energy disorder, including band structure, charge transport, and phase distribution disorder, deteriorates the V_{OC} [176, 26]. In addition, I speculate that the non-radiative recombination at the interface of the 3D-like phase and lower- n phase constrains the FF .

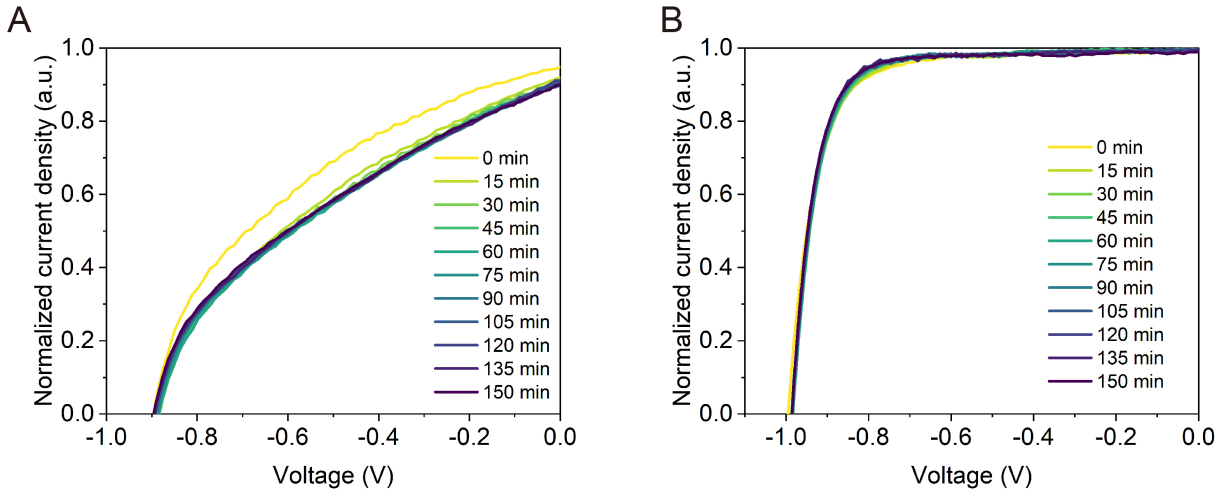


Figure 7.20: The normalized J - V curves as a function of time for (A) RP-based device and (B) DJ-based device under ISOS-L-11 condition. Reproduced from Ref. [68] with permission. Copyright 2024, Wiley-VCH.

The solar cell performance as a function of time is mapped out in Figure 7.20. After 150 min of continuous illumination, the DJ-based device shows negligible degradation, whereas the RP-based device remains at 89% of its initial PCE. Synchrotron-based operando GIWAXS as a function of time is shown in Figure 7.21.

Figure 7.18D and E demonstrate that the $q \sim 1.0 \text{ \AA}^{-1}$ peaks of RP and DJ-based device decrease in intensity and shift to a higher q value, manifesting a lattice compressive strain in all directions. To quantitatively analyze the GIWAXS, the Gaussian profile is used to fit the peak of $q \sim 1.0 \text{ \AA}^{-1}$ (Figure 7.18F). Interestingly, I notice an appreciable increase of strain in the first 40 min in the RP device, followed by a slower increase of strain for the next 60 min. This behavior is in line with the degradation of solar cell performance. Moreover, the strain can also affect the interfaces between different phases in RP, consequently resulting in the degradation of FF . Overall, the RP-based device displays a compressive strain of 0.62% after 150 min of continuous illumination, which is four times higher than that of the DJ-based device (0.13%). In particular, a larger strain along the out-of-plane direction is observed compared to the in-plane direction in the RP-based device (Figure 7.22).

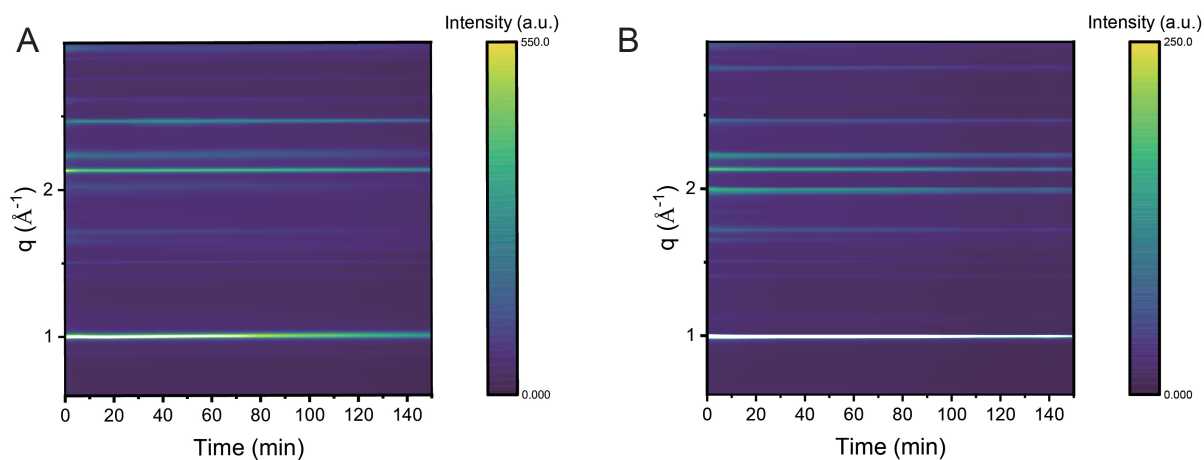


Figure 7.21: Time evolution of operando synchrotron radiation-based GIWAXS data acquired from the azimuthally integrated line profiles of 2D GIWAXS data for the device operated under the protocol of ISOS-L-1I. (A) RP-based device and (B) DJ-based device. Reproduced from Ref. [68] with permission. Copyright 2024, Wiley-VCH.

This strain variation in RP and DJ-based device is correlated with the existence of interfaces induced by phase impurity and their atomic structural rigidity, where the adjacent PbI_6 octahedra of DJ RDPs is directly connected by the long ligand, resulting in a reduced thickness of $\text{I}\cdots\text{I}$ distance (7.18 \AA) [80], a lower structural distortion and thus enhanced structural rigidity [24, 194] compared to RP RDPs ($\sim 8.47 \text{ \AA}$) [211].

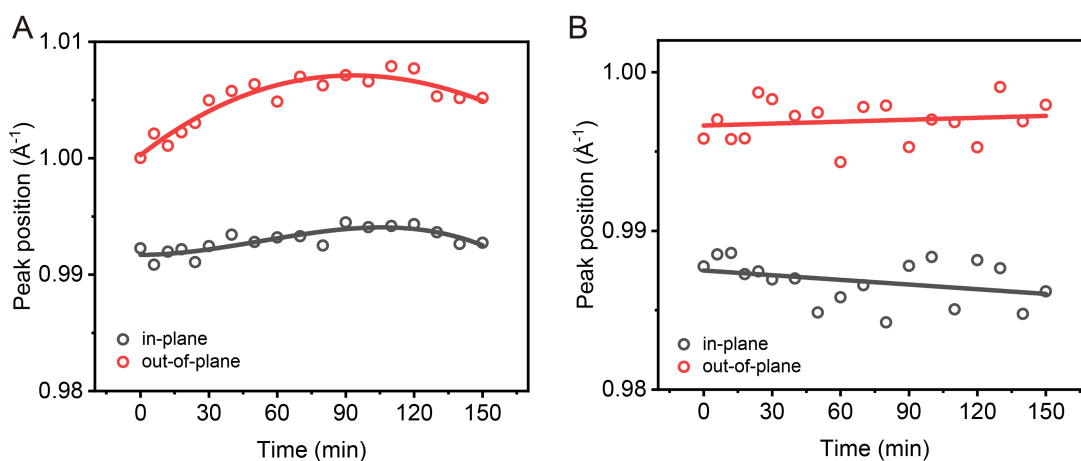


Figure 7.22: Peak positions of $q \sim 1.0 \text{ \AA}^{-1}$ for the device operated under the protocol of ISOS-L-1I, acquired from the in-plane and out-of-plane cuts. (A) The RP-based device, showing the larger out-of-plane compressive strain over the in-plane strain, and (B) DJ-based device. Reproduced from Ref. [68] with permission. Copyright 2024, Wiley-VCH.

7.6 Discussion

In summary, I unravel the structural-photophysical properties of slot-die-coated RP and DJ RDPs with modifying dimensionalities. GIWAXS data confirm that RP RDPs with lower dimensionality exhibit a uniform phase distribution and preferential orientation along the out-of-plane direction, which favors charge transport in solar cells. In addition, they have a longer charge carrier lifetime and better film homogeneity in comparison to DJ, demonstrating the potential to form an ideal 2D/3D heterostructure with desired phase and orientation. In situ GIWAXS discloses the growth kinetics of respective RDPs, showing that the formation of lower- n phases is governed by stoichiometry and the formation energy. Thus, the formation of lower- n phases in RP RDPs is more favorable than DJ RDPs. This highlights the potential of DJ RDPs in narrowing the phase distribution and, thereafter, a homogenous energy landscape. When the dimensionality increases, DJ RDPs demonstrate highly concentrated phase distributions, pronounced orientation, spatially vertical phase homogeneity, and longer charge carrier lifetime, which enhances their device performance and stability under light illumination. Despite solvents and the film deposition method affecting the kinetics and leading to variations in structural properties, this work demonstrates that a rational design of the device architecture—by combining RP RDPs with lower dimensionality as the interface passivation layer and DJ RDPs as the active layer—can alleviate phase impurities and crystal random orientation, potentially achieving highly efficient and large-scale reduced-dimensional PSCs.

Summary and Outlook

Over the past decades, the power conversion efficiency of perovskite solar cells has strongly increased. However, as illustrated in Chapter 1, the obstacles hindering their commercialization remain unsolved. In this regard, in this thesis, I attempt to address these challenges by: optimizing the charge transfer in the buried interface of inverted perovskite solar cells to improve the power conversion efficiency; investigating the operational stability of perovskite solar cells under light and humidity; and fabricating large-area reduced-dimensional perovskite solar cells while concurrently enhance their photostability. To realize these investigations, advanced X-ray scattering methods are utilized. In particular, the excellent brilliance at synchrotron facilities enables the study of perovskite solar cells with high spatial and temporal resolution, allowing for the research of thin film formation kinetics and degradation mechanisms.

The first project demonstrates that the buried interface in inverted perovskite solar cells is overlooked in this field. By adding iodine-substitute phenyl acids, fewer defects can be achieved in NiO_x film. This way, the higher open-circuit voltage V_{OC} can be realized. In addition, the acid groups are also found to be coordinated with Ni vacancies, thereby reducing the probability of charge carrier recombination, which in turn enhances the hole transport ability. In addition, the influence of iodophenyl functional groups on the device performance is studied in terms of iodine locations at the benzene rings. The 4-IPBA modified NiO_x film has a better energy level alignment with perovskite, and due to the stronger halogen bonding between 4-IPBA and perovskite, perovskite film exhibits reduced trap densities. As a result, the power conversion efficiency and long-term stability are largely enhanced.

The second project focuses on the degradation mechanism of perovskite solar cells with a normal configuration under AM 1.5 G illumination and $75 \pm 5\%$ relative humidity. Importantly, a morphological perspective of perovskite solar cells during operation under external stressors is still missing. To address this, grazing-incidence small-angle X-ray

scattering (GISAXS) is used to monitor the morphological evolution. In addition, the effects of bulk modification and the buried interface engineering, particularly with cesium iodide (CsI), on perovskite device performance are examined during the operation test. Throughout the solar cell performance evolution, the fill factor FF and the short-circuit current (J_{SC}) are found to decrease most compared to other solar cell parameters. By correlating these findings with GISAXS, the driving force for PSCs degradation is identified as volume expansion, induced by the incorporation of water molecules. Nevertheless, PSCs with CsI buried interface engineering degrade faster compared to the PSCs with bulk modification, which is ascribed to grain fragmentation and increased grain boundaries. This work highlights the importance of understanding the microscopy morphology during the device operation, a factor often overlooked owing to the lack of proper techniques. More importantly, the addition of CsI in the perovskite active layer can improve their device stability under light and humidity conditions.

The third project investigates the reduced-dimensional perovskites, which have been widely used in highly efficient perovskite solar cells and light-emitting diodes owing to their tunable structure, phase distribution, and energy landscape. Nevertheless, a systematic study that combines dimensionality, structure, growth mechanism, charge carrier behavior, and photostability is still missing. Hence, in this project, I study the aforementioned properties of reduced-dimensional perovskite by grazing-incidence wide-angle X-ray scattering (GIWAXS) and transient absorption spectroscopy. Angular-dependent GIWAXS measurements reveal the structure and the phase distribution of reduced-dimensional perovskite with different dimensionality. In particular, the low-dimensional Ruddlesden-Popper perovskites have demonstrated better phase purity, preferential out-of-plane direction, and longer charge carrier lifetime compared to their Dion-Jacobson perovskite counterparts. In stark contrast, as the dimensionality increases, Dion-Jacobson perovskites demonstrate better phase purity, preferential orientation, and longer charge carrier lifetime. Moreover, the growth kinetics of reduced-dimensional perovskite during slot-die coating are disclosed, which illustrates that the formation of low-dimensional perovskite in Ruddlesden-Popper perovskite is thermodynamically and stoichiometrically favored. Leveraging this knowledge, this work paves the way for utilizing reduced-dimensional perovskite to upscale perovskite solar cells.

In summary, this thesis addresses selected key challenges within the perovskite solar cell field. However, much work remains to be done before perovskite solar cells (PSCs) can be fully commercialized and used in real-world applications. In terms of operational stability, particular attention should be paid to the stability of PSCs under light and heat conditions, as these issues originate from their intrinsic properties and are not easily resolved. However, the stability of PSCs under humidity can theoretically be mitigated

by encapsulation. When addressing the issue of device stability, it is also important to consider the potential instability of other charge transport layers, e.g., Spiro-OMeTAD in n-i-p PSCs and self-assembled monolayers (SAMs) in inverted PSCs, which could be limiting factors in device performance. Therefore, enhancing stability may involve developing suitable encapsulation techniques and new passivation layers, as most degradation sites originate from defects. For commercialization, it is crucial to explore alternative large-scale deposition methods, such as slot-die coating and physical vapor deposition, since these methods require a different understanding of perovskite growth and solvent systems. Thermal evaporation is another large-scale deposition method that could be integrated into industrial pilot lines and warrants more attention.

Tandem perovskite solar cells, which combine mature solar technologies like silicon solar cells with perovskites, show great promise as game-changers. They have the potential to overcome efficiency barriers and significantly boost power conversion efficiency. Recently, Oxford PV has begun commercializing perovskite/silicon tandem solar panels, shipping the first batch to customers with efficiencies above 20%, demonstrating the superior stability and performance of these solar panels. However, as with single-junction PSCs, the efficiency of large-scale tandem perovskite solar cells still lags behind, which underscores the need for a better understanding of large-scale deposition methods. Additionally, stability issues persist in tandem devices. The understanding of perovskite tandem solar cells, particularly in terms of improving efficiency and stability and achieving commercialization, needs to be further developed.

Bibliography

- [1] Hao Chen, Cheng Liu, Jian Xu, Aidan Maxwell, Wei Zhou, Yi Yang, Qilin Zhou, Abdulaziz SR Bati, Haoyue Wan, Zaiwei Wang, et al. „Improved charge extraction in inverted perovskite solar cells with dual-site-binding ligands“. In: *Science* 384.6692 (2024), 189–193.
- [2] Guanhua Ren, Wenbin Han, Yanyu Deng, Wei Wu, Zhuowei Li, Jiaxin Guo, Hongchang Bao, Chunyu Liu, and Wenbin Guo. „Strategies of modifying spiro-OMeTAD materials for perovskite solar cells: a review“. In: *Journal of Materials Chemistry A* 9.8 (2021), 4589–4625.
- [3] Amran Al-Ashouri, Eike Köhnen, Bor Li, Artiom Magomedov, Hannes Hempel, Pietro Caprioglio, José A Márquez, Anna Belen Morales Vilches, Ernestas Kasparavicius, Joel A Smith, et al. „Monolithic perovskite/silicon tandem solar cell with 29% efficiency by enhanced hole extraction“. In: *Science* 370.6522 (2020), 1300–1309.
- [4] Qi Jiang and Kai Zhu. „Rapid advances enabling high-performance inverted perovskite solar cells“. In: *Nature Reviews Materials* (2024), 1–21.
- [5] Xiaopu Wang, Xinyi Tian, Xiaodong Chen, Lingling Ren, and Chunxiang Geng. „A review of end-of-life crystalline silicon solar photovoltaic panel recycling technology“. In: *Solar Energy Materials and Solar Cells* 248 (2022), 111976.
- [6] Mark V Khenkin, Eugene A Katz, Antonio Abate, Giorgio Bardizza, Joseph J Berry, Christoph Brabec, Francesca Brunetti, Vladimir Bulović, Quinn Burlingame, Aldo Di Carlo, et al. „Consensus statement for stability assessment and reporting for perovskite photovoltaics based on ISOS procedures“. In: *Nature Energy* 5.1 (2020), 35–49.
- [7] Yehao Deng, Charles H Van Brackle, Xuezheng Dai, Jingjing Zhao, Bo Chen, and Jinsong Huang. „Tailoring solvent coordination for high-speed, room-temperature blading of perovskite photovoltaic films“. In: *Science advances* 5.12 (2019), eaax7537.

-
- [8] Zhen Li, Mengjin Yang, Ji-Sang Park, Su-Huai Wei, Joseph J Berry, and Kai Zhu. „Stabilizing perovskite structures by tuning tolerance factor: formation of formamidinium and cesium lead iodide solid-state alloys“. In: *Chemistry of Materials* 28.1 (2016), 284–292.
- [9] Lata Chouhan, Sushant Ghimire, Challapalli Subrahmanyam, Tsutomu Miyasaka, and Vasudevanpillai Biju. „Synthesis, optoelectronic properties and applications of halide perovskites“. In: *Chemical Society Reviews* 49.10 (2020), 2869–2885.
- [10] Deying Luo, Rui Su, Wei Zhang, Qihuang Gong, and Rui Zhu. „Minimizing non-radiative recombination losses in perovskite solar cells“. In: *Nature Reviews Materials* 5.1 (2020), 44–60.
- [11] Hao Gu, Junmin Xia, Chao Liang, Yonghua Chen, Wei Huang, and Guichuan Xing. „Phase-pure two-dimensional layered perovskite thin films“. In: *Nature Reviews Materials* (2023), 1–19.
- [12] Giulia Grancini and Mohammad Khaja Nazeeruddin. „Dimensional tailoring of hybrid perovskites for photovoltaics“. In: *Nature Reviews Materials* 4.1 (2019), 4–22.
- [13] Sajjad Ahmad, Ping Fu, Shuwen Yu, Qing Yang, Xuan Liu, Xuchao Wang, Xiuli Wang, Xin Guo, and Can Li. „Dion-Jacobson phase 2D layered perovskites for solar cells with ultrahigh stability“. In: *Joule* 3.3 (2019), 794–806.
- [14] Fei Zhang, Haipeng Lu, Jinhui Tong, Joseph J Berry, Matthew C Beard, and Kai Zhu. „Advances in two-dimensional organic–inorganic hybrid perovskites“. In: *Energy & Environmental Science* 13.4 (2020), 1154–1186.
- [15] Duyen H Cao, Constantinos C Stoumpos, Omar K Farha, Joseph T Hupp, and Mercouri G Kanatzidis. „2D homologous perovskites as light-absorbing materials for solar cell applications“. In: *Journal of the American Chemical Society* 137.24 (2015), 7843–7850.
- [16] Constantinos C Stoumpos, Duyen H Cao, Daniel J Clark, Joshua Young, James M Rondinelli, Joon I Jang, Joseph T Hupp, and Mercouri G Kanatzidis. „Ruddlesden–Popper hybrid lead iodide perovskite 2D homologous semiconductors“. In: *Chemistry of Materials* 28.8 (2016), 2852–2867.
- [17] X Hong, T Ishihara, and AV Nurmikko. „Dielectric confinement effect on excitons in PbI₄-based layered semiconductors“. In: *Physical Review B* 45.12 (1992), 6961.

- [18] Jasmina A Sichert, Yu Tong, Niklas Mutz, Mathias Vollmer, Stefan Fischer, Karolina Z Milowska, Ramon Garcia Cortadella, Bert Nickel, Carlos Cardenas-Daw, Jacek K Stolarczyk, et al. „Quantum size effect in organometal halide perovskite nanoplatelets“. In: *Nano letters* 15.10 (2015), 6521–6527.
- [19] J-C Blancon, Hsinhan Tsai, Wanyi Nie, Costas C Stoumpos, Laurent Pedesseau, Claudine Katan, Mikaël Kepenekian, Chan Myae Myae Soe, Kannatassen Appavoo, Matthew Y Sfeir, et al. „Extremely efficient internal exciton dissociation through edge states in layered 2D perovskites“. In: *Science* 355.6331 (2017), 1288–1292.
- [20] Yun Lin, Yanjun Fang, Jingjing Zhao, Yuchuan Shao, Samuel J Stuard, Masrur Morshed Nahid, Harald Ade, Qi Wang, Jeffrey E Shield, Ninghao Zhou, et al. „Unveiling the operation mechanism of layered perovskite solar cells“. In: *Nature communications* 10.1 (2019), 1008.
- [21] Junxue Liu, Jing Leng, Kaifeng Wu, Jun Zhang, and Shengye Jin. „Observation of internal photoinduced electron and hole separation in hybrid two-dimensional perovskite films“. In: *Journal of the American Chemical Society* 139.4 (2017), 1432–1435.
- [22] Ping Chen, Yan Meng, Mahshid Ahmadi, Qiming Peng, Chunhong Gao, Long Xu, Ming Shao, Zuhong Xiong, and Bin Hu. „Charge-transfer versus energy-transfer in quasi-2D perovskite light-emitting diodes“. In: *Nano energy* 50 (2018), 615–622.
- [23] Mingjian Yuan, Li Na Quan, Riccardo Comin, Grant Walters, Randy Sabatini, Oleksandr Voznyy, Sjoerd Hoogland, Yongbiao Zhao, Eric M Beauregard, Pongsakorn Kanjanaboos, et al. „Perovskite energy funnels for efficient light-emitting diodes“. In: *Nature nanotechnology* 11.10 (2016), 872–877.
- [24] Wenbin Li, Siraj Sidhik, Boubacar Traore, Reza Asadpour, Jin Hou, Hao Zhang, Austin Fehr, Joseph Essman, Yafei Wang, Justin M Hoffman, et al. „Light-activated interlayer contraction in two-dimensional perovskites for high-efficiency solar cells“. In: *Nature nanotechnology* 17.1 (2022), 45–52.
- [25] Qiuyu Shang, Yunuan Wang, Yangguang Zhong, Yang Mi, Liang Qin, Yuefeng Zhao, Xiaohui Qiu, Xinfeng Liu, and Qing Zhang. „Unveiling structurally engineered carrier dynamics in hybrid quasi-two-dimensional perovskite thin films toward controllable emission“. In: *The Journal of Physical Chemistry Letters* 8.18 (2017), 4431–4438.
- [26] Chunqing Ma, Dong Shen, Tsz-Wai Ng, Ming-Fai Lo, and Chun-Sing Lee. „2D perovskites with short interlayer distance for high-performance solar cell application“. In: *Advanced Materials* 30.22 (2018), 1800710.

- [27] Félix Thouin, David A Valverde-Chávez, Claudio Quarti, Daniele Cortecchia, Ilaria Bargigia, David Beljonne, Annamaria Petrozza, Carlos Silva, and Ajay Ram Srimath Kandada. „Phonon coherences reveal the polaronic character of excitons in two-dimensional lead halide perovskites“. In: *Nature materials* 18.4 (2019), 349–356.
- [28] Matthew D Smith, Adam Jaffe, Emma R Dohner, Aaron M Lindenberg, and Hemamala I Karunadasa. „Structural origins of broadband emission from layered Pb–Br hybrid perovskites“. In: *Chemical science* 8.6 (2017), 4497–4504.
- [29] Mikaël Kepenekian, Boubacar Traore, Jean-Christophe Blancon, Laurent Pedesseau, Hsinhan Tsai, Wanyi Nie, Constantinos C Stoumpos, Mercouri G Kanatzidis, Jacky Even, Aditya D Mohite, et al. „Concept of lattice mismatch and emergence of surface states in two-dimensional hybrid perovskite quantum wells“. In: *Nano letters* 18.9 (2018), 5603–5609.
- [30] Géraud Delport, Gabriel Chehade, Ferdinand Lédée, Hiba Diab, Cosme Milesi-Brault, Gaëlle Trippé-Allard, Jacky Even, Jean-Sébastien Lauret, Emmanuelle Deleporte, and Damien Garrot. „Exciton–exciton annihilation in two-dimensional halide perovskites at room temperature“. In: *The journal of physical chemistry letters* 10.17 (2019), 5153–5159.
- [31] Jean-Christophe Blancon, Jacky Even, Costas C Stoumpos, Mercouri G Kanatzidis, and Aditya D Mohite. „Semiconductor physics of organic–inorganic 2D halide perovskites“. In: *Nature nanotechnology* 15.12 (2020), 969–985.
- [32] FL Binsbergen. „Natural and artificial heterogeneous nucleation in polymer crystallization“. In: *Journal of Polymer Science: Polymer Symposia*. Vol. 59. 1. Wiley Online Library. 1977, 11–29.
- [33] Chang Liu, Yi-Bing Cheng, and Ziyi Ge. „Understanding of perovskite crystal growth and film formation in scalable deposition processes“. In: *Chemical Society Reviews* 49.6 (2020), 1653–1687.
- [34] Wiley A Dunlap-Shohl, Yuanyuan Zhou, Nitin P Padture, and David B Mitzi. „Synthetic approaches for halide perovskite thin films“. In: *Chemical reviews* 119.5 (2018), 3193–3295.
- [35] Justin M Hoffman, Joseph Strzalka, Nathan C Flanders, Ido Hadar, Shelby A Cuthriell, Qingteng Zhang, Richard D Schaller, William R Dichtel, Lin X Chen, and Mercouri G Kanatzidis. „In situ grazing-incidence wide-angle scattering reveals mechanisms for phase distribution and disorientation in 2D halide perovskite films“. In: *Advanced Materials* 32.33 (2020), 2002812.

- [36] Amita Ummadisingu and Michael Grätzel. „Revealing the detailed path of sequential deposition for metal halide perovskite formation“. In: *Science advances* 4.2 (2018), e1701402.
- [37] Feng Gao, Yang Zhao, Xingwang Zhang, and Jingbi You. „Recent progresses on defect passivation toward efficient perovskite solar cells“. In: *Advanced Energy Materials* 10.13 (2020), 1902650.
- [38] William Shockley and Hans Queisser. „Detailed balance limit of efficiency of p–n junction solar cells“. In: *Renewable Energy*. Routledge, 2018, Vol2_35–Vol2_54.
- [39] Jean-Francois Guillemoles, Thomas Kirchartz, David Cahen, and Uwe Rau. „Guide for the perplexed to the Shockley–Queisser model for solar cells“. In: *Nature photonics* 13.8 (2019), 501–505.
- [40] Hongwei Zhu, Sam Teale, Muhammad Naufal Lintangpradipto, Suhas Mahesh, Bin Chen, Michael D McGehee, Edward H Sargent, and Osman M Bakr. „Long-term operating stability in perovskite photovoltaics“. In: *Nature Reviews Materials* 8.9 (2023), 569–586.
- [41] Kun Sun and Peter Müller-Buschbaum. „Shedding light on the moisture stability of halide perovskite thin films“. In: *Energy Technology* 11.4 (2023), 2201475.
- [42] Caleb C Boyd, Rongrong Cheacharoen, Tomas Leijtens, and Michael D McGehee. „Understanding degradation mechanisms and improving stability of perovskite photovoltaics“. In: *Chemical reviews* 119.5 (2018), 3418–3451.
- [43] Renjun Guo, Qiu Xiong, Aleksander Ulatowski, Saisai Li, Zijin Ding, Tianxiao Xiao, Suzhe Liang, Julian E Heger, Tianfu Guan, Xinyu Jiang, et al. „Trace water in lead iodide affecting perovskite crystal nucleation limits the performance of perovskite solar cells“. In: *Advanced Materials* (2024), 2310237.
- [44] Jianbing Huang, Shunquan Tan, Peter D Lund, and Huanping Zhou. „Impact of H₂O on organic–inorganic hybrid perovskite solar cells“. In: *Energy & Environmental Science* 10.11 (2017), 2284–2311.
- [45] Qi Wang, Bo Chen, Ye Liu, Yehao Deng, Yang Bai, Qingfeng Dong, and Jinsong Huang. „Scaling behavior of moisture-induced grain degradation in polycrystalline hybrid perovskite thin films“. In: *Energy & Environmental Science* 10.2 (2017), 516–522.
- [46] Nian Li, Shambhavi Pratap, Volker Körstgens, Sundeep Vema, Lin Song, Suzhe Liang, Anton Davydok, Christina Krywka, and Peter Müller-Buschbaum. „Mapping structure heterogeneities and visualizing moisture degradation of perovskite films with nano-focus WAXS“. In: *Nature Communications* 13.1 (2022), 6701.

- [47] Johannes Schlipf, Lorenz Bießmann, Lukas Oesinghaus, Edith Berger, Ezzeldin Metwalli, Johannes A Lercher, Lionel Porcar, and Peter Müller-Buschbaum. „In situ monitoring the uptake of moisture into hybrid perovskite thin films“. In: *The journal of physical chemistry letters* 9.8 (2018), 2015–2021.
- [48] Kun Sun, Renjun Guo, Yuxin Liang, Julian E Heger, Shangpu Liu, Shanshan Yin, Manuel A Reus, Lukas V Spanier, Felix Deschler, Sigrid Bernstorff, et al. „Morphological Insights into the Degradation of Perovskite Solar Cells under Light and Humidity“. In: *ACS Applied Materials & Interfaces* (2023).
- [49] Kyle M Fransishyn, Soumya Kundu, and Timothy L Kelly. „Elucidating the failure mechanisms of perovskite solar cells in humid environments using in situ grazing-incidence wide-angle X-ray scattering“. In: *ACS Energy Letters* 3.9 (2018), 2127–2133.
- [50] Laura T Schelhas, Zhen Li, Jeffrey A Christians, Anuj Goyal, Paul Kairys, Steven P Harvey, Dong Hoe Kim, Kevin H Stone, Joseph M Luther, Kai Zhu, et al. „Insights into operational stability and processing of halide perovskite active layers“. In: *Energy & Environmental Science* 12.4 (2019), 1341–1348.
- [51] Johannes Schlipf, Yinghong Hu, Shambhavi Pratap, Lorenz Bießmann, Nuri Hohn, Lionel Porcar, Thomas Bein, Pablo Docampo, and Peter Müller-Buschbaum. „Shedding light on the moisture stability of 3D/2D hybrid perovskite heterojunction thin films“. In: *ACS Applied Energy Materials* 2.2 (2019), 1011–1018.
- [52] Soumya Kundu and Timothy L Kelly. „In situ studies of the degradation mechanisms of perovskite solar cells“. In: *EcoMat* 2.2 (2020), e12025.
- [53] Nam-Koo Kim, Young Hwan Min, Seokhwan Noh, Eunkyung Cho, Gitaeg Jeong, Minho Joo, Seh-Won Ahn, Jeong Soo Lee, Seongtak Kim, Kyuwook Ihm, et al. „Investigation of thermally induced degradation in CH₃NH₃PbI₃ perovskite solar cells using in-situ synchrotron radiation analysis“. In: *Scientific reports* 7.1 (2017), 4645.
- [54] Tae Woong Kim, Naoyuki Shibayama, Ludmila Cojocar, Satoshi Uchida, Takashi Kondo, and Hiroshi Segawa. „Real-time in situ observation of microstructural change in organometal halide perovskite induced by thermal degradation“. In: *Advanced Functional Materials* 28.42 (2018), 1804039.
- [55] Jiangwei Li, Qingshun Dong, Nan Li, and Liduo Wang. „Direct evidence of ion diffusion for the silver-electrode-induced thermal degradation of inverted perovskite solar cells“. In: *Advanced Energy Materials* 7.14 (2017), 1602922.

- [56] Giorgio Divitini, Stefania Cacovich, Fabio Matteocci, Lucio Cinà, A Di Carlo, and Caterina Ducati. „In situ observation of heat-induced degradation of perovskite solar cells“. In: *Nature Energy* 1.2 (2016), 1–6.
- [57] Guixiang Li, Zhenhuang Su, Laura Canil, Declan Hughes, Mahmoud H Aldamasy, Janardan Dagar, Sergei Trofimov, Luyao Wang, Weiwei Zuo, José J Jerónimo-Rendon, et al. „Highly efficient pin perovskite solar cells that endure temperature variations“. In: *Science* 379.6630 (2023), 399–403.
- [58] Metin Tolan and M Tolan. *X-ray scattering from soft-matter thin films: materials science and basic research*. Vol. 148. Springer, 1999.
- [59] Yoshio Waseda, Eiichiro Matsubara, and Kozo Shinoda. *X-ray diffraction crystallography: introduction, examples and solved problems*. Springer Science & Business Media, 2011.
- [60] Paul Scherrer. „Bestimmung der Grosse und inneren Struktur von Kolloidteilchen mittels Röntgenstrahlen“. In: *Nach Ges Wiss Göttingen* 2 (1918), 8–100.
- [61] A Khorsand Zak, WH Abd Majid, M Ebrahimizadeh Abrishami, and Ramin Yousefi. „X-ray analysis of ZnO nanoparticles by Williamson–Hall and size–strain plot methods“. In: *Solid State Sciences* 13.1 (2011), 251–256.
- [62] Peter Müller-Buschbaum. „The active layer morphology of organic solar cells probed with grazing incidence scattering techniques“. In: *Advanced materials* 26.46 (2014), 7692–7709.
- [63] Y Yoneda. „Anomalous surface reflection of X rays“. In: *Physical review* 131.5 (1963), 2010.
- [64] Julian A Steele, Eduardo Solano, David Hardy, Damara Dayton, Dylan Ladd, Keith White, Peng Chen, Jingwei Hou, Haowei Huang, Rafikul Ali Saha, et al. „How to GIWAXS: Grazing Incidence Wide Angle X-Ray Scattering Applied to Metal Halide Perovskite Thin Films“. In: *Advanced Energy Materials* 13.27 (2023), 2300760.
- [65] Manuel A Reus, Lennart K Reb, Alexander F Weinzierl, Christian L Weindl, Renjun Guo, Tianxiao Xiao, Matthias Schwartzkopf, Andrei Chumakov, Stephan V Roth, and Peter Müller-Buschbaum. „Time-Resolved Orientation and Phase Analysis of Lead Halide Perovskite Film Annealing Probed by In Situ GIWAXS“. In: *Advanced Optical Materials* 10.14 (2022), 2102722.

- [66] Manuel A Reus, Lennart K Reb, David P Kosbahn, Stephan V Roth, and Peter Müller-Buschbaum. „INSIGHT: in situ heuristic tool for the efficient reduction of grazing-incidence X-ray scattering data“. In: *Journal of Applied Crystallography* 57.2 (2024).
- [67] Xinxin Kang, Dourong Wang, Kun Sun, Xue Dong, Wei Hui, Baohua Wang, Lei Gu, Maoxin Li, Yaqi Bao, Jie Zhang, et al. „Unraveling the modification effect at NiO x/perovskite interfaces for efficient and stable inverted perovskite solar cells“. In: *Journal of Materials Chemistry A* 11.42 (2023), 22982–22991.
- [68] Kun Sun, Renjun Guo, Shangpu Liu, Dengyang Guo, Xiongzhao Jiang, Linus Huber, Yuxin Liang, Manuel Reus, Zerui Li, Tianfu Guan, et al. „Deciphering Structure and Charge Carrier Behavior in Reduced-Dimensional Perovskites“. In: (2024).
- [69] Manuel A Reus, Thomas Baier, Christoph G Lindenmeir, Alexander F Weinzierl, Altantulga Buyan-Arivjikh, Simon A Wegener, David P Kosbahn, Lennart K Reb, Jan Rubeck, Matthias Schwartzkopf, et al. „Modular slot-die coater for in situ grazing-incidence x-ray scattering experiments on thin films“. In: *Review of Scientific Instruments* 95.4 (2024).
- [70] Nadesh Fiuza-Maneiro, Kun Sun, Iago López-Fernández, Sergio Gómez-Graña, Peter Müller-Buschbaum, and Lakshminarayana Polavarapu. „Ligand chemistry of inorganic lead halide perovskite nanocrystals“. In: *ACS Energy Letters* 8.2 (2023), 1152–1191.
- [71] Thomas Kirchartz, José A Márquez, Martin Stolterfoht, and Thomas Unold. „Photoluminescence-based characterization of halide perovskites for photovoltaics“. In: *Advanced energy materials* 10.26 (2020), 1904134.
- [72] Changsoon Cho, Sascha Feldmann, Kyung Mun Yeom, Yeoun-Woo Jang, Simon Kahmann, Jun-Yu Huang, Terry Chien-Jen Yang, Mohammed Nabaz Taher Khayyat, Yuh-Renn Wu, Mansoo Choi, et al. „Efficient vertical charge transport in polycrystalline halide perovskites revealed by four-dimensional tracking of charge carriers“. In: *Nature Materials* 21.12 (2022), 1388–1395.
- [73] Jan Tauc. „Optical properties and electronic structure of amorphous Ge and Si“. In: *Materials research bulletin* 3.1 (1968), 37–46.
- [74] Franz Urbach. „The long-wavelength edge of photographic sensitivity and of the electronic absorption of solids“. In: *Physical review* 92.5 (1953), 1324.

- [75] Tze Chien Sum, Nripan Mathews, Guichuan Xing, Swee Sien Lim, Wee Kiang Chong, David Giovanni, and Herlina Arianita Dewi. „Spectral features and charge dynamics of lead halide perovskites: origins and interpretations“. In: *Accounts of chemical research* 49.2 (2016), 294–302.
- [76] Li Na Quan, Yongbiao Zhao, F Pelayo Garcia de Arquer, Randy Sabatini, Grant Walters, Oleksandr Voznyy, Riccardo Comin, Yiyang Li, James Z Fan, Hairen Tan, et al. „Tailoring the energy landscape in quasi-2D halide perovskites enables efficient green-light emission“. In: *Nano letters* 17.6 (2017), 3701–3709.
- [77] Adeline Buffet, André Rothkirch, Ralph Döhrmann, Volker Körstgens, Mottakin M Abul Kashem, Jan Perlich, Gerd Herzog, Matthias Schwartzkopf, Rainer Gehrke, Peter Müller-Buschbaum, et al. „P03, the microfocus and nanofocus X-ray scattering (MiNaXS) beamline of the PETRA III storage ring: the microfocus endstation“. In: *Journal of synchrotron radiation* 19.4 (2012), 647–653.
- [78] WW Van Den Hoogenhof and DKG De Boer. „Glancing-incidence X-ray analysis“. In: *Spectrochimica Acta Part B: Atomic Spectroscopy* 48.2 (1993), 277–284.
- [79] Gunthard Benecke, Wolfgang Wagermaier, Chenghao Li, Matthias Schwartzkopf, Gero Flucke, Rebecca Hoerth, Ivo Zizak, Manfred Burghammer, Ezzeldin Metwalli, Peter Müller-Buschbaum, et al. „A customizable software for fast reduction and analysis of large X-ray scattering data sets: applications of the new DPDAK package to small-angle X-ray scattering and grazing-incidence small-angle X-ray scattering“. In: *Journal of applied crystallography* 47.5 (2014), 1797–1803.
- [80] Yang Liu, Hongpeng Zhou, Yongfeng Ni, Junxue Guo, Ruixue Lu, Can Li, and Xin Guo. „Revealing stability origin of Dion-Jacobson 2D perovskites with different-rigidity organic cations“. In: *Joule* 7.5 (2023), 1016–1032.
- [81] Wei Peng, Jun Yin, Kang-Ting Ho, Olivier Ouellette, Michele De Bastiani, Bannavoth Murali, Omar El Tall, Chao Shen, Xiaohe Miao, Jun Pan, et al. „Ultralow self-doping in two-dimensional hybrid perovskite single crystals“. In: *Nano letters* 17.8 (2017), 4759–4767.
- [82] Shiqiang Luo and Walid A Daoud. „Recent progress in organic–inorganic halide perovskite solar cells: mechanisms and material design“. In: *Journal of Materials Chemistry A* 3.17 (2015), 8992–9010.
- [83] Wei Hui, Yingguo Yang, Quan Xu, Hao Gu, Shanglei Feng, Zhenhuang Su, Miaoran Zhang, Jiaou Wang, Xiaodong Li, Junfeng Fang, et al. „Red-carbon-quantum-dot-doped SnO₂ composite with enhanced electron mobility for efficient and stable perovskite solar cells“. In: *Advanced Materials* 32.4 (2020), 1906374.

- [84] Lei Gu, Deli Li, Lingfeng Chao, He Dong, Wei Hui, Tingting Niu, Chenxin Ran, Yingdong Xia, Lin Song, Yonghua Chen, et al. „Strain engineering of metal–halide perovskites toward efficient photovoltaics: advances and perspectives“. In: *Solar RRL* 5.3 (2021), 2000672.
- [85] Lili Ke, Shiqiang Luo, Xiaoxue Ren, and Yongbo Yuan. „Factors influencing the nucleation and crystal growth of solution-processed organic lead halide perovskites: a review“. In: *Journal of Physics D: Applied Physics* 54.16 (2021), 163001.
- [86] Qingxia Fu, Xianglan Tang, Bin Huang, Ting Hu, Licheng Tan, Lie Chen, and Yiwang Chen. „Recent progress on the long-term stability of perovskite solar cells“. In: *Advanced science* 5.5 (2018), 1700387.
- [87] Lei Meng, Jingbi You, Tzung-Fang Guo, and Yang Yang. „Recent advances in the inverted planar structure of perovskite solar cells“. In: *Accounts of chemical research* 49.1 (2016), 155–165.
- [88] Xuesong Lin, Danyu Cui, Xinhui Luo, Caiyi Zhang, Qifeng Han, Yanbo Wang, and Liyuan Han. „Efficiency progress of inverted perovskite solar cells“. In: *Energy & Environmental Science* 13.11 (2020), 3823–3847.
- [89] Zhen Li, Bo Li, Xin Wu, Stephanie A Sheppard, Shoufeng Zhang, Danpeng Gao, Nicholas J Long, and Zonglong Zhu. „Organometallic-functionalized interfaces for highly efficient inverted perovskite solar cells“. In: *Science* 376.6591 (2022), 416–420.
- [90] Youngwoong Kim, Eui Hyuk Jung, Geunjin Kim, Donguk Kim, Bumjoon J Kim, and Jangwon Seo. „Sequentially fluorinated PTAA polymers for enhancing VOC of high-performance perovskite solar cells“. In: *Advanced Energy Materials* 8.29 (2018), 1801668.
- [91] Ming Wang, Huaxin Wang, Wei Li, Xiaofei Hu, Kuan Sun, and Zhigang Zang. „Defect passivation using ultrathin PTAA layers for efficient and stable perovskite solar cells with a high fill factor and eliminated hysteresis“. In: *Journal of Materials Chemistry A* 7.46 (2019), 26421–26428.
- [92] Qi Bin Ke, Jia-Ren Wu, Chia-Chen Lin, and Sheng Hsiung Chang. „Understanding the PEDOT: PSS, PTAA and P3CT-X hole-transport-layer-based inverted perovskite solar cells“. In: *Polymers* 14.4 (2022), 823.
- [93] Yijie Xia, Guowang Yan, and Jian Lin. „Review on tailoring PEDOT: PSS layer for improved device stability of perovskite solar cells“. In: *Nanomaterials* 11.11 (2021), 3119.

- [94] Artiom Magomedov, Amran Al-Ashouri, Ernestas Kasparavičius, Simona Strazdaite, Gediminas Niaura, Marko Jošt, Tadas Malinauskas, Steve Albrecht, and Vytautas Getautis. „Self-assembled hole transporting monolayer for highly efficient perovskite solar cells“. In: *Advanced energy materials* 8.32 (2018), 1801892.
- [95] E Yalcin, M Can, C Rodriguez-Seco, E Aktas, R Pudi, W Cambarau, S Demic, and E Palomares. „Semiconductor self-assembled monolayers as selective contacts for efficient p-i-n perovskite solar cells“. In: *Energy & Environmental Science* 12.1 (2019), 230–237.
- [96] Christian M Wolff, Laura Canil, Carolin Rehermann, Nguyen Ngoc Linh, Fengshuo Zu, Maryline Ralaizarisoa, Pietro Caprioglio, Lukas Fiedler, Martin Stolterfoht, Sergio Kogikoski Jr, et al. „Perfluorinated self-assembled monolayers enhance the stability and efficiency of inverted perovskite solar cells“. In: *ACS nano* 14.2 (2020), 1445–1456.
- [97] Guangbo Chen, Xiaodong Li, and Xinliang Feng. „Upgrading organic compounds through the coupling of electrooxidation with hydrogen evolution“. In: *Angewandte Chemie International Edition* 61.42 (2022), e202209014.
- [98] Kui Jiang, Jing Wang, Fei Wu, Qifan Xue, Qin Yao, Jianquan Zhang, Yihuang Chen, Guangye Zhang, Zonglong Zhu, He Yan, et al. „Dopant-free organic hole-transporting material for efficient and stable inverted all-inorganic and hybrid perovskite solar cells“. In: *Advanced Materials* 32.16 (2020), 1908011.
- [99] Xianglang Sun, Qifan Xue, Zonglong Zhu, Qi Xiao, Kui Jiang, Hin-Lap Yip, He Yan, et al. „Fluoranthene-based dopant-free hole transporting materials for efficient perovskite solar cells“. In: *Chemical science* 9.10 (2018), 2698–2704.
- [100] Liangsheng Duan, Yu Chen, Jingwen Jia, Xueping Zong, Zhe Sun, Quanping Wu, and Song Xue. „Dopant-free hole-transport materials based on 2, 4, 6-triarylpyridine for inverted planar perovskite solar cells“. In: *ACS Applied Energy Materials* 3.2 (2020), 1672–1683.
- [101] Xinyu Yu, Zhen Li, Xianglang Sun, Cheng Zhong, Zonglong Zhu, Alex K-Y Jen, et al. „Dopant-free dicyanofluoranthene-based hole transporting material with low cost enables efficient flexible perovskite solar cells“. In: *Nano Energy* 82 (2021), 105701.
- [102] Ehsan Rezaee, Xiaoyuan Liu, Qikun Hu, Lei Dong, Qian Chen, Jia-Hong Pan, and Zong-Xiang Xu. „Dopant-free hole transporting materials for perovskite solar cells“. In: *Solar RRL* 2.11 (2018), 1800200.

- [103] Xianglang Sun, Xiang Deng, Zhen Li, Bijin Xiong, Cheng Zhong, Zonglong Zhu, Zhong'an Li, and Alex K-Y Jen. „Dopant-Free Crossconjugated Hole-Transporting Polymers for Highly Efficient Perovskite Solar Cells“. In: *Advanced Science* 7.13 (2020), 1903331.
- [104] Ryan Rhee, Soeun Im, Hongjoo Lee, Jung Hwan Lee, Youngno Kim, Do Hyung Chun, Chanil Park, Sunje Lee, Jung Hyun Kim, and Jong Hyeok Park. „Stretchable hole extraction layer for improved stability in perovskite solar cells“. In: *ACS Sustainable Chemistry & Engineering* 8.21 (2020), 8004–8010.
- [105] Anjan Kumar and Sangeeta Singh. „Advancement in inorganic hole transport materials for inverted perovskite solar cells“. In: *Journal of Electronic Materials* 49 (2020), 5840–5881.
- [106] Towhid H Chowdhury, Md Akhtaruzzaman, Md Emrul Kayesh, Ryuji Kaneko, Takeshi Noda, Jae-Joon Lee, and Ashraful Islam. „Low temperature processed inverted planar perovskite solar cells by r-GO/CuSCN hole-transport bilayer with improved stability“. In: *Solar Energy* 171 (2018), 652–657.
- [107] Gaveshana A Sepalage, Steffen Meyer, Alexander Pascoe, Andrew D Scully, Fuzhi Huang, Udo Bach, Yi-Bing Cheng, and Leone Spiccia. „Copper (I) iodide as hole-conductor in planar perovskite solar cells: probing the origin of J–V hysteresis“. In: *Advanced Functional Materials* 25.35 (2015), 5650–5661.
- [108] Wei-Yi Chen, Lin-Long Deng, Si-Min Dai, Xin Wang, Cheng-Bo Tian, Xin-Xing Zhan, Su-Yuan Xie, Rong-Bin Huang, and Lan-Sun Zheng. „Low-cost solution-processed copper iodide as an alternative to PEDOT: PSS hole transport layer for efficient and stable inverted planar heterojunction perovskite solar cells“. In: *Journal of Materials Chemistry A* 3.38 (2015), 19353–19359.
- [109] Chuantian Zuo and Liming Ding. „Solution-processed Cu₂O and CuO as hole transport materials for efficient perovskite solar cells“. In: *Small* 11.41 (2015), 5528–5532.
- [110] Weili Yu, Feng Li, Hong Wang, Erkki Alarousu, Yin Chen, Bin Lin, Lingfei Wang, Mohamed Nejib Hedhili, Yangyang Li, Kewei Wu, et al. „Ultrathin Cu₂O as an efficient inorganic hole transporting material for perovskite solar cells“. In: *Nanoscale* 8.11 (2016), 6173–6179.
- [111] Yinglong Yang, Haining Chen, Xiaoli Zheng, Xiangyue Meng, Teng Zhang, Chen Hu, Yang Bai, Shuang Xiao, and Shihe Yang. „Ultrasound-spray deposition of multi-walled carbon nanotubes on NiO nanoparticles-embedded perovskite layers for high-performance carbon-based perovskite solar cells“. In: *Nano Energy* 42 (2017), 322–333.

- [112] Md Bodiul Islam, Masatoshi Yanagida, Yasuhiro Shirai, Yoichi Nabetani, and Kenjiro Miyano. „NiO x hole transport layer for perovskite solar cells with improved stability and reproducibility“. In: *ACS omega* 2.5 (2017), 2291–2299.
- [113] Sajid Sajid, Ahmed Mourtada Elseman, Hao Huang, Jun Ji, Shangyi Dou, Haoran Jiang, Xin Liu, Dong Wei, Peng Cui, and Meicheng Li. „Breakthroughs in NiOx-HTMs towards stable, low-cost and efficient perovskite solar cells“. In: *Nano Energy* 51 (2018), 408–424.
- [114] Zonglong Zhu, Yang Bai, Teng Zhang, Zhike Liu, Xia Long, Zhanhua Wei, Zilong Wang, Lixia Zhang, Jiannong Wang, Feng Yan, et al. „High-performance hole-extraction layer of sol–gel-processed NiO nanocrystals for inverted planar perovskite solar cells“. In: *Angewandte Chemie International Edition* 53.46 (2014), 12571–12575.
- [115] Hansol Park, Rajneesh Chaurasiya, Bum Ho Jeong, Perumal Sakthivel, and Hui Joon Park. „Nickel oxide for perovskite photovoltaic cells“. In: *Advanced Photonics Research* 2.8 (2021), 2000178.
- [116] Qin Wang, Chu-Chen Chueh, Ting Zhao, Jiaqi Cheng, Morteza Eslamian, Wallace CH Choy, and Alex K-Y Jen. „Effects of self-assembled monolayer modification of nickel oxide nanoparticles layer on the performance and application of inverted perovskite solar cells“. In: *ChemSusChem* 10.19 (2017), 3794–3803.
- [117] Hae-Jun Seok, Jin-Hyeok Park, Ahra Yi, Hanbin Lee, Jooheon Kang, Hyo Jung Kim, and Han-Ki Kim. „Transition of the NiO x Buffer Layer from a p-Type Semiconductor to an Insulator for Operation of Perovskite Solar Cells“. In: *ACS Applied Energy Materials* 4.6 (2021), 5452–5465.
- [118] Yawen Du, Chenguang Xin, Wei Huang, Biao Shi, Yi Ding, Changchun Wei, Ying Zhao, Yuelong Li, and Xiaodan Zhang. „Polymeric surface modification of NiO x-based inverted planar perovskite solar cells with enhanced performance“. In: *ACS Sustainable Chemistry & Engineering* 6.12 (2018), 16806–16812.
- [119] Ruixue Zhu, Nianci Guan, Dourong Wang, Yaqi Bao, Zhongbin Wu, and Lin Song. „Review of Defect Passivation for NiO x-Based Inverted Perovskite Solar Cells“. In: *ACS Applied Energy Materials* 6.4 (2023), 2098–2121.
- [120] Caiyi Zhang, Xiangqian Shen, Mengjiong Chen, Yan Zhao, Xuesong Lin, Zhenzhen Qin, Yanbo Wang, and Liyuan Han. „Constructing a stable and efficient buried heterojunction via halogen bonding for inverted perovskite solar cells“. In: *Advanced Energy Materials* 13.2 (2023), 2203250.

- [121] Jiaqi Zhang, Jia Yang, Runying Dai, Wangping Sheng, Yang Su, Yang Zhong, Xiang Li, Licheng Tan, and Yiwang Chen. „Elimination of Interfacial Lattice Mismatch and Detrimental Reaction by Self-Assembled Layer Dual-Passivation for Efficient and Stable Inverted Perovskite Solar Cells“. In: *Advanced Energy Materials* 12.18 (2022), 2103674.
- [122] Xiangchuan Meng, Zheren Cai, Yanyan Zhang, Xiaotian Hu, Zhi Xing, Zengqi Huang, Zhandong Huang, Yongjie Cui, Ting Hu, Meng Su, et al. „Bio-inspired vertebral design for scalable and flexible perovskite solar cells“. In: *Nature Communications* 11.1 (2020), 3016.
- [123] Sidharam P Pujari, Luc Scheres, Antonius TM Marcelis, and Han Zuilhof. „Covalent surface modification of oxide surfaces“. In: *Angewandte Chemie International Edition* 53.25 (2014), 6322–6356.
- [124] Xi Xia Cui, Junjun Jin, Junjie Zou, Qiang Tang, Yuan Ai, Xiang Zhang, Zhen Wang, Yuan Zhou, Zhenkun Zhu, Guanqi Tang, et al. „NiOx nanocrystals with tunable size and energy levels for efficient and UV stable perovskite solar cells“. In: *Advanced Functional Materials* 32.31 (2022), 2203049.
- [125] Jinjin He, Enbing Bi, Wentao Tang, Yanbo Wang, Zhongmin Zhou, Xudong Yang, Han Chen, and Liyuan Han. „Ligand-free, highly dispersed NiOx nanocrystal for efficient, stable, low-temperature processable perovskite solar cells“. In: *Solar RRL* 2.4 (2018), 1800004.
- [126] Claudine Noguera. *Physics and chemistry at oxide surfaces*. Cambridge University Press, 1996.
- [127] Qi Chen, Cheng Wang, Yaowen Li, and Liwei Chen. „Interfacial dipole in organic and perovskite solar cells“. In: *Journal of the American Chemical Society* 142.43 (2020), 18281–18292.
- [128] Like Huang, Danli Zhang, Shixiao Bu, Ruixiang Peng, Qiang Wei, and Ziyi Ge. „Synergistic interface energy band alignment optimization and defect passivation toward efficient and simple-structured Perovskite Solar Cell“. In: *Advanced Science* 7.6 (2020), 1902656.
- [129] Nam Joong Jeon, Jun Hong Noh, Woon Seok Yang, Young Chan Kim, Seungchan Ryu, Jangwon Seo, and Sang Il Seok. „Compositional engineering of perovskite materials for high-performance solar cells“. In: *Nature* 517.7535 (2015), 476–480.
- [130] Nam Joong Jeon, Jun Hong Noh, Young Chan Kim, Woon Seok Yang, Seungchan Ryu, and Sang Il Seok. „Solvent engineering for high-performance inorganic–organic hybrid perovskite solar cells“. In: *Nature materials* 13.9 (2014), 897–903.

- [131] Hanul Min, Do Yoon Lee, Junu Kim, Gwisu Kim, Kyoung Su Lee, Jongbeom Kim, Min Jae Paik, Young Ki Kim, Kwang S Kim, Min Gyu Kim, et al. „Perovskite solar cells with atomically coherent interlayers on SnO₂ electrodes“. In: *Nature* 598.7881 (2021), 444–450.
- [132] Yang Zhao, Fei Ma, Zihan Qu, Shiqi Yu, Tao Shen, Hui-Xiong Deng, Xinbo Chu, Xinxin Peng, Yongbo Yuan, Xingwang Zhang, et al. „Inactive (PbI₂) 2RbCl stabilizes perovskite films for efficient solar cells“. In: *Science* 377.6605 (2022), 531–534.
- [133] Qi Jiang, Yang Zhao, Xingwang Zhang, Xiaolei Yang, Yong Chen, Zema Chu, Qiufeng Ye, Xingxing Li, Zhigang Yin, and Jingbi You. „Surface passivation of perovskite film for efficient solar cells“. In: *Nature Photonics* 13.7 (2019), 460–466.
- [134] Zhenghong Dai, Srinivas K Yadavalli, Min Chen, Ali Abbaspourtamijani, Yue Qi, and Nitin P Padture. „Interfacial toughening with self-assembled monolayers enhances perovskite solar cell reliability“. In: *Science* 372.6542 (2021), 618–622.
- [135] Wenxin Mao, Christopher R Hall, Stefano Bernardi, Yi-Bing Cheng, Asaph Widmer-Cooper, Trevor A Smith, and Udo Bach. „Light-induced reversal of ion segregation in mixed-halide perovskites“. In: *Nature materials* 20.1 (2021), 55–61.
- [136] Zehua Chen, Geert Brocks, Shuxia Tao, and Peter A Bobbert. „Unified theory for light-induced halide segregation in mixed halide perovskites“. In: *Nature communications* 12.1 (2021), 2687.
- [137] Waqaas Rehman, David P McMeekin, Jay B Patel, Rebecca L Milot, Michael B Johnston, Henry J Snaith, and Laura M Herz. „Photovoltaic mixed-cation lead mixed-halide perovskites: links between crystallinity, photo-stability and electronic properties“. In: *Energy & Environmental Science* 10.1 (2017), 361–369.
- [138] Suhas Mahesh, James M Ball, Robert DJ Oliver, David P McMeekin, Pabitra K Nayak, Michael B Johnston, and Henry J Snaith. „Revealing the origin of voltage loss in mixed-halide perovskite solar cells“. In: *Energy & Environmental Science* 13.1 (2020), 258–267.
- [139] Eric T Hoke, Daniel J Slotcavage, Emma R Dohner, Andrea R Bowring, Hemamala I Karunadasa, and Michael D McGehee. „Reversible photo-induced trap formation in mixed-halide hybrid perovskites for photovoltaics“. In: *Chemical Science* 6.1 (2015), 613–617.
- [140] R Geetha Balakrishna, Steven M Kobosko, and Prashant V Kamat. „Mixed halide perovskite solar cells. Consequence of iodide treatment on phase segregation recovery“. In: *ACS Energy Letters* 3.9 (2018), 2267–2272.

- [141] Nengxu Li, Yanqi Luo, Zehua Chen, Xiuxiu Niu, Xiao Zhang, Jiuzhou Lu, Rishi Kumar, Junke Jiang, Huifen Liu, Xiao Guo, et al. „Microscopic degradation in formamidinium-cesium lead iodide perovskite solar cells under operational stressors“. In: *Joule* 4.8 (2020), 1743–1758.
- [142] Bo-An Chen, Jin-Tai Lin, Nian-Tzu Suen, Che-Wei Tsao, Tzu-Chi Chu, Ying-Ya Hsu, Ting-Shan Chan, Yi-Tsu Chan, Jye-Shane Yang, Ching-Wen Chiu, et al. „In situ identification of photo-and moisture-dependent phase evolution of perovskite solar cells“. In: *ACS Energy Letters* 2.2 (2017), 342–348.
- [143] Jeffrey A Christians, Pierre A Miranda Herrera, and Prashant V Kamat. „Transformation of the excited state and photovoltaic efficiency of CH₃NH₃PbI₃ perovskite upon controlled exposure to humidified air“. In: *Journal of the American Chemical Society* 137.4 (2015), 1530–1538.
- [144] Kevin Ho, Mingyang Wei, Edward H Sargent, and Gilbert C Walker. „Grain transformation and degradation mechanism of formamidinium and cesium lead iodide perovskite under humidity and light“. In: *ACS Energy Letters* 6.3 (2021), 934–940.
- [145] Panteha Toloueinia, Hamidreza Khassaf, Alireza Shirazi Amin, Zachary M Tobin, S Pamir Alpay, and Steven L Suib. „Moisture-induced structural degradation in methylammonium lead iodide perovskite thin films“. In: *ACS Applied Energy Materials* 3.9 (2020), 8240–8248.
- [146] Jae Sung Yun, Jincheol Kim, Trevor Young, Robert J Patterson, Dohyung Kim, Jan Seidel, Sean Lim, Martin A Green, Shujuan Huang, and Anita Ho-Baillie. „Humidity-induced degradation via grain boundaries of HC (NH₂)₂PbI₃ planar perovskite solar cells“. In: *Advanced Functional Materials* 28.11 (2018), 1705363.
- [147] Zhenyi Ni, Chunxiong Bao, Ye Liu, Qi Jiang, Wu-Qiang Wu, Shangshang Chen, Xuezheng Dai, Bo Chen, Barry Hartweg, Zhengshan Yu, et al. „Resolving spatial and energetic distributions of trap states in metal halide perovskite solar cells“. In: *Science* 367.6484 (2020), 1352–1358.
- [148] Dan Yang, Franziska C Löhner, Volker Körstgens, Armin Schreiber, Bing Cao, Sigrid Bernstorff, and Peter Müller-Buschbaum. „In Operando GISAXS and GI-WAXS Stability Study of Organic Solar Cells Based on PffBT4T-2OD: PC71BM with and without Solvent Additive“. In: *Advanced Science* 7.16 (2020), 2001117.
- [149] Johannes Schlipf and Peter Müller-Buschbaum. „Structure of organometal halide perovskite films as determined with grazing-incidence x-ray scattering methods“. In: *Advanced energy materials* 7.16 (2017), 1700131.

- [150] Yu-Ching Huang, Cheng-Si Tsao, Yi-Ju Cho, Kuan-Chen Chen, Kai-Ming Chiang, Sheng-Yi Hsiao, Chang-Wen Chen, Chun-Jen Su, U-Ser Jeng, and Hao-Wu Lin. „Insight into evolution, processing and performance of multi-length-scale structures in planar heterojunction perovskite solar cells“. In: *Scientific reports* 5.1 (2015), 13657.
- [151] Alexander T Barrows, Samuele Lilliu, Andrew J Pearson, David Babonneau, Alan DF Dunbar, and David G Lidzey. „Monitoring the Formation of a CH₃NH₃PbI₃-xCl_x Perovskite during Thermal Annealing Using X-Ray Scattering“. In: *Advanced Functional Materials* 26.27 (2016), 4934–4942.
- [152] Wenzhe Li, Wei Zhang, Stephan Van Reenen, Rebecca J Sutton, Jiandong Fan, Amir A Haghighirad, Michael B Johnston, Liduo Wang, and Henry J Snaith. „Enhanced UV-light stability of planar heterojunction perovskite solar cells with caesium bromide interface modification“. In: *Energy & Environmental Science* 9.2 (2016), 490–498.
- [153] Hang Xu, Yanfeng Miao, Ning Wei, Haoran Chen, Zhixiao Qin, Xiaomin Liu, Xingtao Wang, Yabing Qi, Taiyang Zhang, and Yixin Zhao. „CsI Enhanced Buried Interface for Efficient and UV-Robust Perovskite Solar Cells“. In: *Advanced Energy Materials* 12.2 (2022), 2103151.
- [154] Qingshun Dong, Chao Zhu, Min Chen, Chen Jiang, Jingya Guo, Yulin Feng, Zhenghong Dai, Srinivas K Yadavalli, Mingyu Hu, Xun Cao, et al. „Interpenetrating interfaces for efficient perovskite solar cells with high operational stability and mechanical robustness“. In: *Nature communications* 12.1 (2021), 973.
- [155] Wei Chen, Renjun Guo, Haodong Tang, Kerstin S Wienhold, Nian Li, Zhengyan Jiang, Jun Tang, Xinyu Jiang, Lucas P Kreuzer, Haochen Liu, et al. „Operando structure degradation study of PbS quantum dot solar cells“. In: *Energy & Environmental Science* 14.6 (2021), 3420–3429.
- [156] Kerstin S Wienhold, Wei Chen, Shanshan Yin, Renjun Guo, Matthias Schwartzkopf, Stephan V Roth, and Peter Müller-Buschbaum. „Following in Operando the Structure Evolution-Induced Degradation in Printed Organic Solar Cells with Non-fullerene Small Molecule Acceptor“. In: *Solar Rrl* 4.9 (2020), 2000251.
- [157] Michael Saliba, Taisuke Matsui, Ji-Youn Seo, Konrad Domanski, Juan-Pablo Correa-Baena, Mohammad Khaja Nazeeruddin, Shaik M Zakeeruddin, Wolfgang Tress, Antonio Abate, Anders Hagfeldt, et al. „Cesium-containing triple cation perovskite solar cells: improved stability, reproducibility and high efficiency“. In: *Energy & environmental science* 9.6 (2016), 1989–1997.

- [158] Ying-Bo Lu, Wei-Yan Cong, ChengBo Guan, Hui Sun, Yanqing Xin, Kunlun Wang, and Shumei Song. „Light enhanced moisture degradation of perovskite solar cell material CH₃NH₃PbI₃“. In: *Journal of Materials Chemistry A* 7.48 (2019), 27469–27474.
- [159] Jun Peng, Daniel Walter, Yuhao Ren, Mike Tebyetekerwa, Yiliang Wu, The Duong, Qiaoling Lin, Juntao Li, Teng Lu, Md Arafat Mahmud, et al. „Nanoscale localized contacts for high fill factors in polymer-passivated perovskite solar cells“. In: *Science* 371.6527 (2021), 390–395.
- [160] Huanhuan Wang, Zaiwei Wang, Zhen Yang, Yuzeng Xu, Yi Ding, Liguang Tan, Chenyi Yi, Zhuang Zhang, Ke Meng, Gang Chen, et al. „Ligand-modulated excess PbI₂ nanosheets for highly efficient and stable perovskite solar cells“. In: *Advanced Materials* 32.21 (2020), 2000865.
- [161] Renjun Guo, Dan Han, Wei Chen, Linjie Dai, Kangyu Ji, Qiu Xiong, Saisai Li, Lennart K Reb, Manuel A Scheel, Shambhavi Pratap, et al. „Degradation mechanisms of perovskite solar cells under vacuum and one atmosphere of nitrogen“. In: *Nature Energy* 6.10 (2021), 977–986.
- [162] P Müller-Buschbaum. „A basic introduction to grazing incidence small-angle X-ray scattering“. In: *Applications of Synchrotron Light to Scattering and Diffraction in Materials and Life Sciences*. Springer, 2009, 61–89.
- [163] Johannes Schlipf, Pablo Docampo, Christoph J Schaffer, Volker Körstgens, Lorenz Bießmann, Fabian Hanusch, Nadja Giesbrecht, Sigrid Bernstorff, Thomas Bein, and Peter Müller-Buschbaum. „A closer look into two-step perovskite conversion with X-ray scattering“. In: *The journal of physical chemistry letters* 6.7 (2015), 1265–1269.
- [164] Parth Raval, Rhiannon M Kennard, Eugenia S Vasileiadou, Clayton J Dahlman, Ioannis Spanopoulos, Michael L Chabinye, Mercouri Kanatzidis, and GN Manjunatha Reddy. „Understanding instability in formamidinium lead halide perovskites: kinetics of transformative reactions at grain and subgrain boundaries“. In: *ACS Energy Letters* 7.4 (2022), 1534–1543.
- [165] Qingzhi An, Fabian Paulus, David Becker-Koch, Changsoon Cho, Qing Sun, Andreas Weu, Sapir Bitton, Nir Tessler, and Yana Vaynzof. „Small grains as recombination hot spots in perovskite solar cells“. In: *Matter* 4.5 (2021), 1683–1701.
- [166] Long Hu, Xinwei Guan, Weijian Chen, Yuchen Yao, Tao Wan, Chun-Ho Lin, Ngoc Duy Pham, Lin Yuan, Xun Geng, Fei Wang, et al. „Linking phase segregation and photovoltaic performance of mixed-halide perovskite films through grain size engineering“. In: *ACS Energy Letters* 6.4 (2021), 1649–1658.

- [167] Paulo Ernesto Marchezi, Eralci Moreira Therézio, Rodrigo Szostak, Hugo Campos Loureiro, Karsten Bruening, Aryeh Gold-Parker, Mauricio A Melo, Christopher J Tassone, Helio CN Tolentino, Michael F Toney, et al. „Degradation mechanisms in mixed-cation and mixed-halide Cs x FA 1- x Pb (Br y I 1- y) 3 perovskite films under ambient conditions“. In: *Journal of Materials Chemistry A* 8.18 (2020), 9302–9312.
- [168] Efrain Ochoa-Martinez, Mario Ochoa, Roberto D Ortuso, Parnian Ferdowsi, Romain Carron, Ayodhya N Tiwari, Ullrich Steiner, and Michael Saliba. „Physical passivation of grain boundaries and defects in perovskite solar cells by an isolating thin polymer“. In: *ACS Energy Letters* 6.7 (2021), 2626–2634.
- [169] Andrés-Felipe Castro-Méndez, Juanita Hidalgo, and Juan-Pablo Correa-Baena. „The role of grain boundaries in perovskite solar cells“. In: *Advanced Energy Materials* 9.38 (2019), 1901489.
- [170] Dongtao Liu, Deying Luo, Affan N Iqbal, Kieran WP Orr, Tiarnan AS Doherty, Zheng-Hong Lu, Samuel D Stranks, and Wei Zhang. „Strain analysis and engineering in halide perovskite photovoltaics“. In: *Nature materials* 20.10 (2021), 1337–1346.
- [171] Tiarnan AS Doherty, Andrew J Winchester, Stuart Macpherson, Duncan N Johnstone, Vivek Pareek, Elizabeth M Tennyson, Sofia Kosar, Felix U Kosasih, Miguel Anaya, Mojtaba Abdi-Jalebi, et al. „Performance-limiting nanoscale trap clusters at grain junctions in halide perovskites“. In: *Nature* 580.7803 (2020), 360–366.
- [172] Timothy W Jones, Anna Osherov, Mejd Alsari, Melany Sponseller, Benjamin C Duck, Young-Kwang Jung, Charles Settens, Farnaz Niroui, Roberto Brenes, Camelia V Stan, et al. „Lattice strain causes non-radiative losses in halide perovskites“. In: *Energy & Environmental Science* 12.2 (2019), 596–606.
- [173] Ding-Jiang Xue, Yi Hou, Shun-Chang Liu, Mingyang Wei, Bin Chen, Ziruo Huang, Zongbao Li, Bin Sun, Andrew H Proppe, Yitong Dong, et al. „Regulating strain in perovskite thin films through charge-transport layers“. In: *Nature communications* 11.1 (2020), 1514.
- [174] Hsinhan Tsai, Reza Asadpour, Jean-Christophe Blancon, Constantinos C Stoumpos, Olivier Durand, Joseph W Strzalka, Bo Chen, Rafael Verduzco, Pulickel M Ajayan, Sergei Tretiak, et al. „Light-induced lattice expansion leads to high-efficiency perovskite solar cells“. In: *Science* 360.6384 (2018), 67–70.
- [175] Michael C Brennan, Sergiu Draguta, Prashant V Kamat, and Masaru Kuno. „Light-induced anion phase segregation in mixed halide perovskites“. In: *ACS Energy Letters* 3.1 (2017), 204–213.

- [176] Tingwei He, Saisai Li, Yuanzhi Jiang, Chaochao Qin, Minghuan Cui, Lu Qiao, Hongyu Xu, Jien Yang, Run Long, Huanhua Wang, et al. „Reduced-dimensional perovskite photovoltaics with homogeneous energy landscape“. In: *Nature communications* 11.1 (2020), 1672.
- [177] Siraj Sidhik, Yafei Wang, Michael De Siena, Reza Asadpour, Andrew J Torma, Tanguy Terlier, Kevin Ho, Wenbin Li, Anand B Puthirath, Xinting Shuai, et al. „Deterministic fabrication of 3D/2D perovskite bilayer stacks for durable and efficient solar cells“. In: *Science* 377.6613 (2022), 1425–1430.
- [178] Ke Ma, Jiaonan Sun, Harindi R Atapattu, Bryon W Larson, Hanjun Yang, Dewei Sun, Ke Chen, Kang Wang, Yoonho Lee, Yuanhao Tang, et al. „Holistic energy landscape management in 2D/3D heterojunction via molecular engineering for efficient perovskite solar cells“. In: *Science Advances* 9.23 (2023), eadg0032.
- [179] Fei Zhang, So Yeon Park, Canglang Yao, Haipeng Lu, Sean P Dunfield, Chuanxiao Xiao, Soňa Uličná, Xiaoming Zhao, Linze Du Hill, Xihan Chen, et al. „Metastable Dion-Jacobson 2D structure enables efficient and stable perovskite solar cells“. In: *Science* 375.6576 (2022), 71–76.
- [180] Yuequn Shang, Yuan Liao, Qi Wei, Ziyu Wang, Bo Xiang, Youqi Ke, Weimin Liu, and Zhijun Ning. „Highly stable hybrid perovskite light-emitting diodes based on Dion-Jacobson structure“. In: *Science advances* 5.8 (2019), eaaw8072.
- [181] Brandon R Sutherland and Edward H Sargent. „Perovskite photonic sources“. In: *Nature Photonics* 10.5 (2016), 295–302.
- [182] Peirui Cheng, Peijun Wang, Zhuo Xu, Xuguang Jia, Qilin Wei, Ningyi Yuan, Jianning Ding, Ruipeng Li, Guangtao Zhao, Yingchun Cheng, et al. „Ligand-size related dimensionality control in metal halide perovskites“. In: *ACS Energy Letters* 4.8 (2019), 1830–1838.
- [183] Enzheng Shi, Biao Yuan, Stephen B Shiring, Yao Gao, Akriti, Yunfan Guo, Cong Su, Minliang Lai, Peidong Yang, Jing Kong, et al. „Two-dimensional halide perovskite lateral epitaxial heterostructures“. In: *Nature* 580.7805 (2020), 614–620.
- [184] Michael Worku, Qingquan He, Liang-jin Xu, Jisook Hong, Ruo Xi Yang, Liang Z Tan, and Biwu Ma. „Phase control and in situ passivation of quasi-2D metal halide perovskites for spectrally stable blue light-emitting diodes“. In: *ACS Applied Materials & Interfaces* 12.40 (2020), 45056–45063.

- [185] Jian Qing, Xiao-Ke Liu, Mingjie Li, Feng Liu, Zhongcheng Yuan, Elizaveta Tiukalova, Zhibo Yan, Martial Duchamp, Shi Chen, Yuming Wang, et al. „Aligned and graded type-II Ruddlesden–Popper perovskite films for efficient solar cells“. In: *Advanced Energy Materials* 8.21 (2018), 1800185.
- [186] Jia Zhang, Jiajun Qin, Miaosheng Wang, Yujie Bai, Han Zou, Jong Kahk Keum, Runming Tao, Hengxing Xu, Haomiao Yu, Stefan Haacke, et al. „Uniform permutation of quasi-2D perovskites by vacuum poling for efficient, high-fill-factor solar cells“. In: *Joule* 3.12 (2019), 3061–3071.
- [187] Da Bin Kim, Seungjin Lee, Chung Hyeon Jang, Jong Hyun Park, Ah-young Lee, and Myoung Hoon Song. „Uniform and large-area cesium-based quasi-2D perovskite light-emitting diodes using hot-casting method“. In: *Advanced Materials Interfaces* 7.8 (2020), 1902158.
- [188] Min Xiong, Wenjun Zou, Ke Fan, Chaochao Qin, Sibao Li, Linfeng Fei, Jizhong Jiang, Haitao Huang, Liang Shen, Feng Gao, et al. „Tailoring phase purity in the 2D/3D perovskite heterostructures using lattice mismatch“. In: *ACS Energy Letters* 7.1 (2022), 550–559.
- [189] Randi Azmi, Esmā Ugur, Akmaral Seitkhan, Faisal Aljamaan, Anand S Subbiah, Jiang Liu, George T Harrison, Mohamad I Nugraha, Mathan K Eswaran, Maxime Babics, et al. „Damp heat–stable perovskite solar cells with tailored-dimensionality 2D/3D heterojunctions“. In: *Science* 376.6588 (2022), 73–77.
- [190] Yao Gao, Enzheng Shi, Shibin Deng, Stephen B Shiring, Jordan M Snaider, Chao Liang, Biao Yuan, Ruyi Song, Svenja M Janke, Alexander Liebman-Peláez, et al. „Molecular engineering of organic–inorganic hybrid perovskites quantum wells“. In: *Nature chemistry* 11.12 (2019), 1151–1157.
- [191] Hao Chen, Sam Teale, Bin Chen, Yi Hou, Luke Grater, Tong Zhu, Koen Bertens, So Min Park, Harindi R Atapattu, Yajun Gao, et al. „Quantum-size-tuned heterostructures enable efficient and stable inverted perovskite solar cells“. In: *Nature Photonics* 16.5 (2022), 352–358.
- [192] Justin M Hoffman, Ido Hadar, Xiaotong Li, Weijun Ke, Eugenia S Vasileiadou, Joseph Strzalka, Lin X Chen, and Mercouri G Kanatzidis. „Film formation mechanisms in mixed-dimensional 2D/3D halide perovskite films revealed by in situ grazing-incidence wide-angle X-ray scattering“. In: *Chem* 8.4 (2022), 1067–1082.
- [193] J-C Blancon, Andreas V Stier, Hsinhan Tsai, Wanyi Nie, Costas C Stoumpos, Boubacar Traore, L Pedesseau, Mikael Kepenekian, Fumiya Katsutani, GT Noe, et al. „Scaling law for excitons in 2D perovskite quantum wells“. In: *Nature communications* 9.1 (2018), 2254.

- [194] Dibyajyoti Ghosh, Debdipto Acharya, Laurent Pedesseau, Claudine Katan, Jacky Even, Sergei Tretiak, and Amanda J Neukirch. „Charge carrier dynamics in two-dimensional hybrid perovskites: Dion–Jacobson vs. Ruddlesden–Popper phases“. In: *Journal of Materials Chemistry A* 8.42 (2020), 22009–22022.
- [195] Yang Li, Jovana V Milić, Amita Ummadisingu, Ji-Youn Seo, Jeong-Hyeok Im, Hui-Seo Kim, Yuhang Liu, M Ibrahim Dar, Shaik M Zakeeruddin, Peng Wang, et al. „Bifunctional organic spacers for formamidinium-based hybrid Dion–Jacobson two-dimensional perovskite solar cells“. In: *Nano letters* 19.1 (2018), 150–157.
- [196] Wen Liang Tan, Nigel M Kirby, Yi-Bing Cheng, and Christopher R McNeill. „Origin of vertical slab orientation in blade-coated layered hybrid perovskite films revealed with in-situ synchrotron X-ray scattering“. In: *Nano Energy* 83 (2021), 105818.
- [197] Li Na Quan, Mingjian Yuan, Riccardo Comin, Oleksandr Voznyy, Eric M Beauregard, Sjoerd Hoogland, Andrei Buin, Ahmad R Kirmani, Kui Zhao, Aram Amassian, et al. „Ligand-stabilized reduced-dimensionality perovskites“. In: *Journal of the American Chemical Society* 138.8 (2016), 2649–2655.
- [198] Ping Fu, Yang Liu, Shuwen Yu, Heng Yin, Bowen Yang, Sajjad Ahmad, Xin Guo, and Can Li. „Dion-Jacobson and Ruddlesden-Popper double-phase 2D perovskites for solar cells“. In: *Nano Energy* 88 (2021), 106249.
- [199] Jian Qiu, Yiting Zheng, Yingdong Xia, Lingfeng Chao, Yonghua Chen, and Wei Huang. „Rapid crystallization for efficient 2D Ruddlesden–Popper (2DRP) perovskite solar cells“. In: *Advanced Functional Materials* 29.47 (2019), 1806831.
- [200] Rafael Quintero-Bermudez, Aryeh Gold-Parker, Andrew H Proppe, Rahim Munir, Zhenyu Yang, Shana O Kelley, Aram Amassian, Michael F Toney, and Edward H Sargent. „Compositional and orientational control in metal halide perovskites of reduced dimensionality“. In: *Nature materials* 17.10 (2018), 900–907.
- [201] Michael B Price, Justinas Butkus, Tom C Jellicoe, Aditya Sadhanala, Anouk Briane, Jonathan E Halpert, Katharina Broch, Justin M Hodgkiss, Richard H Friend, and Felix Deschler. „Hot-carrier cooling and photoinduced refractive index changes in organic–inorganic lead halide perovskites“. In: *Nature communications* 6.1 (2015), 8420.
- [202] Anna Stadlbauer, Lissa Eyre, Alexander Biewald, Felix Rauh, Markus W Heindl, Shangpu Liu, Jonathan Zerhoch, Sascha Feldmann, Achim Hartschuh, and Felix Deschler. „Photoexcitation Control of Excitation Relaxation in Mixed-Phase Ruddlesden-Popper Hybrid Organic-Inorganic Lead-Iodide Perovskites“. In: *Advanced Optical Materials* 12.8 (2024), 2301331.

- [203] Yuanzhi Jiang, Chaochao Qin, Minghuan Cui, Tingwei He, Kaikai Liu, Yanmin Huang, Menghui Luo, Li Zhang, Hongyu Xu, Saisai Li, et al. „Spectra stable blue perovskite light-emitting diodes“. In: *Nature Communications* 10.1 (2019), 1868.
- [204] Guichuan Xing, Bo Wu, Xiangyang Wu, Mingjie Li, Bin Du, Qi Wei, Jia Guo, Edwin KL Yeow, Tze Chien Sum, and Wei Huang. „Transcending the slow bimolecular recombination in lead-halide perovskites for electroluminescence“. In: *Nature communications* 8.1 (2017), 14558.
- [205] Chaochao Qin, Liuhong Xu, Zhongpo Zhou, Jian Song, Shuhong Ma, Zhaoyong Jiao, and Yuhai Jiang. „Carrier dynamics in two-dimensional perovskites: Dion–Jacobson vs. Ruddlesden–Popper thin films“. In: *Journal of Materials Chemistry A* 10.6 (2022), 3069–3076.
- [206] Yuqi Sun, Lishuang Ge, Linjie Dai, Changsoon Cho, Jordi Ferrer Orri, Kangyu Ji, Szymon J Zelewski, Yun Liu, Alessandro J Mirabelli, Youcheng Zhang, et al. „Bright and stable perovskite light-emitting diodes in the near-infrared range“. In: *Nature* 615.7954 (2023), 830–835.
- [207] Elizabeth M Tennyson, Tiarnan AS Doherty, and Samuel D Stranks. „Heterogeneity at multiple length scales in halide perovskite semiconductors“. In: *Nature Reviews Materials* 4.9 (2019), 573–587.
- [208] Haoliang Wang, Yiyi Pan, Xiaoguo Li, Zejiao Shi, Xin Zhang, Tangyao Shen, Yang Tang, Wenyong Fan, Yuchen Zhang, Fengcai Liu, et al. „Band Alignment Boosts over 17% Efficiency Quasi-2D Perovskite Solar Cells via Bottom-Side Phase Manipulation“. In: *ACS Energy Letters* 7.10 (2022), 3187–3196.
- [209] Yifang Qi, Mohammed Almtiri, Hari Giri, Surabhi Jha, Guorong Ma, Abdul Kalam Shaik, Qiqi Zhang, Nihar Pradhan, Xiaodan Gu, Nathan I Hammer, et al. „Evaluation of the passivation effects of PEDOT: PSS on inverted perovskite solar cells“. In: *Advanced Energy Materials* 12.46 (2022), 2202713.
- [210] Rachel E Beal, Nanna Zhou Hagström, Julien Barrier, Aryeh Gold-Parker, Rohit Prasanna, Kevin A Bush, Donata Passarello, Laura T Schelhas, Karsten Brüning, Christopher J Tassone, et al. „Structural origins of light-induced phase segregation in organic-inorganic halide perovskite photovoltaic materials“. In: *Matter* 2.1 (2020), 207–219.
- [211] Md Abdul Kuddus Sheikh, Dominik Kowal, Muhammad Haris Mahyuddin, Roberto Cala’, Etiennette Auffray, Marcin Eugeniusz Witkowski, Michal Makowski, Winicjusz Drozdowski, Hong Wang, Christophe Dujardin, et al. „ $A_2B_{n-1}Pb_nI_{3n+1}$ (A = BA, PEA; B = MA; n = 1, 2): Engineering Quantum-Well Crystals for High Mass

Density and Fast Scintillators“. In: *The Journal of Physical Chemistry C* 127.22 (2023), 10737–10747.

List of Publications

Publications related to the dissertation

- **K. Sun** R. Guo, S. Liu, D. Guo, X. Jiang, L. F. Huber, Y. Liang, M. A. Reus, Z. Li, T. Guan, J. Zhou, M. Schwartzkopf, S. D. Stranks, F. Deschler, P. Müller-Buschbaum. Deciphering Structure and Charge Carrier Behavior in Reduced-Dimensional Perovskites. *Adv. Funct. Mater.* 411153 (2024).
(DOI: 10.1002/adfm.202411153)
- **K. Sun** R. Guo, Y. Liang, J. E. Heger, S. Liu, S. Yin, M. A. Reus, L. V. Spanier, F. Deschler, S. Bernstorff, P. Müller-Buschbaum. Morphological Insights into the Degradation of Perovskite Solar Cells under Light and Humidity. *ACS Appl. Mater. Interfaces.* **15**, 30342-30349 (2023).
(DOI: 10.1021/acsami.3c05671)
- **K. Sun**, P. Müller-Buschbaum. Shedding Light on the Moisture Stability of Halide Perovskite Thin Films. *Energy Technol.* **11**, 2201475 (2023).
(DOI: 10.1002/ente.202201475)
- X. Kang, D. Wang, **K. Sun**, W. Hui, B. Wang, L. Gu, M. Li, Y. Bao, J. Zhang, R. Guo, Z. Li, X. Jiang, P. Müller-Buschbaum, L. Song. Unraveling the modification effect at NiOx/perovskite interfaces for efficient and stable inverted perovskite solar cells. *J. Mater. Chem. A.* **11**, 22982-22991 (2023), contribute equally.
(DOI: 10.1039/d3ta05069f)

Further publications

- I. López-Fernández, D. Valli, C-Y. Wang, S. Samanta, T. Okamoto, Y-T. Huang, **K. Sun**, Y. Liu, V. S. Chirvony, A. Patra, J. Zito, L. Trizio, D. Gaur, H-T. Sun, Z. Xia, X. Li. H. Zeng, I. Mora-Seró, N. Pradhan, J. Martínez-Pastor, P. Müller-Buschbaum, v. Biju, T. Debnath, M. Saliba, E. Debroye, R. Z. Hoyer, I. Infante, L. Manna, L. Polavarapu. Lead-Free Halide Perovskite Materials and Optoelectronic Devices: Progress and Prospective. *Adv. Funct. Mater.* **34**, 2307896 (2023), contribute equally.
(DOI: 10.1002/adfm.202307896)
- Z. Li, Y. Li, R. Guo, **K. Sun**, X. Jiang, P. Wang, S. Tu, M. Schwartzkopf, Z. Li, C. Ma, P. Müller-Buschbaum. “Suppressed Degradation Process of Green-Solvent Based Organic Solar Cells Through ZnO Modification With Sulfhydryl Derivatives. *Adv. Energy Mater.* 2402920 (2024).
(DOI: 10.1002/aenm.202402920)
- D. Sandner, **K. Sun**, A. Stadlbauer, M. W. Heindl, Q. Tan, M. Nuber, C. Soci, R. Kiennberger, P. Müller-Buschbaum, F. Deschler, H. Iglev. “Hole Localization in Bulk and 2D Lead-Halide Perovskites Studied by Time-Resolved Infrared Spectroscopy. *J. Am. Chem. Soc.* **146**, 19852-19862 (2024).
(DOI: 10.1021/jacs.4c02958)
- H. Zhu, Q. Wang, W. Chen, **K. Sun**, H. Zhong, T. Ye, Z. Wang, W. Zhang, P. Müller-Buschbaum, X. Sun, D. Wu, K. Wang. “Chiral perovskite-CdSe/ZnS QDs composites with high circularly polarized luminescence performance achieved through additive-solvent engineering. *J. Chem. Phys.* **160**, 234703 (2024).
(DOI: 10.1063/5.0200692)
- Y. Liang, T. Zheng, **K. Sun**, Z. Xu, F.A. Apfelbeck, P. Ding, I. D. Sharp, Y. Cheng, M. Schwartzkopf, S. V. Roth, P. Müller-Buschbaum. “Operando Study Insights into Lithiation/Delithiation Processes in a Poly(ethylene oxide) Electrolyte of All-Solid-State Lithium Batteries by Grazing-Incidence X-ray Scattering. *ACS Appl. Mater. Interfaces.* **16**, 33307-33315 (2024).
(DOI: 10.1021/acsami.4c01661)

- Z. Shi, R. Guo, R. Luo, X. Wang, J. Ma, J. Feng, X. Niu, E. Alvianto, Z. Jia, X. Guo, H. Liang, J. Chen, Z. Li, **K. Sun**, X. Jiang, Y. Wu, P. Müller-Buschbaum, W. Hu, Y. Hou. “T-shaped” Carbazole Alkylammonium Cation Passivation in Perovskite Solar Cells. *ACS Energy Lett.* **9**, 419-427 (2024).
(DOI: 10.1021/acseenergylett.3c02357)
- R. Guo, Q. Xiong, A. Ulatowski, S. Li, Z. Ding, T. Xiao, S. Liang, J. E. Heger, T. Guan, X. Jiang, **K. Sun**, L. K. Reb, M. A. Reus, A. Chumakov, M. Schwartzkopf, M. Y, Y. Hou, S. V. Roth, L. M. Herz, P. Gao, P. Müller-Buschbaum. Trace Water in Lead Iodide Affecting Perovskite Crystal Nucleation Limits the Performance of Perovskite Solar Cells. *Adv. Mater.* **36**, 2310237 (2024).
(DOI: 10.1039/D3EE02527F)
- M. Li, Y. Bao, W. Hui, **K. Sun**, L. Gu, X. Kang, D. Wang, B. Wang, H. Deng, R. Guo, Z. Li, X. Jiang, P. Müller-Buschbaum, L. Song, W. Huang. In Situ Surface Reconstruction toward Planar Heterojunction for Efficient and Stable FAPbI₃ Quantum Dot Solar Cells. *Adv. Mater.* **36**, 2309890 (2024).
(DOI: 10.1002/adma.202309890)
- R. Guo, X. Wang, X. Jia, X. Guo, J. Li, Z. Li, **K. Sun**, X. Jiang, E. Alvianto, Z. Shi, M. Schwartzkopf, P. Müller-Buschbaum, Y. Hou. Refining the Substrate Surface Morphology for Achieving Efficient Inverted Perovskite Solar Cells. *Adv. Energy Mater.* **13**, 2302280 (2023).
(DOI: 10.1039/D3EE02527F)
- H. Zhu, Q. Wang, **K. Sun**, W. Chen, J. Tang, J. Hao, Z. Wang, J. Sun, W. C. H. Choy, P. Müller-Buschbaum, X. Sun, D. Wu, K. Wang. Solvent Modulation of Chiral Perovskite Films Enables High Circularly Polarized Luminescence Performance from Chiral Perovskite/Quantum Dot Composites. *ACS Appl. Mater. Interfaces.* **15**, 9978–9986 (2023).
(DOI: 10.1021/acсами.2c20716)
- N. Fiuza-Maneiro, **K. Sun**, I. López-Fernández, S. Gómez-Graña, P. Müller-Buschbaum, L. Polavarapu. Ligand Chemistry of Inorganic Lead Halide Perovskite Nanocrystals. *ACS Energy Lett.* **8**, 1152–1191 (2023).
(DOI: 10.1021/acsenergylett.2c02363)

- X. Jiang, A. J. Gillett, T. Zheng, X. Song, J. E. Heger, **K. Sun**, L. V. Spanier, R. Guo, S. Liang, S. Bernstorff, P. Müller-Buschbaum. Operando study of the influence of small molecule acceptors on the morphology induced device degradation of organic solar cells with different degrees of π - π stacking. *Energy Environ. Sci.* **16**, 5970-5981 (2023).

(DOI: 10.1039/D3EE02527F)

- X. Song, K. Zhang, R. Guo, **K. Sun**, Z. Zhou, S. Huang, L. Huber, M. Reus, J. Zhou, M. Schwartzkopf, S. V. Roth, W. Liu, Y. Liu, W. Zhou, P. Müller-Buschbaum. Process-Aid Solid Engineering Triggers Delicately Modulation of Y-Series Non-Fullerene Acceptor for Efficient Organic Solar Cells. *Adv. Mater.* **34**, 2200907 (2022).

(DOI: 10.1002/adma.202200907)

Conference Contributions

Contributed Talks

- *Deciphering the Interplay of Structure and Charge Carrier Dynamics in Reduced-Dimensional Perovskites.*
245th ECS Meeting
San Francisco, America, 26.05.–30.05.2024.
- *Deciphering the Interplay of Structure and Charge Carrier Dynamics in Reduced-Dimensional Perovskites.*
Deutsche Physikalische Gesellschaft DPG-Frühjahrstagung
Berlin, Germany, 17.03.–22.03.2024.
- *Perovskites.*
E13 Summer School
Nassfeld, Austria, 18.07.–21.07.2023.
- *Solar Cell Characterization.*
E13 Summer School
Nassfeld, Austria, 12.07.–15.07.2022.

Posters

- K. Sun, R. Guo, J. E. Heger, M. A. Reus, L. V. Spanier, S. Bernstroff, P. Müller-Buschbaum.
Operando study of humidity on the performance of perovskite solar cells.
MLZ User Meeting 2022, 08 – 09 December 2022
- K. Sun, R. Guo, L. F. Huber, M. A. Reus, J. Zhou, M. Schwartzkopf, S. V. Roth, P. Müller-Buschbaum.
In-situ observation of growth mechanisms during printing of 2D perovskite film.
SolTech Conference 2022, 10 – 13 October 2022
- K. Sun, R. Guo, L. F. Huber, M. A. Reus, J. Zhou, M. Schwartzkopf, S. V. Roth, P. Müller-Buschbaum.
In-situ observation of growth mechanisms during printing of 2D perovskite film.
e-conversion Conference 2022, 04 – 07 October 2022
- K. Sun, R. Guo, J. E. Heger, M. A. Reus, L. V. Spanier, S. Bernstroff, P. Müller-Buschbaum.
Operando study of light and moisture induced degradation of perovskite solar cell.
DPG conference Regensburg, 04 – 09 September 2022
- K. Sun, R. Guo, J. E. Heger, M. A. Reus, L. V. Spanier, S. Bernstroff, P. Müller-Buschbaum.
Operando study of light and moisture induced degradation of perovskite solar cell.
12th Energy Colloquium, 28 July 2022
- K. Sun, P. Müller-Buschbaum.
Operando study of humidity on the performance of perovskite solar cell.
MLZ User Meeting 2021, 07 – 08 December 2021
- K. Sun, P. Müller-Buschbaum
In-Operando study of humidity on the performance of perovskite solar cell.
DPG Spring Meeting, 28 September 2021
- K. Sun, P. Müller-Buschbaum.
In-situ Study of Compositional Engineering for Perovskite Solar Cells.
11th Energy Colloquium of the Munich School of Engineering, 27 July 2021

Scientific Reports

- K. Sun, S. Bernstorff, P. Müller-Buschbaum. Degradation mechanism of layered perovskites under light and heat conditions. *Annual Report of Chair of Functional Materials*, 2023.
- K. Sun, S. Bernstorff, P. Müller-Buschbaum. Synergistic effect of light and moisture on the degradation of perovskite solar cells. *Annual Report of Chair of Functional Materials*, 2022.
- K. Sun, S. Bernstorff, P. Müller-Buschbaum. Degradation mechanism of perovskite solar cells under 1-sun illumination and humidity. *Annual Report of Chair of Functional Materials*, 2021.

Acknowledgments

This thesis not only presents the results of four years of dedicated work in E13 but also encapsulates the knowledge, achievements, abilities, challenges, and experiences encountered along the journey. I extend my heartfelt gratitude to my family, friends, colleagues, collaborators, and supervisor for their support and encouragement throughout this endeavor!

First and foremost, I would like to express my gratitude to my PhD supervisor, Peter Müller-Buschbaum, for welcoming me into his research group and for his invaluable guidance and support throughout my doctoral thesis. His continuous assistance and mentorship in data processing, academic writing, and project management have been instrumental in shaping my journey. Additionally, I am grateful for his trust in assigning me various tasks, which have not only expanded my skill set but also fortified my mindset. I am also appreciative of the freedom he has afforded me over the past four years, enabling me to explore and develop different projects.

I am immensely grateful to my collaborators and colleagues who have played crucial roles in this journey. Without the collaboration of Sigrid Bernstorff and Matthias Schwartzkopf, invaluable X-ray scattering data would not have been possible, leading to significant publications. Moreover, I owe a debt of gratitude to the previous generation of colleagues, including Dr. Renjun Guo, Dr. Suzhe Liang, Dr. Lennart Reb, Dr. Manuel Reus, Dr. Julian E. Heger, and Dr. Shanshan Yin, whose knowledge and expertise have been instrumental. In particular, I would like to acknowledge Dr. Renjun Guo for imparting numerous skills in device fabrication and scientific drawing, and for engaging in endless discussions to address my queries. I vividly recall my first day in the lab, where Dr. Lennart Reb provided me with my initial training on pipette, UV-vis spectroscopy, spin-coating, and more. His guidance during this transitional period exemplified what it means to be a mature and patient team leader. Additionally, I am indebted to Dr. Manuel Reus for his unwavering support during beamtime, tirelessly addressing my questions even at

5 am, and providing invaluable insights into GIWAXS. I extend my heartfelt thanks to my fellow beamtime members, including Dr. Julian E. Heger, Lukas Spanier, Zerui Li, Dr. Renjun Guo, Xiongzhuo Jiang, Linus Huber, and Simon Wegener, for their unwavering support during challenging beamtime sessions. Their presence was indispensable in navigating through stressful situations. Furthermore, I deeply appreciate the scientific discussions and insights shared by Xiongzhuo Jiang, Zerui Li, and Yuxin Liang. Their contributions have significantly enriched my research journey.

Moreover, without the following colleagues, a success of this dissertations will be impossible. Fabian Apfelbeck, Thomas Baier, Altantulga Buyan-Arivijikh, Lyuyang Chen, Xiaojing Ci, Christopher Everett, Reinhold Funer, Christina Geiger, Tianfu Guan, Constantin Harder, Zhaonan Jin, Xinyu Jiang, David Kosbahn, Morgan Le Dû, Lixing Li, Nian Li, Yanan Li, Dr. Anna Lena Oechsle, Guangjiu Pan, Thien An Pham, Dominik Petz, Ivana Pivarnikova, Ruoxuan Qi, Julija Reitenbach, Dr. Dominik Schwaiger, Dr. Ting Tian, Dr. Suo Tu, Dr. Apostolos Vagias, Dr. Peixi Wang, Dr. Christian Weindl, Alexander Weinzierl, Lea Westphal, Tianxiao Xiao, Zhuijun Xu, Yingying Yan, Jinsheng Zhang, Peiran Zhang, Feifei Zheng, Tianle Zheng, Huaying Zhong.

Carola Kappauf, Sanja Ulrich, and Marion Waletzki, I extend my heartfelt gratitude for your unwavering support and patience throughout the four years, especially in handling numerous paperwork and administrative tasks.

Huge thanks to my entire family for always standing by my side and providing unwavering support: Yuancheng Sun, Juan Li, Manman Sun, Li Lin. Special thanks to my fiancée, Yuxin Liang, for her selfless dedication and continuous support. I am deeply grateful to each one of you from the bottom of my heart.

Finally, I want to express my heartfelt gratitude to my parents, Yuancheng and Juan, for their unwavering love and support. There are no words to adequately express my gratefulness and love for you both. This dissertation is dedicated to you.